Multi-functional converter for three-phase motor drives : Modeling, analysis and fault-tolerant control

Xiaokang Zhang

N°d'ordre NNT : 2022LYSEI021

THESE de DOCTORAT DE L'UNIVERSITE DE LYON
opérée au sein de
L'Institut National des Sciences Appliquées de Lyon

Ecole Doctorale N° 160
Electronique, Electrotechnique, Automatique (EEA)

Spécialité de doctorat : Génie Electrique

Soutenue publiquement le 24/03/2022, par :

Xiaokang ZHANG

Multi-functional converter for three-phase motor drives: modeling, analysis and fault-tolerant control

---

Devant le jury composé de :

NAHID-MOBARAKEH, Babak	Professeur des universités McMaster University	Rapporteur
BETHOUX, Olivier	Professeur des universités Université Sorbonne	Rapporteur
DIALLO, Demba	Professeur des universités Université Paris-Saclay	Examinateur
LIN-SHI, Xuefang	Professeur des Universités INSA de Lyon	Directrice de thèse
GAUTHIER, Jean-Yves	Maître de Conférences INSA de Lyon	Co-encadrant de thèse

Département FEDORA – INSA Lyon - Ecoles Doctorales

SIGLE	ECOLE DOCTORALE	NOM ET COORDONNEES DU RESPONSABLE
CHIMIE	**CHIMIE DE LYON** **https://www.edchimie-lyon.fr** Sec. : Renée EL MELHEM Bât. Blaise PASCAL, 3e étage secretariat@edchimie-lyon.fr	**M. Stéphane DANIELE** C2P2-CPE LYON-UMR 5265 Bâtiment F308, BP 2077 43 Boulevard du 11 novembre 1918 69616 Villeurbanne **directeur@edchimie-lyon.fr**
E.E.A.	**ÉLECTRONIQUE, ÉLECTROTECHNIQUE, AUTOMATIQUE** **https://edeea.universite-lyon.fr** Sec. : Stéphanie CAUVIN Bâtiment Direction INSA Lyon Tél : 04.72.43.71.70 secretariat.edeea@insa-lyon.fr	**M. Philippe DELACHARTRE** INSA LYON Laboratoire CREATIS Bâtiment Blaise Pascal, 7 avenue Jean Capelle 69621 Villeurbanne CEDEX Tél : 04.72.43.88.63 **philippe.delachartre@insa-lyon.fr**
E2M2	**ÉVOLUTION, ÉCOSYSTÈME, MICROBIOLOGIE, MODÉLISATION** **http://e2m2.universite-lyon.fr** Sec. : Sylvie ROBERJOT Bât. Atrium, UCB Lyon 1 Tél : 04.72.44.83.62 secretariat.e2m2@univ-lyon1.fr	**M. Philippe NORMAND** Université Claude Bernard Lyon 1 UMR 5557 Lab. d'Ecologie Microbienne Bâtiment Mendel 43, boulevard du 11 Novembre 1918 69 622 Villeurbanne CEDEX **philippe.normand@univ-lyon1.fr**
EDISS	**INTERDISCIPLINAIRE SCIENCES-SANTÉ** **http://ediss.universite-lyon.fr** Sec. : Sylvie ROBERJOT Bât. Atrium, UCB Lyon 1 Tél : 04.72.44.83.62 secretariat.ediss@univ-lyon1.fr	**Mme Sylvie RICARD-BLUM** Institut de Chimie et Biochimie Moléculaires et Supramoléculaires (ICBMS) - UMR 5246 CNRS - Université Lyon 1 Bâtiment Raulin - 2ème étage Nord 43 Boulevard du 11 novembre 1918 69622 Villeurbanne Cedex Tél : +33(0)4 72 44 82 32 **sylvie.ricard-blum@univ-lyon1.fr**
INFOMATHS	**INFORMATIQUE ET MATHÉMATIQUES** **http://edinfomaths.universite-lyon.fr** Sec. : Renée EL MELHEM Bât. Blaise PASCAL, 3e étage Tél : 04.72.43.80.46 infomaths@univ-lyon1.fr	**M. Hamamache KHEDDOUCI** Université Claude Bernard Lyon 1 Bât. Nautibus 43, Boulevard du 11 novembre 1918 69 622 Villeurbanne Cedex France Tél : 04.72.44.83.69 **hamamache.kheddouci@univ-lyon1.fr**
Matériaux	**MATÉRIAUX DE LYON** **http://ed34.universite-lyon.fr** Sec. : Yann DE ORDENANA Tél : 04.72.18.62.44 yann.de-ordenana@ec-lyon.fr	**M. Stéphane BENAYOUN** Ecole Centrale de Lyon Laboratoire LTDS 36 avenue Guy de Collongue 69134 Ecully CEDEX Tél : 04.72.18.64.37 **stephane.benayoun@ec-lyon.fr**
MEGA	**MÉCANIQUE, ÉNERGÉTIQUE, GÉNIE CIVIL, ACOUSTIQUE** **http://edmega.universite-lyon.fr** Sec. : Stéphanie CAUVIN Tél : 04.72.43.71.70 Bâtiment Direction INSA Lyon mega@insa-lyon.fr	**M. Jocelyn BONJOUR** INSA Lyon Laboratoire CETHIL Bâtiment Sadi-Carnot 9, rue de la Physique 69621 Villeurbanne CEDEX **jocelyn.bonjour@insa-lyon.fr**
ScSo	**ScSo*** **https://edsciencessociales.universite-lyon.fr** Sec. : Mélina FAVETON INSA : J.Y. TOUSSAINT Tél : 04.78.69.77.79 melina.faveton@univ-lyon2.fr	**M. Christian MONTES** Université Lumière Lyon 2 86 Rue Pasteur 69365 Lyon CEDEX 07 **christian.montes@univ-lyon2.fr**

*ScSo : Histoire, Géographie, Aménagement, Urbanisme, Archéologie, Science politique, Sociologie, Anthropologie

On ne voit bien qu'avec le coeur.

Antoine de SAINT-EXUPÉRY

Acknowledgement

Up to now, I have been spending unforgettable three years at Lyon, in France. It is undoubtedly a pretty precious experience in my life. I feel really grateful and fortunate that I could have the opportunity to carry out a scientific research at the Laboratory of AMPERE with my supervisors, Prof. Xuefang Lin-Shi and Dr. Jean-Yves Gauthier, where I began to touch the door of scientific research, learned to built up my confidence and gained comprehensive research training.

First and foremost, I would like to express the best sincere gratitude to my supervisor, Prof. Xuefang Lin-Shi, who has inspired me a lot in the past three years. She is not only a superexcellent supervisor in my research but also an amiable friend in my daily life. I deeply appreciate her patient guidance and constructive advice in numerous difficulties which I have ever encountered. In addition to the academic guidance, she always encourages me to participate in international conferences so that I can keep tracking the research trends and discuss with many excellent researchers, which is indeed significant to my research insight.

My deepest appreciation also goes to my co-supervisor, Dr. Jean-Yves Gauthier, for his self-giving guidance and help in my research. He is an enthusiastic and passionate scholar, who can always answer my questions and his door is invariably open for me. Every time talk with him, I can always obtain some new ideas and thoughts to improve my research. In addition to the academic guidance, Dr. Jean-Yves Gauthier always encourages me to speak French. After the first year, he tried to talk to me in French patiently. Day by day, my french is improved gradually. As a result, I can give a Travaux Pratique (TP) course (80 h) to students in French at INSA de Lyon.

Then, I would like to send my sincere thanks to the jury of my thesis: Prof. Babak NAHID-MOBARAKEH, Prof. Olivier BETHOUX and Prof. Demba DIALLO, for their valuable and professional comments and suggestions which significantly improved the quality of this manuscript.

I would also like to thank all the colleagues of the laboratory of AMPERE who have helped me a lot directly or indirectly. Firstly, I would like to express my thanks to Prof. Bruno Allard and Prof. Christian Vollaire, who are the former director and present director of AMPERE, respectively, for their administrative assistance. At the same time, I would like to thank Ms. KHAMMALI Laura, for her indispensable administrative support. Then, I really appreciate Dr. Romain Delpoux, for his assistance in my first experimental test-bench. Meanwhile, I would like to say thanks to Dr. Jean-François Trégouët, for his valuable comments in my first paper. To be honest, his rigorous academic attitude has a great influence on me. I also want to say thanks to Prof. Xavier Bruno and Dr. Vincent Lechappe, for their suggestions and help to my teaching skills in the course of TP. I would like to thank my bro, Dr. Aboubacar Ndoye, for his support and encouragement on the way of my writing. I would also like to thank my friends, Mr. Adrien Prevost, Mr. Arnaud Duvernois, Mr. Laurent Schuller, Mr. Tangue Simon, Mr. Mian Mohammad Arsalan ASIF, Mr. Gabriel De Carvalho Ferreira Silva, Dr. Cedric Escudero. I can not list all the people of AMPERE, however, it is my great fortune to spend such memorable time with you.

Moreover, I would like to thank all my chinese friends, especially Dr. Xiaoyang Yue, Dr. Chenchen Chu, Dr. Ting Shi, Dr. Yaqiang Jin and Dr. Kelin Wu, for their selfless and infinite friendships and assistants.

Besides, I would like to send the most affectionate gratitude to my family, my parents, my grandparents, my sister, my brother-in-law and my little nephew. I would not be able to put an end to this journey without you.

Finally, I would like to thank my motherland (China) and China Scholarship Council (CSC) for the funding support.

Xiaokang Zhang
Lyon

Contents

List of Figures

List of Tables

Nomenclature

Acronymes

3-D	Three-dimension.
AC	Alternating current.
Back-EMF	Back electromotive force.
CFI	Capacitor-based four-leg inverter.
CFNI	Capacitor-based four-leg neutral-point-connected inverter.
DC	Direct current.
DCSUR	DC-source voltage utilization ratio.
DOF	Degree of freedom.
ESS	Energy storage system.
EV	Electric vehicle.
FFT	Fast fourier transform.
FI	Fundamental current.
FOC	Field-oriented control.
FV	Fundamental voltage.
GaN	Gallium nitride.
HEV	Hybrid electric vehicle.
IGBT	Insulated gate bipolar transistor.
KCL	Kirchhoff's current law.
KVL	Kirchhoff's voltage law.

LPF	low-pass filter.
MFCS	Multi-functional converter system.
MFCS-I	A variant of the basic MFCS by using a series inductor.
MFCS-II	A variant of the basic MFCS by using an auxiliary inverter leg.
MPC	Model predictive control.
NP	Neutral point.
OPF	Open-phase fault.
PMSM	Permanent magnet synchronous machine.
PPRF	Post-Fault power rating factor.
PWM	pulse-width modulation.
RMS	Root mean square.
SFI	Switch-based four-leg inverter.
SFNI	Switch-based four-leg neutral-point-connected inverter.
SiC	Silicon carbide.
SOCF	Silicon overrating cost factor.
SPWM	Sinusoidal pulse width modulation.
SVPWM	Space vector PWM.
TRIAC	Triode for alternating current.
VSI	Voltage source inverter.
ZSVIPWM	Zero-sequence voltage injected PWM.

Notations

$\hat{x}$	Denote the predicted value of a variable (x).
$\overline{x}$	Denote the mean of a variable (x) in one electrical period.

$Eff1 = AC\,FUNDAMENT/DC\,RMS$ Normalization of the fundamental AC current (related to the fundamental torque) to the input current.

$Eff2 = DC\,RMS/AC\,FUNDAMENTAL$ Normalization of the input current to the fundamental AC current (related to the fundamental torque).

$x(k)$ Denote a variable (x) in the $(k)^{th}$ sampling interval.

$x(k+1)$ Denote a variable (x) in the $(k+1)^{th}$ sampling interval.

x_c Denote a variable (x) in the conventional drive.

x_f Denote a variable (x) of the MFCS-I in post-fault conditions.

x_m Denote a variable (x) in the basic MFCS.

x_mI Denote a variable (x) in the MFCS-I.

x_n Denote a variable (x) of the MFCS-I in normal conditions.

x^* Denote the reference of a variable (x).

Variables physiques

α_F Duty-cycle of the fourth leg in the MFCS-II.

α_h Average duty-cycle of the traction inverter.

$\boldsymbol{\alpha}_{ABC} := [\alpha_A \quad \alpha_B \quad \alpha_C]^T$ Duty-cycles of inverter's legs.

$\boldsymbol{\alpha}_{dq0} := [\alpha_d \quad \alpha_q \quad \alpha_0]^T$ Duty-cycles of the inverter converted into d-q-0 coordinate.

$\boldsymbol{\Phi}_{ABC} := [\Phi_A \quad \Phi_B \quad \Phi_C]^T$ Stator flux linkages of a PMSM in A-B-C coordinate.

$\boldsymbol{e}_{ABC} := [e_A \quad e_B \quad e_C]^T$ Back-EMFs of a PMSM.

$\boldsymbol{e}_{dq0} := [e_d \quad e_q \quad e_0]^T$ d-axis, q-axis and 0-axis back-EMFs.

$\boldsymbol{i_{s\_npj}}$ and $\boldsymbol{i_{s\_fpj}}$ Projections of the current vector in healthy conditions and in post-fault conditions, respectively.

$\boldsymbol{i_s}$ Current vector.

$\boldsymbol{i}_{ABC} := [i_A \quad i_B \quad i_C]^T$ Phase-currents of a PMSM in A-B-C coordinate.

$\boldsymbol{L}_{ABC}$ Inductance matrix of a PMSM.

$\boldsymbol{L}_{dq0} := diag(L_d \quad L_q \quad L_0)$ Inductance matrix in d-q-0 coordinate.

$\boldsymbol{u}_{ABC} := [u_{AN} \quad u_{BN} \quad u_{CN}]^T$ Phase-voltages of a PMSM in A-B-C coordinate.

$\boldsymbol{u}_{dq0} := [u_d \quad u_q \quad u_0]^T$ d-axis, q-axis and 0-axis voltages of a PMSM.

$\boldsymbol{u}_{invABC} := [u_{AO} \quad u_{BO} \quad u_{CO}]^T$ Terminal voltages of the inverter.

$\boldsymbol{u}_{invdq0} := [u_{invd} \quad u_{invq} \quad u_{inv0}]^T$ Terminal voltages of the inverter converted to d-q-0 coordinate.

ΔE	Energy provided by the power source u_{in} from point b to c.
Δi_A	Current ripple on phase-A.
Δu_{bus}	Voltage ripple on the DC-bus capacitor.
$\dot{\varepsilon_\omega}$	Integral action of the speed-loop.
η	Total efficiency.
ω_{Etraj}	Desired natural frequency of the second-order filter.
ω_m	Mechanical angular velocity of the rotor.
Φ_f	Permanent magnet flux linkage.
θ_e	Electrical position of the rotor.
ε	Error index between the predicted and measured currents.
ε_{th}	A threshold for the OPF detection.
ζ_{Etraj}	Desired damping ratio of the second-order filter.
a_L	Multiple of L_{aux} to L_0.
B_m	Coefficient of viscous friction.
C_{bus}	DC-bus capacitance.
E	Energy stored in the inductor and capacitor in the equivalent boost.
E^*	Energy reference of E.
E_{traj}	Desired energy trajectory in the equivalent boost.
f_{ele}	Electrical frequency of the motor.
i_{bus}	DC-bus current.
i_{lo}	Equivalent load current in the equivalent boost function.
i_N	Neutral current.
J_m	Rotational inertia of the motor.
K_ω, K_{ω_I}	Two feedback gains of the state feedback controller in the speed-loop.

K_Φ Torque coefficient.

k_{pk} Proportional gain of a PI controller.

L_σ, L_Σ and L_Δ Leakage inductance, average inductance and inductance fluctuation.

L_{AA}, L_{BB} and L_{CC} Self-inductance.

L_{aux} The series inductor of the MFCS-I.

L_E The equivalent inductance in the MFCS-I and MFCS-II.

m Modulation ratio

$m_0 = i_{0\_n}/i_{q\_n}$ Proportion between i_{0_n} and i_{q_n}.

$M_{AB} = M_{BA}$, $M_{AC} = M_{CA}$ and $M_{BC} = M_{CB}$ Mutual inductance.

m_i Current overrating ratio.

n Motor mechanical speed (rpm).

P_{in} Input power of the MFCS-I.

P_{mec} Mechanical power of a motor.

R Stator resistance of a PMSM.

r_0 Step-up ratio of the equivalent boost.

r_1 Value of DCSUR.

r_2 Proportion of zero-sequence voltage to the DC-source voltage.

R_{eq} The equivalent load of the equivalent function in the MFCS-I and MFCS-II.

R_{flo} Assessment index of a similar NP in the MFCS-I.

T_e Electromagnetic torque.

T_f Fundamental period.

T_{ik} Integral time coefficient of a PI controller.

T_L Load torque.

T_{set} OPF detection time.

T_s Switching period.

u_{bias} Voltage bias in the MFCS-I.

u_{bus_filter}	Average value of the DC-bus voltage.
u_{bus_fmax}	Peak value of u_{bus}.
u_{bus_fmin}	valley value of u_{bus}.
u_{bus}	DC-bus voltage.
u_{in}	DC-source voltage.
u_{NO}	Neutral point voltage.
u_{XN1amp}	Amplitude of the fundamental phase-voltage.
u^*_{XN1}	Fundamental voltage reference.
u_{XNamp}	Amplitude of the actual phase-voltage.
u^*_{XN}	Phase-voltage reference.
u_{ZS}	Zero-sequence voltage of the motor.

Résumé

Cette thèse porte sur un système d'entraînement de machine synchrone à aimants permanents triphasée alimentée par un onduleur qui intègre un étage de conversion continu/continu, en utilisant le point neutre de la machine. Cette architecture, appelée système de convertisseur multifonctionnel (MFCS), peut être avantageusement utilisée dans des applications de traction automobile dans le cas où une élévation de tension est nécessaire. Premièrement, une analyse approfondie est présentée afin de comprendre et de modéliser le MFCS. Une méthode de modulation spécifique est, de plus, proposée utilisant la particularité que le courant homopolaire n'est pas nul. Deuxièmement, deux nouvelles variantes nommées MFCS-I et MFCS-II ont été conçues afin d'améliorer le MFCS de base. Pour la première, une inductance en série est ajoutée pour diminuer l'ondulation du courant. Pour la seconde, l'ajout d'un bras d'onduleur auxiliaire améliore le rapport d'élévation effectif de la tension. Pour contrôler ces variantes de MFCSs, une stratégie de commande universelle est développée dans laquelle une commande vectorielle peut être prise en compte pour la fonction moteur et un contrôleur basé sur la platitude différentielle est utilisé pour réguler la tension du bus continu. Troisièmement, compte tenu de la connexion intrinsèque du point neutre dans le MFCS-I, son potentiel de tolérance aux fautes contre un défaut de phase ouverte est exploré pour la première fois. Une étude théorique permet de formuler les conditions pour atteindre cette propriété et une nouvelle trajectoire vectorielle de courant est proposée, générant un couple constant et une tension moyenne stable du bus continu après un défaut. Pour finir, les idées et les stratégies de contrôle présentées ci-dessus sont systématiquement validées expérimentalement sur des plateformes de prototypage rapide de lois de commande.

Abstract

This thesis focuses on a two-level voltage-source-inverter fed three-phase permanent magnet synchronous machine drive which integrates an equivalent direct current (DC)/DC boost function by utilizing the machine's neutral point (NP). Such a drive system is referred to as multi-functional converter system (MFCS), and can be a promising alternative to the two-stage converter-based electric traction system in electric vehicles. First, to clearly reveal the mechanism, the average model of the basic MFCS is built. Then, different equivalent circuits are developed to explain the integrated boost function. Due to the conducting of the zero-sequence circuit, a specified modulation method named zero-sequence voltage injected pulse-width modulation is proposed. Second, to improve the basic MFCS, two new variants named MFCS-I and MFCS-II are further proposed. For the former, it employs a series inductor to suppress the current ripple. For the latter, it employs an auxiliary inverter leg to improve the effective step-up ratio. To control different MFCSs, a universal control strategy is proposed where the classic field-oriented control can still be used to control the motor function and a differential flatness-based controller is used to regulate the DC-bus voltage. Third, considering the innately connected NP in the MFCS-I, its fault-tolerant potential against an open-phase fault is explored for the first time. To this end, three constraints are found to achieve the fault-tolerant possibility. Then, a novel post-fault current vector trajectory is proposed which contributes to a constant torque and a stable average DC-bus voltage in post-fault conditions. Finally, the effectiveness of above ideas and control strategies is verified on experimental platforms.

Résumé étendu en français

Contexte et motivation

Le travail présenté dans ce manuscrit de thèse porte sur la modélisation, la commande et l'exploration des capacités de tolérance aux fautes des systèmes de conversion multifonctionnels (MFCS) pour alimenter des machines électriques triphasées. Cette thèse a été financée par le China Scholarship Council (CSC) et s'est déroulée au sein du Laboratoire AMPERE, sur le site de l'INSA de LYON à Villeurbanne pendant 42 mois. Ces travaux sont à l'interface de deux disciplines scientifiques : le Génie Électrique et l'Automatique. Plus précisément, ils sont liés aux domaines de recherche des machines électriques, de l'électronique de puissance et de la commande des systèmes dynamiques.

Les préoccupations environnementales et leurs exigences strictes motivent l'industrie actuelle à réduire les émissions de dioxyde de carbone[1]. Plus particulièrement, dans le domaine de l'industrie automobile, l'électrification des véhicules s'est imposée comme la meilleure solution pour le transport individuel vert et l'on prévoit une croissance importante de ce secteur d'activité au cours des prochaines décennies[2][3]. À l'heure actuelle, les niveaux d'électrification des véhicules peuvent être divisés en trois catégories : véhicule électrique hybride (HEV), véhicule électrique hybride rechargeable et véhicule électrique pur (EV)[4].

Dans ces véhicules, afin de connecter le système de stockage d'énergie (ESS) au moteur électrique de traction, deux configurations sont principalement adoptées[5][6] : (1) une architecture à un étage, dans laquelle l'ESS est directement connecté au bus à courant continu (DC) de l'onduleur de traction, comme indiqué sur la figure R.1(a) ; (2) une architecture à deux étages, dans laquelle un convertisseur DC/DC intermédiaire est utilisé, comme le montre la figure R.1(b). Dans le cas de la première architecture, la tension nominale de l'ESS détermine entièrement la tension du bus DC. Afin de répondre aux exigences de fonctionnement à grande vitesse et à haut rendement du moteur de traction, un niveau de tension relativement haut est requis sur le pack batterie. Cela complique la conception du pack batterie et engendre souvent une augmentation de la taille de celui-ci, car la haute tension est obtenue en empilant de nombreuses cellules élémentaires[7][8]. Sur la base des considérations ci-dessus et plus particulièrement dans le cadre des HEV [9]–[11], pour lesquels la limitation de la taille du pack batterie est plus stricte, de nombreux véhicules du marché ont adoptés une architecture à deux étages afin d'alimenter le système de traction électrique. Le tableau R.1 répertorie ainsi les caractéristiques de conception et certaines spécifications publiées de quatre HEV (Lexus LS600h 2008, Camry hybride, Prius 2004 et Prius 2010)[11].

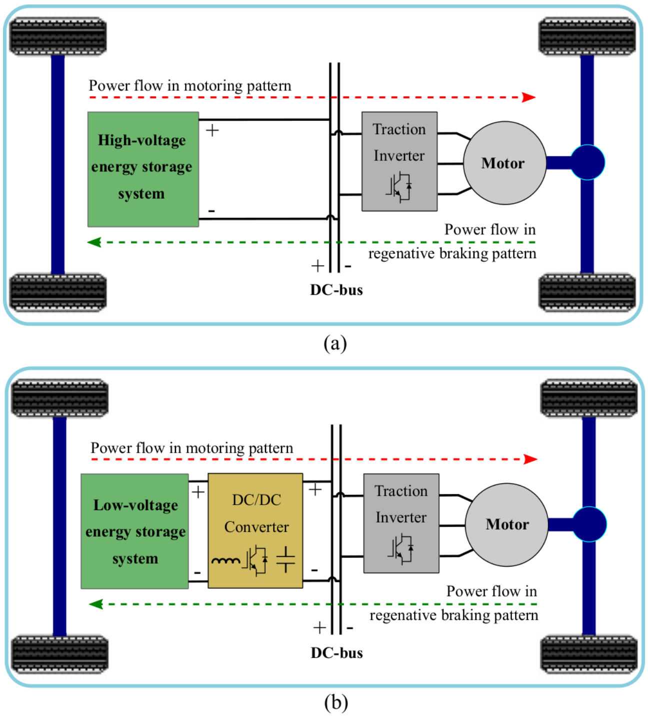

FIGURE R.1: Systèmes de traction électrique. (a) Configuration à un étage avec un ESS haute tension. (b) Configuration à deux étages avec un ESS basse tension et un convertisseur intermédiaire DC/DC boost.

TABLE R.1: Comparaison des HEV commerciaux en ce qui concerne les caractéristiques de conception et les spécifications publiées.

Caractéristique de conception	**2008 LS 600h**	**Hybrid Camry**	**2004 Prius**	**2010 Prius**
Puissance maximale du moteur	165 kW	105 kW	50 kW	60 kW
Tension du bus DC	288-650 V DC	250-650 V DC	200-500 V DC	200-650 V DC
Puissance nominale du convertisseur DC/DC	36,5 kW	30 kW	20 kW	27 kW
Tension de la batterie	288 V	244,8 V	201,6 V	201,6 V

Nous pouvons remarquer que la tension du bus DC est généralement 2 à 3 fois plus grande que la tension de la batterie. Ceci est possible grâce à l'utilisation d'un convertisseur

DC/DC intermédiaire. Différents types de convertisseurs ont été étudiés dans la littérature, tels que les convertisseurs élévateurs DC/DC à une seule branche [12], les convertisseurs DC/DC entrelacés[13] et les convertisseurs DC/DC à double pont actif[14]. Avec l'aide de ce convertisseur, le système de traction électrique est capable d'obtenir une tension de bus DC suffisante en l'absence d'un pack batteries haute tension et peut gérer de manière flexible le flux de puissance entre le moteur de traction et l'ESS[15]. Cependant, l'utilisation du convertisseur DC/DC supplémentaire apporte à son tour quelques inconvénients. D'une part, cela augmente le coût et le volume de l'ensemble du système de conversion et, d'autre part, la fiabilité du système peut être dégradée car plus de dispositifs électroniques de puissance sont utilisés.

Le niveau de fiabilité devient un critère de plus en plus important de manière générale et tout particulièrement dans le cadre de la traction électrique afin de garantir un meilleur niveau de service et une plus grande sécurité pour les passagers. Une manière de l'augmenter consiste à utiliser des systèmes qui sont capables de continuer à fonctionner malgré l'apparition d'un défaut électrique (circuit ouvert ou court-circuit). Dans le cadre de solutions conventionnelles d'alimentation des moteurs triphasés à partir d'un onduleur à deux niveau de tension (VSI), il est nécessaire d'ajouter des dispositifs auxiliaires afin d'atteindre cet objectif de tolérance aux fautes. Cependant, ces dispositifs auxiliaires augmentent le coût, le volume et le poids des systèmes de traction électrique.

Dans le domaine des variateurs pour moteurs à courant alternatif (AC) triphasé, les systèmes de conversion multifonctionnels (MFCS) forment une catégorie spéciale de convertisseurs qui intègrent les fonctionnalités d'un convertisseur élévateur DC/DC et d'un onduleur DC/AC sur un seul VSI triphasé à deux niveaux. Ceci est rendu possible grâce à la connexion du point neutre du moteur électrique à la source d'alimentation DC, contrairement aux systèmes conventionnels pour lesquels le point neutre n'est pas connecté. Le MFCS est ainsi une alternative prometteuse pour remplacer le système de traction électrique à deux étages dans les EVs et les HEVs. Cependant, dans la littérature scientifique, le MFCS n'a pas reçu une grande attention jusqu'à présent, engendrant certaines lacunes concernant les explications du mécanisme et du principe du MFCS. Il n'y a que peu d'études approfondies à propos de la modélisation, de la méthode de modulation, de la stratégie de commande et de l'évaluation expérimentale.

Objectifs

Sur ces bases et sur le potentiel fort intérêt applicatif de ce système, cette thèse va étudier le MFCS de manière globale et approfondie avec les objectifs suivants :

- Le premier objectif de cette thèse sera d'apporter une vision explicite du mécanisme de conversion du MFCS de base. Il s'agira d'expliquer comment la fonctionnalité d'élévation de tension (convertisseur DC/DC équivalent) apparaît dans ce système grâce à la simple connexion du point neutre du moteur à courant alternatif triphasé. Étant donné que le point neutre est connecté, un courant homopolaire circule. Ainsi, les méthodes de modulation conventionnelles ne sont pas applicables dans le MFCS de base. Pour répondre à ce problème, une méthode de modulation spéciale est nécessaire.

- Certains inconvénients existent dans le MFCS de base comme le fait que les ondulations de courant sont plus importantes, ce qui augmente les pertes fer ou encore que le rapport d'élévation du convertisseur DC/DC équivalent est limité. Par conséquent, le second objectif sera d'améliorer ce MFCS de base. D'autre part, une comparaison complète avec le système conventionnel à deux étages est nécessaire pour clarifier les avantages et les inconvénients.

- Compte tenu de la connexion naturelle du point neutre dans ces systèmes, il existe une possibilité de réaliser des opérations tolérantes aux fautes sans utiliser de composants auxiliaires lorsqu'un défaut en phase ouverte (OPF) se produit dans les MFCS. Le dernier objectif sera donc d'explorer cette piste et de tester cette capacité.

Chapitre 1 : Opportunités apportées par le point neutre d'un moteur triphasé

Une machine à courant alternatif triphasé a trois enroulements, qui peuvent être connectés de deux manières - étoile (Y) ou triangle (Δ). dans le cas de la connexion en Y, le point neutre (NP) devient accessible. Dans la plupart des cas, le NP n'est pas utilisé et caché à l'intérieur de la coque du moteur. Cependant, dans certaines applications spéciales, ce NP peut être sorti et utilisé pour obtenir des avantages supplémentaires.

Le MFCS est un exemple qui utilise le NP pour obtenir un convertisseur boost DC/DC équivalent pour un moteur almenté par un VSI classique sans utiliser de composants supplémentaires. L'idée du MFCS de base remonte à environ vingt ans où il a d'abord été proposé pour les systèmes de transmission électrique dans les véhicules électriques hybrides par Toyota et Fuji Electric Co., Ltd., au Japon. Afin de réduire le coût et le volume du système de groupe motopropulseur configuré à deux étages, les ingénieurs et les chercheurs de Toyota et Fuji Electric ont tenté de supprimer l'étage DC/DC. Pour conserver cette fonctionnalité, le NP des moteurs de traction est alors volontairement connecté. Le MFCS de base se compose d'un moteur AC avec neutre sorti, d'un VSI triphasé à deux niveaux et de deux sources DC, mais pas de convertisseur DC/DC. Les principales caractéristiques du MFCS de base peuvent être résumées comme suit :

- Doter un variateur de fréquence triphasé de la fonctionnalité d'un convertisseur DC/DC en connectant exclusivement le NP du moteur qui est rarement utilisé dans un variateur conventionnel.

- Utiliser l'inductance homopolaire du moteur en tant qu'inductance de filtrage et réutiliser l'onduleur de traction comme hacheur équivalent.

Comme le montre le schéma du MFCS de base sur la figure R.2, la source DC haute tension (v_h) est connectée du côté du bus DC. Et contrairement à une configuration conventionnelle, la source DC basse tension (v_l) est connectée au NP du moteur. Étant donné que le NP est connecté à une source d'alimentation, le MFCS de base est similaire à un convertisseur DC/DC multiphase à trois branches où les trois enroulements du moteur auront le rôle d'inductances.

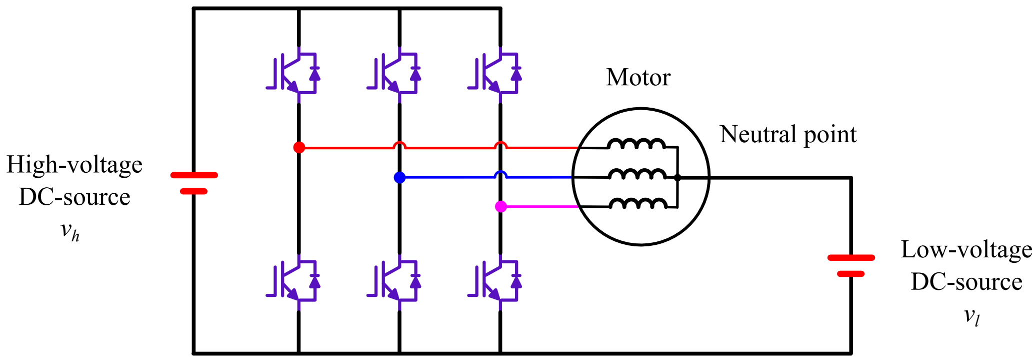

FIGURE R.2: Schéma électrique du MFCS de base.

En plus du MFCS de base, des idées similaires peuvent également être trouvées dans la littérature. Par exemple, le MFCS à deux étages, le MFCS à deux moteurs, etc. Dans le domaine des chargeurs embarqués, le système de traction peut être également reconfiguré en convertisseur boost avec correction du facteur de puissance (PFC) ou en convertisseur abaisseur en connectant le NP des moteurs de traction.

De plus, dans le domaine des variateurs AC triphasés tolérants aux fautes, le NP peut également être utilisé pour fournir un chemin de circulation pour les courants homopolaires afin qu'un couple constant puisse être maintenu lorsqu'un défaut en phase ouverte (OPF) se produit. Il existe deux topologies tolérantes aux fautes classiques qui utilisent le NP pour tolérer un OPF, comme le montre la figure R.3 et la figure R.4. La première, nommée CFNI, consiste à connecter le point neutre au point médian du bus DC grâce à un interrupteur et un pont de condensateur. La seconde, nommée SFI, connecte également le point neutre en cas de défaut mais, cette fois-ci à un quatrième bras de pont constitué de transistors.

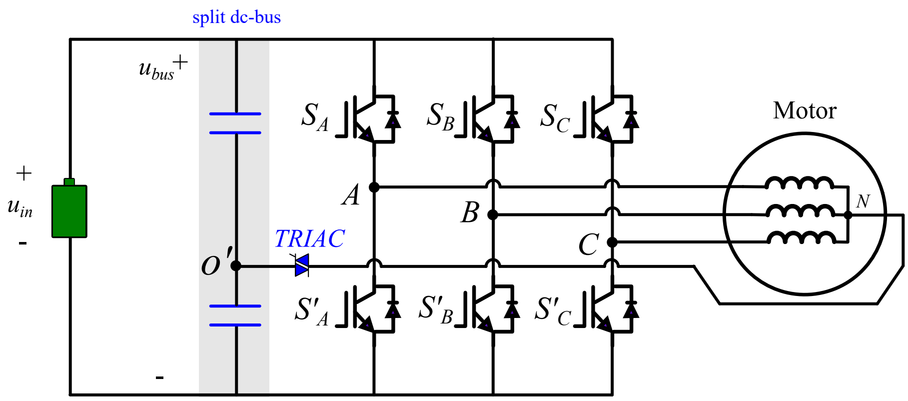

FIGURE R.3: Schéma du CFNI.

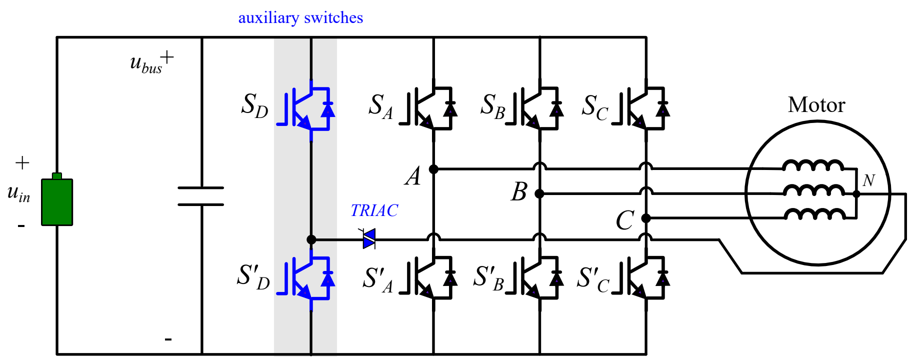

FIGURE R.4: Schéma du SFNI.

En conséquence, on peut conclure qu'il existe deux opportunités créées par l'utilisation du NP:

- **Opportunité 1:** Utilisation de l'homopolaire pour obtenir une conversion DC/DC à bas prix.
- **Opportunité 2:** Possibilité de tolérer un défaut en OPF en créant champ tournant.

Chapitre 2: Analyse d'un MFCS de base avec PMSM

Dans ce chapitre, nous étudions de manière exhaustive le MFCS basé sur une machine synchrone à aimants permanents (PMSM). Tout d'abord, le modèle moyen de ce système peut être construit en se basant sur les lois de Kirchhoff et sur l'approche classique de définition des variables correspondant à une moyenne temporelle sur une période de découpage. En coordonnées d-q-0, le modèle est :

$$\begin{cases} \alpha_d u_{bus} = u_d = Ri_d + L_d \dfrac{\mathrm{d}i_d}{\mathrm{d}t} - \omega_e L_q i_q \\ \alpha_q u_{bus} = u_q = Ri_q + L_q \dfrac{\mathrm{d}i_q}{\mathrm{d}t} + \omega_e (L_d i_d + \Phi_m) \\ \alpha_h u_{bus} = -\dfrac{R}{3} i_N - \dfrac{L_0}{3} \dfrac{\mathrm{d}i_N}{\mathrm{d}t} + u_{in} \\ \quad i_{bus} = C_{bus} \dfrac{\mathrm{d}u_{bus}}{\mathrm{d}t} = \alpha_h i_N - \underbrace{(\alpha_d i_d + \alpha_q i_q)}_{i_{lo}} \end{cases} \tag{R.1}$$

où α_d est le rapport cyclique sur l'axe d; α_q est le rapport cyclique sur l'axe q; α_h est le rapport cyclique moyen; u_{bus} est la tension du bus DC; u_d et u_q sont les tensions aux bornes du moteur sur les axes d et q respectivement; i_d et i_q sont les courants dans le moteur sur les axes d et q respectivement; i_{bus} est le courant du bus; i_N est le courant dans le neutre; L_d, L_q et L_0 sont respectivement les inductances d-q-0 du moteur; R est la résistance du moteur; u_{in} est la tension de la source DC; C_{bus} est la capacité du condensateur du bus DC; i_{lo} est un courant équivalent.

D'après l'équation (R.1), il est possible de construire un circuit équivalent du MFCS, comme le montre la figure R.5. Il est bien connu que l'utilisation de la commande vectorielle facilite la commande d'un moteur à courant alternatif en découplant son couple électromagnétique et sa gestion du flux. Dans le repère d-q, un moteur à courant alternatif peut être considéré comme un moteur à courant continu équivalent. Par conséquent, nous pouvons utiliser un hacheur équivalent pour alimenter un moteur à courant continu équivalent afin de représenter la fonction motrice du MFCS. Pour incarner la signification physique de α_d et α_q, nous utilisons deux ponts en H virtuels nommés « H1 » et « H2 » pour piloter le moteur à courant continu équivalent. Les deux ponts en H sont construits par huit commutateurs virtuels S_{v1}, S'_{v1}, S_{v2}, S'_{v2}, S_{v3}, S'_{v3}, S_{v4} et S'_{v4}. Pour être plus précis, α_d représente la différence entre les rapports cycliques de conduction de S_{v3} et S_{v4} ; α_q représente la différence entre les rapports cycliques de conduction de S_{v2} et S_{v5}. Ceci permet de représenter physiquement les deux premières équations de (R.1). Afin d'obtenir une signification physique pour les deux dernières équations de (R.1), nous introduisons un hacheur virtuel 'C1' qui est construit par deux commutateurs virtuels S_{v1} et S'_{v1}. Étant donné que les rapports cycliques de l'onduleur (α_A, α_B et α_C) sont compris entre 0 et 1, la plage accessible pour $\alpha_h = (\alpha_A + \alpha_B + \alpha_C)/3$ est aussi (0-1). Par conséquent, α_h peut être parfaitement représenté par le hacheur virtuel dans le modèle moyen, où α_h désigne le rapport cyclique de conduction de S_{v1}. Dans ce cas, la troisième équation de (R.1) est visualisée par le contour 'K' sur la figure R.5. La quatrième équation de (R.1) est représentée par le nœud 'P'. Par conséquent, nous pouvons affirmer que les deux dernières équations de (R.1) peuvent être représentées par un convertisseur élévateur DC/DC équivalent. L'inductance homopolaire

$L_0/3$ joue le rôle d'inductance dans la fonction boost. Enfin, l'ensemble du système MFCS peut être considéré comme un variateur pour moteur à courant continu à deux étages. Le hacheur équivalent du moteur à courant continu équivalent peut être considéré comme une charge équivalente pour le convertisseur élévateur DC/DC équivalent. Le courant de charge équivalent i_{lo} est égal à $(\alpha_d i_d + \alpha_q i_q)$.

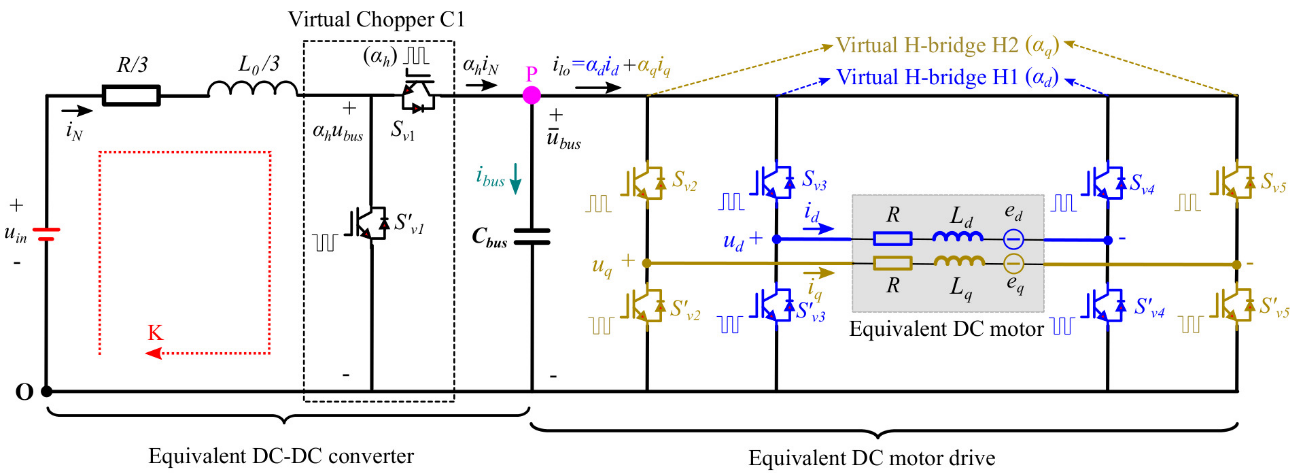

FIGURE R.5: Circuit équivalent du MFCS basé sur un PMSM.

En ce qui concerne la modulation, comme le neutre est relié, la technique de modulation de largeur d'impulsion vectorielle (SVPWM) ne peut pas être utilisée car elle injecte naturellement des tensions avec des harmoniques multiples de 3. Pour résoudre ce problème, nous proposons une nouvelle technique de modulation appelée modulation de largeur d'impulsion avec injection de tension homopolaire (ZSVIPWM). Comme le montre la figure R.6, en plus de la tension fondamentale, une composante homopolaire constante est requise. En utilisant une méthode d'échantillonnage régulière, le rapport cyclique (α_X) pour le bras X est obtenu de la manière suivante :

$$\alpha_X = \frac{u_{XN}{}^* + u_{in}}{u_{bus}} = \alpha_h + \frac{u_{XN1}{}^*}{u_{bus}} \tag{R.2}$$

où u^*_{XN} est la référence de tension de phase réelle; u^*_{XN1} est la référence de tension fondamentale.

Enfin, des expériences comparatives ont été réalisées sur un banc d'essai de 52,5 W. Les principales caractéristiques du MFCS par rapport au variateur classique sont résumées dans le tableau R.2. Les performances en régime permanent sont similaires. La fonction d'élévation de la tension (convertisseur DC/DC équivalent) permet bien d'augmenter le ratio d'utilisation de la tension (DCSUR). Cependant, l'ajout de la fonctionnalité boost mène à une ondulation du courant du MFCS beaucoup plus importante ainsi qu'un rendement de conversion moins bon.

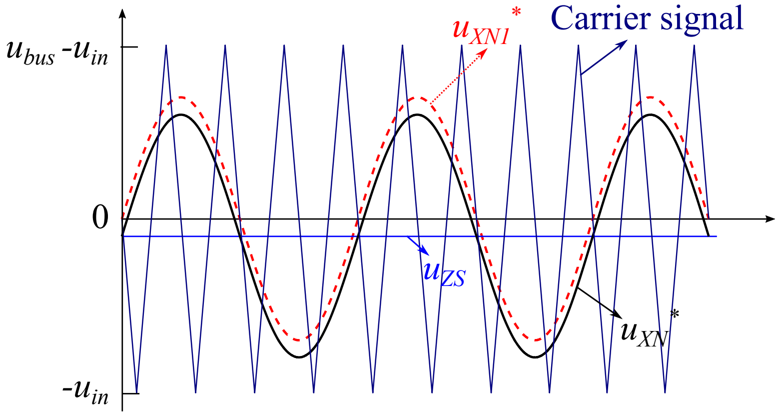

FIGURE R.6: Schéma de principe de ZSVIPWM.

TABLE R.2: Principales caractéristiques du MFCS par rapport au variateur conventionnel.

Caractéristique	Évaluation
Performances en régime permanent	Similaires
Ratio d'utilisation de la tension	Plus grand (1 vs 0,58)
Fonction boost intégrée	OUI vs NON
Ondulation du courant	Plus grande
Pertes	Plus importantes (cas d'une PMSM de 52,5 W : 11,5%)

Chapitre 3 : Améliorations du MFCS de base et stratégie générique de commande en boucle fermée

Le MFCS de base présente deux inconvénients majeurs. Le premier est la plus grande ondulation de courant causée par le fait que la tension de neutre est fixe, ce qui entraîne plus de pertes de fer. Le deuxième problème est que le rapport d'augmentation effectif maximum du boost équivalent n'est que de 2.

Afin de supprimer l'ondulation du courant, une évolution de cette architecture, nommée MFCS-I, est proposée en ajoutant une inductance en série, comme le montre la figure R.7.

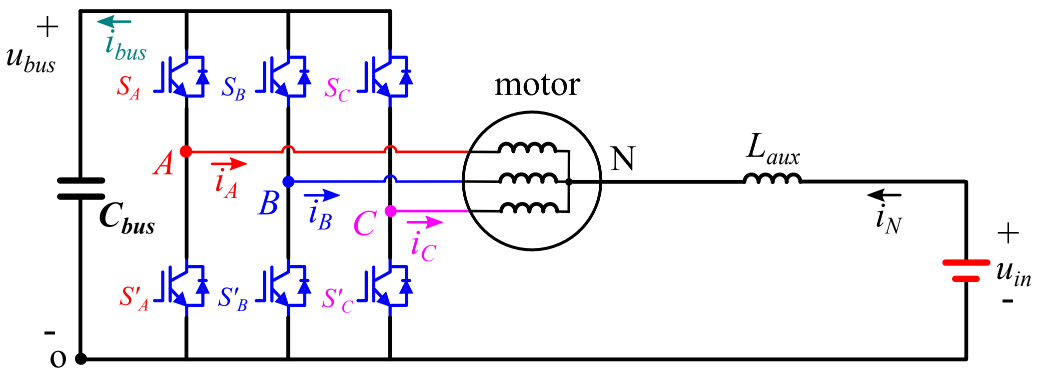

FIGURE R.7: Schéma électrique du MFCS-I (ajout d'une inductance en série L_{aux}).

Le modèle moyen du MFCS-I peut s'écrire de la manière suivante :

$$\begin{cases} \alpha_d u_{bus} = u_d = Ri_d + L_d \dfrac{\mathrm{d}i_d}{\mathrm{d}t} - \omega_e L_q i_q \\ \alpha_q u_{bus} = u_q = Ri_q + L_q \dfrac{\mathrm{d}i_q}{\mathrm{d}t} + \omega_e (L_d i_d + \Phi_m) \\ \alpha_h u_{bus} = -\dfrac{R}{3} i_N - \underbrace{(\dfrac{L_0}{3} + L_{aux})}_{L_E} \dfrac{\mathrm{d}i_N}{\mathrm{d}t} + u_{in} \\ \quad i_{bus} = C_{bus} \dfrac{\mathrm{d}u_{bus}}{\mathrm{d}t} = \alpha_h i_N - \underbrace{(\alpha_d i_d + \alpha_q i_q)}_{i_{lo}} \end{cases} \tag{R.3}$$

où L_E est une inductance équivalente.

Évidemment, on peut conclure que l'ajout de l'inductance en série augmente de fait l'inductance équivalente du boost équivalent. Par conséquent, l'ondulation des courants homopolaires (ou du courant de neutre) peut être réduite, limitant ainsi l'ondulation totale des courants et les pertes fer. Théoriquement, une inductance série d'une valeur de cinq fois l'inductance homopolaire du moteur peut conduire à un NP flottant similaire à celui obtenu avec un variateur conventionnel.

Cependant, dans cette architecture, le rapport de surélévation effectif du MFCS-I reste limité à 2. Afin de l'augmenter, une nouvelle architecture, nommée MFCS-II, est proposée en utilisant un bras de pont auxiliaire, comme le montre la figure R.8.

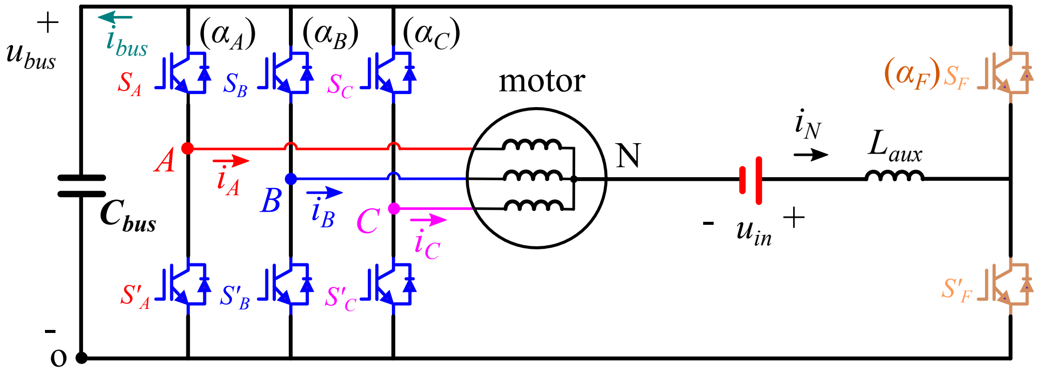

FIGURE R.8: Schéma électrique du circuit du MFCS-II avec ajout d'un bras de pont.

Le modèle moyen du MFCS-II peut également être construit :

$$\begin{cases} \alpha_d u_{bus} = u_d = Ri_d + L_d \dfrac{\mathrm{d}i_d}{\mathrm{d}t} - \omega_e L_q i_q \\ \alpha_q u_{bus} = u_q = Ri_q + L_q \dfrac{\mathrm{d}i_q}{\mathrm{d}t} + \omega_e (L_d i_d + \Phi_m) \\ (\alpha_F - \alpha_h) u_{bus} = -\dfrac{R}{3} i_N - \underbrace{(\dfrac{L_0}{3} + L_{aux})}_{L_E} \dfrac{\mathrm{d}i_N}{\mathrm{d}t} + u_{in} \\ i_{bus} = C_{bus} \dfrac{\mathrm{d}u_{bus}}{\mathrm{d}t} = (\alpha_F - \alpha_h) i_N - \underbrace{(\alpha_d i_d + \alpha_q i_q)}_{i_{lo}} \end{cases} \tag{R.4}$$

où α_F est le rapport cyclique du quatrième bras.

En régime permanent, le rapport de surélévation effectif r_0 et le DCSUR r_1 de ce convertisseur en fonction du rapport cyclique α_F sont indiqués sur la figure R.9. Dans la région 1, r_0 et r_1 sont tous deux positifs alors qu'ils sont négatifs dans la région 2. Dans le cas présenté ici où u_{in} est positif, le MFCS-II doit être utilisé dans la région 1. Ainsi, la plage disponible de α_F est (0,5-1). Lorsque α_F vaut 1, r_0 vaut 2 et r_1 vaut 1 : ce cas particulier correspond au MFCS-I. En diminuant α_F, r_0 et r_1 augmentent. Lorsque α_F tend vers 0,5, r_0 et r_1 tendent vers l'infini : cela indique que le MFCS-II est capable d'atteindre un rapport d'augmentation théoriquement très élevé et n'est plus limité comme dans le MFCS classique. Bien-entendu, comme pour un convertisseur élévateur DC/DC classique, son rapport d'élévation sera limité par les contraintes physiques des composants.

Des travaux ont été également réalisés concernant la stratégie de commande. Le schéma fonctionnel de cette stratégie de commande en boucle fermée (universelle pour le MFCS-I et le MFCS-II) est illustré sur la figure R.10. Une référence de courant i_q^* est obtenue, soit directement lors d'un pilotage en couple, soit via un régulateur de vitesse. La référence de courant i_d^* sera définie à 0 car il s'agit ici de commander un PMSM avec aimants montés en surface et sans

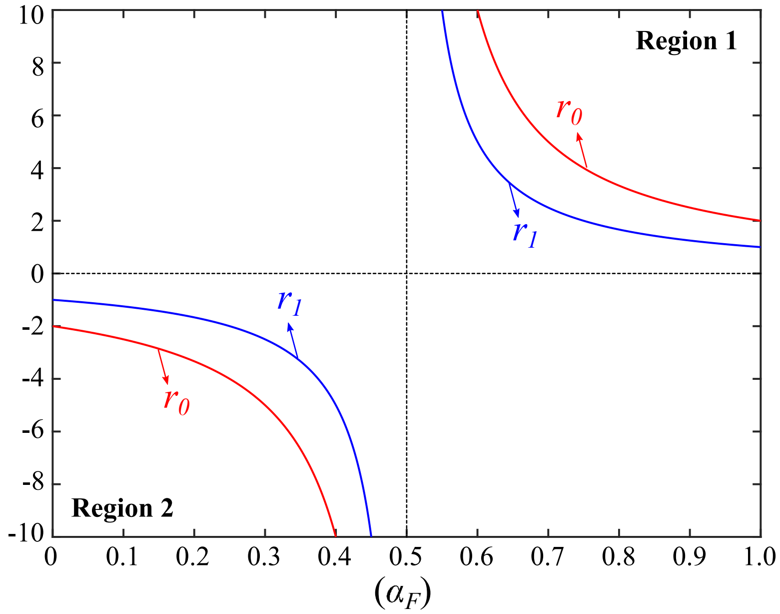

FIGURE R.9: Rapport de surélévation effectif r_0 et DCSUR r_1 du MFCS-II en fonction du rapport cyclique α_F.

utiliser de défluxage pour atteindre des modes de sur-vitesse. Ensuite, les deux références de courant (i_d^* et i_q^*) sont envoyées vers des régulateurs PI avec découplage afin de produire les tensions de référence u_d^* et u_q^*. En utilisant la transformation de Park inverse, les référence de tension fondamentale u_{AN1}^*, u_{BN1}^* et u_{CN1}^* sont obtenues. Un contrôleur basé sur la platitude différentielle est adopté pour asservir la référence de tension du bus continu u_{bus}^{ref} pour obtenir la variable de commande générale α_E. Pour le MFCS-I, α_E est directement utilisé pour générer les rapports cycliques réels α_A, α_B et α_C basés sur l'algorithme ZSVIPWM présenté dans (2.23). Pour le MFCS-II, α_h est défini à 0,5 dans l'algorithme ZSVIPWM (Une modulation SPWM classique est utilisée du côté de l'onduleur). Par conséquent, α_E est utilisé pour générer le rapport cyclique du 4ème bras dans le MFCS-II, via : $\alpha_F = \alpha_E + 0,5$.

Des expériences ont été menées sur un banc d'essai avec une PMSM de 1,2 kW pour vérifier l'efficacité des architectures MFCS-I et MFCS-II ainsi que leur commande.

Pour évaluer de manière réaliste le MFCS-I, celui-ci est comparé à un variateur basé sur un convertisseur à deux étages, où la même inductance L_{aux} est utilisée dans le convertisseur DC/DC boost. D'après les résultats expérimentaux, le MFCS-I admet un taux de distorsion harmonique un peu plus élevé sur les courants de phase mais il peut atteindre un meilleur rendement aussi bien en mode moteur qu'en mode de freinage par récupération, grâce au nombre réduit de ses dispositifs de commutation.

En ce qui concerne le MFCS-II, une source de courant continu de seulement 40 V est

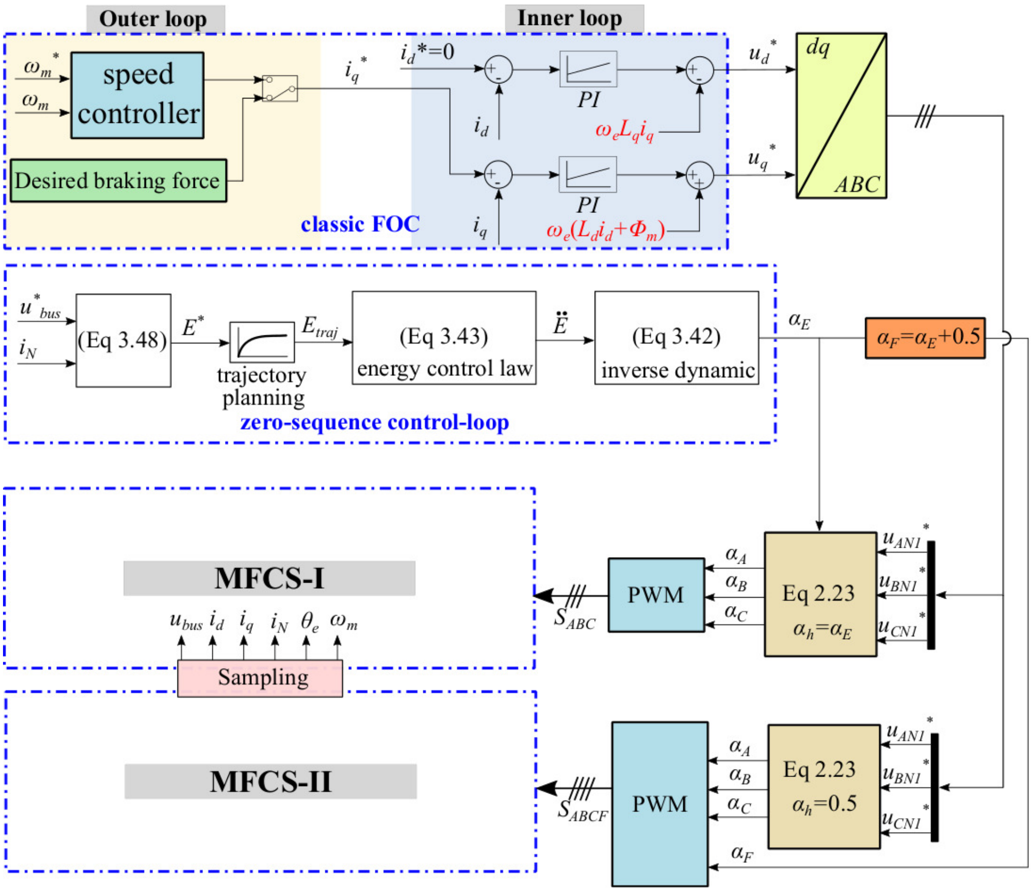

Figure R.10: Stratégie de commande universelle pour le MFCS-I et le MFCS-II.

utilisée. Et, d'après les validations expérimentales, nous pouvons observer une tension de bus continu qui peut atteindre environ 400 V avec un moteur qui peut alors fonctionner à grande vitesse et en condition de charge nominale.

Chapitre 4: Commande tolérante aux fautes du MFCS-I

D'après l'état de l'art présenté au chapitre 1, il existe quatre topologies tolérantes aux fautes typiques (CFI, SFI, CFNI et SFNI). Seules les deux topologies qui utilisent le point neutre du moteur (CFNI et SFNI) peuvent tolérer un défaut de phase ouverte se produisant sans aucune distinction du côté onduleur ou du côté machine électrique. Grâce à la possibilité d'avoir un courant homopolaire non nul, le moteur peut alors générer un champ magnétique tournant avec seulement deux phases actives. Cependant, le CFNI et le SFNI nécessitent toujours des composants additionnels (une paire de condensateurs séparés, deux IGBT auxiliaires et un TRIAC) pour pouvoir atteindre cette tolérance aux fautes. Ces composants additionnels augmentent non seulement le coût de l'ensemble du système, mais compliquent également le circuit de commande car des signaux de commande supplémentaires doivent être générés par la carte de commande principale et cela affectera indirectement la fiabilité du système.

Grâce au point neutre intrinsèquement connecté dans le MFCS-I, celui-ci possède une tolérance aux fautes vis-à-vis d'une OPF sans utiliser de composants additionnels.

Nous allons étudier le MFCS-I avec un défaut de phase ouverte (phase A) comme représenté sur la figure R.11. Étant donné que la phase A est déconnectée de l'alimentation, elle ne peut pas être utilisée pour générer le champ magnétique tournant dans la machine. En d'autres termes, seules les phases B et C sont disponibles pour contribuer à la conversion électro-mécanique après le défaut.

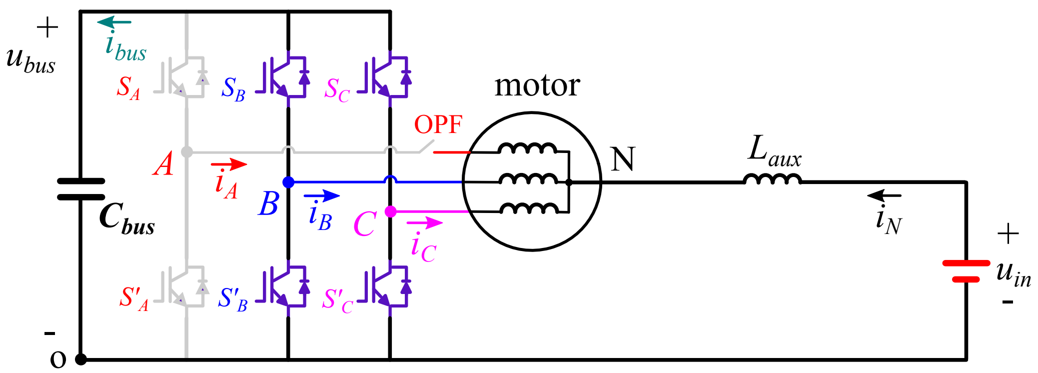

FIGURE R.11: Schéma du circuit du MFCS-I lorsque la phase A est ouverte.

Pour garantir un couple de sortie constant et une tension de bus DC moyenne stable dans ces conditions d'après défaut, trois contraintes sont à respecter et sont décrites successivement dans les sous-sections suivantes.

Contrainte 1 : conservation du couple

D'une manière générale, l'objectif principal d'une commande tolérante aux fautes pour un variateur est de préserver, si possible, le couple généré même dans les conditions de défauts. Ainsi, pour un PMSM monté en surface, le courant après défaut i_{q_f} doit être identique au courant i_{q_n} avant l'apparition du défaut (conditions normales de fonctionnement). Par conséquent, cela donne la première contrainte :

$$i_{q\_f} = i_{q\_n} \tag{R.5}$$

Contrainte 2 : relation entre les courants d-q-0 après défaut

Le défaut impose un courant de phase à zéro, cela engendre alors une dépendance entre les courants dans le repère d-q-0 qui ne sont plus indépendants. Cette relation est la suivante :

$$i_{0\_f} = i_{q\_f} sin\theta_e - i_{d\_f} cos\theta_e \tag{R.6}$$

Contrainte 3 : Préservation de la puissance moyenne

Entre les conditions de fonctionnement saines et les conditions de fonctionnement en défaut, la puissance de sortie du moteur devrait être invariante si tout se passe bien car le couple et la vitesse du moteur devraient être maintenues. Côté source, il n'est pas forcément toujours possible de maintenir une puissance constante, mais il est nécessaire tout de même de garantir une puissance moyenne constante sur une période électrique. La valeur moyenne du courant i_{0_f} (représenté par une barre) est directement liée à cette puissance moyenne dans ce système. On en déduit une troisième condition de fonctionnement :

$$\begin{gathered} \overline{P}_{in\_f} = u_{in}\bar{i}_{N\_f} = -3u_{in}\bar{i}_{0\_f} = \frac{P_{mec\_n}}{\eta} = P_{in\_n} = -3u_{in}i_{0\_n} \\ \Downarrow \\ \bar{i}_{0\_f} = i_{0\_n} \end{gathered} \tag{R.7}$$

Trajectoires des courants dans le repère d-q-0 en cas de défaut

Une trajectoire pour les courants i_{d_f}, i_{q_f} et i_{0_f} qui permet de respecter les 3 précédentes contraintes (R.5), (R.6) et (R.7) est proposée comme suit (les indices $_f$ correspondent aux courants après défaut et les indices $_n$ correspondent aux courants en régime de fonctionnement normal) :

$$\begin{cases} i_{d\_f} = i_{d\_n} - 2i_{0\_n}cos\theta_e \\ i_{q\_f} = i_{q\_n} \\ i_{0\_f} = i_{q\_n}sin\theta_e - i_{d\_n}cos\theta_e + 2i_{0\_n}cos^2\theta_e \\ \qquad = i_{q\_n}sin\theta_e - i_{d\_n}cos\theta_e + i_{0\_n} + i_{0\_n}cos2\theta_e \end{cases} \tag{R.8}$$

La figure R.12(a) décrit la trajectoire du courant (appelée $\boldsymbol{i_{s\_f}}$) dans un exemple de fonctionnement où la proportion de i_{0_n} et i_{q_n} est égale à -0,45 ($m_0 = -0,45$). A titre de comparaison, la trajectoire en régime de fonctionnement normal ($\boldsymbol{i_{s\_n}}$) y est aussi représentée. Les tracés $\boldsymbol{i_{s\_fpj}}$ et $\boldsymbol{i_{s\_npj}}$ correspondent aux projections de ces trajectoires sur le plan α-β.

Dans les conditions normales, la trajectoire $\boldsymbol{i_{s\_n}}$ est un cercle. Sa composante sur l'axe 0 i_{0_n} est constante et égale à -0,45i_{q_n}. En revanche, dans les conditions de défaut, $\boldsymbol{i_{s\_f}}$ et $\boldsymbol{i_{s\_fpj}}$ ne sont plus circulaires : ils présentent une trajectoire en forme de cœur.

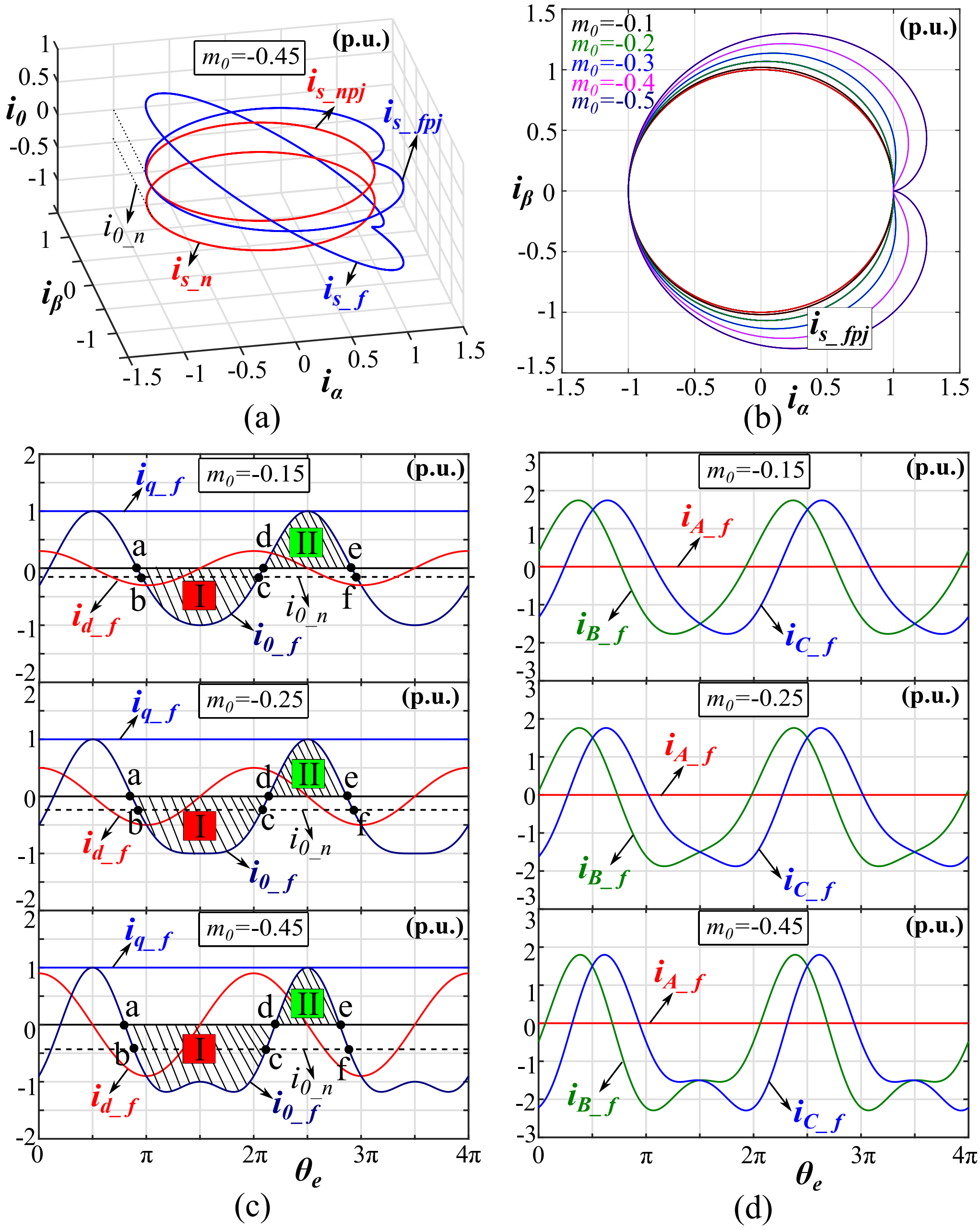

FIGURE R.12: Trajectoire théorique des courants à imposer après un défaut de circuit ouvert sur la phase A. (a) Représentation spatiale des courants et projection sur le plan α-β dans des conditions normales et après défaut. (b) Évolution de la projection des courants sur le plan α-β en fonction de m_0. (c) Chronogrammes des courants dans le repère d-q-0 après défaut pour différents m_0. (d) Chronogrammes des courants dans le repère a-b-c après défaut pour différents m_0.

La figure R.12(b) présente l'évolution de $\boldsymbol{i}_{s\_fpj}$ par rapport à m_0. On peut observer que la caractéristique évolue d'une forme de cercle à une forme de cœur de plus en plus prononcée avec la diminution de m_0. En d'autres termes, plus la composante de courant homopolaire est grande (liée à une grande puissance consommée), plus la caractéristique en forme de cœur est apparente.

Dans les MFCS, et contrairement à la plupart des autres solutions de systèmes tolérants aux fautes, il n'y a pas de modifications de la structure à faire lors de l'apparition d'un défaut car le point neutre est déjà connecté. Par conséquent, le principe d'asservissement peut rester le même avant et après l'apparition du défaut (concept de système virtuel sain). La seule chose à faire est alors de remplacer simplement les références nominales $i^*_{d\_n}$, $i^*_{q\_n}$ et $i^*_{0\_n}$ par les références de courant précédemment proposées $i^*_{d\_f}$, $i^*_{q\_f}$ et $i^*_{0\_f}$. Si le système était sain, l'objectif de commande serait de forcer activement i_{A_f} à 0 A. Dans le système avec défaut, le courant dans la phase A est physiquement nul mais de cette manière un cadre uniforme pour la commande est introduit, comme le montre la figure R.13. Dans la boucle externe, la vitesse du moteur et la tension moyenne du bus DC sont les principaux objectifs de contrôle. Dans la boucle interne, les courants d-q-0 doivent suivre les réféences dans (R.8). Afin de suivre les références de courant non constantes, une commande deadbeat et une commande basée sur la platitude différentielle sont proposées.

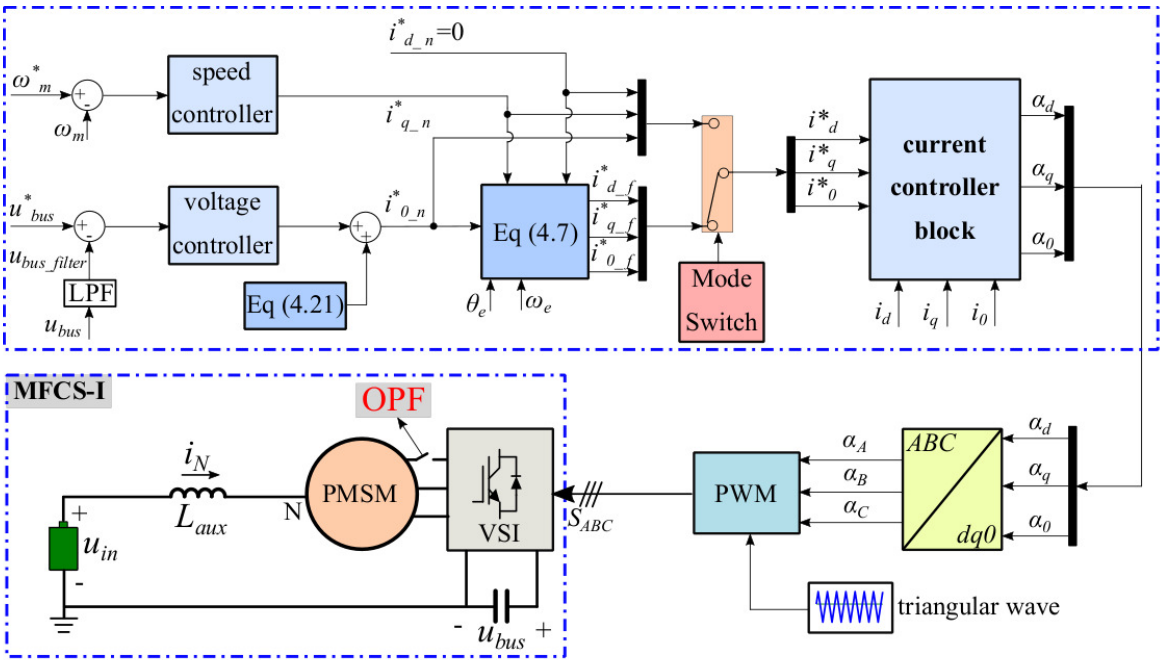

FIGURE R.13: Cadre commande uniforme (avec ou sans faute).

Des validations expérimentales ont été effectuées sur un PMSM de 52,5 W et sur un PMSM de 1,2 kW afin de valider le principe proposé de commande tolérante aux fautes. Le moteur fonctionne même en cas d'OPF sur une large plage de vitesses. La valeur du couple atteignable après défaut est d'environ 55% du couple nominal dans le MFCS-I basé sur le PMSM de 1,2 kW.

Les commandes par réponse pile et par platitude différentielle affichent des performances de suivi de courant remarquables en dépit du fait que les références de courant ne soient pas constantes. Les performances dynamiques du moteur avant et après l'apparition du défaut sont identiques.

Par conséquent, le MFCS-I présente deux avantages: le premier est une fonction d'amplification DC/DC intégrée sans utiliser de véritable hacheur. Le second est la propriété de tolérance aux fautes envers un OPF sans utiliser de composants supplémentaires. Pour conclure, le tableau R.3 résume les principales caractéristiques du MFCS-I par rapport aux quatre topologies tolérantes aux fautes typiques.

TABLE R.3: Caractéristiques du MFCS-I par rapport aux quatre topologies tolérantes aux fautes typiques.

Topologie	Fonction boost gratuite	Bus DC divisé	NP accessible	Composants semi-conducteurs auxiliaires	PPRF	SOCF	localisation de la faute	
							Côté moteur	Côté onduleur
CFI	NON	OUI	NON	3 (TRIAC)	0.50	1.50	X	√
SFI	NON	NON	NON	2 (IGBT) 3 (TRIAC)	1	1.83	X	√
CFNI	NON	OUI	OUI	1 (TRIAC)	0.50	1.29	√	√
SFNI	NON	NON	OUI	2 (IGBT) 1 (TRIAC)	0.58	1.87	√	√
MFCS-I	**OUI**	**NON**	OUI	**0**	(0.52-0.71) (résultat théorique) 0.55 (résultat expérimental)	**1**	√	√

Conclusion et perspectives

Conclusion

L'objectif principal de cette thèse a été de développer une alternative à faible coût et à haute fiabilité pour le système d'entraînement d'une PMSM typique basé sur un convertisseur à deux étages dans les applications HEV et EV. Inspiré par l'idée originale du MFCS de base qui utilise le point neutre d'un moteur triphasé pour réaliser une fonction d'élévation de tension DC/DC gratuite sur un VSI triphasé à deux niveaux, une étude complète impliquant la modélisation, le contrôle, l'amélioration et la capacité de tolérance aux fautes a été menée. Les principales contributions de ces travaux peuvent se résumer comme suit :

- En construisant le modèle moyen et en développant les circuits équivalents, le mécanisme du MFCS de base est clairement explicité. Une technique de modulation spécifique nommée ZSVIPWM a été proposée afin que les degrés de liberté de contrôle de la machine et de la fonction boost équivalente puissent être synthétisés ensemble.

- Afin de réduire l'ondulation de courant et d'améliorer le rapport d'augmentation de tension effectif du MFCS de base, deux solutions améliorées ont été proposées et testées expérimentalement, qui ont conduit au MFCS-I et au MFCS-II. Ensuite, une stratégie de commande universelle en boucle fermée a été proposée où un FOC classique peut être utilisé pour contrôler le moteur et un contrôleur basé sur la caractéristique de la platitude différentielle a été utilisé pour contrôler le boost équivalent. Une comparaison expérimentale est menée entre un entraînement basé sur un convertisseur à deux étages et le MFCS-I.
- La possibilité de tolérance aux fautes du MFCS-I vis-à-vis d'un défaut en phase ouverte sans utiliser de composants auxiliaires a été étudiée pour la première fois. Pour réaliser cette possibilité, une nouvelle trajectoire vectorielle de courant a été proposée et validée expérimentalement.

Perspectives

Suite aux travaux présentés ici, quelques perspectives peuvent être envisagées :

- **Éléments concernant le système d'électronique de puissance :** Avec le développement des dispositifs de commutation à large bande interdite (tels que les composants à base de carbure de silicium (SiC) ou de nitrure de gallium (GaN)), l'onduleur pourrait fonctionner à une fréquence de découpage plus élevée. Dans ce cas, le problème de l'ondulation de courant intrinsèque au principe de fonctionnement du MFCS peut être réduit. Par conséquent, la bobine à ajouter en série dans le MFCS-I pourrait être de taille très réduite voire même inutile et donc le MFCS de base pourrait être directement utilisé. Du point de vue de l'architecture, le concept de MFCS peut également être étendu aux systèmes d'onduleurs multi-niveaux (3 niveaux, 5 niveaux ou autres) car l'ondulation de courant des systèmes d'onduleurs multi-niveaux est plus faible. De plus, il serait également intéressant d'appliquer le concept de MFCS dans certains variateurs connectés au réseau (variateurs de moteur AC/AC), où le point neutre du moteur peut être connecté à une source AC monophasée.
- **Considérations autour du moteur (analyse et conception) :** Dans les MFCS, le moteur est utilisé dans des conditions non conventionnelles avec une composante continue sur les courants et des ondulations de courants plus importantes. Des analyses plus détaillées pourraient être menées concernant la saturation magnétique et la dissipation thermique du moteur dans ces conditions. De plus, des conseils pourraient être donnés

pour concevoir une machine spéciale avec un plus grand L_0.

- **Force contre-électromotrice du moteur non sinusoïdale :** Dans le cas où un PMSM contiendrait des back-EMFs de troisième harmonique, la back-EMF homopolaire (e_0) dans (2.6) ne serait pas nulle. Par conséquent, elle générera un couple additionnel de troisième harmonique puisque le courant homopolaire du MFCS n'est pas nul. Pour éliminer ce couple de troisième harmonique, une nouvelle méthode de modulation et une nouvelle stratégie de contrôle devront être développées.

- **Choix de la tension du bus DC :** La tension de bus DC a été régulée à une valeur constante dans les travaux présentés ici, mais, étant donné que le MFCS intègre une fonction boost DC/DC équivalente, cette tension peut être choisie de manière optimale afin de répondre au plus juste à la demande en tension du moteur (lors d'un fonctionnement à basse vitesse, un niveau de tension faible suffirait). Dans ce cas, l'efficacité globale du système d'entraînement pourrait être améliorée. À cette fin, une stratégie de génération de trajectoire pour la consigne de la tension de bus DC pourrait être intéressante dans le cadre des MFCS.

- **Machines avec saillance magnétique comme la machine synchrone avec aimants enterrés (IPMSM) ou la machine synchrone à réluctance variable (SynRM) :** Dans le cadre de la commande tolérante aux fautes du MFCS-I, nous avons considéré ici que le couple ne venait que du courant i_q. Mais pour une IPMSM ou une SynRM, le couple de réluctance n'est pas nul car L_d est différent de L_q. Dans ce cas, les références de courant proposées ne permettent pas de maintenir un couple stable. Pour étendre la capacité de tolérance aux fautes à ce type de machines, une nouvelle trajectoire vectorielle de courant devrait être proposée.

General introduction

Context and motivations

The present work of this thesis focuses on the modeling, analysis and exploration of fault-tolerant capabilities for multi-functional converter systems (MFCSs). This thesis is jointly funded by China Scholarship Council (CSC) and Laboratoire Ampère, Villeurbanne, France (CNRS UMR5005, Université de Lyon, Institut National des Sciences Appliquées de Lyon, Ecole Centrale de Lyon, Université Claude Bernard Lyon 1) for 42 months. The work mainly involves with the knowledge of two disciplines, electrical engineering and automation. Specifically, it is mostly related to the research fields of electrical machines, power electronics and automatic controls.

Environmental concerns and their stringent requirements are motivating the modern industry to reduce carbon dioxide emissions[1]. In the field of automotive industry, vehicle electrification has been emerged as the best solution for green transportation thus is expected to be in the phase of vigorous growth over the next decades[2][3]. At present, the electrification levels of vehicles can be divided into three categories: hybrid electric vehicle (HEV), plug-in hybrid electric vehicle and pure electric vehicle (EV)[4].

In terms of electric traction systems, there are two well-known configurations which are adopted to connect the energy storage system (ESS) with the traction drive[5][6]: (1) single-stage configuration, in which the ESS is directly connected with the direct current (DC)-bus of the traction inverter, as shown in figure G.1(a); (2) two-stage configuration, in which an intermediate DC/DC converter is employed, as shown in figure G.1(b). For the former, the voltage rating of the ESS completely determines the DC-bus voltage. In order to meet the high-speed and high-efficiency operating requirements of the traction motor, a sufficient high-voltage battery bank is required[7][8]. Many commercial vehicles, especially HEVs [9]–[11] in which the size limitation for the battery bank is tighter, prefer to adopt the two-stage configuration in the electric traction system. A comparison of design features and published specifications among

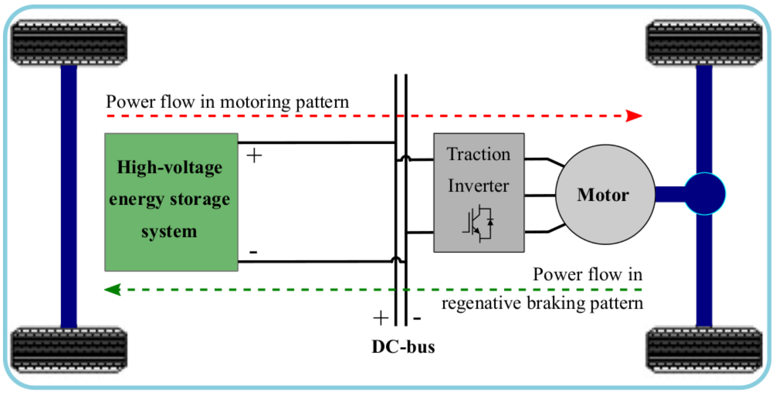

(a)

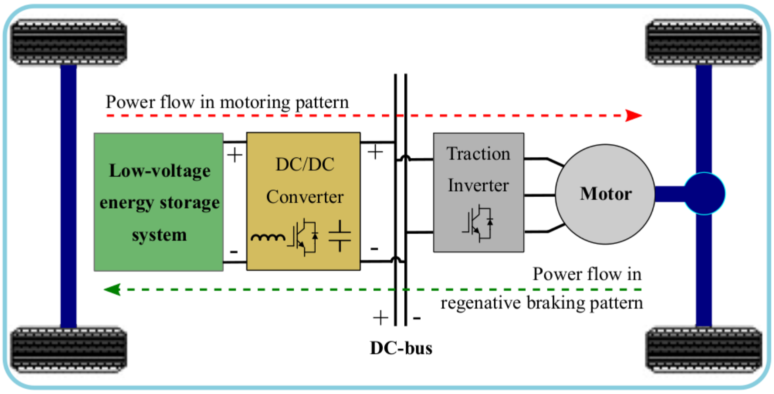

(b)

FIGURE G.1: Electric traction systems. (a) Single-stage configuration with a high-voltage ESS. (b) Two-stage configuration with a low-voltage ESS and an intermediate DC/DC boost covnerter.

TABLE G.1: Comparison of commercial HEVs with respect to design features and published specifications.

Design Feature	2008 LS 600h	Hybrid Camry	2004 Prius	2010 Prius
Motor peak power rating	165 kW	105 kW	50 kW	60 kW
DC-bus voltage	288-650 V DC	250-650 V DC	200-500 V DC	200-650 V DC
DC/DC converter power rating	36.5 kW	30 kW	20 kW	27 kW
Battery voltage	288 V	244.8 V	201.6 V	201.6 V

four HEVs (2008 Lexus LS600h, hybrid Camry, 2004 Prius and 2010 Prius)[11] is listed in table G.1. It can be seen that the DC-bus voltage is usually regulated at around 2-3 times the battery voltage by using an intermediate DC/DC boost converter. Different types of DC/DC converters have been studied in previous researches, such as single-phase DC/DC boost converters[12], interleaved DC/DC converters[13] and dual-active bridge DC/DC converters[14]. With the assistance of the DC/DC converter, the electric traction system is able to obtain a sufficient

DC-bus voltage in the absence of a high-voltage battery bank, and to flexibly manage the power flow between the traction motor and the ESS[15]. However, the use of the additional DC/DC converter brings some compromises in turn. On the one hand, it increases the cost and volume of the whole powertrain system. On the other hand, the system reliability may be degraded since more power electronic devices are used.

With the use of more power electronic devices in electric traction drives, the fault-tolerance towards electrical failures (open-circuit or closed-circuit faults) is gaining more and more attentions since the security of passengers is quite crucial. In the literature, the existing fault-tolerant solutions for three-phase two-level voltage-source inverter (VSI)-fed motor drives always require auxiliary components (a redundant bridge arm or a pair of split DC-bus capacitors) to achieve the fault-tolerant objective. Obviously, these auxiliary components will further increase the cost, volume and weight of electric traction systems.

In the field of alternating current (AC) motor drive system, the MFCS is a special category, which integrates the functionalities of a DC/DC boost converter and a DC/AC inverter upon only one three-phase two-level VSI. Different from the unconnected neutral point (NP) of a conventional motor drive, the NP of MFCSs is connected to a DC power-source. Roughly speaking, the MFCS is a promising alternative to replace the two-stage electric traction system in EVs and HEVs. However, in the literature, it does not get a lot of attentions. Up to now, the mechanism and operating principle of MFCSs are not clearly revealed and explained. There is also no a comprehensive study that presents the modeling, modulation method, control strategy and experimental evaluations for MFCSs. Besides, the possibility of fault-tolerant operations of MFCSs has not been explored and studied.

Objectives

Carrying a strong interest toward the concept of MFCSs, this thesis is going to investigate MFCSs comprehensively and deeply with the following objectives:

- The first objective of this thesis is to deeply study the basic MFCS. It intends to explicitly reveal the mechanism and evaluate the characteristics of the basic MFCS. In other words, we are going to explain the reason why there is an equivalent DC/DC boost converter function existing in a three-phase AC motor drive by merely connecting its NP. Since the NP is connected, the zero-sequence path of the basic MFCS is circulated. Thus, the common modulation methods that do not consider the zero-sequence components are not applicable in the basic MFCS. To address this problem, a specialized modulation method is required.

- Although the circulated zero-sequence circuit of the basic MFCS contributes to an equivalent DC/DC boost function, the clamped NP results in bigger current ripples reversely. In addition, the effective step-up ratio of the equivalent DC/DC boost function in the basic MFCS is limited. Therefore, the second objective is to improve the basic MFCS. Moreover, a comprehensive comparison between an improved MFCS and a conventional two-stage drive is necessary to clarify the advantages and disadvantages of the improved MFCS.
- Due to the innately connected NP in MFCSs, the circulated zero-sequence circuit can naturally provides a path for zero-sequence currents, which is necessary to generate a stable rotating magnetic field when the motor encounters an open-phase fault (OPF). Thereby, it exists a possibility to realize fault-tolerant operations without using auxiliary components when an OPF occurs in MFCSs. This has never been studied in the literature. Deservedly, the final objective is to explore and achieve the fault-tolerant possibility.

Organization of the thesis

On the purpose of achieving above objectives, this thesis is organized with four chapters, as shown below:

- **Chapter 1** reviews the opportunities of the NP of a three-phase star-connected AC motor in the literature. The NP can be connected with a DC power-source to gain an equivalent DC/DC boost function without extra costs. This is the origin of the basic MFCS. Some variants presented in the literature are also introduced. Besides, the NP can also be used to fault-tolerant applications. According to the state of the art of present three-phase fault-tolerant AC drives, it can be connected with a redundant bridge arm or a pair of split DC-bus capacitors to achieve fault-tolerant operations in case of an OPF. Objective speaking, these fault-tolerant solutions always need auxiliary hardwares.
- **Chapter 2** comprehensively investigates a permanent magnet synchronous motor (PMSM)-based basic MFCS. First, the mathematical model of PMSMs with zero-sequence components is derived. Then, the average model of the PMSM-based basic MFCS is built. Three equivalent circuits are proposed to facilitate the understanding of the mechanism of the basic MFCS. Second, the infeasibility of conventional pulse-width modulation (PWM) techniques used in the basic MFCS is discussed. To address this issue, a specialized zero-sequence voltage injected PWM is proposed. Then, the DC-source voltage utilization ratio of the basic MFCS is analyzed. Finally, comparative experiments are carried out on

a 52.5 W test-bench to verify the effectiveness.

- **Chapter 3** proposes two improved solutions for the basic MFCS while considering the issues of bigger current ripples and the limited effective step-up ratio of the equivalent boost function. The first one is referred to as MFCS-I, which uses a series inductor connected between the NP and the DC-source to reduce the current ripple. A sizing method of the series inductor is proposed based on the concept of a re-floating NP. The second solution is referred to as MFCS-II, which employs an auxiliary leg to improve the effective step-up ratio. Then, a universal closed-loop control strategy is proposed for both MFCS-I and MFCS-II. Experiments are carried out on a 1.2 kW drive platform to verify the effectivenss.
- **Chapter 4** explores the possibility of fault-tolerant operations of the MFCS-I towards an OPF without using any auxiliary hardware. First, the fault-tolerant potential of the MFCS-I is discussed. Three constraints of post-fault currents are found to guarantee a constant torque and a stable average DC-bus voltage in post-fault conditions. Second, a novel current vector trajectory which can fulfill the three constraints is proposed. Detailed analysis concerning the power conversion process and post-fault output capability is also presented. Then, two current tracking controllers are introduced to track the variable current trajectories. Experiments are carried out on the 52.5 W and 1.2 kW test-benches to verify the effectiveness, respectively.

Finally, conclusions and perspectives are given in the end.

Chapter 1

Opportunities of three-phase motor's neutral point (NP)

Contents

Introduction

A three-phase AC machine has three branches, which can be connected in two ways - Star (Y) or Delta (Δ). For the Y-connected one, it has an extra neutral point (NP). In most cases, the NP is not used and hidden inside the motor shell. However, in some special applications, this NP can be picked out and utilized to obtain additional benefits. For example, multi-functional converter system (MFCS) is a typical example that utilizes the NP to gain an equivalent DC/DC boost converter without using additional components in addition to a motor and a VSI. In the field of on-board chargers, the traction system can be reconfigured as a boost converter with power factor correction (PFC) or as a buck converter by connecting the NP of traction motors. In addition, in the domain of three-phase fault-tolerant AC drives, the NP can also be utilized to provide a path for zero-sequence currents so that a constant torque can be maintained when an open-phase fault (OPF) occurs. This chapter reviews these special applications, which take advantage of three-phase AC motor's NPs.

This chapter is organized as follows:

- In section 1, the concept of the basic MFCS and its variants are presented by reviewing the limited literature. On-board chargers using the NP of traction motors are also illustrated in this section since its fundamental is similar to MFCSs.
- In section 2, the state of the art of three-phase fault-tolerant AC drives is summarized. Four typical fault-tolerant topologies are illustrated and compared in detail with respect to the cost and post-fault output capability.

1.1 Concept of multi-functional converter system (MFCS)

1.1.1 Basic MFCS

The idea of the basic MFCS dates back from about twenty years ago[16][17]. It was firstly proposed for electric powertrain systems in HEVs by Toyota and Fuji Electric Co., Ltd., in Japan. In order to reduce the cost and volume of the two-stage configured powertrain system, engineers and researchers from Toyota and Fuji Electric attempted to remove the frond-end DC/DC stage. To retain the same functionalities provided by the DC/DC stage, the NP of traction motors is deliberately connected so that the traction drive can be an intermediary of energy exchange. The basic MFCS consists of an AC motor, a three-phase two-level VSI, two DC-sources and a neutral wiring. But there is no real DC/DC converter. The main features of the basic MFCS can be summarized as follows[18][19]:

- Endowing a three-phase AC motor drive with the functionality of a DC/DC converter by exclusively connecting the NP of the motor, which is rarely used in a conventional drive.
- Utilizing the zero-sequence inductance of the motor to function as the filtering inductor and reusing the traction inverter as the equivalent chopper.

The schematic of the basic MFCS is shown in figure 1.1. Different from a conventional configuration where both the high-voltage DC-source (v_h) and the low-voltage DC-source (v_l) are connected to the DC-bus side, the basic MFCS connects the low-voltage DC-source (v_l) to the NP of the motor. Since the NP is connected to a DC-source, the basic MFCS is similar to a three-phase DC/DC converter where the three windings of the motor are considered as the corresponding reactors for each branch.

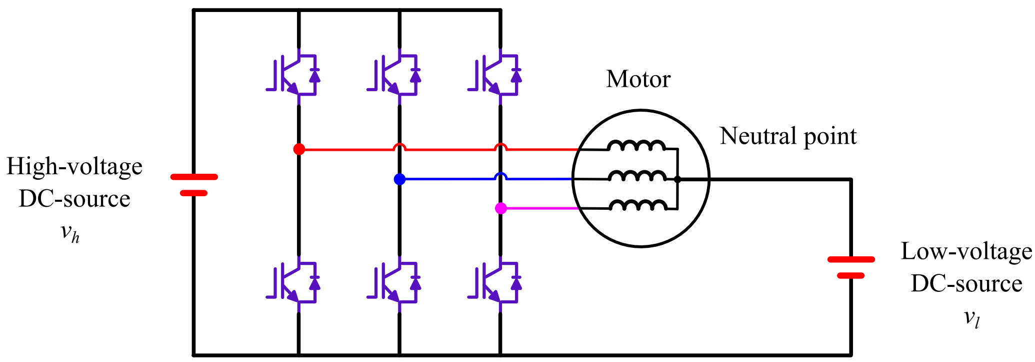

FIGURE 1.1: Schematic of the basic MFCS.

In different switching-states, corresponding circuits of the basic MFCS are illustrated in figure 1.2. If the basic MFCS is only operated with the two zero switching-states (111 and 000), it is easy to understand that it can be seen as a three-phase DC/DC converter by adjusting the duty cycle between the two zero switching-states. However, it needs to emphasize that the basic MFCS is different from a conventional three-phase DC/DC converter because the three-phase windings of the motor are coupled. Moreover, the back electromotive force (back-EMF) existing in each phase should be considered when the motor speed is non-zero.

However, there is no electromagnetic torque generated if the basic MFCS is only operated with the two zero switching-states. In order to rotate the motor, the six non-zero switching-states should be utilized. Since the non-zero switching-states are involved, the basic MFCS becomes a hybrid system which deals with not only DC/DC conversion but also DC/AC conversion via only one VSI. As we all know, for a conventional three-phase motor drive whose NP is not used, the inverter's switching-states are determined by the targeted voltage-vector and the adopted modulation method under the framework of field-oriented control (FOC). If the conventional control strategy and modulation method are adopted in the basic MFCS without

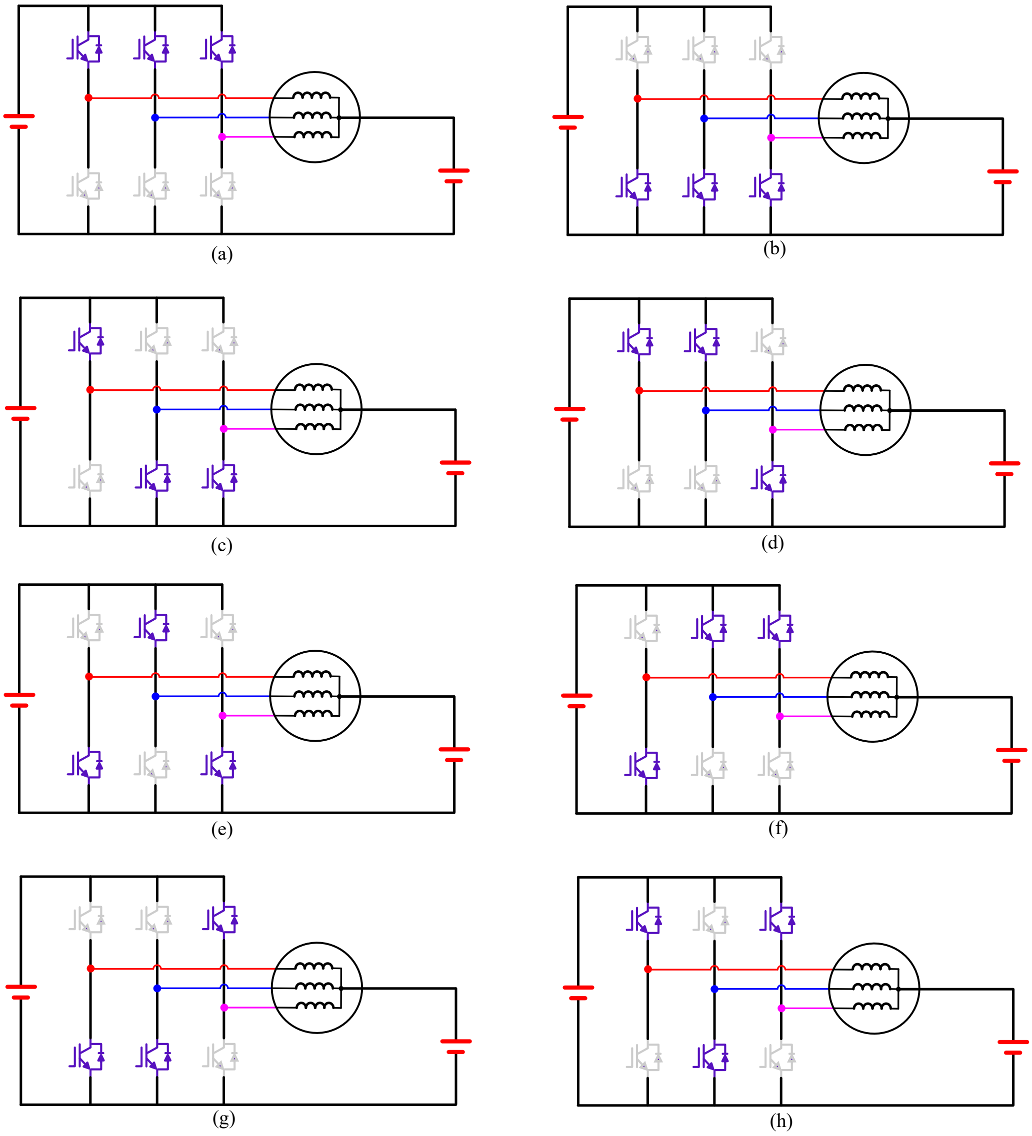

FIGURE 1.2: Specific circuits of the basic MFCS under different switching-states. (a) 111. (b) 000. (c) 100. (d) 110. (e) 010. (f) 011. (g) 001. (h) 101.

modifications, the control behavior of FOC will affect the power flow between the two power sources. Therefore, the key point is to find the independent control degree of freedom (DOFs) for the motor function and the equivalent DC/DC converter function.

In [19], the characteristic equations of the inverter in the basic MFCS are firstly derived. By considering the 0-axis elements, the available space voltage vectors of the inverter were constructed in a three-dimension (3-D) coordinate instead of the common α-β plane. In this case, the available area of inverter's output voltages is a cube in the 3-D coordinate rather than a hexagon. Then, the voltage applied to the motor under different voltage vectors was further analyzed. The authors indicated that the d-q equations of the basic MFCS are consistent with those of a conventional drive. However, the connected NP of the basic MFCS leads to a unique 0-axis equation, as

$$v_{0inv} - \sqrt{3}v_l = Ri_0 + L_0\frac{\mathrm{d}i_0}{\mathrm{d}t} \tag{1.1}$$

where v_{0inv} represents the 0-axis potential of the inverter; R is the resistance of the motor; i_0 is the 0-axis current; L_0 is the 0-axis inductance of the motor.

The available motor control area of the basic MFCS was also analyzed in [19] by comparing the surface of $u_{0inv} = \sqrt{3}v_l$ with the voltage cube in the 3-D coordinate. According to geometrical analysis, the authors indicated that the available motor control area of the basic MFCS changes with the voltage ratio $r = v_h/v_l$. The effect of the step-up v_h is recognized when $r < 3$. It is not beneficial any more when $r > 3$. However, in [18], the authors thought that $v_h = 2v_l$ is the best condition for driving the motor. Both [18] and [19] did not present a comprehensive analysis and explanation for the effective step-up ratio of the MFCS. Moreover, there were no adequately experimental results presented to verify the effectiveness of their analysis.

In [20], the authors connected the battery to the NP of a generator powered by an internal combustion engine in HEV applications. The proposed topology uses a single-stage PWM rectifier to process the power from two different sources. The PWM rectifier is used to convert the AC voltage produced by the generator and to function as a DC/DC boost converter for the battery. Essentially, this application is equivalent to the basic MFCS when the traction motor is operated under regenerative braking modes.

The interest of using motor's NPs is not limited to vehicle applications. The authors in [21] applied the similar idea in a solar powered water pump to reduce the cost and complexity of a classic system where a DC/DC boost converter is typically used to step up the solar panel voltage and achieve maximum power point tracking control, and then to supply a brushless-DC motor via a three-phase two-level VSI for driving a water pump. By connecting the solar panel to the NP of the brushless-DC motor, the inverter's bridges act as not only the inverter function but also the chopper of a DC/DC boost converter simultaneously.

Although the connected NP contributes to a free DC/DC boost function in the basic MFCS, it brings some adverse impacts in turn, e.g. the issue of bigger current ripples. [22] and [23] applied the basic MFCS on an automotive electric-power-steering system on the purpose of cost reductions. The issue of bigger current ripples was investigated in detail by building a high-frequency model. It indicates that the phase-current ripples in the basic MFCS can be divided into two parts, which are related to the mutual inductance and the zero-sequence inductance of the motor. For the first part, it can be reduced significantly with interleaved PWM technique. However, the interleaved PWM may deteriorate the torque performance of the motor, which is not discussed by the authors. In terms of the second part, it can be reduced by increasing the zero-sequence inductance with special winding arrangements. Three different winding arrangements were analyzed to increase the zero-sequence inductance of a synchronous machine with a double-layer tooth-coil winding. Experimental results indicate that the phase-current ripple and neutral current ripple can be reduced by half with the proposed winding arrangement. However, the requirement of special winding arrangements can not be fulfilled in a common motor. In this thesis, we will introduce a method to reduce the current ripple by using a series inductor. The detailed sizing method for the series inductor will be given. In addition to the issue of bigger current ripples, another limitation of the basic MFCS is the limited step-up ratio of the equivalent boost function.

1.1.2 Other variants

1.1.2.1 Variant 1

In a conventional two-stage motor drive system, the DC/DC boost converter requires a large boost-up reactor, which is costly and bulky. Although the basic MFCS can realize a reactor free boost converter, its effective step-up ratio is limited. In [24] and [25], the authors followed the basic MFCS and proposed a variant. They investigated a two-stage boost converter by using the NP of a motor, as shown in figure 1.3. Different from the basic MFCS, the proposed circuit connects the NP of the motor to a first-stage boost converter. Thanks to the utilization of the motor's leakage inductance, the volume of the boost-up reactor in the first-stage can be reduced compared to a conventional two-stage drive system. Besides, thanks to the first-stage boost, the step-up ratio of the whole system can be higher than the basic MFCS. Regarding the control scheme, the V/F control collaborated with the six-step operation is used to control the motor. The cascaded PI is used to regulate the DC-bus voltage. In order to compensate the voltage fluctuation caused by the floating NP, a feed-forward control is applied to the current regulator in the first-stage boost. In addition, the loss evaluation was also implemented to investigate the

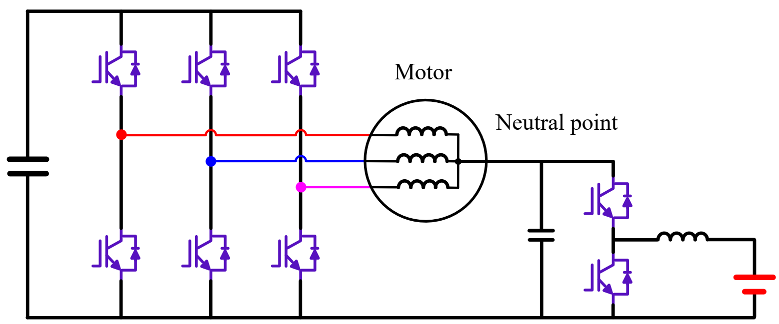

FIGURE 1.3: A two-stage boost converter using the NP of a motor.

influence of the imposed DC current in the motor. According to the finite element simulation implemented on a 1.5 kW interior permanent magnet motor, the authors indicated that the torque ripple of the motor was increased by 10% and the copper loss was increased by 25%. A trade-off relationship between the converter and motor losses has been demonstrated.

1.1.2.2 Variant 2

In HEVs, the energy distribution system occupies a big part of volumes and costs. One part of this system is the DC/DC converter that transfers power between the low- and high-voltage buses, as shown in figure 1.4(a). In order to reduce the cost and volume of the DC/DC converter, [26] and [27] proposed a novel concept for integrating the DC/DC converter functionality into the traction drive system, as shown in figure 1.4(b). By using the traction inverter and the machine to function as a primary bridge leg of an isolated full-bridge DC/DC converter, the total costs and weight of the whole system can be reduced. Furthermore, three different switching strategies were proposed in [28] to improve the efficiency of the total system. Starting from the phase-shift modulation known from the conventional dual active bridge, the switching instants are optimized regarding efficiency to obtain the optimal modulation. The proposed concept was validated on a scaled prototype with a 3 kW machine. The resulting measurements agree well with simulations and the analytical model.

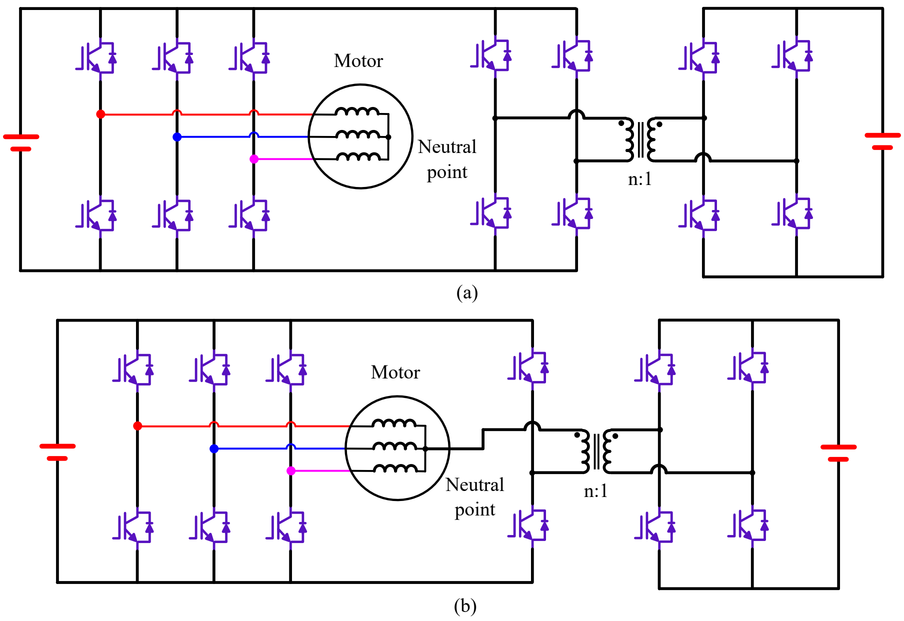

FIGURE 1.4: Energy distribution system in HEVs. (a) Conventional configuration. (b) Integrated configuration.

1.1.2.3 Variant 3

For a drive system with two motors, the two NPs can be completely used. Therefore, a two-motor type MFCS was also introduced in [18] and [19]. The circuit configuration of the two-motor type MFCS is shown in figure 1.5, which consists of two traction inverters, two three-phase AC motors, a high-voltage DC-source connected with the bus line and a low-voltage DC-source interfaced with the two NPs. Compared to the basic MFCS, the two-motor type MFCS can utilize the zero-sequence inductance of two motors and the DOFs of two traction inverters. Thus, the neutral current ripple in the two-motor type MFCS can be reduced into 1/4.5 of that in the basic MFCS, and the available motor control area is wider. A control strategy for the two-motor type MFCS with zero-voltage compensations was introduced in [19]. However, the authors did not present experimental results to verify the effectiveness of the proposed control strategy when the two motors are operated under dynamic conditions.

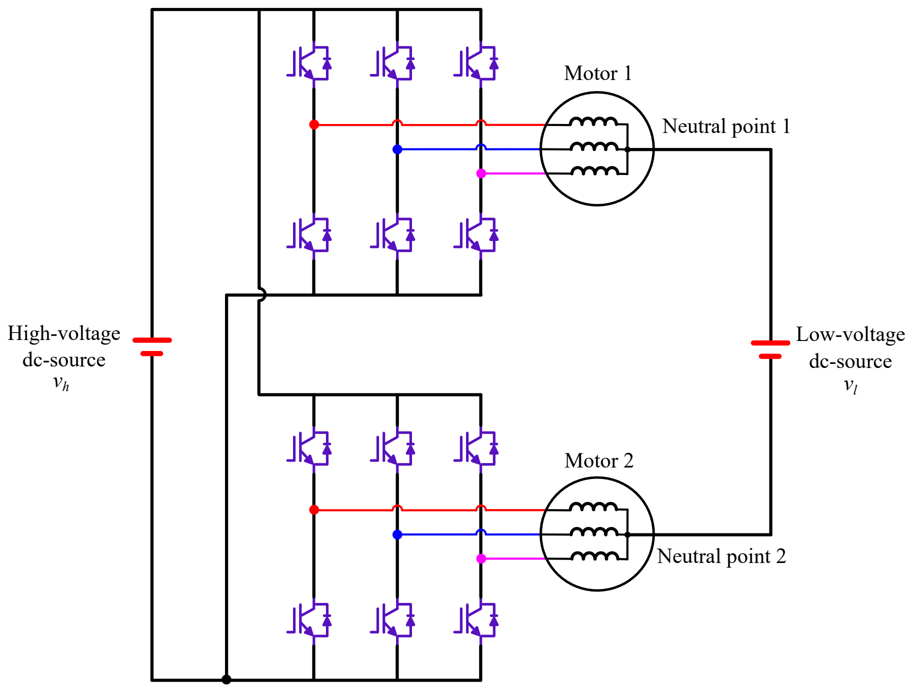

FIGURE 1.5: Two-motor type MFCS.

1.1.3 Integrated on-board charger

The concept of utilizing motor's NPs can also be found in integrated on-board charger applications[29]–[33]. A non-isolated single-phase (220 V and 50 Hz AC) integrated battery charger was proposed in [31] for an electrical scooter. The battery charger is derived from the powertrain system of the scooter, whose circuit configuration is shown in figure 1.6. In the motoring mode, the switch K1 is open. Therefore, the battery is connected with the DC-bus to power the motor. In the charging mode, the switch K1 is closed. Then, a single-phase AC source is connected with the NP of the motor via a single-phase rectifier and a LC filter. The neutral current can be regulated by means of inverter's common-mode voltage while the differential-mode current components are regulated to zero for current balancing. Thus, the AC drive system actually becomes a three-phase DC/DC boost with the PFC capability. To minimize the current ripple, the phase interleaved technique can be utilized.

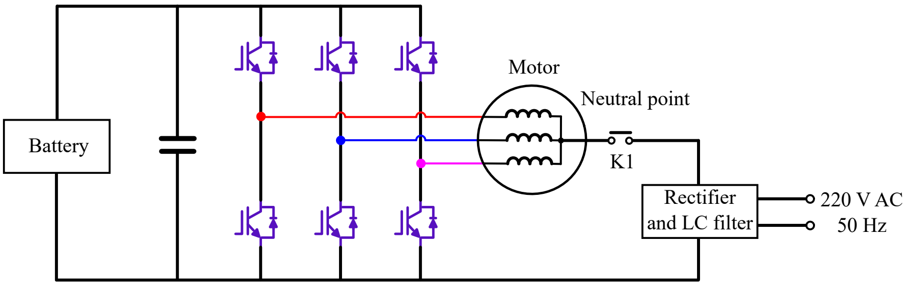

FIGURE 1.6: Single-phase integrated battery charger for an electric scooter.

In [33], the authors introduced an integrated propulsion/charging system for EVs, as shown in figure 1.7. In the propulsion mode, only switch S3 is closed. In this case, the battery is connected with the DC-bus of the traction inverter for propulsion requirements. In the charging mode, switches S1, S2 and S4 are closed and S3 is open. In other words, the single-phase AC source is connected with the DC-bus of the traction inverter via a rectifier. The battery is connected with the NP of the traction motor. In this case, the AC drive becomes a DC/DC buck converter for charging requirements. A safe charging operation strategy was proposed by independently controlling three-phase currents to avoid the unwanted electromagnetic torque during the charging process.

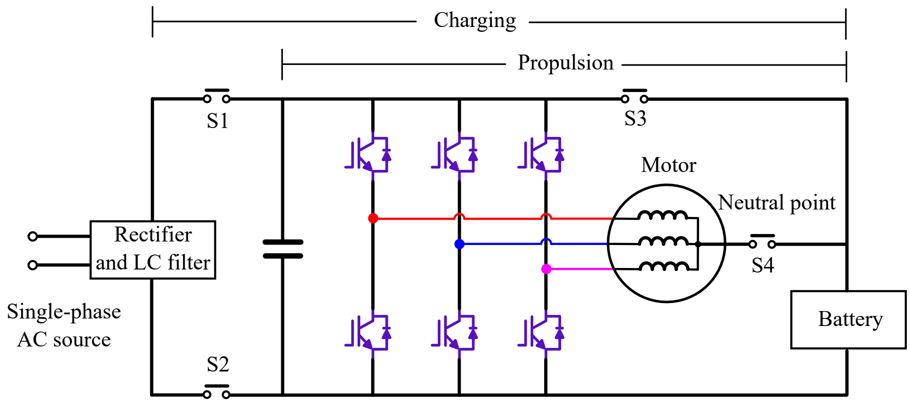

FIGURE 1.7: A propulsion/charging system for EVs.

An integrated battery charger has been reported for a four-wheel EV by Sul and Lee [29] in 1995. The propulsion system consists of four induction motors and four three-phase VSIs with a battery connected with the DC-bus, as shown in figure 1.8. In the motoring pattern, the switch K2 is closed on top. So, the battery is connected to the DC-bus capacitor. The four inverters are connected with the DC-bus together. Each NP of the four motors is floating in the motoring pattern. In the charging mode, the transfer switch K2 changes the connection of the battery. The drive system can be reconfigured as a single-phase battery charger. As shown in figure 1.8, the single-phase AC source is connected between two NPs of motors 1 and 2. Meanwhile, the battery is connected between two NPs of motor 3 and 4. From functionality point of view, motors 1, 2 and inverters 1, 2 function as a single-phase boost converter with the PFC capability. Motors 3, 4 and inverters 3, 4 become two buck converters[32] to charge the battery.

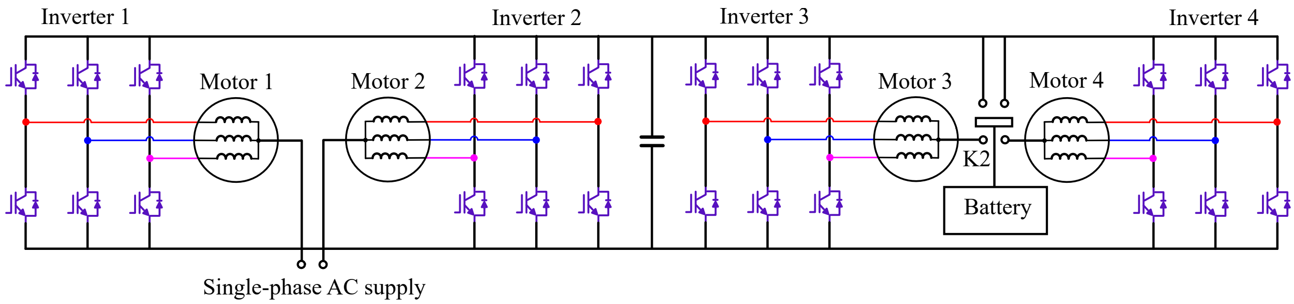

FIGURE 1.8: Single-phase integrated battery charger for a four-wheel EV.

Essentially, the fundamental of above integrated on-board chargers is similar to the concept of MFCSs where the drive system is reconfigured as boost or buck converters according to different requirements by utilizing the NP of traction motors. The difference between these on-board chargers and MFCSs is that the traction motors do not need to produce torque in charging patterns. Thus, the control strategy for integrated on-board chargers is simpler.

1.2 State of the art of three-phase fault-tolerant motor drives

In addition to the applications in MFCSs and integrated on-board chargers, three-phase AC motor's NPs can also be utilized to tolerate an OPF. In the field of EVs, system reliability and fault tolerance are very critical[34]. As the dominant power take-off, the electrical drive is desired to be equipped with the ability of continuous operations in case of the occurrence of failures. Many different failures can afflict electrical drives, such as machine faults[35][36], sensor faults[37], and power converter faults[38]. Among the machine and power converter faults, open-circuit and short-circuit failures are the most common failures in motor drives[39][40]. Considering that the phase winding can always be cut off with the power supply by circuit breakers or fuses during short-circuit faults, the short-circuit faults can be eventually converted to open-circuit faults. Therefore, the OPF has received more attention in recent years[41].

Different from multi-phase drives [42]–[44] with the inherent fault-tolerance, a standard VSI fed three-phase AC motor drive with Y-connection is unable to maintain a stable torque when an OPF occurs. After the appearance of an OPF, one of the motor phases will be disconnected from the power supply. In this case, the currents in the remaining phases have an equal amplitude but opposite sign. Thus, if there is no fault-tolerant solution adopted, the currents in remaining phases can not generate a circular rotating electromagnetic field. In order to improve the reliability and security of three-phase AC drives, numerous fault-tolerant topologies have been proposed over the past decades[45]. In general, these topologies always require assistant devices to achieve fault-tolerant operations.[41], [46]–[64]

At present, the well-known fault-tolerant topologies of three-phase AC motors can be divided into four categories[65][66][1]:

1. CFI: capacitor-based four-leg inverter.
2. SFI: switch-based four-leg inverter.
3. CFNI: capacitor-based four-leg neutral-point-connected inverter.
4. SFNI: switch-based four-leg neutral-point-connected inverter.

1.2.1 Fault-tolerant solutions without using NP

The CFI is an early attempt to endow a standard three-phase VSI fed AC motor drive with the fault-tolerant capability, as shown in figure 1.10. This topology incorporates three triode for alternating current (TRIACs) and two split DC-bus capacitors which form the fourth leg to tolerate an OPF occurring on any of inverter's legs. In healthy operations, all TRIACs are not triggered thus the condition of the motor is consistent with that of a standard VSI fed drive. When an OPF occurs, the faulty inverter leg is isolated with the DC-bus and the corresponding TRIAC of the faulty phase is triggered. In this case, the terminal of the faulty phase of the motor is connected to the midpoint of the DC-bus. Essentially, the circuit configuration in post-fault conditions is similar to the three-phase four-switch AC drive where the motor is controlled through only two active inverter legs. Although one of motor phase terminals is clamped to the midpoint of the DC-bus, three-phase windings of the motor can still be used to produce the electromagnetic torque. Therefore, the current output capability in the post-fault case is

[1] Open-end winding motor drives are not considered in this manuscript because they need two inverters

identical to that in the healthy case[67]. Objectively speaking, the CFI is a cost-effective fault-tolerant topology in which no additional insulated gate bipolar transistors (IGBT) is employed. However, the voltage output capability has been decreased by a half due to the loss of voltage vectors[68]. It needs to note that the issue of DC-bus midpoint voltage fluctuations and the lack of zero vectors result in the increase of torque ripples and deteriorate the performance of the fault-tolerant control[69]. For the first defect, [69] proposed a *p*-*z* coordinate to compensate the voltage fluctuation. Essentially, it is equivalent to synthesize the voltage vector by considering the voltage fluctuation since the midpoint voltage is measurable through voltage sensors. The use of *p*-*z* coordinate can simplify the intermediate calculations, e.g., sector judging can be avoided, the computation burden can be reduced. To address the second problem, the zero vector can be synthesized by two inverse vectors. It is pointed out that using the nearest three primary vectors can minimize the torque ripple caused by modulations[70].

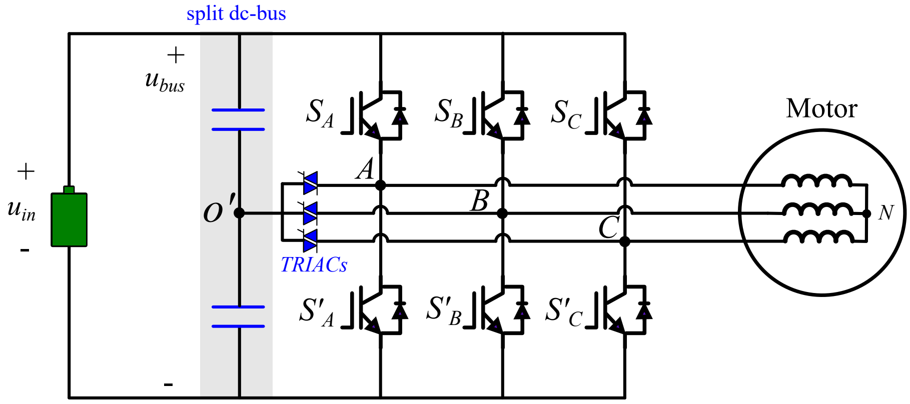

FIGURE 1.9: Capacitor-based four-leg inverter (CFI).

In the SFI, a redundant inverter leg constructed by two auxiliary IGBTs and three TRIACs are employed to recover the original circuit structure when an OPF occurs, as shown in figure 1.10. Essentially, the situation of the motor remains unchanged before and after the fault. Therefore, the rated output capability can be completely remained in the SFI. However, compared to the CFI, the SFI suffers from higher hardware costs.

1.2.2 Fault-tolerant solutions using NP

From the functionality point of view, the CFI and SFI can only tolerate an OPF which occurs in the inverter side. If an OPF caused by internal failures of motor windings occurs, one of the stator phases becomes disabled and the motor has to be operated with only two active phases. In this case, the CFI and SFI do not work any more. A feasible way to accommodate this fault is to utilize the NP of the motor. Along this line of thought, the CFNI (see figure 1.11) and SFNI (see figure 1.12) were proposed where the NP is respectively connected to the

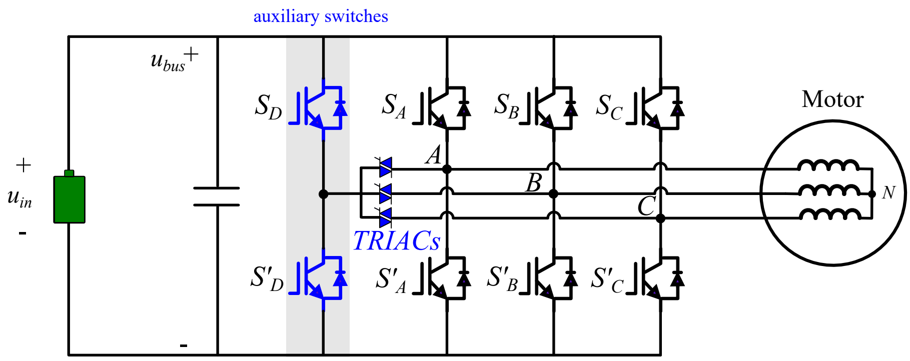

FIGURE 1.10: Switch-based four-leg inverter (SFI).

midpoint of the DC-bus [71] and an auxiliary inverter leg [72] via a TRIAC. In order to maintain a constant flux trajectory and preserve the torque output, the phase-current in remaining phases needs to be increased in magnitude by a factor of $\sqrt{3}$[73]. Meanwhile, the phase angle should be shifted 30° away from the faulted phase[74]. As a result, the torque output capability of the CFNI and SFNI is reduced by a factor of $1/\sqrt{3}$ due to the current limits. The increase in phase-currents is in the form of zero-sequence currents flowing through the NP, and is necessary to guarantee a circular flux trajectory[75]. The amplitude of neutral currents in post-fault conditions is increased by a factor of $\sqrt{3}$ compared to that in remaining phases[76]. The NP voltage of the motor in the CFNI is clamped to half of the DC-bus voltage while it can switch between 0 and the whole DC-bus voltage in the SFNI due to the auxiliary leg. This implies that the CFNI can only apply $\pm 1/2$ of the DC-bus voltage across each active phase while the SFNI is able to utilize the whole DC-bus voltage. Therefore, the reachable space vector voltage is decreased from 0.58 to 0.5 per unit (pu) in the CFNI, while it can be maintained invariable in the SFNI[77]. In addition, the CFNI also suffers from the issue of DC-bus midpoint fluctuations. The SFNI requires higher hardware costs to achieve the fault-tolerance.

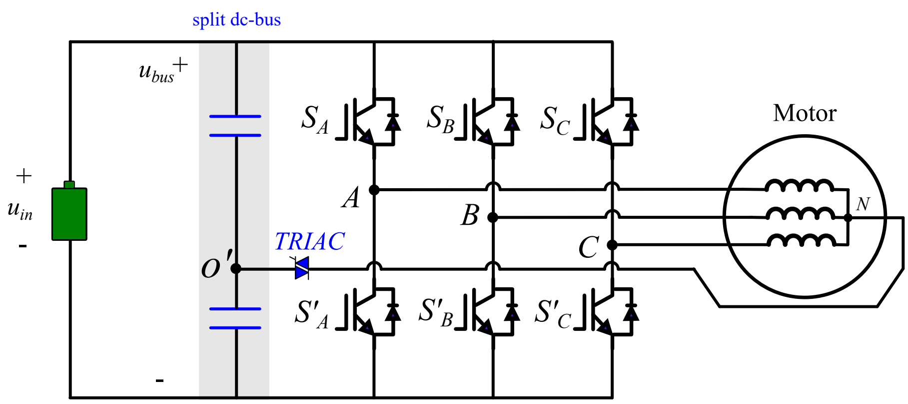

FIGURE 1.11: Capacitor-based four-leg neutral-point-connected inverter (CFNI).

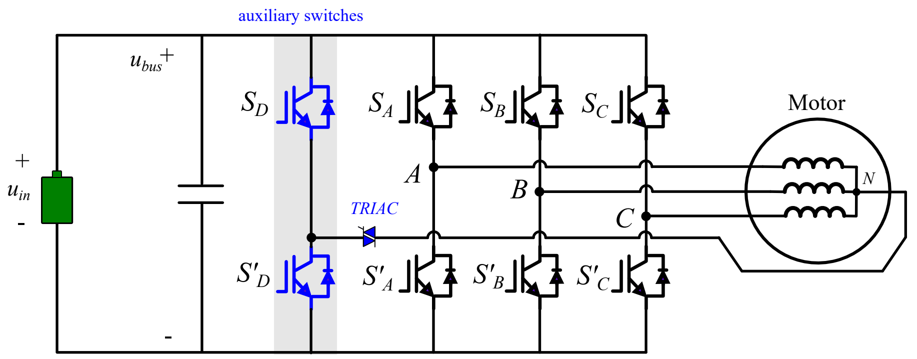

FIGURE 1.12: Switch-based four-leg neutral-point-connected inverter (SFNI).

1.2.3 Comparison

In an effort to quantify the post-fault output capability and the overall cost associated with the four typical fault-tolerant topologies, two evaluation criteria are defined as:

- $\text{PPRF} = \dfrac{\text{maximum kVA rating under fault}}{\text{rated kVA rating in health}}$

- $\text{SOCF} = \dfrac{\text{weighted kVA rating of all silicon devices}}{\text{rated kVA rating of six basic IGBTs}}$

The PPRF defines a normalization of the maximum available apparent power magnitude (kVA) in post-fault operations to the nominal apparent power magnitude (kVA) under healthy conditions. The SOCF defines a normalization of the weighted power magnitude (kVA) sustained by all the silicon devices under post-fault operations to the rated apparent power magnitude (kVA) sustained by six basic IGBTs in healthy conditions. Based on above definitions, the bigger PPRF means the drive system can output larger power in fault-tolerant conditions. The bigger SOCF means the drive system requires more costs to achieve the fault-tolerance.

To implement this calculation, each silicon device is considered to withstand a DC-bus voltage of 1 pu and convey a phase-current root mean square (RMS) of 1 pu. Therefore, a healthy drive system has a SOCF of 1. To simplify the comparison, the cost of a TRIAC is assumed to be the same as an IGBT[65]. Based on these hypotheses, the characteristics of each existing fault-tolerant topology can be evaluated respectively. For example, the CFI has a PPRF of 0.5 because the reachable voltage vector is degraded by a factor of 0.5 while the available current is consistent. Regarding its SOCF, it can be calculated by $(3+6)/6 = 1.5$ due to the use of three extra TRIACs. The SFI has a PPRF of 1 because the situation of the motor is not changed after the fault. In terms of its SOCF, it can be calculated by $(2+3+6)/6 = 1.83$ due to the use of three TRIACs and two auxiliary IGBTs. The CFNI has a PPRF of 0.5 because the attainable voltage vector is reduced from 0.58 to 0.5 pu and the torque output capability is decreased by a factor of $1/\sqrt{3}$. The SOCF of the CFNI can be calculated by $(1 * \sqrt{3} + 6)/6 = 1.29$ because the TRIAC connected with the NP has to be designed sufficiently to withstand the neutral current, which is larger than the phase-current by a factor of $\sqrt{3}$. In the same way, the PPRF of the SFNI is evaluated as 0.58 and the SOCF is $(3 * \sqrt{3} + 6)/6 = 1.87$. A comprehensive comparison of these fault-tolerant topologies is summarized in table 1.1.

Table 1.1: Characteristics of two-level three-phase fault-tolerant topologies towards OPFs.

Topology Name	Split DC Bus	Accessible NP	Auxiliary Silicon Components	Post-Fault Power Rating Factor (PPRF)	Silicon Overrating Cost Factor (SOCF)	Tolerate Fault Occurring in	
						Motor Side	Inverter Side
CFI	YES	NO	3 (TRIAC)	0.50	1.50	X	$\surd$
SFI	NO	NO	2 (IGBT) 3 (TRIAC)	1	1.83	X	$\surd$
CFNI	YES	YES	1 (TRIAC)	0.50	1.29	$\surd$	$\surd$
SFNI	NO	YES	2 (IGBT) 1 (TRIAC)	0.58	1.87	$\surd$	$\surd$

From table 1.1, we can see that both CFI and SFI do not require an accessible NP. However, they can only tolerate an OPF which occurs in the inverter. The SFI has a higher PPRF than the CFI while it also requires a higher SOCF (1.83 to 1.5). The CFNI and SFNI require an available NP so that they can tolerate an OPF which can occur in the motor or the inverter. The SFNI has a higher PPRF (0.58 to 0.50) than the CFNI while it requires a higher SOCF (1.87 to 1.29). In general, all these existing fault-tolerant topologies require assistant devices (at least one TRIAC) to achieve the fault-tolerant operation. These assistant devices increase not only the cost of the whole drive system but also complicate the control circuit because additional control signals need to be designed for auxiliary TRIACs and IGBTs. This will indirectly increase the cost and affect the reliability of the drive system.

Conclusion

The NP of three-phase Y-connection AC motors can be utilized to obtain extra benefits. In the basic MFCS and its variants, AC motor's NPs are directly or indirectly connected with the DC-source to achieve a DC/DC converter function without or with less passive and active components. In some integrated on-board chargers, the traction drive can be configured as a boost converter with PFC or a buck converter to charge the battery by connecting its NP.

Essentially, the connected NP leads to the circulation of zero-sequence currents in the traction drive. Thus, the leakage inductance of traction motors become an available resource to construct a DC/DC converter. However, only few researchers focus on the concept of MFCSs and there is no much literature that can be found concerning MFCSs. Objectively speaking, the mechanism of MFCSs is not well explained by a clear analytic model. There is no a closed-loop control strategy presented for MFCSs in the literature. The advantages and disadvantages of the basic MFCS are not comprehensively elaborated while it is compared to a conventional two-stage drive.

From another point of view, the connected NP in AC drives also contributes to the fault-tolerance towards OPFs. In the CFNI and SFNI, the NP is connected to the midpoint of split capacitors and a fourth leg respectively. As a result, the motor is able to output a stable torque even if one of motor phases is disconnected from the power supply. However, the use of additional hardwares is inevitable in the CFNI and SFNI. To be specific, the CFNI requires 1 TRIAC and a pair of split capacitors. The SFNI requires 1 TRIAC and 2 extra IGBTs.

Considering the innately connected NP in MFCSs, it exists a possibility that the MFCS can also achieve the fault-tolerance without using auxiliary components compared to the CFNI and SFNI.

Chapter 2

Investigation of a PMSM-based basic MFCS

Contents

Introduction

According to the brief introduction of the basic MFCS in Chapter 1, we know that it can obtain a cost-free DC/DC boost function by utilizing the NP of the motor. Therefore, it can be a promising alternative to the two-stage converter-based drive, which employs an intermediate DC/DC boost converter to raise the DC-bus voltage. However, in the literature, the operating principle and mechanism of the basic MFCS are not clearly revealed by an analytic model. Moreover, the modulation method for the basic MFCS is not normalized.

In this chapter, we intend to investigate a PMSM-based basic MFCS comprehensively. It is organized as follows:

- Starting from the very beginning, Section 1 presents the mathematical model of the PMSM from A-B-C to d-q-0 coordinates by considering the zero-sequence components, which are usually neglected in a conventional drive.
- In Section 2, the average model of the PMSM-based basic MFCS is built based on time-averaging equivalent modeling approach and Kirchhoff's laws. To facilitate the understanding of the mechanism of the basic MFCS, three different equivalent circuits are illustrated.
- In Section 3, the classic SVPWM technique is discussed if it is used in the basic MFCS. The theoretical analysis indicates that it can not provide an independent control DOF to the equivalent boost function of the basic MFCS. To address this issue, a customized zero-sequence voltage injected PWM (ZSVIPWM) is proposed. Then, the characteristics of the PMSM-based basic MFCS is analyzed with respect to its DC-source voltage utilization ratio (DCSUR) and the effective step-up ratio of the equivalent boost function.
- In Section 4, elementary experiments are carried out on a 52.5 W PMSM platform to verify the phenomenon of the integrated boost function. An experimental comparison between the basic MFCS with a 15 V DC-source and a conventional drive with a 30 V DC-source is given.

2.1 PMSM model with zero-sequence components

The two-phase equivalent model built in direct-quadrature (d-q) plane is typically used to analyze a conventional PMSM drive and to design the control strategy. Due to the Y-connection winding layout, there is no zero-sequence current circulated in motor windings when the NP is not connected. Thus, the zero-sequence model of PMSMs is usually neglected by researchers.

As mentioned before, the connected NP in a MFCS will provide a circulated path for the zero-sequence current. Therefore, the zero-sequence model of a PMSM should be considered in a MFCS.

Throughout the whole derivation, the following assumptions are given:

- Stator windings are symmetric in three phases;
- Stator electric potentials are sinusoidally distributed along air-gap as far as the mutual effects with the rotor are concerned;
- Eddy current and hysteresis effects are neglected;
- Resistances are independent of temperature and frequency;
- Magnetic saturation effects are negligible.

2.1.1 Electrical dynamics in A-B-C coordinate

The schematic diagram of a three-phase PMSM with one pole is depicted in figure 2.1. Modeling of the PMSM in d-q-0 coordinate frame starts with the basic model in A-B-C coordinate frame. By specifying the positive directions, the flux linkage equations are given as

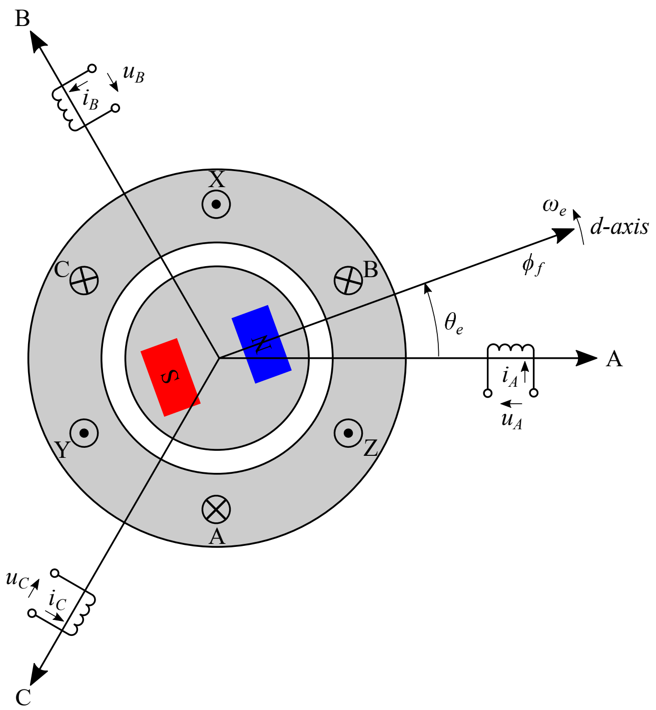

FIGURE 2.1: Schematic diagram of a three-phase PMSM.

$$\boldsymbol{\Phi}_{ABC} = \underbrace{\begin{bmatrix} L_{AA} & M_{AB} & M_{AC} \\ M_{BA} & L_{BB} & M_{BC} \\ M_{CA} & L_{CB} & L_{CC} \end{bmatrix}}_{\boldsymbol{L}_{ABC}} \boldsymbol{i}_{ABC} + \Phi_f \begin{bmatrix} cos\theta_e \\ \cos(\theta_e - 2\pi/3) \\ cos(\theta_e + 2\pi/3) \end{bmatrix} \tag{2.1a}$$

with

$$\begin{cases} L_{AA} = L_\sigma + L_\Sigma + L_\Delta \cos 2\theta_e \\ L_{BB} = L_\sigma + L_\Sigma + L_\Delta \cos 2\left(\theta_e - 2\pi/3\right) \\ L_{CC} = L_\sigma + L_\Sigma + L_\Delta \cos 2\left(\theta_e + 2\pi/3\right) \\ M_{AB} = M_{BA} = -L_\Sigma/2 + L_\Delta \cos 2\left(\theta_e + 2\pi/3\right) \\ M_{BC} = M_{CB} = -L_\Sigma/2 + L_\Delta \cos 2\theta_e \\ M_{AC} = M_{CA} = -L_\Sigma/2 + L_\Delta \cos 2\left(\theta_e - 2\pi/3\right) \end{cases} \tag{2.1b}$$

where

- $\boldsymbol{\Phi}_{ABC} := [\Phi_A \quad \Phi_B \quad \Phi_C]^T$ denotes the stator flux linkages in A-B-C coordinate frame;
- $\boldsymbol{i}_{ABC} := [i_A \quad i_B \quad i_C]^T$ denotes the phase-currents in A-B-C coordinate frame;
- $\boldsymbol{L}_{ABC}$ is an inductance matrix, including self-inductances (L_{AA}, L_{BB} and L_{CC}) and mutual inductances ($M_{AB} = M_{BA}$, $M_{AC} = M_{CA}$ and $M_{BC} = M_{CB}$);
- Φ_f denotes the permanent magnet flux linkage;
- θ_e denotes the electrical position of the rotor;
- L_σ denotes the leakage inductance;
- L_Σ denotes the average inductance;
- L_Δ denotes the inductance fluctuation (for a surface-mounted PMSM, $L_\Delta = 0$; for an interior PMSM, $L_\Delta < 0$).

According to Faraday's law of electromagnetic induction, the stator voltage equations are derived by

$$
\begin{aligned}
\boldsymbol{u}_{ABC} =& \underbrace{\begin{bmatrix} R & 0 & 0 \\ 0 & R & 0 \\ 0 & 0 & R \end{bmatrix}}_{\boldsymbol{R}} \boldsymbol{i}_{ABC} + \frac{\mathrm{d}\boldsymbol{\Phi}_{ABC}}{\mathrm{d}t} \\
=& \boldsymbol{R}\boldsymbol{i}_{ABC} + \boldsymbol{L}_{ABC}\frac{\mathrm{d}\boldsymbol{i}_{ABC}}{\mathrm{d}t} + \frac{\mathrm{d}\boldsymbol{L}_{ABC}}{\mathrm{d}t}\boldsymbol{i}_{ABC} - \Phi_f\omega_e \begin{bmatrix} sin\theta_e \\ sin(\theta_e - 2\pi/3) \\ sin(\theta_e + 2\pi/3) \end{bmatrix} \\
=& \boldsymbol{R}\boldsymbol{i}_{ABC} + \boldsymbol{L}_{ABC}\frac{\mathrm{d}\boldsymbol{i}_{ABC}}{\mathrm{d}t} \\
& - 2L_{\Delta}\omega_e \begin{bmatrix} sin2\theta_e & sin2(\theta_e + 2\pi/3) & sin2(\theta_e - 2\pi/3) \\ sin2(\theta_e + 2\pi/3) & sin2(\theta_e - 2\pi/3) & sin2\theta_e \\ sin2(\theta_e - 2\pi/3) & sin2\theta_e & sin2(\theta_e + 2\pi/3) \end{bmatrix} \boldsymbol{i}_{ABC} \\
& - \Phi_f\omega_e \begin{bmatrix} sin\theta_e \\ sin(\theta_e - 2\pi/3) \\ sin(\theta_e + 2\pi/3) \end{bmatrix}
\end{aligned}
\tag{2.2}
$$

where

- $\boldsymbol{u}_{ABC} := [u_{AN} \quad u_{BN} \quad u_{CN}]^T$ denotes the phase-voltages in A-B-C coordinate frame;
- $\boldsymbol{R}$ is a resistance matrix, including the stator resistance (R);

Obviously, in A-B-C coordinate, the mathematical model of the PMSM contains inductance terms which vary with the rotor position θ_e which in turn varies with time. This induces complexity in analyzing machine problems.

2.1.2 Electrical dynamics in d-q-0 coordinate

A much simpler form leading to a legible model can be obtained by appropriate transformation of stator variables. To meet the condition of power conservation, we use the Park transformation (power invariant) in the following analysis, whose transformation matrices ($\boldsymbol{T}_C$ and $\boldsymbol{T}_C^{-1}$) are shown in Appendix A. In the control part, the Park transformation (amplitude invariant) is used since it has no square root operation, whose transformation matrices ($\boldsymbol{T}_P$ and $\boldsymbol{T}_P^{-1}$) are also presented in Appendix A. If the Park transformation (amplitude invariant) is used, the expression of motor's torque equation should be multiplied by a factor of 3/2.

By applying the Park transformation (power invariant) to (2.1a), the flux linkage equations in d-q-0 coordinate frame can be expressed by

$$\begin{aligned}
\boldsymbol{\Phi}_{dq0} = \boldsymbol{T}_C \boldsymbol{\Phi}_{ABC} &= \boldsymbol{T}_C \left(\boldsymbol{L}_{ABC} \boldsymbol{i}_{ABC} + \Phi_f \begin{bmatrix} cos\theta_e \\ \cos(\theta_e - 2\pi/3) \\ cos(\theta_e + 2\pi/3) \end{bmatrix} \right) \\
&= \boldsymbol{T}_C \boldsymbol{L}_{ABC} \boldsymbol{T}_C^{-1} \boldsymbol{i}_{dq0} + \boldsymbol{T}_C \Phi_f \begin{bmatrix} cos\theta_e \\ \cos(\theta_e - 2\pi/3) \\ cos(\theta_e + 2\pi/3 \end{bmatrix} \\
&= \underbrace{\begin{bmatrix} L_\sigma + \frac{3}{2} L_\Sigma + \frac{3}{2} L_\Delta & 0 & 0 \\ 0 & L_\sigma + \frac{3}{2} L_\Sigma - \frac{3}{2} L_\Delta & 0 \\ 0 & 0 & L_\sigma \end{bmatrix}}_{\boldsymbol{L}_{dq0}} \boldsymbol{i}_{dq0} + \Phi_m \begin{bmatrix} 1 \\ 0 \\ 0 \end{bmatrix}
\end{aligned} \tag{2.3}$$

where

- $\boldsymbol{L}_{dq0} := diag(L_d \quad L_q \quad L_0)$ is the inductance matrix in d-q-0 coordinate frame, including the d-axis inductance (L_d), q-axis inductance (L_q) and 0-axis inductance (L_0). We can thereby conclude that the 0-axis inductance (L_0) is equal to the leakage inductance (L_σ);
- $\boldsymbol{i}_{dq0} := [i_d \quad i_q \quad i_0]$ denotes the d-axis, q-axis and 0-axis currents;
- $\Phi_m = \sqrt{\frac{3}{2}} \Phi_f$ is a constant coefficient (If the Park transformation (amplitude invariant) is adopted, $\Phi_m = \Phi_f$);

According to inverse Park transformation (power invariant), the voltage equations of (2.2) can be represented by

$$\boldsymbol{T}_C^{-1} \boldsymbol{u}_{dq0} = \boldsymbol{R} \boldsymbol{T}_C^{-1} \boldsymbol{i}_{dq0} + \frac{\mathrm{d} \boldsymbol{T}_C^{-1} \boldsymbol{\Phi}_{dq0}}{\mathrm{d}t} \tag{2.4}$$

where

- $\boldsymbol{u}_{dq0} := [u_d \quad u_q \quad u_0]^T$ denotes the motor voltages in d-q-0 coordinate frame.

By left-multiplying $\boldsymbol{T}_C$ to (2.4), we obtain

$$\boldsymbol{u}_{dq0} = \boldsymbol{T}_C \boldsymbol{R} \boldsymbol{T}_C^{-1} \boldsymbol{i}_{dq0} + \boldsymbol{T}_C \frac{\mathrm{d} \boldsymbol{T}_C^{-1} \boldsymbol{\Phi}_{dq0}}{\mathrm{d}t} \tag{2.5}$$

Then, substituting (2.3) into (2.5), the voltage equations of PMSMs in d-q-0 coordinate can be expressed as:

d-q-0 model of PMSMs obtained by the Park transformation (power invariant):

Voltage equation:

$$\begin{bmatrix} u_d \\ u_q \\ u_0 \end{bmatrix} = \begin{bmatrix} R & 0 & 0 \\ 0 & R & 0 \\ 0 & 0 & R \end{bmatrix} \begin{bmatrix} i_d \\ i_q \\ i_0 \end{bmatrix} + \begin{bmatrix} L_d & 0 & 0 \\ 0 & L_q & 0 \\ 0 & 0 & L_0 \end{bmatrix} \begin{bmatrix} \frac{\mathrm{d}i_d}{\mathrm{d}t} \\ \frac{\mathrm{d}i_q}{\mathrm{d}t} \\ \frac{\mathrm{d}i_0}{\mathrm{d}t} \end{bmatrix} + \underbrace{\begin{bmatrix} -\omega_e L_q i_q \\ \omega_e (L_d i_d + \Phi_m) \\ 0 \end{bmatrix}}_{\boldsymbol{e}_{dq0}} \tag{2.6}$$

where

- $u_0 = \dfrac{u_{AN} + u_{BN} + u_{CN}}{\sqrt{3}}$;
- $i_0 = \dfrac{i_A + i_B + i_C}{\sqrt{3}}$;
- $\boldsymbol{e}_{dq0} := [e_d \quad e_q \quad e_0]^T$ denotes the d-axis, q-axis and 0-axis back-EMFs.

Torque equation:

According to power conversion law, the electromagnetic torque can be derived by

$$\begin{aligned} T_e &= \frac{p}{\omega_e}(e_A i_A + e_B i_B + e_C i_C) = \frac{p}{\omega_e} \boldsymbol{e}_{ABC}^T \boldsymbol{i}_{ABC} = \frac{p}{\omega_e} (\boldsymbol{T}_C^{-1} \boldsymbol{e}_{dq0})^T \boldsymbol{T}_C^{-1} \boldsymbol{i}_{dq0} \\ &= \frac{p}{\omega_e} \boldsymbol{e}_{dq0}^T (\boldsymbol{T}_C^{-1})^T \boldsymbol{T}_C^{-1} \boldsymbol{i}_{dq0} = \frac{p}{\omega_e} \boldsymbol{e}_{dq0}^T \boldsymbol{i}_{dq0} \\ &= p[\Phi_m i_q + (L_d - L_q) i_d i_q] = p[\frac{\sqrt{3}}{2} \Phi_f i_q + (L_d - L_q) i_d i_q] \end{aligned} \tag{2.7}$$

where

- $\boldsymbol{e}_{ABC} := [e_A \quad e_B \quad e_C]^T$ denotes the back-EMFs in A-B-C coordinate;
- p is the number of pole pairs;

According to (2.6), it can be seen that the 0-axis back-EMF term (e_0) is 0. Therefore, the zero-sequence model of a PMSM can be considered as a first-order system.

For a surface-mounted PMSM ($L_d = L_q$), the electromagnetic torque can be simplified by

$$T_e = p \Phi_m i_q \tag{2.8}$$

If the Park transformation (amplitude invariant) is adopted, corresponding d-q-0 model can be derived in the same way. In this case, the voltage and torque equations are summarized below:

d-q-0 model of PMSMs obtained by the Park transformation (amplitude invariant):

Voltage equation:

$$\begin{bmatrix} u_d \\ u_q \\ u_0 \end{bmatrix} = \begin{bmatrix} R & 0 & 0 \\ 0 & R & 0 \\ 0 & 0 & R \end{bmatrix} \begin{bmatrix} i_d \\ i_q \\ i_0 \end{bmatrix} + \begin{bmatrix} L_d & 0 & 0 \\ 0 & L_q & 0 \\ 0 & 0 & L_0 \end{bmatrix} \begin{bmatrix} \frac{\mathrm{d}i_d}{\mathrm{d}t} \\ \frac{\mathrm{d}i_q}{\mathrm{d}t} \\ \frac{\mathrm{d}i_0}{\mathrm{d}t} \end{bmatrix} + \begin{bmatrix} -\omega_e L_q i_q \\ \omega_e(L_d i_d + \Phi_f) \\ 0 \end{bmatrix} \tag{2.9}$$

where

- $u_0 = \dfrac{u_{AN} + u_{BN} + u_{CN}}{3}$;
- $i_0 = \dfrac{i_A + i_B + i_C}{3}$;

Torque equation:

$$T_e = \frac{3}{2} p[\Phi_f i_q + (L_d - L_q) i_d i_q] \tag{2.10}$$

2.1.3 Mechanical dynamics

According to Newton's second law, the motion equation of the motor can be formulated by

$$J_m \frac{\mathrm{d}\omega_m}{\mathrm{d}t} = T_e - B_m \omega_m - T_L \tag{2.11}$$

where

- J_m denotes the rotational inertia;
- ω_m denotes the mechanical angular velocity of the rotor;
- B_m denotes the coefficient of viscous friction;
- T_L denotes the load torque;

2.2 Analytical model of a PMSM-based basic MFCS

The circuit configuration of a conventional three-phase PMSM fed by a three-phase two-level VSI is shown in figure 2.2. The NP (N) of the motor is untapped. Therefore, there is no zero-sequence current generated inside the motor.

The circuit structure of a PMSM-based basic MFCS is illustrated in figure 2.3. Compared to the conventional drive, it connects the NP to the DC-source while remaining the same

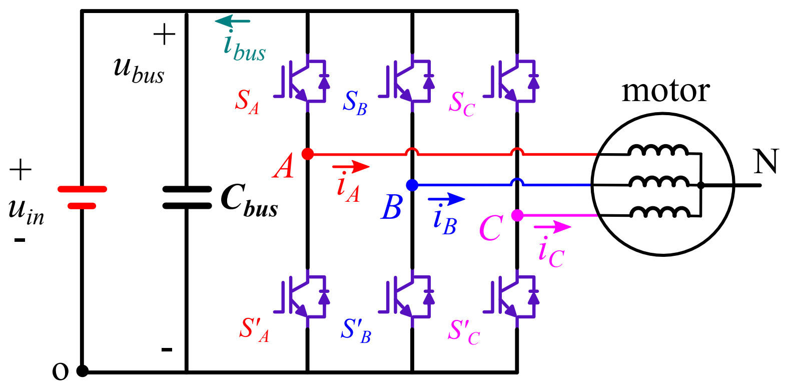

FIGURE 2.2: Circuit configuration of a conventional PMSM drive.

components without any auxiliary hardware. On the DC-bus side, only the DC-bus capacitor remains.

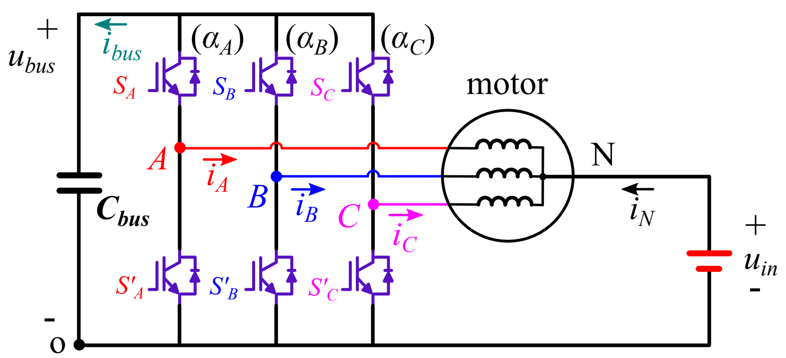

FIGURE 2.3: Circuit configuration of a PMSM-based basic MFCS.

In order to study and analyze the characteristics of the PMSM-based basic MFCS, the system model including the inverter circuit will be built in this section. Throughout the derivation, the following assumptions are given:

- All the switching devices are considered as ideal switches whose voltage drop, dead time and non-linearity are neglected;
- The DC-bus capacitor is regarded as an ideal capacitor whose equivalent series resistance is neglected;
- The DC power-source is considered as an ideal DC source with a constant and stable voltage.
- The switching frequency is considered as constant;

2.2.1 Average model

Based on aforementioned hypotheses, the switching functions (S_X and $S_X^{'}$) of the VSI are defined as

$$\begin{aligned} S_X &= \begin{cases} 1 & \text{when the upper switch is ON} \\ 0 & \text{when the lower switch is ON} \end{cases}, (x = A, B, C) \\ S_X^{'} = \overline{S}_X &= \begin{cases} 1 & \text{when the lower switch is ON} \\ 0 & \text{when the upper switch is ON} \end{cases}, (x = A, B, C) \end{aligned} \tag{2.12}$$

According to time-averaging equivalent modeling approach and Kirchhoff's laws, the average model of the basic MFCS (illustrated in figure 2.3) can be built within one switching period. On the basis of Kirchhoff's voltage Law (KVL), the average voltage equations of the basic MFCS can be derived as

$$\underbrace{\begin{bmatrix} u_{AO} \\ u_{BO} \\ u_{CO} \end{bmatrix}}_{\boldsymbol{u}_{invABC}} = \underbrace{\begin{bmatrix} \alpha_A \\ \alpha_B \\ \alpha_C \end{bmatrix}}_{\boldsymbol{\alpha}_{ABC}} u_{bus} = \underbrace{\begin{bmatrix} u_{AN} \\ u_{BN} \\ u_{CN} \end{bmatrix}}_{\boldsymbol{u}_{ABC}} + \begin{bmatrix} u_{in} \\ u_{in} \\ u_{in} \end{bmatrix} \tag{2.13}$$

According to Kirchhoff's current Law (KCL), the average current equations can be given as

$$\begin{cases} i_N = -(i_A + i_B + i_C) \\ i_{bus} = C_{bus} \dfrac{\mathrm{d}u_{bus}}{\mathrm{d}t} = -\boldsymbol{\alpha}_{ABC}^T \boldsymbol{i}_{ABC} \end{cases} \tag{2.14}$$

where

- $\boldsymbol{u}_{invABC} := [u_{AO} \quad u_{BO} \quad u_{CO}]^T$ denotes the terminal voltages of the inverter;
- $\boldsymbol{\alpha}_{ABC} := [\alpha_A \quad \alpha_B \quad \alpha_C]^T$ denotes the duty-cycles of inverter's legs;
- u_{bus} is the DC-bus voltage;
- u_{in} is the DC-source voltage;
- i_N is the neutral current, which can also be seen as the input current of the whole system;
- i_{bus} is the DC-bus current;
- C_{bus} is the DC-bus capacitance;
- All above variables represent the mean values within one switching period; And all the positive directions are defined by the arrows shown in figure 2.3.

By using the Park transformation (power invariant), (2.13) can be transformed from A-B-C to d-q-0 coordinates, as

$$\underbrace{\begin{bmatrix} u_{invd} \\ u_{invq} \\ u_{inv0} \end{bmatrix}}_{\boldsymbol{u}_{invdq0}} = \underbrace{\begin{bmatrix} \alpha_d \\ \alpha_q \\ \alpha_0 \end{bmatrix}}_{\boldsymbol{\alpha}_{dq0}} u_{bus} = \underbrace{\begin{bmatrix} u_d \\ u_q \\ u_0 \end{bmatrix}}_{\boldsymbol{u}_{dq0}} + \begin{bmatrix} 0 \\ 0 \\ \sqrt{3}u_{in} \end{bmatrix} \tag{2.15}$$

where

- $\boldsymbol{u}_{invdq0} := [u_{invd} \quad u_{invq} \quad u_{inv0}]^T$ denotes the terminal voltages of the inverter converted to d-q-0 coordinate;
- $\boldsymbol{\alpha}_{dq0} := [\alpha_d \quad \alpha_q \quad \alpha_0]^T$ includes the values of duty-cycles converted into d-q-0 coordinate frame;

In the same way, (2.14) can also be transformed from A-B-C to d-q-0 coordinates, as

$$\begin{cases} i_N = -(i_A + i_B + i_C) = -\sqrt{3}i_0 \\ i_{bus} = C_{bus}\dfrac{\mathrm{d}u_{bus}}{\mathrm{d}t} = -\boldsymbol{\alpha}_{ABC}^T \boldsymbol{i}_{ABC} = -(\boldsymbol{T}_p^{-1}\boldsymbol{\alpha}_{dq0})^T \boldsymbol{T}_p^{-1}\boldsymbol{i}_{dq0} = -\boldsymbol{\alpha}_{dq0}^T \boldsymbol{i}_{dq0} \end{cases} \tag{2.16}$$

By substituting (2.6) into (2.16) and by combining with (2.14), the average model of the basic MFCS in d-q-0 coordinate can be rewritten as:

d-q-0 average model obtained by the Park transformation (power invariant):

[a]

$$\begin{cases} u_{invd} = \alpha_d u_{bus} = u_d = Ri_d + L_d\dfrac{\mathrm{d}i_d}{\mathrm{d}t} - \omega_e L_q i_q \\ u_{invq} = \alpha_q u_{bus} = u_q = Ri_q + L_q\dfrac{\mathrm{d}i_q}{\mathrm{d}t} + \omega_e(L_d i_d + \Phi_m) \\ u_{inv0} = \alpha_0 u_{bus} = \underbrace{Ri_0 + L_0\dfrac{\mathrm{d}i_0}{\mathrm{d}t}}_{u_0} + \sqrt{3}u_{in} \\ i_{bus} = C_{bus}\dfrac{\mathrm{d}u_{bus}}{\mathrm{d}t} = -(\alpha_d i_d + \alpha_q i_q + \alpha_0 i_0) \end{cases} \tag{2.17a}$$

By replacing i_0 with $-i_N/\sqrt{3}$, it further yields

$$\begin{cases} \alpha_d u_{bus} = u_d = Ri_d + L_d \dfrac{\mathrm{d}i_d}{\mathrm{d}t} - \omega_e L_q i_q \\ \alpha_q u_{bus} = u_q = Ri_q + L_q \dfrac{\mathrm{d}i_q}{\mathrm{d}t} + \omega_e (L_d i_d + \Phi_m) \\ \alpha_h u_{bus} = -\dfrac{R}{3} i_N - \dfrac{L_0}{3} \dfrac{\mathrm{d}i_N}{\mathrm{d}t} + u_{in} \\ i_{bus} = C_{bus} \dfrac{\mathrm{d}u_{bus}}{\mathrm{d}t} = \alpha_h i_N - \underbrace{(\alpha_d i_d + \alpha_q i_q)}_{i_{lo}} \end{cases} \tag{2.17b}$$

where

- $\alpha_h = \dfrac{\alpha_0}{\sqrt{3}} = \dfrac{\alpha_A + \alpha_B + \alpha_C}{3}$ denotes the average duty-cycle of the inverter.
- i_{lo} is seen as an equivalent load current.

[a]The model obtained by the Park transformation (power invariant) will be used in the following analysis and the construction of equivalent circuits.

In (2.17b), the first two equations are similar to the well-known *d*-*q* model of a PMSM, which are usually used to design the classic FOC. However, the last two equations are unique in the basic MFCS due to the circulated zero-sequence path. The circulated zero-sequence current will enable the power flow between the DC-bus capacitor and the DC-source. Therefore, the last two equations can not be ignored in the basic MFCS.

In steady-state, the motor power is assumed to be constant. According to power conservation law, the input current (i.e. the neutral current i_N) of the basic MFCS is constant. Thus, i_0 is also constant. In this case, the derivative term ($L_0 \frac{\mathrm{d}i_0}{\mathrm{d}t}$) in (2.17a) and the derivative term ($\frac{L_0}{3} \frac{\mathrm{d}i_N}{\mathrm{d}t}$) in (2.17b) are equal to 0. By further neglecting the voltage drop across the resistance R, we obtain

$$u_{bus} \approx \frac{u_{in}}{\alpha_0/\sqrt{3}} = \frac{u_{in}}{\alpha_h} = \frac{3u_{in}}{\alpha_A + \alpha_B + \alpha_C} \tag{2.18}$$

According to (2.18), it can be observed that the DC-bus voltage u_{bus} is able to reach higher value than the DC-source voltage u_{in} as long as α_h is smaller than 1. This phenomenon is similar to a DC/DC boost converter.

If the Park transformation (amplitude invariant) is used, (2.17a) and (2.17b) become

***d*-*q*-0 average model obtained by the Park transformation (amplitude invariant):**

[a] voltage equation:

$$\begin{cases} u_{invd} = \alpha_d u_{bus} = u_d = Ri_d + L_d \dfrac{\mathrm{d}i_d}{\mathrm{d}t} - \omega_e L_q i_q \\ u_{invq} = \alpha_q u_{bus} = u_q = Ri_q + L_q \dfrac{\mathrm{d}i_q}{\mathrm{d}t} + \omega_e (L_d i_d + \Phi_m) \\ u_{inv0} = \alpha_0 u_{bus} = \underbrace{Ri_0 + L_0 \dfrac{\mathrm{d}i_0}{\mathrm{d}t}}_{u_0} + u_{in} \\ i_{bus} = C_{bus} \dfrac{\mathrm{d}u_{bus}}{\mathrm{d}t} = -\dfrac{3}{2}(\alpha_d i_d + \alpha_q i_q + 2\alpha_0 i_0) \end{cases} \tag{2.19a}$$

Replacing i_0 by $-i_N/3$, it further yields

$$\begin{cases} \alpha_d u_{bus} = u_d = Ri_d + L_d \dfrac{\mathrm{d}i_d}{\mathrm{d}t} - \omega_e L_q i_q \\ \alpha_q u_{bus} = u_q = Ri_q + L_q \dfrac{\mathrm{d}i_q}{\mathrm{d}t} + \omega_e (L_d i_d + \Phi_m) \\ \alpha_h u_{bus} = -\dfrac{R}{3} i_N - \dfrac{L_0}{3} \dfrac{\mathrm{d}i_N}{\mathrm{d}t} + u_{in} \\ i_{bus} = C_{bus} \dfrac{\mathrm{d}u_{bus}}{\mathrm{d}t} = \alpha_h i_N - \underbrace{\dfrac{3}{2}(\alpha_d i_d + \alpha_q i_q)}_{i_{lo}} \end{cases} \tag{2.19b}$$

where

- $\alpha_h = \alpha_0 = \dfrac{\alpha_A + \alpha_B + \alpha_C}{3}$ denotes the average duty-cycle.
- i_{lo} is seen as an equivalent load current.

[a] The model obtained by the Park transformation (amplitude invariant) will be used in the following control design.

2.2.2 Equivalent circuits

Although (2.18) reveals the existence of an equivalent DC/DC boost function which is integrated in the basic MFCS, how does the boost interact with the motor is still indistinct. Therefore, this should be studied in detail. As we all know, using equivalent circuit is an effective means to simplify the analysis and understanding of a complex circuit system. In this subsection, different equivalent circuits will be presented to facilitate the mechanism of the basic MFCS. To construct the equivalent circuit, the *d*-*q*-0 model obtained by using the Park transformation (power invariant) is used.

2.2.2.1 d-q-0 equivalent circuit

Actually, (2.17a) presents the electrical relationship of the basic MFCS in d-q-0 coordinate. Based on that, we can know that the d-q voltages (u_{invd} and u_{invq}) of the inverter are still equal to the d-q voltages (u_d and u_q) of the motor. This indicates that the connection of motor's NP does not affect the relationship between the inverter and the motor in d-q plane. In other words, the conventional FOC can still be used to control the torque and flux of the motor through d-axis and q-axis currents.

However, the connected NP does induce some changes on the 0-axis. The zero-sequence item of (2.17a) implies that the connected NP enables the zero-sequence circuit of the drive system by providing a zero-sequence path for the zero-sequence current to flow. The zero-sequence voltage (u_{inv0}) of the inverter is different from the zero-sequence voltage (u_0) of the motor. Based on (2.17a), we can draw the corresponding d-q-0 equivalent circuit of the PMSM-based basic MFCS, as displayed in figure 2.4. It consists of a typical d-q circuit and a unique zero-sequence circuit. The d-axis and q-axis are coupled through i_d and i_q. The zero-sequence circuit is coupled with the d-q circuit to u_{bus} and i_{bus} (see the fourth equation of (2.17a)).

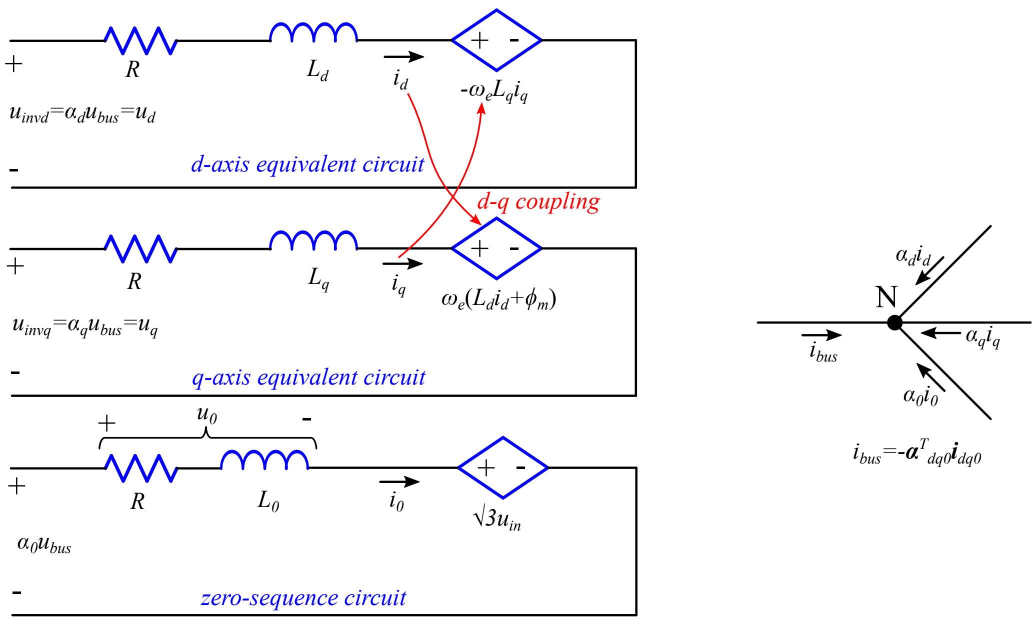

FIGURE 2.4: d-q-0 equivalent circuit of the PMSM-based basic MFCS.

2.2.2.2 Visualized equivalent circuit

Although the d-q-0 equivalent circuit reveals the link between the d-q circuit and the zero-sequence circuit, the physical significance of the equivalent boost function is still not intuitive. Normally, a typical DC/DC boost converter consists of a DC-source, a filtering inductor, a chopper, a capacitor and a load. Thus, what components of the basic MFCS do construct the equivalent boost function is still confusing in the d-q-0 equivalent circuit.

To further reveal the equivalent boost function, (2.17b) is referenced to establish a more visualized and comprehensible equivalent circuit since the neutral current i_N is more intuitional than i_0. The visualized equivalent circuit is shown in figure 2.5. It is well-known that the invention of FOC makes it easier to control an AC motor by decoupling its electromagnetic torque and flux linkage. In d-q plane, an AC motor can be seen as an equivalent DC motor. Therefore, we can use an equivalent DC motor drive to represent the motor function of the basic MFCS. To embody the physical significance of α_d and α_q, we use two virtual H-bridges named as 'H1' and 'H2' to drive the equivalent DC motor hypothetically. The two H-bridges are constructed by eight virtual switches S_{v1}, S'_{v1}, S_{v2}, S'_{v2}, S_{v3}, S'_{v3}, S_{v4} and S'_{v4}. To be specific, α_d represents the difference between the duty-cycles of S_{v3} and S_{v4}; α_q represents the difference between the duty-cycles of S_{v2} and S_{v5}. Based on the above hypotheses, it is obvious that the physical significance of the first two equations of (2.17b) is well visualized in the dual H-bridge circuit. Essentially, it is similar to a DC motor drive.

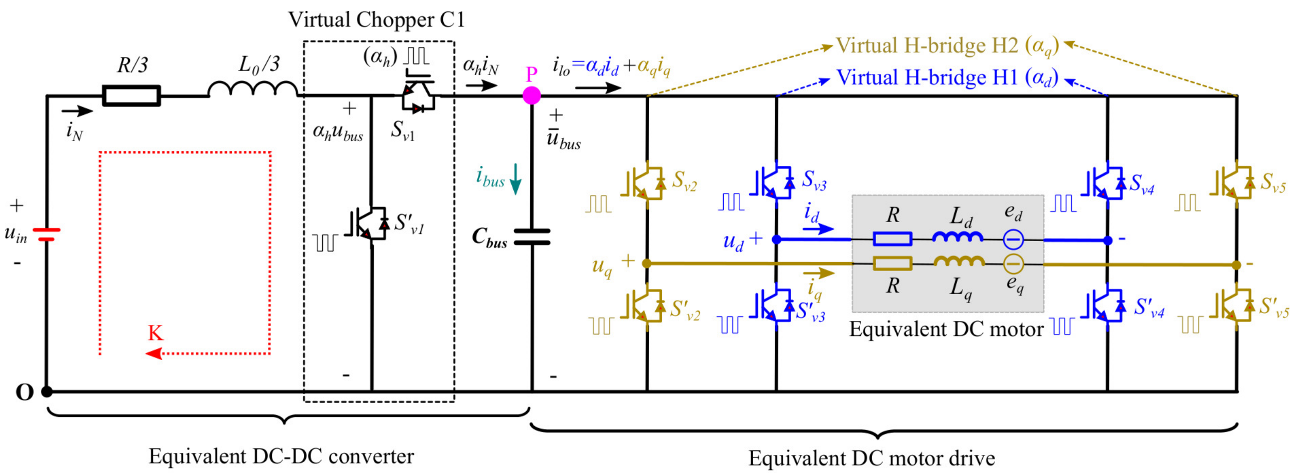

FIGURE 2.5: Visualized equivalent circuit of the PMSM-based basic MFCS.

In order to embody the physical significance of the last two equations of (2.17b), we introduce a virtual chopper 'C1', which is constructed by two virtual switches S_{v1} and S'_{v1}. Because the physical limitation of inverter's duty cycles (α_A, α_B and α_C) is between 0 and 1, the reachable range of $\alpha_h = (\alpha_A + \alpha_B + \alpha_C)/3$ is also (0-1). Therefore, α_h can be perfectly represented by the virtual chopper in the average model, where α_h denotes the duty-cycle of S_{v1}. In this case, the third equation of (2.17b) is visualized by the contour 'K' in figure 2.5. The fourth equation of (2.17b) is visualized on the node 'P' in figure 2.5. Therefore, it is reasonable to say that the last two equations of (2.17b) can be represented by an equivalent DC/DC boost converter. The zero-sequence inductance $L_0/3$ plays the role of the filtering reactor in the boost function. Finally, the basic MFCS system can be seen as a two-stage DC motor drive. The equivalent DC motor drive function as an equivalent load for the equivalent DC/DC boost converter. The equivalent load current (i_{lo}) is equal to ($\alpha_d i_d + \alpha_q i_q$).

2.2.2.3 Generalized equivalent circuit

To further elaborate the power conversion process, it is reasonable to separate all the zero-sequence components from the motoring function by cutting off the NP hypothetically. Once the NP is disconnected, the basic MFCS can be divided into two parts, one is the zero-sequence part and the other is the conventional part where the NP is not connected.

Based on the above hypotheses, generalized equivalent circuits are presented in figure 2.6. These equivalent circuits can represent a basic MFCS based on any kind of three-phase AC machines, such as induction machines and synchronous reluctance machines.

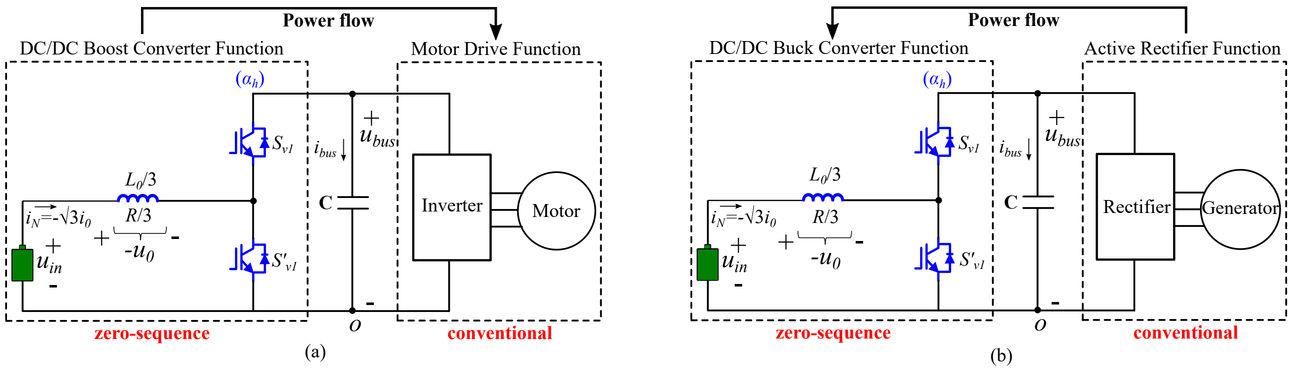

FIGURE 2.6: Generalized equivalent circuits of a basic MFCS. (a) In motoring pattern. (b) In regenerative braking pattern.

During motoring patterns, the zero-sequence part functions as a DC/DC boost converter, to raise the DC-bus voltage. The conventional part acts as a common motor drive whose NP is not used. The system power flows from the zero-sequence part to the conventional part, i.e. the DC-source is discharged. During regenerative braking patterns, the motor becomes a generator and the conventional part functions as an active rectifier. In this case, the zero-sequence part functions as a DC/DC buck converter, and the system power flows from the conventional part to the zero-sequence part, i.e. the DC-source is charged. Therefore, from the functionality point of view, the generalized equivalent circuits further reveal that the basic MFCS system is similar to a two-stage converter. However, compared to a real two-stage converter, it employs fewer switching devices and passive components by taking advantage of its zero-sequence circuit.

2.3 Modulation method and steady-state characteristic

The proposed average model and equivalent circuits indicate that the zero-sequence circuit of the basic MFCS can be used as a boost. The average duty cycle (α_h) of the inverter can be used as the control DOF for the equivalent boost function. However, how to implement the control DOF (α_h) into the modulation method is a complex issue.

2.3.1 Discussion of SVPWM used in the basic MFCS

As we all know, a VSI-fed three-phase AC motor drive usually uses PWM techniques to realize the conversion from DC to AC[78]. Normally, SPWM and SVPWM are two typical and commonly used modulation methods. In particular, SVPWM is chosen preferentially due to its high voltage utilization and low harmonics ratio[79]. Compared to SPWM, the modulation ratio m of SVPWM can be improved by 15% in the absence of over-modulation[80]. In the classic SVPWM technique, the reference voltage vector is synthesized in α-β plane divided into six sectors. In each switching period, adjacent vectors and zero vectors are utilized to synthesize the reference voltage.

From the carrier-based modulation technique point of view, the classic SVPWM can be approximatively treated as a particular form of SPWM where the modulating signal is superposed with a third harmonic[81][82]. As shown in figure 2.7, by superposing the third harmonic, the amplitude of fundamental voltages is improved and the linear modulation range can be extended. In fact, the superposed third harmonic is a typical type of zero-sequence voltages. This zero-sequence voltage does not generate zero-sequence currents in a conventional three-phase drive system due to the Y-connection winding layout. In other words, the DOF of zero-sequence voltages is well utilized in the classic SVPWM to the purpose of improving the voltage output capability of a three-phase two-level VSI. However, if the classic SVPWM is used in the basic MFCS, the superposed third harmonic voltage will induce third harmonic currents caused by the connected NP thus further resulting in voltage oscillations on the DC-bus.

We calculate the value of α_h[1] when the classic SVPWM is applied. Figure 2.8 presents the evolution of α_h with respect to the electrical position and the modulation ratio m. It can be seen that for a given m, the shape of α_h is similar to a triangular wave in one electrical period. The mean value of α_h is 0.5 and its frequency is three times that of the fundamental wave. The amplitude of α_h increases with the increase of m. Because the modulation ratio m is related to the operating condition of the motor, α_h is directly determined by the control of the motor. In the case of $m = 1.15$, the peak and valley of α_h can reach around 0.66 and 0.34

[1]The calculation is detailed in Appendix B.

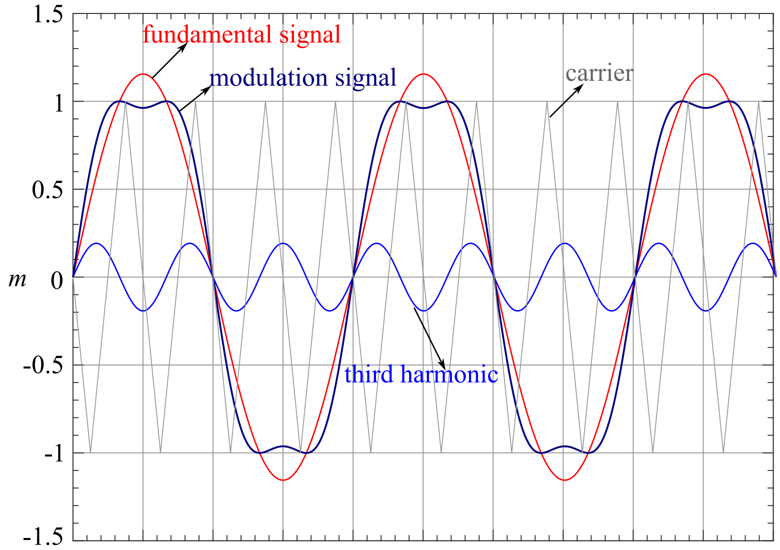

FIGURE 2.7: Effect of superposing a third harmonic voltage in the carrier based modulation.

respectively. Therefore, if the classic SVPWM is used in the basic MFCS, the control of the motor will directly affect the equivalent DC/DC boost function. It can be predicted that the DC-bus voltage will oscillate with the change of α_h. Consequently, if the classic SVPWM is used in the basic MFCS, there is no control DOF available for the equivalent boost since α_h is determined by the control of the motor.

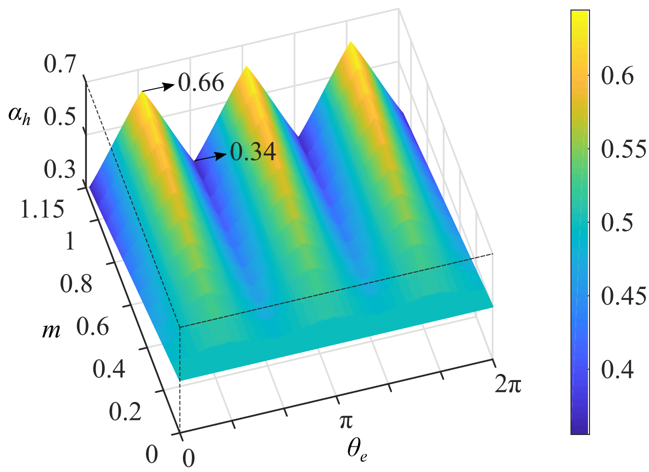

FIGURE 2.8: The evolution of α_h when the classic SVPWM is used.

2.3.2 Zero-sequence voltage injected PWM

Since the classic SVPWM is inapplicable in the basic MFCS based on the above analysis, we propose a carrier-based modulation method, which is called zero-sequence voltage injected PWM (ZSVIPWM). In order to control the equivalent boost function, a certain amount of zero-sequence voltage is required and should be independent of the control of the motor. The requisite zero-sequence voltage (u_{ZS}) is defined as

$$u_{ZS} = \frac{(u_{AN} + u_{BN} + u_{CN})}{3} = \frac{u_0}{\sqrt{3}} \tag{2.20}$$

According to (2.17a), u_{ZS} can be represented by

$$u_{ZS} = \frac{u_0}{\sqrt{3}} = \alpha_h u_{bus} - u_{in} \tag{2.21}$$

In steady-state, the derivative term of (2.17b) $\frac{L_0}{3}\frac{di_N}{dt}$ is 0. By combining with (2.21), we obtain that u_{ZS} is equal to $\frac{-Ri_N}{3}$. In motoring conditions, the DC-source should provide power to the motor. Therefore, the input current (i.e. neutral current) i_N is positive. Based on this, we know that the required zero-sequence voltage u_{ZS} is negative. On the contrary, in regenerative braking conditions, u_{ZS} is positive. In the following, we consider the motoring condition for analysis.

By considering the zero-sequence voltage u_{ZS}, the actual phase-voltage reference (${u_{XN}}^*$) in the basic MFCS is not a standard sinusoidal signal. It should be the sum of the fundamental voltage reference (u^*_{XN1}) and the required zero-sequence voltage (u_{ZS}). Then, by combining with (2.21), we obtain

$${u_{XN}}^* = {u_{XN1}}^* + u_{ZS} = {u_{XN1}}^* + \alpha_h u_{bus} - u_{in}, \quad X \in \{A, B, C\} \tag{2.22}$$

Due to the clamped NP in the basic MFCS, the carrier signal of ZSVIPWM is asymmetrical. To be specific, the positive and negative amplitudes of the carrier signal are respectively equal to $u_{bus} - u_{in}$ and $-u_{in}$, as shown in figure 2.9. Moreover, the actual modulating signal (${u_{XN}}^*$) shows a downward offset due to the required zero-sequence voltage (u_{ZS}) compared to the fundamental voltage reference (u^*_{XN1}). In this case, by comparing the modulating signal ${u_{XN}}^*$ with the carrier signal, the actual PWM signals can be generated.

In digital control system, the control input is the duty cycle ($\alpha_X, \quad X \in \{A, B, C\}$). If the regular-sampling method (see figure 2.10) is adopted, the final duty-cycle α_X used for digital control can be derived by

$$\alpha_X = \frac{\delta/2}{T_s/2} = \frac{{u_{XN}}^* + u_{in}}{u_{bus}} = \alpha_h + \frac{{u_{XN1}}^*}{u_{bus}} \tag{2.23}$$

where

- δ is the high-level time of S_X in one PWM period.

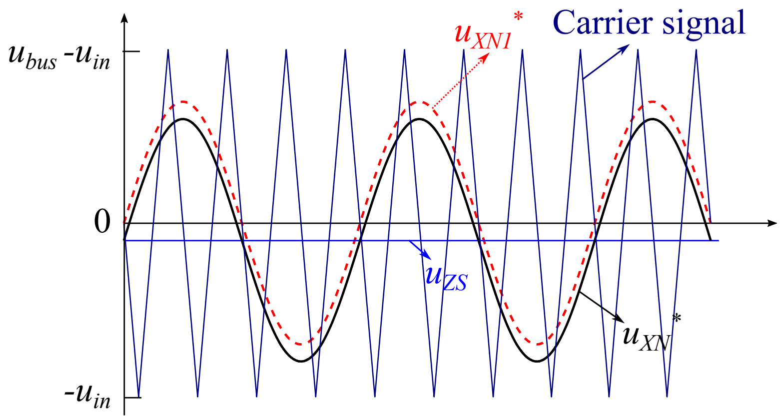

FIGURE 2.9: Schematic diagram of ZSVIPWM.

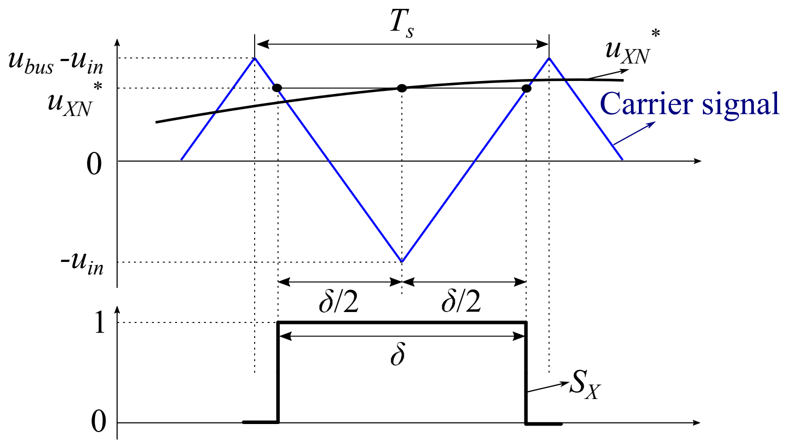

FIGURE 2.10: Schematic diagram of regular sampling method.

Consequently, (2.23) is the final algorithm of ZSVIPWM where α_h is an independent control DOF for the equivalent DC/DC boost function and the fundamental voltage reference u^*_{XN1} is the control DOF for the motor. Especially, when $\alpha_h = 0.5$, (2.23) actually corresponds to the algorithm of the classic SPWM by using the regular sampling method. However, if the classic SPWM is adopted, u_{bus} can be only regulated to double u_{in} in an open-loop way since no independent control DOF can be provided by the classic SPWM. This issue is similar to the classic SVPWM. By comparison, we can say that the proposed ZSVIPWM skillfully decouple the control DOFs of the equivalent boost function and the motor function. This makes it possible to actively regulate the power flow between the motor and the DC-source or to control the DC-bus voltage.

2.3.3 DC-source voltage utilization ratio

Thanks to the equivalent DC/DC boost function, u_{bus} can reach a higher value than u_{in} in the basic MFCS. However, the reachable AC voltages for the motor are bounded. In other words, the effective step-up ratio of the equivalent DC/DC boost has a limit due to the coupling between α_d, α_q and α_h when saturation occurs. If the boosted DC-bus voltage can not improve the fundamental AC voltages, it makes no sense. It may even result in higher switching losses. Therefore, it is necessary to study the relationship between the step-up ratio of the equivalent DC/DC boost and the DC-source voltage utilization ratio (DCSUR).

The step-up ratio (r_0) of the equivalent boost is defined as

$$r_0 = \frac{u_{bus}}{u_{in}} \tag{2.24a}$$

To evaluate the reachable AC voltages, the DCSUR (r_1) is defined as

$$r_1 = \frac{u_{XN1amp}}{u_{in}} \tag{2.24b}$$

where

- u_{XN1amp} is the amplitude of fundamental AC voltages.

For the sake of analysis, the proportion (r_2) between the zero-sequence voltage and the DC-source voltage is defined as

$$r_2 = \frac{|u_{ZS}|}{u_{in}} \tag{2.24c}$$

As mentioned before, the positive and negative amplitudes of the carrier signal are equal to $u_{bus} - u_{in}$ and $-u_{in}$, respectively. In order to guarantee $u_{XN}{}^*$ to be within the linear modulation region, the amplitude of $u_{XN}{}^*$ (which is defined as u_{XNamp}) is limited by the lowest one between u_{in} and $u_{bus} - u_{in}$. Accordingly, the amplitude of fundamental AC voltages (u_{XN1amp}) is also limited. Considering different conditions, there are five cases to be discussed:

1) $u_{bus} > 2u_{in}$ (i.e. $r_0 > 2$)

   In this case, the carrier signal is asymmetrical because $u_{bus} - u_{in}$ is larger than u_{in}. The offset of the carrier signal is $(u_{bus} - 2u_{in})/2$, which is larger than 0. Meanwhile, the actual modulating signal $u_{XN}{}^*$ shows a downward offset because of the injected zero-sequence voltage u_{ZS}. Based on all above conditions, it is obvious that the lower edge of $u_{XN}{}^*$ will firstly reach the limit of $-u_{in}$ with the rise of the modulation ratio, as shown in figure 2.11(a). As a result, the limit of u_{XNamp} is u_{in} and the limit of u_{XN1amp} is evaluated as $u_{in} - |u_{ZS}|$ (i.e. $r_1 = 1 - r_2$).

2) $u_{bus} = 2u_{in}$ (i.e. $r_0 = 2$)

   When $u_{bus} = 2u_{in}$, the carrier signal is symmetrical because the offset $(u_{bus} - 2u_{in})/2$ of the carrier signal is 0. The actual modulating signal $u_{XN}{}^*$ still shows a downward

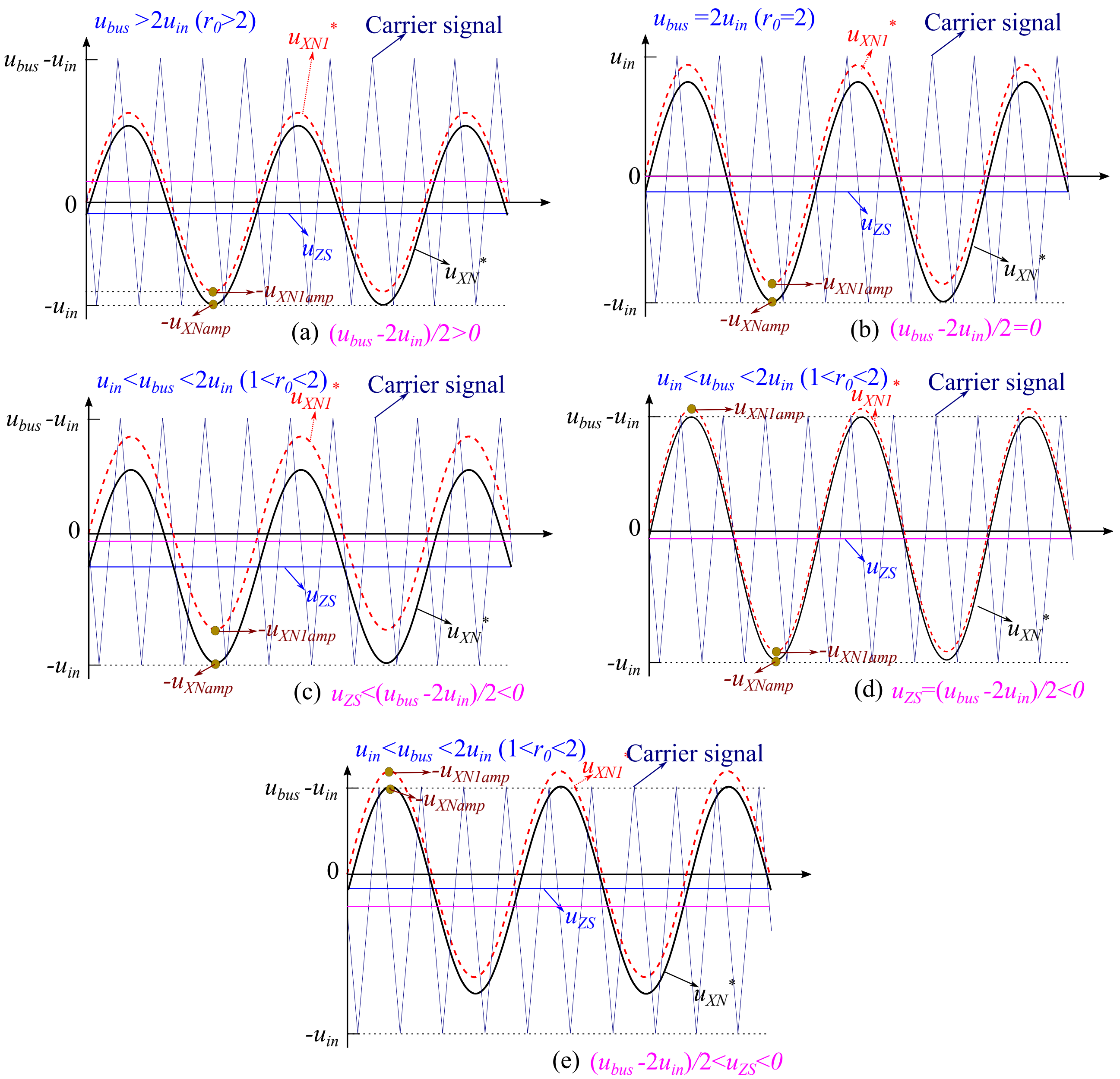

FIGURE 2.11: Five specific cases of the basic MFCS.

offset because of the injected zero-sequence voltage u_{ZS}. In this case, the lower edge of ${u_{XN}}^*$ will also firstly reach the limit of $-u_{in}$, as shown in figure 2.11(b). As a result, the limit of u_{XNamp} is still u_{in} and the limit of u_{XN1amp} is still evaluated as $u_{in} - |u_{ZS}|$ (i.e. $r_1 = 1 - r_2$).

3) $u_{in} < u_{bus} < 2u_{in}$ (i.e. $1 < r_0 < 2$) and $u_{ZS} < (u_{bus} - 2u_{in})/2$

In this case, the carrier signal is asymmetrical. It shows a upward offset because the offset $(u_{bus} - 2u_{in})/2$ is smaller than 0. However, $(u_{bus} - 2u_{in})/2$ is larger than u_{ZS}, i.e. $r_0 > 2 - 2r_2$. This indicates that the downward offset of ${u_{XN}}^*$ is bigger than the upward offset of the carrier signal. In this case, the lower side of ${u_{XN}}^*$ will firstly reach the limit of $-u_{in}$, as shown in figure 2.11 (c). As a result, the limit of u_{XNamp} is u_{in} and the limit of u_{XN1amp} is evaluated as $u_{in} - |u_{ZS}|$ (i.e. $r_1 = 1 - r_2$).

4) $u_{in} < u_{bus} < 2u_{in}$ (i.e. $1 < r_0 < 2$) and $u_{ZS} = (u_{bus} - 2u_{in})/2$

   In this case, the downward offset of ${u_{XN}}^*$ is equal to the upward offset of the carrier signal, i.e. $r_0 > 2 - 2r_2$, as shown in figure 2.11(d). This implies that the positive and negative edges of ${u_{XN}}^*$ will reach the limits at the same time. Therefore, the limit of the limit of u_{XNamp} is still u_{in} and the limit of u_{XN1amp} is still $u_{in} - |u_{ZS}|$ (i.e. $r_1 = 1 - r_2$).

5) $u_{in} < u_{bus} < 2u_{in}$ (i.e. $1 < r_0 < 2$) and $u_{ZS} > (u_{bus} - 2u_{in})/2$

   In this case, the downward offset of ${u_{XN}}^*$ is smaller than the upward offset of the carrier signal, i.e. $r_0 < 2 - 2r_2$, as shown in figure 2.11(e). This indicates that the positive edge of ${u_{XN}}^*$ will firstly reach the limit $(u_{bus} - u_{in})$. As a result, the limit of u_{XNamp} is $u_{bus} - u_{in}$ and the limit of u_{XN1amp} is $u_{bus} - u_{in} + |u_{ZS}|$ (i.e. $r_1 = r_0 + r_2 - 1$).

Based on the above analysis, we can summarize that for a given r_2, r_1 equals to $1 - r_2$ in the case of $r_0 \geq (2 - 2r_2)$. For the sake of explanations, the relationship between r_0, r_1 and r_2 are visualized in figure 2.12. It can be seen that r_1 decreases with the decline of r_0 in the case of $1 < r_0 < (2 - 2r_2)$. Therefore, the largest DCSUR is $1 - r_2$ and the point 'a' ($r_0 = 2 - 2r_2$) is the optimal operating point for the whole system. When r_2 reduces to r_2', r_1 becomes r_1'. In this case, the largest DCSUR increases to $1 - {r_2}'$ and the best operating point moves to 'b'. Further, when r_2 reduces to 0, r_1 becomes r_1''. In this case, the largest DCSUR is 1 and the best operating point moves to the point '2', i.e. $u_{bus} = 2u_{in}$.

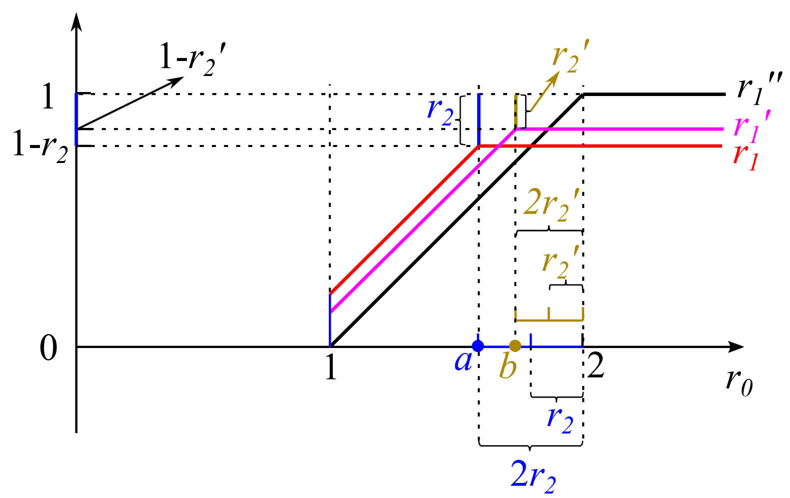

FIGURE 2.12: Analysis of DCSUR with respect to different r_0 and r_2.

In steady-state, u_{ZS} is equal to $\frac{-Ri_N}{3}$. This indicates that $|u_{ZS}|$ is equal to the voltage drop across $R/3$. Generally speaking, the stator resistance of a PMSM is relatively small. Therefore, r_2 is relatively small. If we neglect r_2, the largest DCSUR of the basic MFCS approximates to 1 and the maximum effective step-up ratio r_0 of the equivalent boost is 2. As emphasized before, the DCSUR of a conventional drive (without using its NP) is only 0.58[83] by using the classic SVPWM. Once more, this proves that the basic MFCS has higher DCSUR than a conventional drive due to the equivalent boost function (1 against 0.58).

2.3.4 Influence of the clamped NP on current ripples

Although the basic MFCS can obtain a free DC/DC boost function, the clamped NP will induce some adverse problems. To explicitly explain the influence of the clamped NP, instantaneous voltage and current waves will be compared between a conventional drive and the basic MFCS in the following.

For a conventional drive whose NP is not connected (thus is floating), the instantaneous NP voltage (u_{NO}) can be formulated by

$$u_{NO} = \frac{(u_{AO} + u_{BO} + u_{CO})}{3} = \frac{(S_A + S_B + S_C)}{3} u_{bus} \tag{2.25}$$

when the motor is balanced in three-phase, the instantaneous phase-voltages (u_{AN}, u_{BN} and u_{CN}) of the motor can be expressed by

$$\begin{bmatrix} u_{AN} \\ u_{BN} \\ u_{CN} \end{bmatrix} = \frac{u_{bus}}{3} \begin{bmatrix} 2 & -1 & -1 \\ -1 & 2 & -1 \\ -1 & -1 & 2 \end{bmatrix} \begin{bmatrix} S_A \\ S_B \\ S_C \end{bmatrix} \tag{2.26}$$

From (2.26), it can be known that there are totally five voltage-levels available to each motor phase while considering eight available switching states. To be specific (taking u_{AN} as an example), u_{AN} equals to 0 V under S_{000} and S_{111}; $\pm\frac{1}{3}u_{bus}$ V under S_{110}, S_{101}, S_{010} and S_{001}; $\pm\frac{2}{3}u_{bus}$ V under S_{100} and S_{011}.

For the basic MFCS where the NP is connected to the DC-source (thus is clamped), the instantaneous phase-voltages can be expressed by

$$\begin{bmatrix} u_{AN} \\ u_{BN} \\ u_{CN} \end{bmatrix} = u_{bus} \begin{bmatrix} S_A \\ S_B \\ S_C \end{bmatrix} - \begin{bmatrix} u_{in} \\ u_{in} \\ u_{in} \end{bmatrix} \tag{2.27}$$

Apparently, there are only two voltage-levels ($u_{bus} - u_{in}$ and $-u_{in}$) available for each motor phase. When u_{bus} is regulated at double u_{in}, the two voltage-levels are $\pm\frac{1}{2}u_{bus} = \pm u_{in}$.

For a given switching frequency, the instantaneous voltage and current waveforms of the basic MFCS and a conventional drive are compared in figure 2.13. The DC-bus voltage u_{bus} is consistent in the two drives. Therefore, the basic MFCS only needs a DC-source with the voltage of $u_{bus}/2$ while the conventional drive needs a DC-source with the voltage of u_{bus}. For the sake of explanations, the subscript $\_c$ denotes a variable in the conventional drive, $\_m$ denotes a variable in the basic MFCS. From figure 2.13, it can be seen that u_{NO_c} has four voltage-levels (0, $\frac{1}{3}u_{bus}$, $\frac{2}{3}u_{bus}$ and u_{bus}) while u_{NO_m} is clamped to $\frac{1}{2}u_{bus}$ throughout. u_{AN_c} has three voltage-levels (0, $\frac{1}{3}u_{bus}$ and $\frac{2}{3}u_{bus}$) to choose, which switches six times in one switching period (T_s) while u_{NO_m} only has two voltage-levels ($\pm\frac{1}{2}u_{bus}$) available and merely switches twice. Therefore, it can be observed that the current ripple Δi_{A_m} in the basic MFCS is much bigger than Δi_{A_c} in the conventional drive. Consequently, we can conclude that although the connected NP contributes to a free boost function, it will induce bigger current ripples. The increasing current ripples may result in more iron losses in the motor.

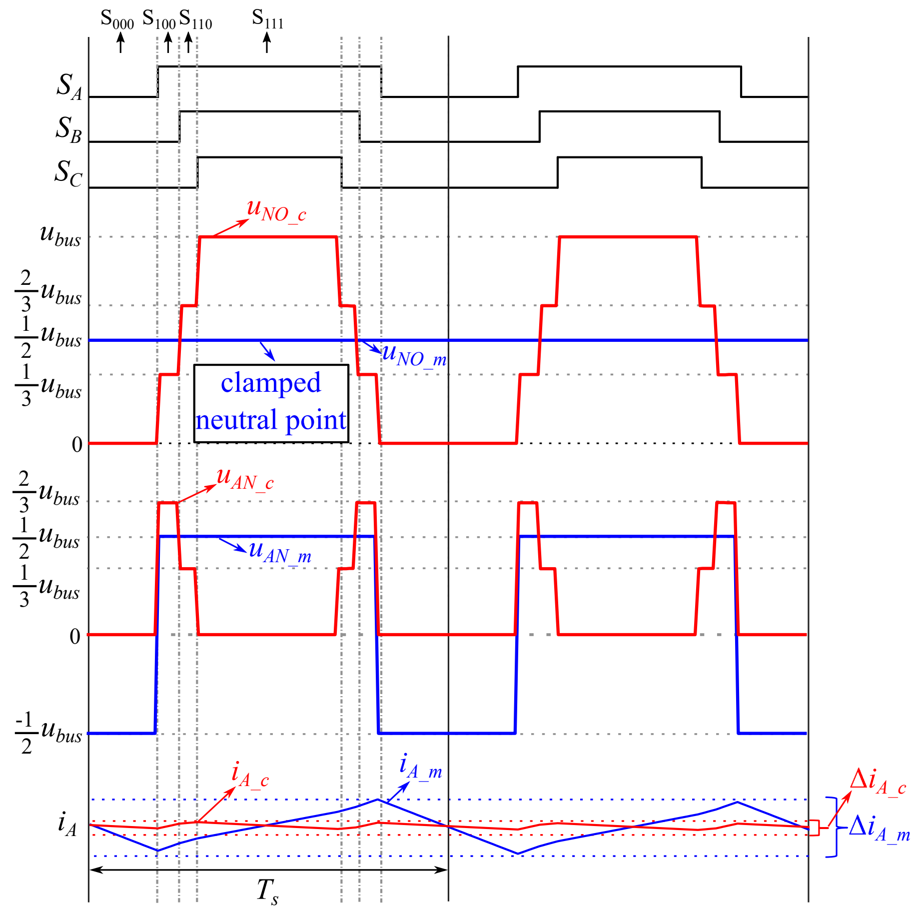

FIGURE 2.13: Detailed comparisons of voltage and current waveforms between the basic MFCS (blue) and a conventional drive (red).

2.4 Experimental verification

To construct a PMSM-based basic MFCS, a PMSM with an available NP is necessary. However, many commercial PMSM products do not provide the neutral terminal. In order to obtain the NP, we disassemble a 52.5 W PMSM and pull out its NP. Experiments will be implemented on this PMSM to verify the effectiveness. In the test-bench (see figure 2.14), hall current and voltage sensors are used to measure the phase currents, neutral current and DC-bus voltage. Control programs are implemented on a dSPACE MicroLabBox rapid prototyping system. An oscilloscope (Tektronix oscilloscope MDO3000) is used to observe the instantaneous voltages and currents. The main parameters of the test-bench are shown in table 2.2.

2.4.1 Zero-sequence inductance measurement

Considering that L_0 is a rarely used parameter in a conventional drive, we will introduce a practical method for identifying the value of L_0. According to (2.6), the zero-sequence model of the PMSM can be seen as a first-order system. In this case, the inductance parameter L_0

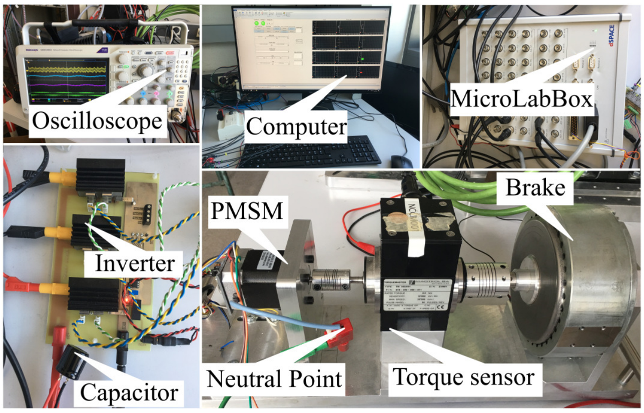

FIGURE 2.14: 52.5 W test-bench.

TABLE 2.1: Basic parameters of the 52.5 W PMSM-based test-bench.

Parameter	Value	Unit	Parameter	Value	Unit
R	0.5	Ω	p	4	-
L_d	1.1	mH	L_q	1.1	mH
L_0	0.86	mH	C_{bus}	1000	μF
Φ_f	0.0056	Wb	Nominal speed	4000	rpm/s
J_m	0.0005	$Kg \cdot m^2$	Nominal power	52.5	W
B_m	0.0001	N·m/rad	Nominal torque	125	mN·m

can be identified by testing the dynamic response of the first-order system. To configure the zero-sequence circuit, the terminals of three phases are connected together, as shown in figure 2.15(a). Then, a voltage pulse of 1 V magnitude is applied between the terminals and the NP. Then, the corresponding current response is captured by the oscilloscope, as illustrated in figure 2.15(b). Based on this, $L_0/3$ can be estimated by

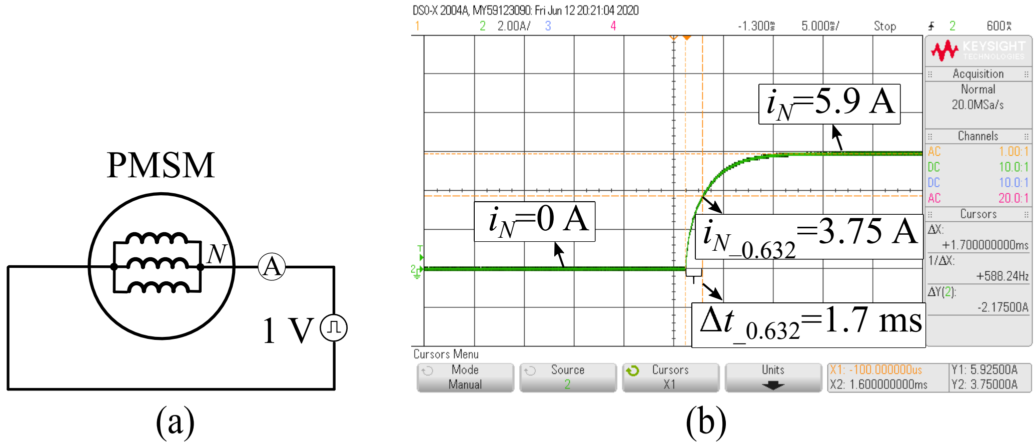

FIGURE 2.15: Zero-sequence inductance measurement. (a) Zero-sequence configuration. (b) Step response.

$$\frac{L_0}{3} = \frac{R}{3} \cdot \Delta t_{\_0.632} = \frac{1(\mathrm{V})}{5.9(\mathrm{A})} \cdot 1.7(\mathrm{ms}) = 0.29(\mathrm{mH}) \tag{2.28}$$

where $\Delta t_{\_0.632}$ is the response time of the first-order system.

Therefore, the value of L_0 of this PMSM is equal to 0.86 mH.

2.4.2 Validation of the equivalent DC/DC boost function

Based on the modeling analysis and equivalent circuits, we know that the DC-bus voltage u_{bus} is associated with the average duty cycle α_h. Therefore, a simple way to test the effect of the equivalent DC/DC boost function is to adjust α_h in an open-loop manner. Simulation verification is firstly conducted to verify the equivalent DC/DC boost functionality before conducting experiments. The simulation model is built in MATLAB/SIMULINK environment, in which the PMSM with an available neutral terminal is provided by the Simscape library. Simulation step is set as 1e-6 s and the ode1(Euler) solver is chosen. The switching frequency is set at 20 kHz. The DC-source voltage u_{in} is 15 V. At the beginning, α_h is 1. At 0.5 s, α_h is decreased to 0.5. Corresponding simulation results are shown in figure 2.16(a). It can be seen that u_{bus} is 15 V before 0.5 s. When α_h is decreased to 0.5 suddenly, u_{bus} is boosted to 32 V. In steady states, it is equal to 30 V. This verifies the existence of a voltage boosting functionality integrated in the basic MFCS. Figure 2.16(a) shows the experimental results with the same setup. Obviously, the DC-bus voltage can be also boosted to 30 V when α_h is set at 0.5.

2.4.3 Experimental comparisons in steady-states

Figure 2.17 illustrates the steady-state performance of the basic MFCS and a conventional drive when the motor is operated at the nominal condition (4000 rpm and 125 mN·m)[2]. For the basic MFCS, its DC-bus voltage can reach 30 V even if a 15 V DC-source is used thanks to the equivalent boost function. u_{bus} is boosted at 30 V stably while α_h is around 0.47 (considering the voltage drop on motor's resistance R, α_h is not exactly 0.5). The motor speed remains stable at 4000 rpm with slight fluctuations of 11 rpm (0.27%). The electromagnetic torque T_e is maintained at 125 mN·m stably with 10 mN·m (8%) fluctuations. For the conventional drive, a 30 V DC-source is connected to the DC-bus directly. Therefore, the ripple of u_{bus} is caused by the charge-discharge of the DC-bus capacitor in different switching states. However, for the basic MFCS, u_{bus} has to be actively controlled at 30 V by the equivalent boost function. In

[2]The control design for the equivalent boost is detailed in Appendix C, the classic FOC is used to control the motor.

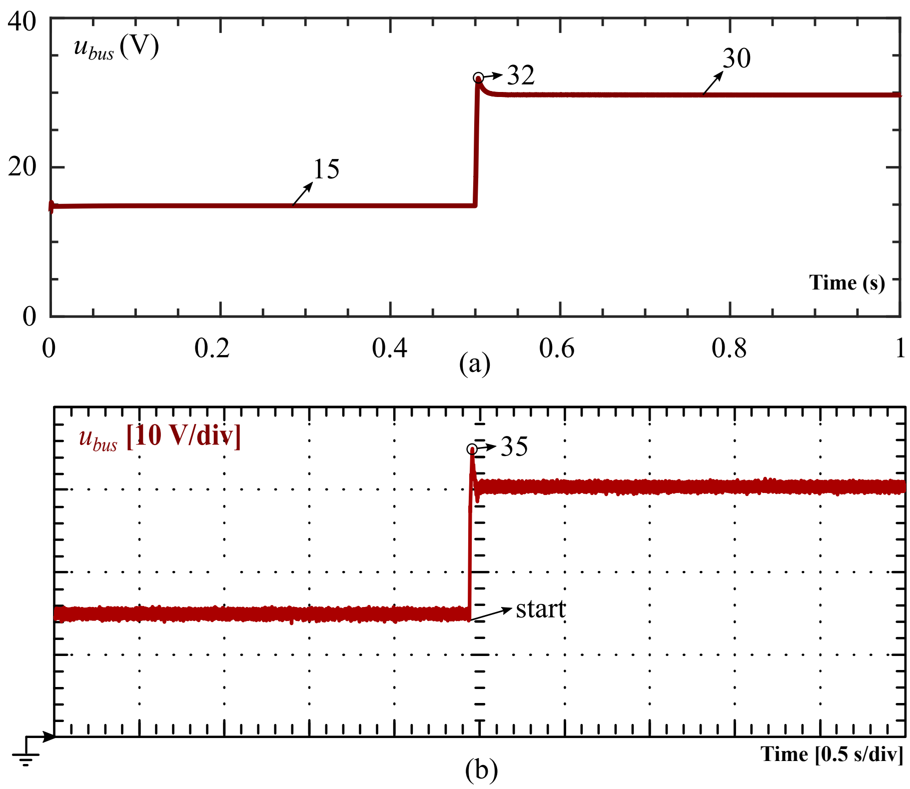

FIGURE 2.16: Simulation and experiment results of the equivalent DC/DC boost effect. (a) Simulation result. (b) Experimental result.

other words, the ripples of u_{bus} in the basic MFCS results from not only the charge-discharge of the DC-bus capacitor but also the control dynamic. Therefore, the DC-bus voltage ripple of the basic MFCS is slightly larger than that of the conventional drive (3 V to 2 V). Even so, the motor performance (speed and torque ripples) of both drives is similar.

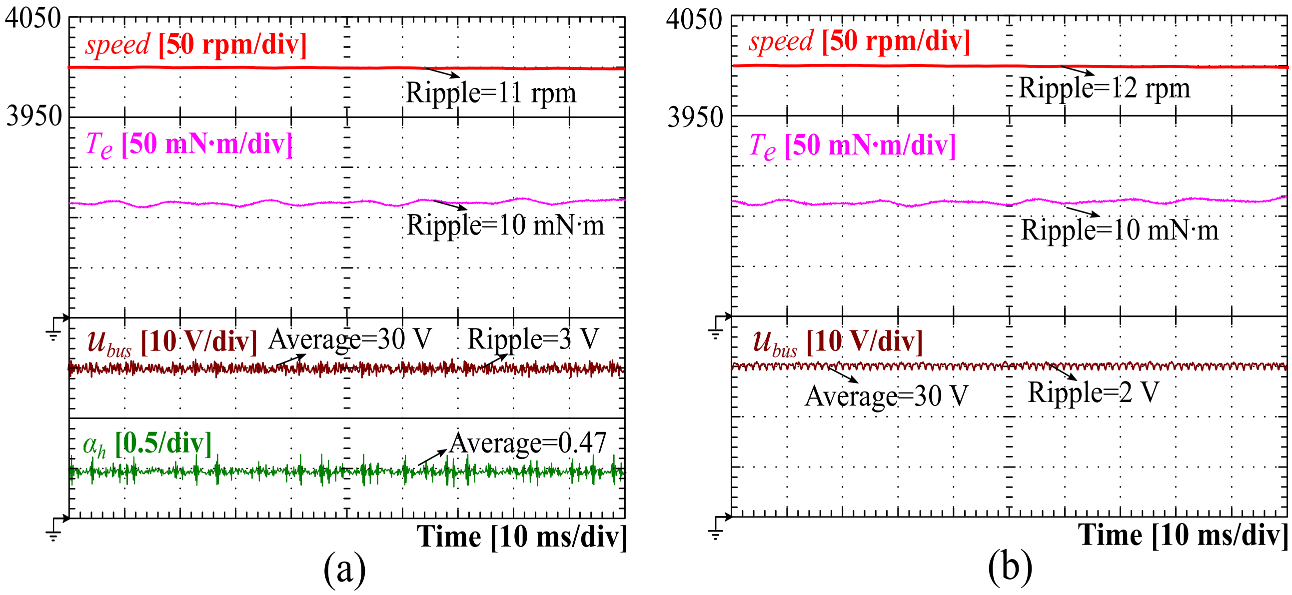

FIGURE 2.17: Steady-state performance (motor speed, torque and DC-bus voltage) at the nominal condition. (a) The basic MFCS with a 15 V DC-source. (b) The conventional drive with a 30 V DC-source.

As mentioned before, in the basic MFCS, the clamped NP results in the reduction of available voltage-levels to motor phases in one switching period. This will lead to an issue of bigger current ripples. In order to evaluate the impact caused by the clamped NP, comparative experiments are further carried out. In steady-states, phase voltages and currents are compared in detail. The real-time datum recorded by the oscilloscope (which can record 1 M points in a 40 ms period) are shown in figure 2.18(a) and (c).

Firstly, in figure 2.18(a), it can be seen that the mean values of i_B and i_C are respectively -1.58 A and -1.49 A. This means that the phase-currents of the basic MFCS shift downward due to the zero-sequence current. The offset approximates to -1/3 of the mean value of i_N (4.46 A). Comparatively speaking, the phase-currents in the conventional drive are symmetrical whose mean values are near 0 A, as shown in figure 2.18(c). Secondly, figure 2.18(a) shows that the phase-voltage u_{CN} in the basic MFCS only has two voltage-levels, $u_{bus} - u_{in}$ (15 V) and $-u_{in}$ (-15 V) due to the clamped NP. The phase-voltage u_{CN} in the conventional drive has five voltage-levels $\pm\frac{1}{3}u_{bus}$ (±10 V), 0 V and $\pm\frac{2}{3}u_{bus}$ (±20 V) thanks to the floating NP, as shown in figure 2.18(c).

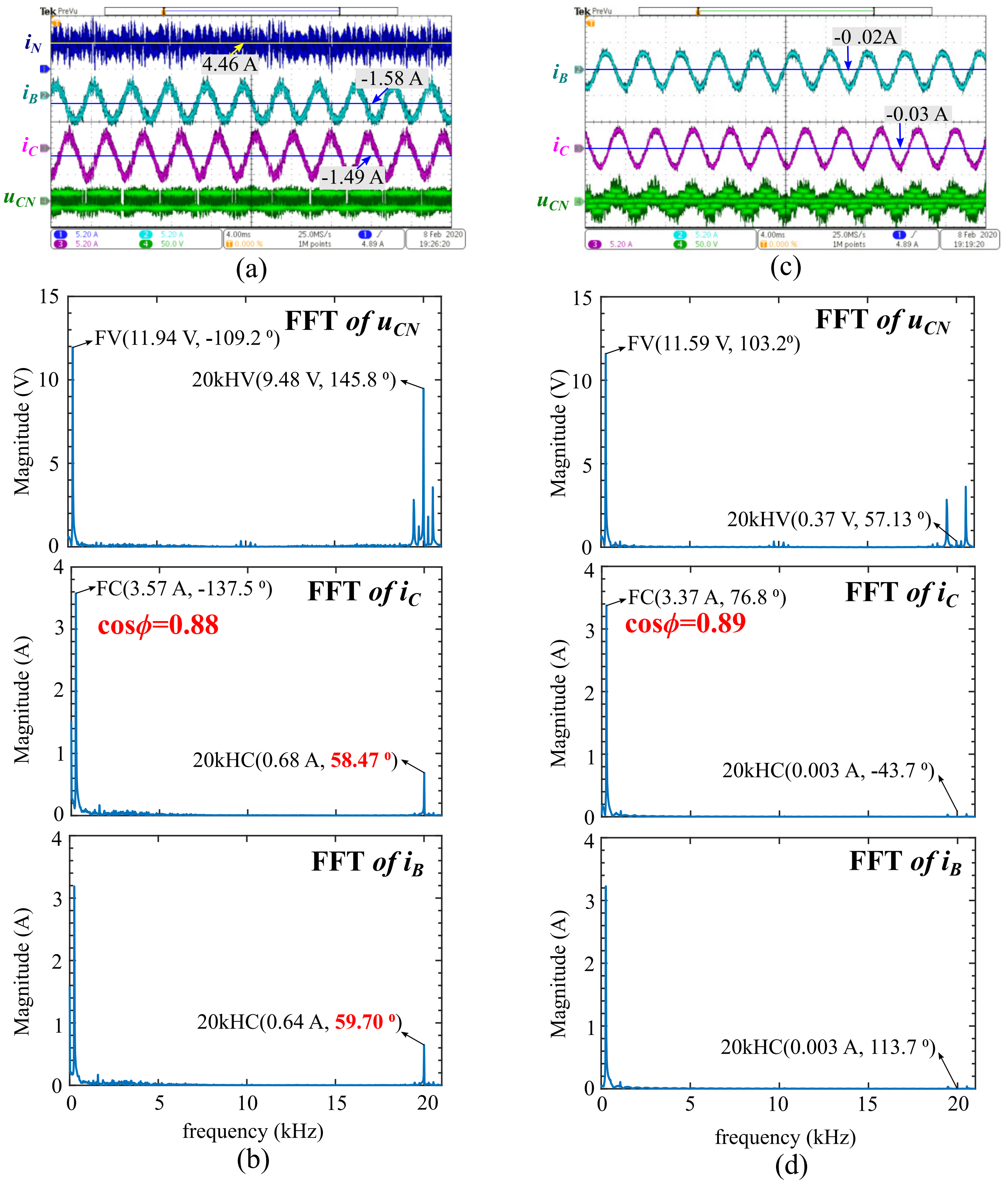

FIGURE 2.18: Steady-state performance (neutral current, phase-currents, phase-voltages and FFT analysis) at the nominal condition. (a), (b) The basic MFCS with a 15 V DC-source. (c), (d) The conventional drive with a 30 V DC-source.

The Fast Fourier Transform (FFT) analysis of u_{CN}, i_B and i_C in both drive systems is shown in figure 2.18(b) and (d). Firstly, the fundamental voltage (FV) amplitude and fundamental current (FI) amplitude are respectively 11.94 V and 3.57 A in the basic MFCS while they are respectively 11.59 V and 3.37 A in the conventional drive. The fundamental power factor ($cos\phi$) is about 0.88 in the basic MFCS while it is 0.89 in the conventional drive. Comparatively speaking, these fundamental characteristics are similar in both drives.

Secondly, for the basic MFCS, the zero-sequence current flowing into the motor undoubtedly produces more losses. To calculate the total active power of the motor, a simple method of accumulating the power generated by all the harmonics (including zero-sequence and fundamental components) is adopted. The result indicates that the total active power of the motor in the basic MFCS increases by 6.02 W compared to that in the conventional drive. Therefore, it can be concluded that the increased motor losses in the basic MFCS is about 11.5% of the nominal power at the nominal condition. The increased copper losses caused by the zero-sequence current are the power consumed across $R/3$, which can be calculated by ${i_N}^2\frac{R}{3} = 3.98$ W (7.6%). Therefore, the increased iron losses are about 2.04 W (3.9%). Although the motor losses of the basic MFCS increase, they can be mitigated by designing a winding layout with larger L_0. For example, [22] and [23] indicated that a motor with the two-layer fractional slot winding can obtain larger leakage inductance than the motor with side-by-side placed winding.

Thirdly, the 20 kHz harmonic voltage (20kHV) amplitude of u_{CN} in the basic MFCS is larger than that of the conventional drive (9.48 V to 0.37 V). Thus, it can be seen that the 20 kHz harmonic current (20kHC) amplitude of i_C in the basic MFCS is also larger than that in the conventional drive (0.68 A to 0.003 A). However, the 20kHC in the basic MFCS does not affect the electromagnetic torque because the 20kHCs of i_B and i_C almost have the same amplitude (0.68 A to 0.64 A) and phase position (58.47° to 59.70°). In other words, the 20kHCs do not generate harmonic torque. Therefore, although the phase-current ripple of the basic MFCS is larger, the torque performance can be maintained.

In general, the main characteristics of the basic MFCS compared to the conventional drive are summarized in table 2.2.

Conclusion

A PMSM-based MFCS is a special three-phase AC drive system where the DC power supply is connected with the NP of the motor. Due to this connection, it is possible to reach a higher DC-bus voltage without using a physical DC/DC boost converter. To investigate

Table 2.2: The main characteristics of the basic MFCS compared to the conventional drive.

Characteristic	Evaluation
Steady-state performance	Similar
DCSUR	Larger (1 vs 0.58)
Integrated boost function	YES vs NO
Current ripple	Bigger
Losses	Bigger (11.5% for the 52.5 W PMSM)

such a special system, the mathematical model of PMSMs with zero-sequence considerations is given firstly. Then, according to time-averaging equivalent modeling approach and Kirchhoff's law, the average model of the MFCS is built in A-B-C coordinate, and then is converted into d-q-0 coordinate. By building different equivalent circuits, it is easy to understand that the zero-sequence circuit of the MFCS is equal to an equivalent DC/DC boost converter where the average duty cycle (α_h) of the inverter can be the control DOF.

The infeasibility of SVPWM used in the MFCS is explained by studying the distribution of α_h with respect to the modulation ratio. It indicates that if SVPWM is used, α_h will be completely determined by the control of the motor. Moreover, α_h varies at three times of the fundamental frequency, which will result in the issue of voltage oscillations on the DC-bus. To solve this problem, a ZSVIPWM is proposed and the expression of final duty cycles is given for digital implementations. To guarantee the modulating signal to be within the linear modulation region, the DCSUR of the MFCS is analyzed. The result indicates that it can reach 1 while it is only 0.58 in a conventional drive by using SVPWM. Although the MFCS can harvest a free boost function, the clamped NP induces bigger current ripples. From the switching model point of view, the increasing ripples are caused by the decreasing number of available voltage-levels in each phase within one switching period.

Elementary verification is carried on a 52.5 W PMSM to verify the phenomenon of the equivalent DC/DC boost, which is integrated in the MFCS. Simulation and experimental results show that the DC-bus voltage is able to reach double the DC-source voltage. However, the phase-current ripples in the MFCS are much bigger than that in a conventional drive. Fortunately, this increase does not affect the torque performance of the motor.

Chapter 3

Improvements of the basic MFCS and generic closed-loop control strategy

Contents

Introduction

In Chapter 2, the mathematical model, equivalent circuits and modulation method were presented for the basic MFCS. Experimental validations carried out on a 52.5 W PMSM was provided to demonstrate the effect of the integrated boost function. However, the basic MFCS has two salient drawbacks. The first one is the bigger current ripples caused by the clamped NP, which results in more losses (11.5% for the 52.5 W PMSM). The second defect is that the maximum effective step-up ratio of the equivalent boost is only 2.

To address the above issues, we intend to propose two solutions, which lead to two new variants of the basic MFCS. This Chapter is organized as follows:

- In Section 1, we propose a new variant, which is referred to as MFCS-I for the basic MFCS on the purpose of solving the issue of bigger current ripples caused by the clamped NP. The main idea is to add a series inductor between the NP and the DC-source so that the NP becomes floating again. Due to the change of the circuit structure, the average model and equivalent circuit are built for the MFCS-I.

- To improve the effective step-up ratio, another variant is proposed in Section 2 by using an auxiliary inverter leg, which is called as MFCS-II. In the same way, the corresponding mathematical model and equivalent circuit are built to investigate and analyze its characteristics.

- From the equivalent circuit point of view, the MFCS-I and MFCS-II are similar. Therefore, in Section 3, a unified closed-loop control strategy is proposed for the MFCS-I and MFCS-II. The classic FOC is employed to control the motor and a differential flatness-based controller is presented to control the equivalent boost function.

- In Section 4, experimental results are given to verify the effectiveness. In particular, the MFCS-I is compared in detail with a two-stage converter-based drive.

3.1 Improvement 1: using a series inductor (MFCS-I)

As mentioned before, a salient drawback of the basic MFCS is the bigger current ripple caused by the clamped NP. Such a big current ripple will produce more iron losses in the motor thus reducing the efficiency of the whole drive system. In order to suppress the current ripple, a series inductor (L_{aux}) is added between the NP and the DC-source, as shown in figure 3.1.

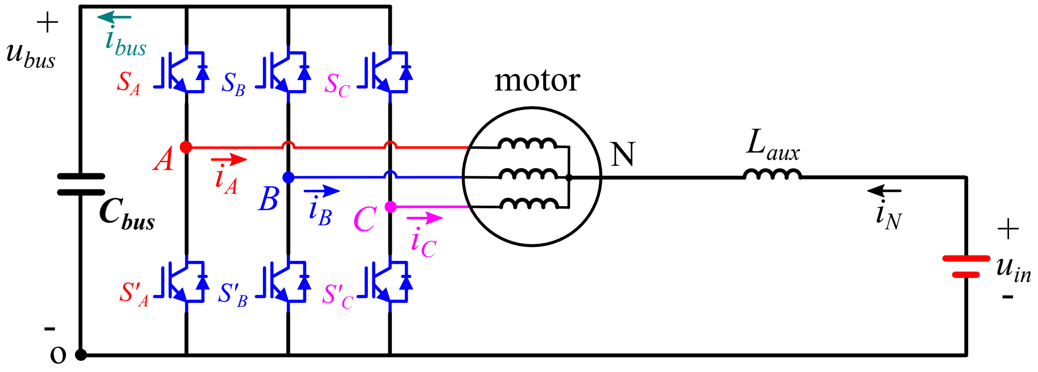

FIGURE 3.1: Circuit configuration of the MFCS-I by using a series inductor (L_{aux}).

3.1.1 Average model and equivalent circuit

The same modeling method as that of the basic MFCS can be adopted for the MFCS-I. In A-B-C coordinate, the average voltage and current equations of the MFCS-I are given by

$$\underbrace{\begin{bmatrix} u_{AO} \\ u_{BO} \\ u_{CO} \end{bmatrix}}_{\boldsymbol{u}_{invABC}} = \underbrace{\begin{bmatrix} \alpha_A \\ \alpha_B \\ \alpha_C \end{bmatrix}}_{\boldsymbol{\alpha}_{ABC}} u_{bus} = \underbrace{\begin{bmatrix} u_{AN} \\ u_{BN} \\ u_{CN} \end{bmatrix}}_{\boldsymbol{u}_{ABC}} + \begin{bmatrix} -L_{aux}\frac{\mathrm{d}i_N}{\mathrm{d}t} + u_{in} \\ -L_{aux}\frac{\mathrm{d}i_N}{\mathrm{d}t} + u_{in} \\ -L_{aux}\frac{\mathrm{d}i_N}{\mathrm{d}t} + u_{in} \end{bmatrix} \tag{3.1a}$$

$$\begin{cases} i_N = -(i_A + i_B + i_C) \\ i_{bus} = C_{bus}\dfrac{\mathrm{d}u_{bus}}{\mathrm{d}t} = -\boldsymbol{\alpha}_{ABC}^T \boldsymbol{i}_{ABC} \end{cases} \tag{3.1b}$$

In the same way, the above mathematical model can be transformed into d-q-0 coordinate by using the Park transformation (power invariant), as:

d-q-0 average model of the MFCS-I obtained by the Park transformation (power invariant):

$$\begin{cases} u_{invd} = \alpha_d u_{bus} = u_d = Ri_d + L_d\dfrac{\mathrm{d}i_d}{\mathrm{d}t} - \omega_e L_q i_q \\ u_{invq} = \alpha_q u_{bus} = u_q = Ri_q + L_q\dfrac{\mathrm{d}i_q}{\mathrm{d}t} + \omega_e(L_d i_d + \Phi_m) \\ u_{inv0} = \alpha_0 u_{bus} = \underbrace{Ri_0 + L_0\dfrac{\mathrm{d}i_0}{\mathrm{d}t}}_{u_0} - \sqrt{3}L_{aux}\dfrac{\mathrm{d}i_N}{\mathrm{d}t} + \sqrt{3}u_{in} \\ \qquad i_{bus} = C_{bus}\dfrac{\mathrm{d}u_{bus}}{\mathrm{d}t} = -(\alpha_d i_d + \alpha_q i_q + \alpha_0 i_0) \end{cases} \tag{3.2a}$$

Replacing i_0 by $-i_N/\sqrt{3}$, it yields

$$\begin{cases} \alpha_d u_{bus} = u_d = R i_d + L_d \dfrac{\mathrm{d}i_d}{\mathrm{d}t} - \omega_e L_q i_q \\ \alpha_q u_{bus} = u_q = R i_q + L_q \dfrac{\mathrm{d}i_q}{\mathrm{d}t} + \omega_e (L_d i_d + \Phi_m) \\ \alpha_h u_{bus} = -\dfrac{R}{3} i_N - \underbrace{(\dfrac{L_0}{3} + L_{aux})}_{L_E} \dfrac{\mathrm{d}i_N}{\mathrm{d}t} + u_{in} \\ \quad i_{bus} = C_{bus} \dfrac{\mathrm{d}u_{bus}}{\mathrm{d}t} = \alpha_h i_N - \underbrace{(\alpha_d i_d + \alpha_q i_q)}_{i_{lo}} \end{cases} \tag{3.2b}$$

where

- L_E is an equivalent inductance which is the sum of $L_0/3$ and L_{aux};

According to (3.2b), we can further build the equivalent circuit for the MFCS-I, where R_{eq} representing the motor function is seen as an equivalent load for the equivalent boost function, as shown in figure 3.2. Obviously, it can be concluded that the use of the series inductor actually increases the equivalent inductance of the equivalent boost. A bigger inductor contributes to a smaller input current ripple. Therefore, the current ripple of zero-sequence currents or neutral current can be reduced by using the series inductor.

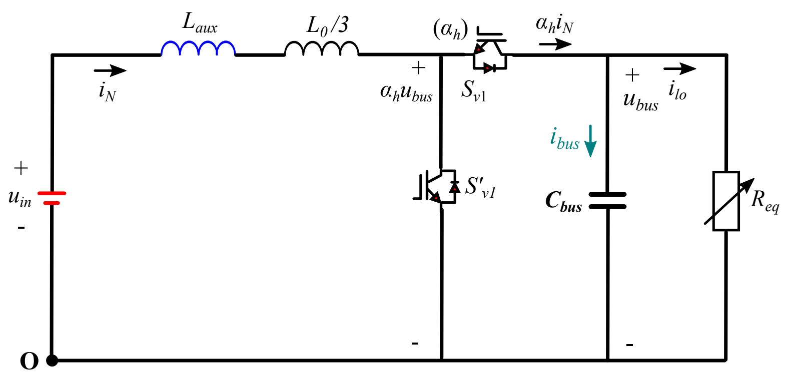

FIGURE 3.2: Equivalent circuit of the MFCS-I.

If the Park transformation (amplitude invariant) is used, (3.2a) and (3.2b) become

d-q-0 average model of the MFCS-I obtained by the Park transformation (amplitude invariant):

voltage equation:

$$\begin{cases} u_{invd} = \alpha_d u_{bus} = u_d = Ri_d + L_d \dfrac{\mathrm{d}i_d}{\mathrm{d}t} - \omega_e L_q i_q \\ u_{invq} = \alpha_q u_{bus} = u_q = Ri_q + L_q \dfrac{\mathrm{d}i_q}{\mathrm{d}t} + \omega_e (L_d i_d + \Phi_m) \\ u_{inv0} = \alpha_0 u_{bus} = \underbrace{Ri_0 + L_0 \dfrac{\mathrm{d}i_0}{\mathrm{d}t}}_{u_0} - L_{aux} \dfrac{\mathrm{d}i_N}{\mathrm{d}t} + u_{in} \\ \qquad i_{bus} = C_{bus} \dfrac{\mathrm{d}u_{bus}}{\mathrm{d}t} = -\dfrac{3}{2}(\alpha_d i_d + \alpha_q i_q + 2\alpha_0 i_0) \end{cases} \tag{3.3a}$$

Replacing i_0 by $-i_N/3$, it further yields

$$\begin{cases} \alpha_d u_{bus} = u_d = Ri_d + L_d \dfrac{\mathrm{d}i_d}{\mathrm{d}t} - \omega_e L_q i_q \\ \alpha_q u_{bus} = u_q = Ri_q + L_q \dfrac{\mathrm{d}i_q}{\mathrm{d}t} + \omega_e (L_d i_d + \Phi_m) \\ \alpha_h u_{bus} = -\dfrac{R}{3} i_N - \underbrace{(\dfrac{L_0}{3} + L_{aux})}_{L_E} \dfrac{\mathrm{d}i_N}{\mathrm{d}t} + u_{in} \\ \qquad i_{bus} = C_{bus} \dfrac{\mathrm{d}u_{bus}}{\mathrm{d}t} = \alpha_h i_N - \underbrace{\dfrac{3}{2}(\alpha_d i_d + \alpha_q i_q)}_{i_{lo}} \end{cases} \tag{3.3b}$$

where

- L_E is an equivalent inductance which is made up of $L_0/3$ and L_{aux};

3.1.2 Steady-state characteristic

According to the equivalent circuit and by neglecting the resistance of the motor and the series inductor, the step-up ratio of the equivalent boost function is still

$$r_0 = \frac{u_{bus}}{u_{in}} \approx \frac{1}{\alpha_h} \tag{3.4}$$

According to the ZSVIPWM algorithm presented in (2.23), the actual duty cycles of the inverter can be expressed by

$$\alpha_X = \alpha_h + \frac{{u_{XN1}}^*}{u_{bus}}, \quad X \in \{A, B, C\} \tag{3.5}$$

Because the limit of actual duty cycles is between 0 and 1, we obtain

$$0 \leq \alpha_X = \alpha_h + \frac{{u_{XN1}}^*}{u_{bus}} \leq 1 \quad \forall X \in \{A, B, C\} \tag{3.6}$$

By simplifying (3.6), the allowable u_{XN1}^* can be expressed as

$$-\alpha_h u_{bus} \leq {u_{XN1}}^* \leq (1-\alpha_h) u_{bus} \quad \forall X \in \{A, B, C\} \tag{3.7}$$

By substituting (3.4) into (3.7), we obtain

$$-u_{in} \leq {u_{XN1}}^* \leq \frac{1-\alpha_h}{\alpha_h} u_{in} \qquad \forall X \in \{A, B, C\} \tag{3.8}$$

According to (3.8), it can be seen that ${u_{XN1}}^*$ is bounded. The lower boundary is $-u_{in}$ and the upper boundary is $u_{in}(1-\alpha_h)/\alpha_h$. Generally speaking, the ideal ${u_{XN1}}^*$ is a standard sinusoidal signal. Thus, the amplitude (u_{XN1amp}) of ${u_{XN1}}^*$ is restricted by the smaller one between u_{in} and $u_{in}(1-\alpha_h)/\alpha_h$. For the case of $0 < \alpha_h \leq 0.5$, u_{XN1amp} is equal to u_{in}. In the case of $0.5 < \alpha_h \leq 1$, u_{XN1amp} equals to $u_{in}(1-\alpha_h)/\alpha_h$.

Therefore, the DCSUR of the MFCS-I can be evaluated by

$$r_1 = \frac{u_{XN1amp}}{u_{in}} = \begin{cases} 1, & 0 < \alpha_h \leq 0.5 \\ \dfrac{1-\alpha_h}{\alpha_h}, & 0.5 < \alpha_h \leq 1 \end{cases} \tag{3.9}$$

To evaluate the effective step-up ratio of the MFCS-I, the graphs of r_0 and r_1 with respect to α_h are drawn in figure 3.3. In Region 1, the step-up ratio r_0 reduces with the rise of α_h while the DCSUR r_1 is always maintained at 1. This indicates that, although u_{bus} can be larger than double u_{in}, the reachable AC voltage for the motor is limited. Therefore, the MFCS-I

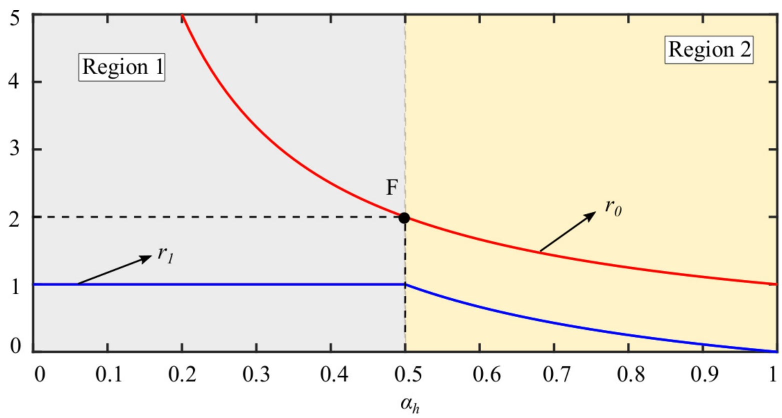

FIGURE 3.3: Analysis of the effective step-up ratio of the MFCS-I.

is unexpected to be operated within Region 1 since the boosted DC-bus voltage is unhelpful in expanding the operating range of the motor. On the contrary, the MFCS-I is desired to be operated in Region 2 where the boosted DC-bus voltage can improve the DCSUR. At the point 'F' ($\alpha_h = 0.5$), the step-up ratio is 2 and the DCSUR is 1.

Consequently, although the MFCS-I can solve the issue of bigger current ripples by adding a series inductor, the DCSUR is not improved compared to the basic MFCS.

3.1.3 Series inductor selection

As discussed in Chapter 2, the bigger current ripples of the basic MFCS is mainly caused by the high-frequency component (20kHC), i.e. the ripple in the neutral current. Therefore, it is obvious that the neutral current ripples can be reduced by increasing the value of the filtering inductor of the equivalent boost converter. However, how to choose an appropriate series inductor is a big issue. For a real DC/DC boost converter, the inductor design is usually based on the desired current and voltage ripples at nominal conditions[84][85] with a constant duty cycle. However, in the MFCS-I, the duty cycles of the inverter are not constant when the motor speed is not zero. Therefore, this method is not applicable for the MFCS-I. In the following, we will introduce a simple method to select the series inductor based on the concept of a re-floating NP.

According to the analysis in Section 2.3.4, we know that the clamped NP results in the reduction of the number of phase-voltage levels in one switching period. This directly results in the increase of phase-current ripples. By comparison, the NP of a conventional drive is floating. As a result, its phase-current ripple is smaller. Therefore, if the MFCS-I has a similar NP with the conventional drive, it can be considered that its phase-current ripple is acceptable. Thus, we take the floating NP of the conventional drive as a criterion, the objective of designing L_{aux} is to recreate a similar NP with that of the conventional drive.

In order to analyze the transient voltage of the NP in the MFCS-I, the switching model is required, which can be built as

$$\begin{bmatrix} u_{AO} \\ u_{BO} \\ u_{CO} \end{bmatrix} = \begin{bmatrix} S_A \\ S_B \\ S_C \end{bmatrix} u_{bus} = \begin{bmatrix} u_{AN} \\ u_{BN} \\ u_{CN} \end{bmatrix} + \begin{bmatrix} u_{NO} \\ u_{NO} \\ u_{NO} \end{bmatrix} = \begin{bmatrix} u_{AN} \\ u_{BN} \\ u_{CN} \end{bmatrix} + \begin{bmatrix} -L_{aux}\frac{di_N}{dt} + u_{in} \\ -L_{aux}\frac{di_N}{dt} + u_{in} \\ -L_{aux}\frac{di_N}{dt} + u_{in} \end{bmatrix} \tag{3.10}$$

By adding the three terms of (3.10), the zero-sequence switching model of the MFCS-I is given by

$$u_{in} - S_0 u_{bus} = \frac{R}{3} i_N + (\frac{L_0}{3} + L_{aux})\frac{di_N}{dt} \tag{3.11}$$

where $S_0 = (S_A + S_B + S_C)/3$.

By assuming that u_{bus} is regulated at double u_{in}, then by neglecting the resistance term $(R/3)$, the derivative term $(\frac{\mathrm{d}i_N}{\mathrm{d}t})$ of (3.11) approximates to

$$\frac{\mathrm{d}i_N}{\mathrm{d}t} \approx \frac{(0.5 - S_0)u_{bus}}{L_0/3 + L_{aux}} \tag{3.12}$$

In this case, the transient voltage of the NP (u_{NO}) can be formulated by

$$\begin{aligned} u_{NO} &= \frac{(u_{AO} + u_{BO} + u_{CO})}{3} - \frac{(u_{AN} + u_{BN} + u_{CN})}{3} \\ &= \frac{(u_{AO} + u_{BO} + u_{CO})}{3} + \frac{R}{3} i_N + \frac{L_0}{3}\frac{di_N}{dt} \\ &\approx \frac{(u_{AO} + u_{BO} + u_{CO})}{3} + \frac{L_0}{3}\frac{di_N}{dt} \\ &\approx \underbrace{\frac{(S_A + S_B + S_C)}{3} u_{bus}}_{u_{NO\_c}} + \underbrace{\frac{L_0/3}{L_0/3 + L_{aux}}(0.5 - S_0)u_{bus}}_{u_{bias}} \end{aligned} \tag{3.13}$$

According to (3.13), it can be seen that u_{NO} consists of two terms, one is the NP voltage (u_{NO_c}) of a conventional drive, the other is named as the voltage bias (u_{bias}). Due to the voltage bias, the NP in the MFCS-I is able to be floating again. Notably, when u_{bias} approximates 0 with a large L_{aux}, the transient voltage of the NP in the MFCS-I is the same as u_{NO_c}.

Furthermore, the actual phase-voltages of the MFCS-I can be formulated by

$$\begin{aligned} \begin{bmatrix} u_{AN} \\ u_{BN} \\ u_{CN} \end{bmatrix} &= \begin{bmatrix} u_{AO} \\ u_{BO} \\ u_{CO} \end{bmatrix} - \begin{bmatrix} u_{NO} \\ u_{NO} \\ u_{NO} \end{bmatrix} = \underbrace{\frac{u_{bus}}{3} \begin{bmatrix} 2 & -1 & -1 \\ -1 & 2 & -1 \\ -1 & -1 & 2 \end{bmatrix} \begin{bmatrix} S_A \\ S_B \\ S_C \end{bmatrix}}_{\boldsymbol{u_{ABC\_c}}} \\ &- \begin{bmatrix} 1 \\ 1 \\ 1 \end{bmatrix} \underbrace{\frac{L_0/3}{L_0/3 + L_{aux}}(0.5 - S_0)u_{bus}}_{u_{bias}} \end{aligned} \tag{3.14}$$

According to (3.14), we can see that the actual phase-voltages also include two terms, one is the phase-voltage ($\boldsymbol{u_{ABC\_c}}$) of the conventional drive, and the other is the voltage bias (u_{bias}). In the same way, if u_{bias} approximates 0, the actual phase-voltages of the MFCS-I are the same as $\boldsymbol{u_{ABC\_c}}$. The detailed comparisons of voltage and current curves of the MFCS-I and a conventional drive are shown in figure 3.4, where the switching states S_{000}, S_{100}, S_{110} and S_{111} are used during the switching period. For the sake of analysis, the subscript $\_mI$ is given to denote a variable in the MFCS-I.

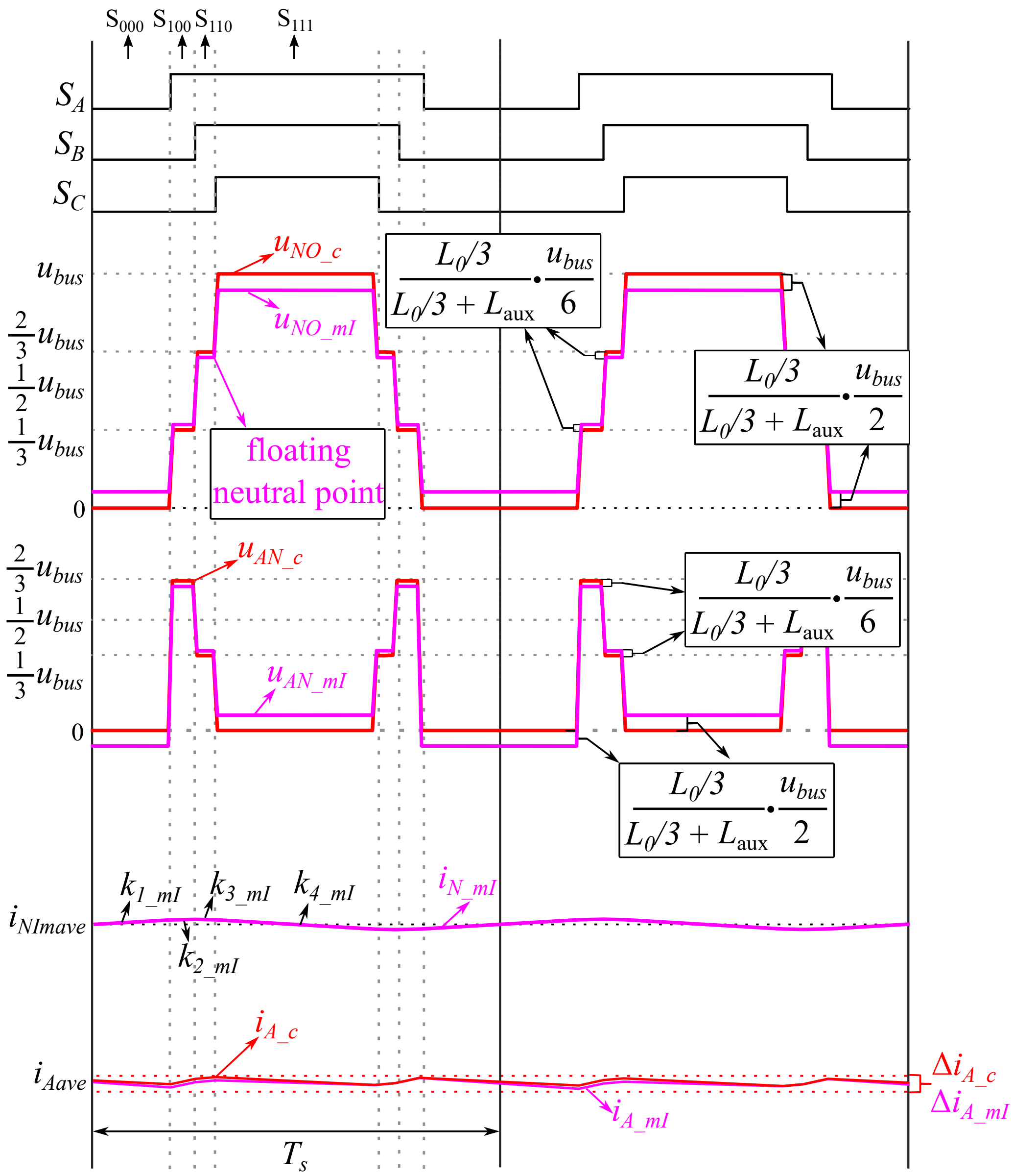

FIGURE 3.4: Detailed comparison of voltage and current curves between the MFCS-I and a conventional drive.

From figure 3.4, it is clear that u_{NO_mI} is no longer clamped by the DC-source. Thanks to the series inductor, it has four voltage-levels in one switching period. The phase-voltage u_{AN_mI} is also able to obtain four voltage-levels within one switching period. Compared to the conventional drive, the voltage difference under switching states S_{000} and S_{111} is

$$\frac{L_0/3}{L_0/3+L_{aux}}\frac{u_{bus}}{2} \tag{3.15}$$

Under switching states S_{100} and S_{110}, the voltage difference is

$$\frac{L_0/3}{L_0/3+L_{aux}}\frac{u_{bus}}{6} \tag{3.16}$$

If we consider a similar NP with the conventional drive as an evaluation criteria to choose the series inductor, we hope that the bigger voltage difference presented in (3.15) is small enough. For the sake of analysis, an assessment index (R_{flo}) is defined to judge a similar NP, as

$$R_{flo} = \frac{L_0/3}{L_0/3 + L_{aux}} \frac{1}{2} = \frac{0.5}{1 + 3a_L} \tag{3.17}$$

where

- $a_L = \dfrac{L_{aux}}{L_0}$ represents the rate of the auxiliary L_{aux} compared to L_0.

The evolution of R_{flo} with respect to a_L is illustrated in figure 3.5. It can be seen that R_{flo} can be effectively decreased when a_L is increased from 0 to 5. When $a_L = 5$, R_{flo} is 0.03. This implies that if L_{aux} is chosen as $5L_0$, the voltage difference of phase-voltages between the MFCS-I and a conventional drive is only $0.03u_{bus}$. Roughly speaking, it is small enough and can be ignored. In this case, the NP can be considered as a similar NP with that of the conventional drive. If a_L is larger than 5, the improved effect is not significant. In turn, too bigger auxiliary will increase the cost and volume of the whole system. In practice, the selection of a_L is a trade-off between the current ripples and the cost.

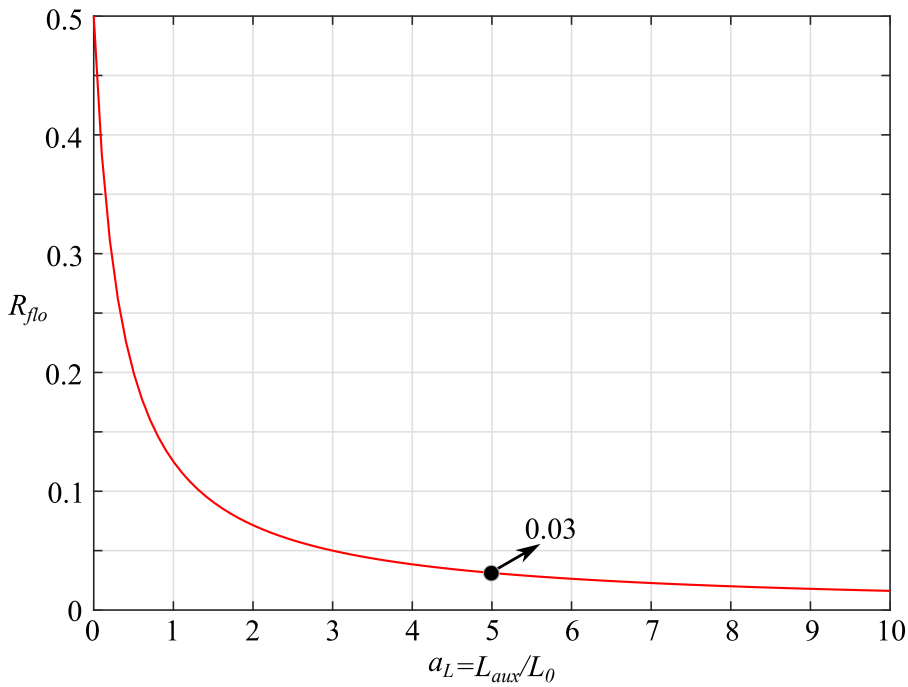

FIGURE 3.5: Evaluation of R_{flo} with respect to a_L.

3.2 Improvement 2: using an auxiliary leg (MFCS-II)

Although the MFCS-I can suppress the current ripples by employing a series inductor, the effective step-up ratio of the equivalent boost function is still 2 due to the limited control DOF provided by the traction inverter. In order to improve the effective step-up ratio, another improvement named as MFCS-II is proposed in this section, as shown in figure 3.6. Compared to the MFCS-I, an auxiliary inverter leg is employed. The negative pole of the DC-source source is connected with the NP of the motor. The positive pole of the DC-source is connected to an auxiliary leg (fourth leg) through the series inductor.

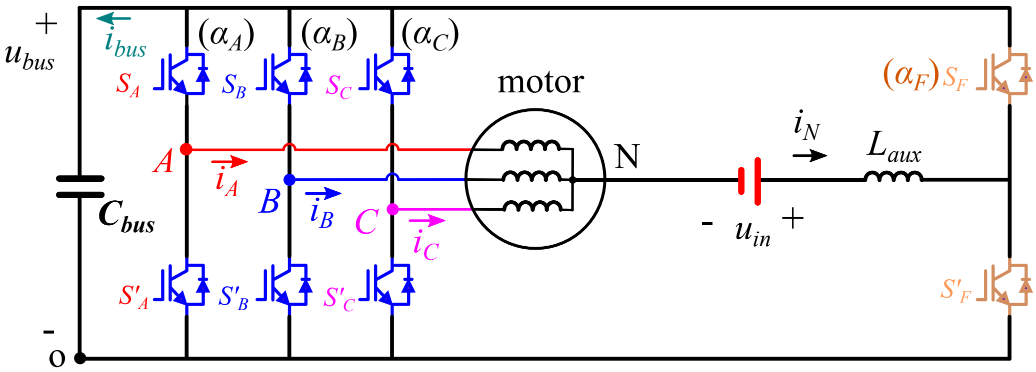

FIGURE 3.6: Circuit configuration of the MFCS-II.

3.2.1 Average model and equivalent circuit

For the fourth leg, the duty cycle of the upper switch is defined as α_F. By using the same modeling method, the average voltage and current relationships of the MFCS-II are given by

$$\underbrace{\begin{bmatrix} u_{AO} \\ u_{BO} \\ u_{CO} \end{bmatrix}}_{\boldsymbol{u}_{invABC}} = \underbrace{\begin{bmatrix} \alpha_A \\ \alpha_B \\ \alpha_C \end{bmatrix}}_{\boldsymbol{\alpha}_{ABC}} u_{bus} = \underbrace{\begin{bmatrix} u_{AN} \\ u_{BN} \\ u_{CN} \end{bmatrix}}_{\boldsymbol{u}_{ABC}} + \begin{bmatrix} -u_{in} + L_{aux}\frac{\mathrm{d}i_N}{\mathrm{d}t} + \alpha_F u_{bus} \\ -u_{in} + L_{aux}\frac{\mathrm{d}i_N}{\mathrm{d}t} + \alpha_F u_{bus} \\ -u_{in} + L_{aux}\frac{\mathrm{d}i_N}{\mathrm{d}t} + \alpha_F u_{bus} \end{bmatrix} \tag{3.18a}$$

$$\begin{cases} i_N = i_A + i_B + i_C \\ i_{bus} = C_{bus}\dfrac{\mathrm{d}u_{bus}}{\mathrm{d}t} = -\boldsymbol{\alpha}_{ABC}^T \boldsymbol{i}_{ABC} + \alpha_F i_N \end{cases} \tag{3.18b}$$

In the same way, the above mathematical model can be transformed into d-q-0 coordinate by using the Park transformation (power invariant), as:

d-q-0 average model of the MFCS-II obtained by the Park transformation (power invariant):

$$\begin{cases} u_{invd} = \alpha_d u_{bus} = u_d = Ri_d + L_d \dfrac{\mathrm{d}i_d}{\mathrm{d}t} - \omega_e L_q i_q \\ u_{invq} = \alpha_q u_{bus} = u_q = Ri_q + L_q \dfrac{\mathrm{d}i_q}{\mathrm{d}t} + \omega_e (L_d i_d + \Phi_m) \\ u_{inv0} = \alpha_0 u_{bus} = \underbrace{Ri_0 + L_0 \dfrac{\mathrm{d}i_0}{\mathrm{d}t}}_{u_0} - \sqrt{3} u_{in} + \sqrt{3} L_{aux} \dfrac{\mathrm{d}i_N}{\mathrm{d}t} + \sqrt{3} \alpha_F u_{bus} \\ i_{bus} = C_{bus} \dfrac{\mathrm{d}u_{bus}}{\mathrm{d}t} = -(\alpha_d i_d + \alpha_q i_q + \alpha_0 i_0) + \alpha_F i_N \end{cases} \tag{3.19a}$$

Replacing i_0 by $i_N/\sqrt{3}$, it further yields

$$\begin{cases} \alpha_d u_{bus} = u_d = Ri_d + L_d \dfrac{\mathrm{d}i_d}{\mathrm{d}t} - \omega_e L_q i_q \\ \alpha_q u_{bus} = u_q = Ri_q + L_q \dfrac{\mathrm{d}i_q}{\mathrm{d}t} + \omega_e (L_d i_d + \Phi_m) \\ (\alpha_F - \alpha_h) u_{bus} = -\dfrac{R}{3} i_N - \underbrace{(\dfrac{L_0}{3} + L_{aux})}_{L_E} \dfrac{\mathrm{d}i_N}{\mathrm{d}t} + u_{in} \\ i_{bus} = C_{bus} \dfrac{\mathrm{d}u_{bus}}{\mathrm{d}t} = (\alpha_F - \alpha_h) i_N - \underbrace{(\alpha_d i_d + \alpha_q i_q)}_{i_{lo}} \end{cases} \tag{3.19b}$$

If the Park transformation (amplitude invariant) is used, (3.19a) and (3.19b) become

d-q-0 average model of the MFCS-II obtained by the Park transformation (amplitude invariant):

voltage equation:

$$\begin{cases} u_{invd} = \alpha_d u_{bus} = u_d = Ri_d + L_d \dfrac{\mathrm{d}i_d}{\mathrm{d}t} - \omega_e L_q i_q \\ u_{invq} = \alpha_q u_{bus} = u_q = Ri_q + L_q \dfrac{\mathrm{d}i_q}{\mathrm{d}t} + \omega_e (L_d i_d + \Phi_m) \\ u_{inv0} = \alpha_0 u_{bus} = \underbrace{Ri_0 + L_0 \dfrac{\mathrm{d}i_0}{\mathrm{d}t}}_{u_0} - u_{in} + L_{aux} \dfrac{\mathrm{d}i_N}{\mathrm{d}t} + \alpha_F u_{bus} \\ i_{bus} = C_{bus} \dfrac{\mathrm{d}u_{bus}}{\mathrm{d}t} = -\dfrac{3}{2}(\alpha_d i_d + \alpha_q i_q + 2\alpha_0 i_0) + \alpha_F i_N \end{cases} \tag{3.20a}$$

Replacing i_0 by $i_N/3$, it further yields

$$
\begin{cases}
\alpha_d u_{bus} = u_d = Ri_d + L_d \dfrac{\mathrm{d}i_d}{\mathrm{d}t} - \omega_e L_q i_q \\
\alpha_q u_{bus} = u_q = Ri_q + L_q \dfrac{\mathrm{d}i_q}{\mathrm{d}t} + \omega_e (L_d i_d + \Phi_m) \\
(\alpha_F - \alpha_h) u_{bus} = -\dfrac{R}{3} i_N - \underbrace{(\dfrac{L_0}{3} + L_{aux})}_{L_E} \dfrac{\mathrm{d}i_N}{\mathrm{d}t} + u_{in} \\
i_{bus} = C_{bus} \dfrac{\mathrm{d}u_{bus}}{\mathrm{d}t} = (\alpha_F - \alpha_h) i_N - \underbrace{\dfrac{3}{2}(\alpha_d i_d + \alpha_q i_q)}_{i_{lo}}
\end{cases}
\tag{3.20b}
$$

According to (3.19b), the equivalent circuit of the MFCS-II is shown in figure 3.7. By comparison, we can find that the equivalent duty cycle of the equivalent boost in the MFCS-II becomes $(\alpha_F - \alpha_h)$. In other words, the MFCS-II has two control DOFs to regulate the DC-bus voltage. One is the mean duty cycle (α_h) of the traction inverter and the other is the duty cycle α_F of the fourth leg.

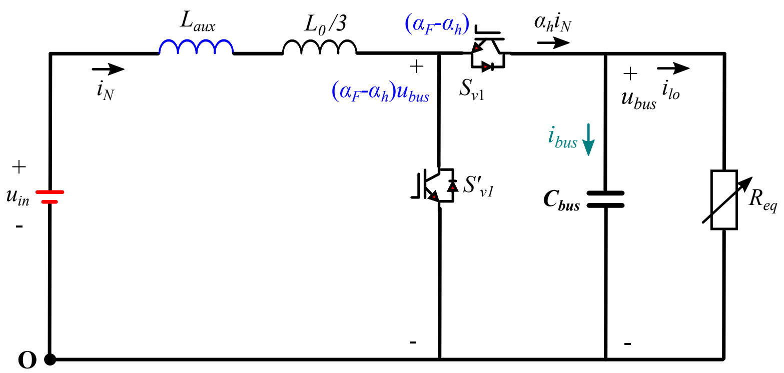

FIGURE 3.7: Equivalent circuit of the MFCS-II.

3.2.2 Steady-state characteristic

According to the equivalent circuit shown in figure 3.7 and by neglecting the resistance of the motor and of the series inductor, the step-up ratio (r_0) of the equivalent boost can be formulated by

$$r_0 = \frac{u_{bus}}{u_{in}} \approx \frac{1}{\alpha_F - \alpha_h} \tag{3.21}$$

In the inverter side, the average terminal voltage of inverter's legs is between 0 and u_{bus} when the duty cycle is respectively set as 0 and 1. For the fourth leg, its terminal voltage can be expressed as $\alpha_F u_{bus}$. Then, the average voltage of the NP u_{NO} can be expressed as $(-u_{in} + \alpha_F u_{bus})$ by neglecting the voltage drop across the series inductor. Therefore, the average phase-voltage of the motor can be expressed by

$$\begin{gathered} 0 - u_{NO} \leq u_{XN} \leq u_{bus} - u_{NO}, \quad X \in (A, B, C) \\ \Downarrow \\ -(-u_{in} + \alpha_F u_{bus}) \leq u_{XN} \leq u_{bus} - (-u_{in} + \alpha_F u_{bus}) \end{gathered} \tag{3.22}$$

If we neglect the superimposed zero-sequence voltage, $u_{XN} \approx u_{XN1}$. Then, by substituting (3.21) into (3.22), we obtain

$$-\frac{\alpha_h}{\alpha_F - \alpha_h} u_{in} \leq u_{XN1} \leq \frac{1 - \alpha_h}{\alpha_F - \alpha_h} u_{in} \tag{3.23}$$

Generally speaking, the fundamental phase-voltage of the motor is desired to be sinusoidal and symmetric. To this end, a simple way is to set α_h at 0.5[1] so that u_{XN1} can be symmetric. In this case, α_F becomes the only control DOF for the equivalent boost. Therefore, r_0 and r_1 of the MFCS-II can be evaluated by

$$\begin{cases} r_0 = \dfrac{u_{bus}}{u_{in}} = \dfrac{1}{\alpha_F - 0.5} \\ r_1 = \dfrac{u_{XN1amp}}{u_{in}} = \dfrac{0.5}{\alpha_F - 0.5} \end{cases} \tag{3.24}$$

[1] α_h can also be variable under different operating conditions. In this case, a control allocation strategy between α_h and α_F is necessary.

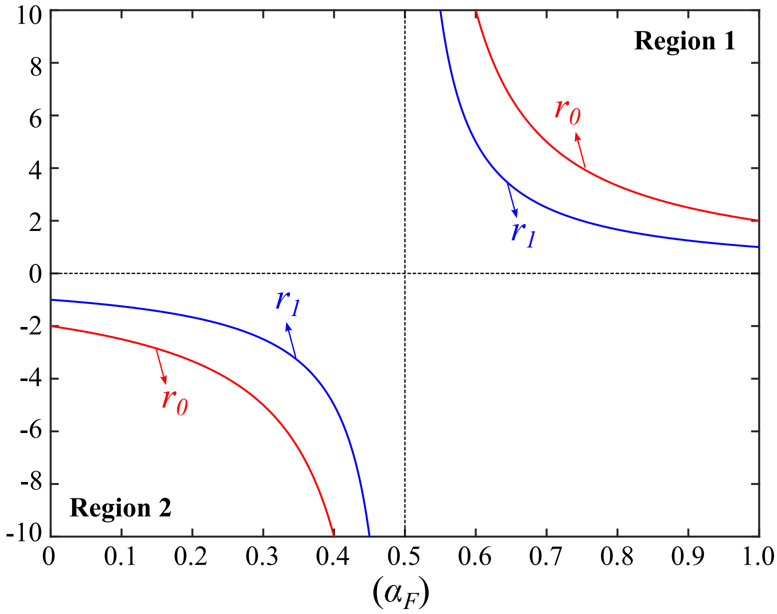

FIGURE 3.8: Analysis of the effective step-up ratio of the MFCS-II.

The curves of r_0 and r_1 with respect to α_F are shown in figure 3.8. In Region 1, both r_0 and r_1 are positive while they are negative in Region 2. If u_{in} is positive, the MFCS-II is desired to be operated in Region 1 to obtain a positive DC-bus voltage. Thus, the available range of α_F is (0.5-1). When α_F is 1, r_0 is 2 and r_1 is equal to 1. This special case actually corresponds to the MFCS-I. With the decrease of α_F, both r_0 and r_1 increase. When α_F is close to 0.5, both r_0 and r_1 can reach high values. This indicates that the MFCS-II is able to achieve a highly effective step-up ratio when the duty cycle of the fourth leg is near 0.5. If u_{in} is negative (connected reversely), the MFCS-II is desired to be operated in Region 2. In addition, if u_{in} is a single-phase AC power source, the MFCS-II can be operated in both Region 1 and Region 2.

3.3 Universal closed-loop control strategy

According to the aforementioned analysis, we know that the MFCSs (including the MFCS-I and MFCS-II) are hybrid power conversion systems, which conduct not only DC/AC but also DC/DC conversions simultaneously thanks to the motor function and the equivalent DC/DC boost function. Meanwhile, we know that both the MFCS-I and the MFCS-II have the similar equivalent circuit. The only difference between them is the control DOF of their boost functions. In the MFCS-I, α_h is the control DOF for the equivalent boost. In the MFCS-II, α_h is set at 0.5 throughout. So $(\alpha_F - 0.5)$ becomes its control DOF for the equivalent boost function. Therefore, we can use a universal closed-loop control strategy to control MFCS-I and MFCS-II. It has two control objectives. The first one is the motor torque or speed and the second one is the equivalent boost. For the motor, the classic FOC controller can still be used since the connected NP does not affect the *d*-*q* model. It consists of two current controllers and one speed controller. For the equivalent boost, it is a typical nonlinear system. Therefore, we adopt a differential flatness-based nonlinear controller. In the following, the detailed design for all controllers will be detailed.

3.3.1 Design of FOC

The classic FOC is a cascaded control framework for AC machines where the current-loop is the inner-loop and the speed-loop is the outer-loop.

3.3.1.1 PI control for d-q current-loops

For the inner-loop, two PI controllers are utilized to regulate the d, q-axis currents. The detailed design process is presented as follows:

According to the modeling analysis in chapter 2, the d-q voltage equation of the PMSM can be expressed by

$$\begin{cases} u_d = Ri_d + L_d \dfrac{\mathrm{d}i_d}{\mathrm{d}t} - \omega_e L_q i_q \\ u_q = Ri_q + L_q \dfrac{\mathrm{d}i_q}{\mathrm{d}t} + \omega_e (L_d i_d + \Phi_m) \end{cases} \tag{3.25}$$

By using the state feedback decoupling approach, new control variables v_d and v_q are given as

$$\begin{cases} u_d = v_d - \omega_e L_q i_q \\ u_q = v_q + \omega_e (L_d i_d + \Phi_m) \end{cases} \tag{3.26}$$

After the decoupling, the d-axis and q-axis current-loops are simplified as

$$\begin{cases} L_d \dfrac{\mathrm{d}i_d}{\mathrm{d}t} = v_d - Ri_d \\ L_q \dfrac{\mathrm{d}i_q}{\mathrm{d}t} = v_q - Ri_q \end{cases} \tag{3.27}$$

Then, by applying Laplace transformation to (3.27), both d-axis and q-axis current-loops can be expressed by a first-order system plant $G_k(s)$, as

$$G_k(s) = \frac{1}{L_k s + R} \tag{3.28}$$

where k can be replaced by d or q.

In this case, a linear control technique, such as the PI controller can be used. The transfer function of a PI controller $PI_k(s)$ is given by

$$PI_k(s) = k_{pk} \left(1 + \frac{1}{T_{ik} s}\right) \tag{3.29}$$

where k_{pk} is the proportional gain, T_{ik} is the integral time coefficient.

When the PI controller is applied, the block diagram of the closed-loop system is shown in figure 3.9 where the inverter non-linearity and the PWM delay effect are neglected. According to pole-zero cancellation method, it is easy to calculate the control gains k_{pk} and T_{ik}.

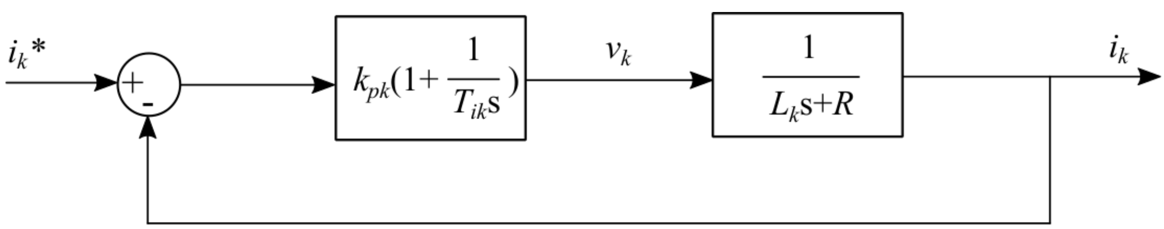

FIGURE 3.9: Block diagram of d-q current-loop after decoupling.

3.3.1.2 State feedback control with an integral action for the speed-loop

Assuming that the current-loops have been correctly synthesized with respect to frequency separation principle, the closed-loop current dynamics is faster than the desired mechanical dynamics. Thus, the speed-loop can be designed without considering the current-loops. Considering a motor without a load, the mechanical dynamic can be expressed as

$$\dot{\omega}_m = -\frac{B_m}{J_m}\omega_m + \frac{K_\Phi}{J_m}i_q^* \tag{3.30}$$

where $K_\Phi = 1.5p\Phi_m$, i_q^* is the reference of q-axis current.

The control objective is to ensure that the actual speed ω_m is equal to the speed reference ω_m^*. To guarantee a zero steady-state error, an integral action is necessary, as $\dot{\varepsilon_\omega} = \omega_m^* - \omega_m$. By adding the integral action, (3.30) can be extended as

$$\begin{bmatrix} \dot{\omega}_m \\ \dot{\varepsilon}_\omega \end{bmatrix} = \begin{bmatrix} -\frac{B_m}{J_m} & 0 \\ -1 & 0 \end{bmatrix} \begin{bmatrix} \omega_m \\ \varepsilon_\omega \end{bmatrix} + \begin{bmatrix} \frac{K_\Phi}{J_m} \\ 0 \end{bmatrix} i_q^* + \begin{bmatrix} 0 \\ 1 \end{bmatrix} \omega_m^* \tag{3.31}$$

For such a system, a control law is given as

$$i_q^* = -K_\omega \omega_m - K_{\omega\_I}\varepsilon_\omega \tag{3.32}$$

where K_ω and K_{ω_I} are two feedback gains.

By substituting (3.32) into (3.30), the closed-loop system can be expressed as

$$\begin{bmatrix} \dot{\omega}_m \\ \dot{\varepsilon}_\omega \end{bmatrix} = \underbrace{\begin{bmatrix} -\frac{B_m + K_\Phi K_\omega}{J_m} & -\frac{K_\Phi K_{\omega\_I}}{J_m} \\ -1 & 0 \end{bmatrix}}_{A_{ext}} \begin{bmatrix} \omega_m \\ \varepsilon_\omega \end{bmatrix} + \begin{bmatrix} 0 \\ 1 \end{bmatrix} \omega_m^* \tag{3.33}$$

where A_{ext} is the extended matrix.

The closed-loop dynamic depends on the eigenvalues of A_{ext}, one has

$$\text{eig}\left(\begin{bmatrix} -\frac{B_m + K_\Phi K_\omega}{J_m} & -\frac{K_\Phi K_{\omega\_I}}{J_m} \\ -1 & 0 \end{bmatrix}\right) = \det\left(sI - \begin{bmatrix} -\frac{B_m + K_\Phi K_\omega}{J_m} & -\frac{K_\Phi K_{\omega\_I}}{J_m} \\ -1 & 0 \end{bmatrix}\right) \tag{3.34}$$

It leads to a characteristic equation, as

$$P(s) = s^2 + \frac{B_m + K_\Phi K_\omega}{J_m}s - \frac{K_\Phi K_{\omega\_I}}{J_m} \tag{3.35}$$

Obviously, (3.35) represents a second-order system. Therefore, K_ω and K_{ω_I} can be calculated by the method of pole assignments.

3.3.2 Differential flatness-based control for the equivalent boost

Boost converter is a typical nonlinear system in power electronics fields. Usually, the small-signal model is used to design the controller by linearizing the large-signal model at a specific operating point. However, in the MFCS-I or MFCS-II, the motor functions as an equivalent load of the equivalent boost converter. It has a wide operating range, which may change from the null power to the nominal power. Therefore, the linearized small-signal model is inapplicable. To control such a system, a nonlinear controller is required. For example, the sliding mode control[86][87], passivity-based control[88][89] and differential flatness-based control[90][91] can be adopted. In this research, we choose the differential flatness-based control due to its simplicity.

3.3.2.1 Brief introduction to differential flatness theory

The differential flatness theory was proposed by Fliess et al. using the formalism of differential algebra[92]. For a nonlinear system, it can be expressed with the following form:

$$\dot{x}(t) = f(x(t), u(t)) \tag{3.36}$$

where $x(t) \in \mathbb{R}^n$, $u(t) \in \mathbb{R}^m$ and $(m \leq n) \in \mathbb{N}$.

This system is said to be differential flat if one can find a variable, called as the flat output. An output y is flat if the following smooth functions exist[93]

$$\begin{aligned} h &: \mathbb{R}^n \times (\mathbb{R}^m)^{p+1} \to \mathbb{R}^m \\ \eta &: (\mathbb{R}^m)^p \to \mathbb{R}^n \\ \vartheta &: (\mathbb{R}^m)^{p+1} \to \mathbb{R}^m \end{aligned}$$

such that

$$\begin{aligned} y &= h(x, u, \dot{u}, ..., u^{(p)}) \\ x &= \eta(y, \dot{y}, ..., y^{(p-1)}) \\ u &= \vartheta(y, \dot{y}, ..., y^{(p)}) \end{aligned} \tag{3.37}$$

where p is the number of derivatives.

This implies that the state vector x of a differential flat system and its input vector u can be represented by a function of the flat output and its finite derivatives. If the output vector y can be proved to be flat, the design of trajectory tracking control for each desired output y_{traj} become straightforward[94]. A linear feedback control law can be adopted to ensure that the tracking errors $e = (y - y_{traj})$ asymptotically vanish, as

$$[y^{(p)} - y_{traj}^{(p)}] + K_{p-1}[y^{(p-1)} - y_{traj}^{(p-1)}] + ... + K_0[y - y_{traj}] = 0 \tag{3.38}$$

where the set of control gains K_{p-1},...K_0 can be chosen such that the closed-loop characteristic polynomial is Hurwitz. Different from input-output linearization control for nonlinear systems, flatness-based control does not lead to zero dynamics. Consequently, the stability of the whole closed-loop system can be guaranteed. The block diagram of the differential flatness-based control is shown in figure 3.10[95][96].

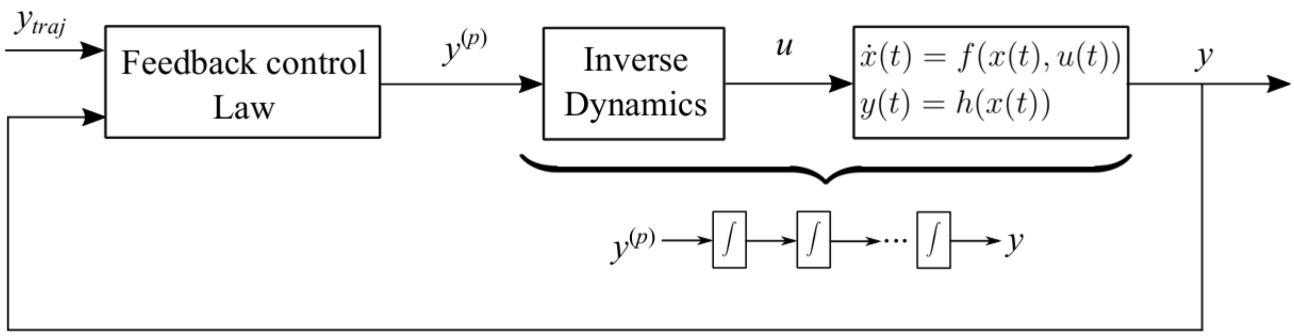

FIGURE 3.10: Block diagram of the differential flatness-based control.

3.3.2.2 Parameterization of the differential flatness-based controller

By neglecting the resistance of the motor and the series inductor, the mathematical model of the equivalent boost function of the MFCS-I and MFCS-II can be built as

$$\begin{cases} \dot{i}_N = -\dfrac{u_{bus}}{L_E}\alpha_E + \dfrac{u_{in}}{L_E} \\ \dot{u}_{bus} = \dfrac{i_N}{C_{bus}}\alpha_E - \dfrac{u_{bus}}{R_{eq}C_{bus}} \end{cases} \tag{3.39}$$

In (3.39), although we do not know the value of the equivalent load R_{eq}, it can be calculated by u_{bus}/i_{lo}, where i_{lo} is equal to $\frac{3}{2}(\alpha_d i_d + \alpha_q i_q)$ as shown in (3.3b) and (3.20b). Assuming that control dynamics of i_d and i_q are much faster than the dynamic of u_{bus}, thus, the average model of the equivalent boost can be rewritten by

$$\begin{cases} \dot{i}_N = -\dfrac{u_{bus}}{L_E}\alpha_E + \dfrac{u_{in}}{L_E} \\ \dot{u}_{bus} = \dfrac{i_N}{C_{bus}}\alpha_E - \dfrac{i_{lo}}{C_{bus}} \end{cases} \tag{3.40}$$

For the equivalent boost of the MFCS-I, the control variable is $u := \alpha_E = \alpha_h$. For the equivalent boost in the MFCS-II, the control variable is $u := \alpha_E = \alpha_F - 0.5$. The state variables of (3.40) are i_N and u_{bus}. The flat output candidate is chosen as the energy E which is stored in the DC-bus capacitor and the equivalent inductor L_E[97]:

$$y := E = \frac{1}{2}(L_E i_N^2 + C_{bus}u_{bus}^2) \tag{3.41}$$

With this candidate, we can find that:

$$\begin{cases} i_N = \dfrac{\frac{u_{in}C_{bus}\dot{E}}{i_{lo}^2} + \sqrt{\frac{u_{in}^2 C_{bus}^2 \dot{E}^2}{i_{lo}^4} - (2L_E + \frac{2C_{bus}u_{in}^2}{i_{lo}^2})(\frac{\dot{E}^2 C_{bus}}{2i_{lo}^2} - E)}}{(L_E + \frac{C_{bus}u_{in}^2}{i_{lo}^2})} = \eta_1(E,\dot{E}) \\ u_{bus} = \dfrac{u_{in}\eta_1(E,\dot{E}) - \dot{E}}{i_{lo}} = \eta_2(E,\dot{E}) \\ \alpha_E = \dfrac{\frac{u_{in}^2}{L_E} + \dot{u_{in}}\eta_1(E,\dot{E}) + \frac{i_{lo}^2}{C_{bus}} - \dot{i_{lo}}\eta_2(E,\dot{E}) - \ddot{E}}{\frac{\eta_2(E,\dot{E})u_{in}}{L_E} + \frac{\eta_1(E,\dot{E})i_{lo}}{C_{bus}}} = \vartheta(E,\dot{E},\ddot{E}) \end{cases} \tag{3.42}$$

Obviously, all the states and input can be expressed by the energy E and its first-order and second-order derivatives. Thus, the equivalent boost function can be considered as a flat system with $y = E$ as the flat output.

Then, to track a predefined energy trajectory E_{traj}, a feedback control law is given as follows, where an integral action is also added to guarantee a zero steady-state error.

$$\ddot{E} = \ddot{E}_{traj} - K_{dE}(\dot{E} - \dot{E}_{traj}) - K_{pE}(E - E_{traj}) - K_{iE}\int_0^t (E(\tau) - E_{traj}(\tau))d\tau \tag{3.43}$$

Defining the tracking error as $e_E = (E - E_{traj})$ and conducting the time derivative to (3.43), it yields

$$\dddot{e}_E + K_{dE}\ddot{e}_E + K_{pE}\dot{e}_E + K_{iE}e_E = 0 \tag{3.44}$$

The error will asymptotically converge to zero if the control parameters K_{dE}, K_{pE} and K_{iE} are chosen such that all roots of the characteristic polynomial of the closed-loop system are located in the left half plane. The associated characteristic polynomial can be written as

$$\begin{gathered} p(s) = s^3 + K_{dE}s^2 + K_{pE}s + K_{iE} \\ \Downarrow \\ p(s) = (s + a1)(s^2 + 2\zeta_E\omega_E s + \omega_E^2) \end{gathered} \tag{3.45}$$

where ω_E and ζ_E are respectively the desired damping ratio and natural frequency; $a1 > 0$, $\omega_E > 0$ and $\zeta_E > 0$.

Therefore, K_{dE}, K_{pE} and K_{iE} can be determined by

$$K_{dE} = 2\zeta_E\omega_E + a1, \quad K_{pE} = 2a1\zeta_E\omega_E + \omega_E^2, \quad K_{iE} = a1\omega_E^2 \tag{3.46}$$

Finally, the control law is synthesized according to the inverse dynamic expression presented in (3.42) (α_E).

3.3.2.3 Trajectory planing

Trajectory planning is an important step in the realization of a differential flatness-based controller. Since all the states and input are written as functions of the chosen flat output y, the flat output trajectory y_{traj} determines the trajectories of states and input. So, a well-known waveform can be considered so that all the transient behaviors can be predicted where physical constraints can be taken into account in the trajectory planning. To limit the derivative terms in (3.43), a low-pass second-order filter can be used to produce a desired trajectory for the flat output E_{traj} (energy). The transfer function of the second-order filter is given by

$$\frac{E_{traj}}{E^*} = \frac{\omega_{Etraj}^2}{s^2 + 2\zeta_{Etraj}\omega_{Etraj}s + \omega_{Etraj}^2} \tag{3.47}$$

where ζ_{Etraj} and ω_{Etraj} are respectively the desired damping ratio and natural frequency of the second-order filter, which determine the dynamic of the desired energy trajectory; E^* is the predefined energy reference, as

$$E^* = \frac{1}{2}(L_E i_N^2 + C_{bus}(u_{bus}^*)^2) \tag{3.48}$$

Note that E^* is related to the predefined reference voltage.

3.3.3 Control framework

Finally, the block diagram of the universal closed-loop control strategy for the MFCS-I and MFCS-II is shown in figure 3.11. The speed controller generates the q-axis current reference i_q^* under motoring conditions. In regenerative braking conditions, i_q^* is directly given by the desired braking force. The d-axis current reference i_d^* is set as 0 for a surface-mounted PMSM. Then, the two current references (i_d^* and i_q^*) are given into the current-loop PI controllers, which output the d-axis voltage reference u_d^* and q-axis voltage reference u_q^*. By using inverse Park transformation, the fundamental voltage reference u_{AN1}^*, u_{BN1}^* and u_{CN1}^* are obtained.

The differential flatness-based controller is adopted in the zero-sequence control-loop. The energy reference E^* is calculated by the voltage reference u_{bus}^* and the measured neutral current i_N. Then, the desired energy trajectory E_{traj} is obtained by the trajectory planning process presented in (3.47). By using the error feedback control presented in (3.43), the second-order derivative of the energy is obtained. Substituting the second-order derivative of the energy into the inverse dynamic presented in (3.42), the general control variable α_E in obtained. For the MFCS-I, α_E is directly used to generated the real duty cycles α_A, α_B and α_C based on the ZSVIPWM algorithm presented in (2.23). For the MFCS-II, α_h is set as 0.5 in the ZSVIPWM algorithm. Essentially, the classic SPWM is used on the inverter side. Therefore, α_E is used to generate the duty cycle of the fourth leg in the MFCS-II, as $\alpha_F = \alpha_E + 0.5$.

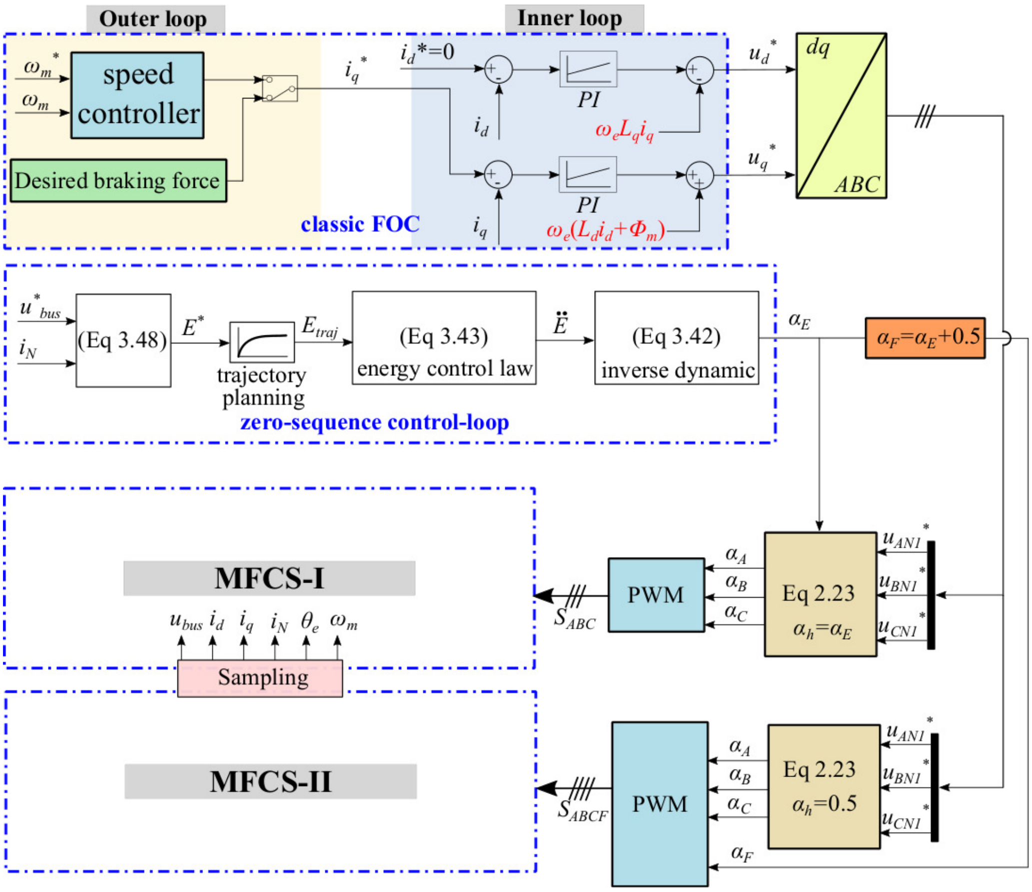

FIGURE 3.11: Universal control strategy for the MFCS-I and the MFCS-II.

3.4 Experimental results

The effectiveness of the MFCS-I and MFCS-II is verified on a 1.2 kW PMSM drive platform, as shown in figure 3.12. The PMSM is customized by a chinese company with an available NP. The traction inverter is constructed with an intelligent power module (ON Semiconductor STK581U3C2D-E). A 1.5 kW PMSM is used as the load motor, which is driven by an industrial inverter (LEROY SOMER). The load motor can be operated in either torque-controlled or speed-controlled modes. All the control algorithms are implemented on a dSPACE DS1202 MicrolabBox rapid prototyping system. The main parameters of the 1.2 kW test-bench are presented in table 3.1.

3.4.1 Current ripples analysis of the MFCS-I

To verify the effect of current ripples suppression in the MFCS-I by using a series inductor, two different inductors are tested whose values are respectively 1.3 mH and 13 mH. The instantaneous voltage and current waveforms are recorded when the motor is operated in both

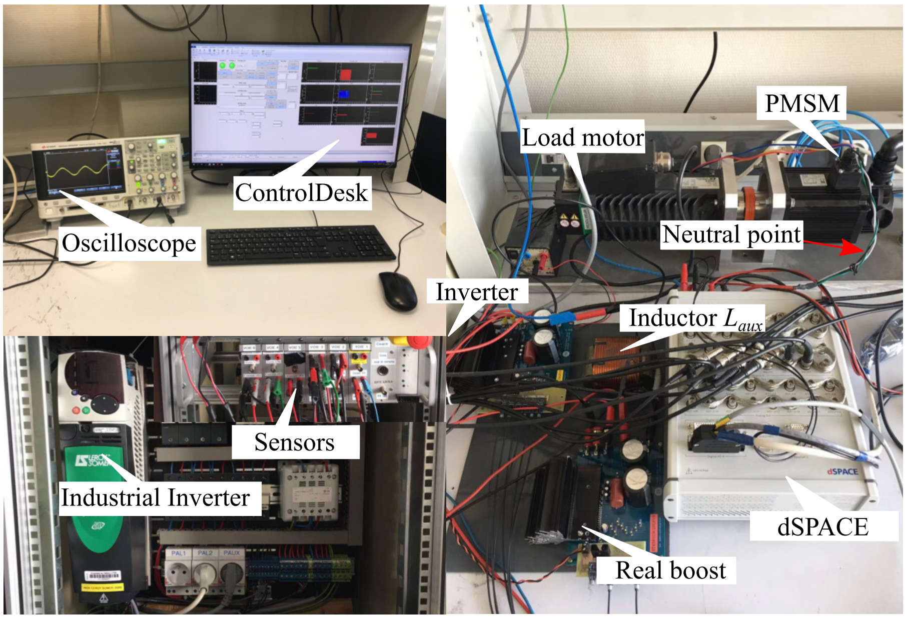

FIGURE 3.12: Test-bench of a 1.2 kW PMSM drive.

TABLE 3.1: The parameters of the 1.2 kW test-bench.

Parameter	Value	Unit	Parameter	Value	Unit
Stator resistance R	0.5	Ω	Pole pairs p	4	-
d-axis inductance L_d	1.7	mH	d-axis inductance L_q	1.7	mH
0-axis inductance L_0	0.0024	H	DC-bus capacitance C_{bus}	940	μF
Flux linkage Φ_f	0.1053	Wb	Nominal speed	3000	rpm/s
Mechanical inertial J_m	0.0009	$Kg \cdot m^2$	Nominal power	1.2	kW
Friction coefficient B_m	0.001	N·m/rad	Nominal torque	4	N·m
DC-source voltage u_{in}	180	V	DC-bus voltage u_{bus}^{ref}	360	V

standstill and motoring conditions. The basic MFCS is also compared.

3.4.1.1 In standstill condition

Thanks to the equivalent boost function, the DC-bus voltage of the basic MFCS and MFCS-I can be boosted to double the DC-source voltage, i.e. 360 V. In standstill conditions, the motor speed is null. Therefore, the actual duty cycles of the inverter in the three phases are perfectly consistent. In this case, the transient currents of three phases are also consistent. Therefore, we only illustrate the current wave of phase-A in the following analysis. In steady states, the experimental results are shown in figure 3.13, which are related to the basic MFCS, the MFCS-I with a 1.3 mH series inductor and the MFCS-I with a 13 mH series inductor.

For the basic MFCS (see figure 3.13(a)), it can be observed that the neutral voltage (u_{NO}) is exactly equal to the DC-source voltage (180 V) because the NP is clamped. The phase-voltage (u_{AN}) has two voltage-levels (180 V and -180 V). As analyzed before, in a conventional drive, the phase voltage is 0 V under the two zero voltage vectors if the motor speed is null. Therefore, the phase-current ripple is 0 in a conventional drive if the motor speed is 0. However, since u_{AN} is not 0 V in the basic MFCS, this voltage applied on each phase will produce current. As a result, we can clearly see the current ripples of i_A and i_N in figure 3.13(a), whose values are 5 A and 15 A respectively. Obviously, such large ripples are adverse to the motor and will result in big iron losses. Therefore, we can conclude that the zero-sequence inductance ($L_0 = L_\sigma$) or leakage inductance of the motor is insufficient to suppress the current ripple in the equivalent boost function.

By adopting a 1.3 mH series inductor, the value of a_L can be calculated as $1.3/2.4 = 0.54$. In other words, the inductance of the series inductor is equal to $0.54L_0$. In this case, the value

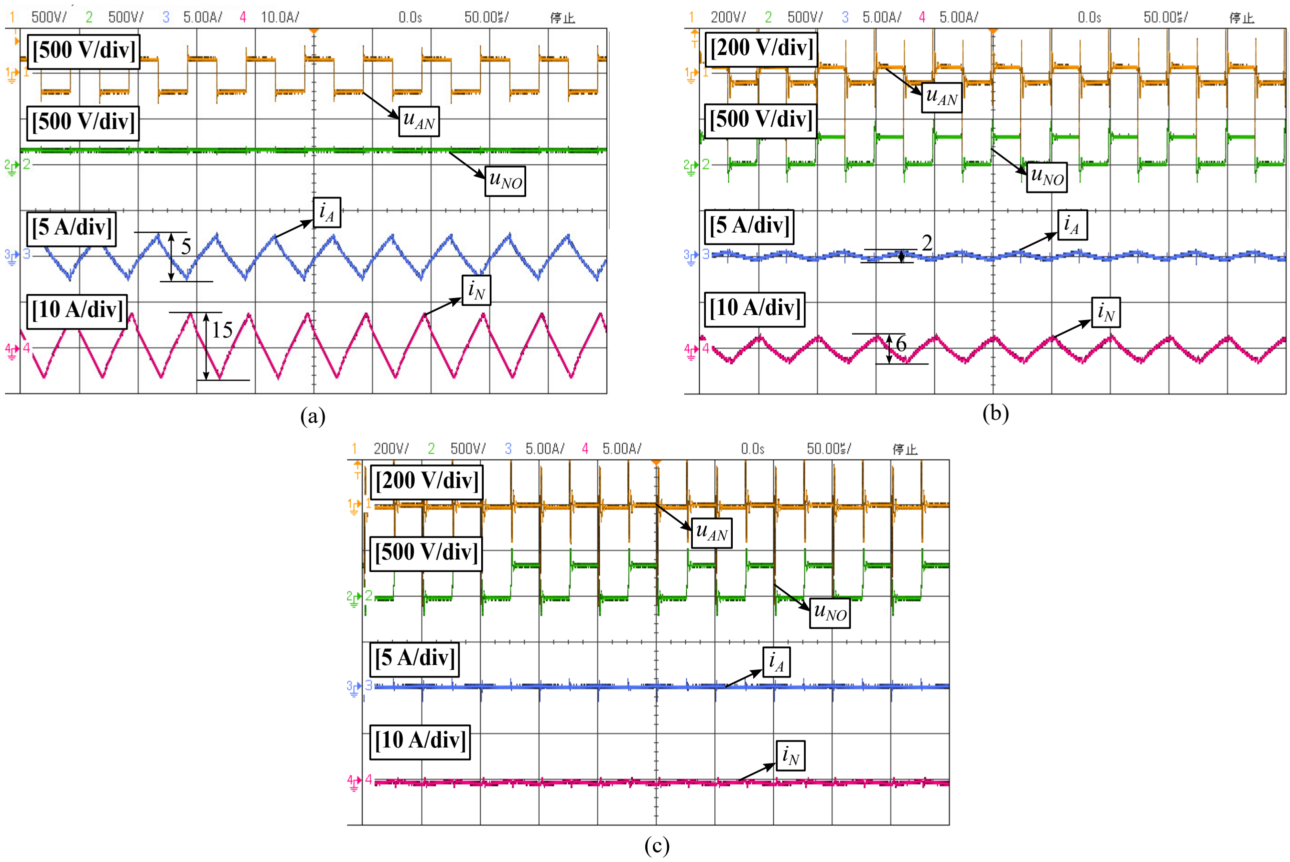

FIGURE 3.13: Phase-A voltage, neutral voltage, phase-A current and neutral current in standstill conditions. (a) The basic MFCS without a series inductor. (b) The MFCS-I with a 1.3 mH series inductor. (c) The MFCS-I with a 13 mH series inductor.

of R_{flo} is further evaluated as 0.19. This means that the voltage bias (see (3.15)) is $0.19u_{bus}$ $\approx$ 68 V under the two zero voltage vectors. From figure 3.13(b), we can see that the u_{AN} still has two voltage-levels. However, compared to that in figure 3.13(a), the voltage amplitude is reduced to around 68 V. This verifies the correctness of the theoretical analysis. Because u_{AN} is still not 0 V, there is still a current ripple in i_A. However, the ripple of i_A is decreased to 2 A compared to that in the basic MFCS. Roughly speaking, the 1.3 mH inductor is still insufficient to suppress the current ripple into an acceptable range.

By using a 13 mH series inductor, the value of a_L is calculated as $13/2.4 = 5.4$. In other words, the inductance of the series inductor is equal to $5.4L_0$. In this case, the value of R_{flo} is 0.03. This means that the voltage bias (see (3.15)) is $0.03u_{bus} \approx 11$ V under the two zero voltage vectors. From figure 3.13(c), it is obvious that the voltage amplitude of u_{AN} is close to 0. This implies that the NP is almost similar to that of a conventional drive. As a result, the ripples of i_A and i_N are much smaller and acceptable in practice.

3.4.1.2 In motoring condition

When the motor is operated at a 1000 rpm speed and a 2 N·m load, the phase-A voltages, neutral voltages, phase-A currents and neutral currents of the basic MFCS, the MFCS-I with a 1.3 mH series inductor and the MFCS-I with a 13 mH series inductor are further illustrated in figure 3.14. For the basic MFCS, u_{AN} only has two voltage-levels (around 180 and -180 V) due to the clamped NP, as shown in figure 3.14(a) and (b). Apparently, both i_A and i_N have big ripples. Meanwhile, i_A is severely distorted whose shape is not a perfect sinusoidal wave. Therefore, we can conclude that the basic MFCS is unpractical in practice.

By using a 1.3 mH series inductor, u_{AN} is not limited between 180 and -180 V. Thanks to the series inductor, u_{AN} and u_{NO} are able to have four voltage levels within one switching period. This shows good agreements with the theoretical analysis. However, the ripple of i_A and i_N are still relatively large. Meanwhile, the shape of i_A is still distorted. By using a 13 mH series inductor, the ripples of i_A and i_N are smaller, as shown in figure 3.14(e). Meanwhile, the shape of i_A is closer to a sinusoidal wave. Therefore, it can be concluded that, the basic MFCS concept can not be directly used in practice because the zero-sequence inductance of the motor is relatively small which is insufficient to act as a suitable filtering inductor in the equivalent boost function. The MFCS-I structure can suppress the current ripple into an acceptable range by employing a series inductor whose inductance is five times the zero-sequence inductance of the motor.

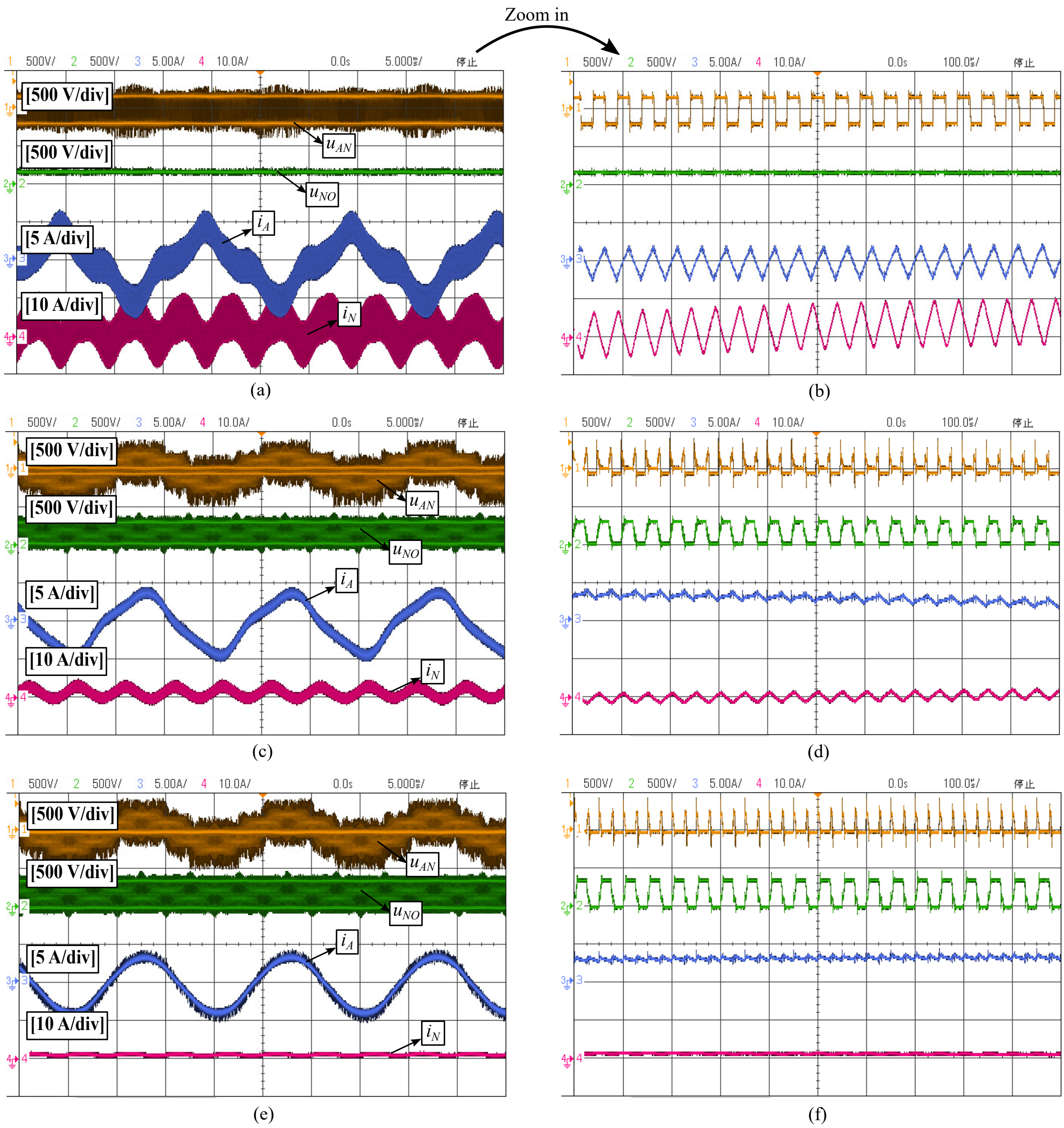

FIGURE 3.14: Phase-A voltage, neutral voltage, phase-A current and neutral current in motoring conditions (1000 rpm and 2 N·m). (a), (b) The basic MFCS without a series inductor. (c), (d) The MFCS-I with a 1.3 mH series inductor. (e), (f) The MFCS-I with a 13 mH series inductor.

3.4.2 Comparison between the MFCS-I (with the 13 mH series inductor) and a real two-stage converter-based drive

Compared to a real two-stage converter-based drive, the MFCS-I is still more economical because it can save a real boost chopper. Therefore, it is more meaningful to compare the performance of the MFCS-I with a real two-stage converter-based drive. To construct a real DC/DC boost converter, another STK581U3C2D-E is employed where only one leg is activated. To be fair, the same inductor L_{aux} (13 mH) is used in the real boost stage. For the two-stage converter-based drive, the control strategy presented in figure 3.11 can also be used, in which the classic FOC is used to control the motor and the differential flatness-based is used to control the real boost converter. Completely consistent control parameters listed in table 3.2 are used in the MFCS-I and the two-stage drive. For clarity, the circuit diagrams of the two studied drives are shown in figure 3.15.

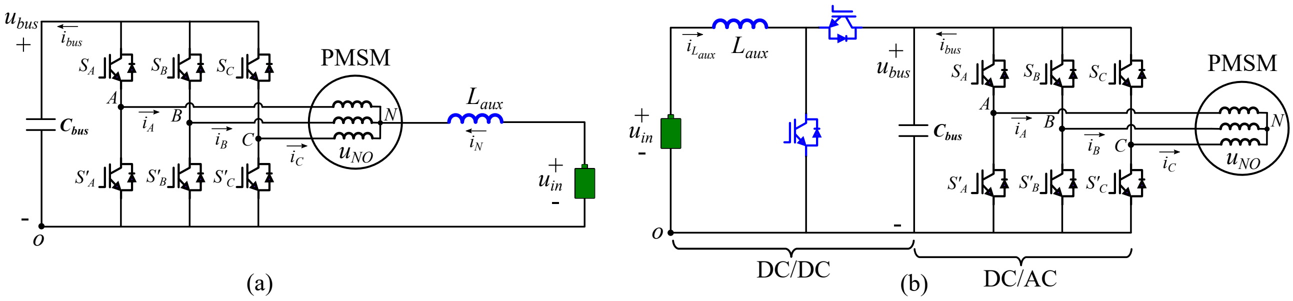

FIGURE 3.15: Circuit diagrams of two PMSM drives. (a) MFCS-I with a 13 mH series inductor. (b) two-stage converter-based drive.

TABLE 3.2: Parameters of controllers.

Current-loop PIs	Speed-loop state feedback controller with an integral action	Boost differential flatness-based controller
$kpd = 5.0$ $Tid = 0.0033$ s $kpq = 5.0$ $Tiq = 0.0033$ s	$K_\omega = 0.0734$ $K_{\omega\_I} = -0.9878$	$\zeta_E = 1$, $\omega_E = 94.8$ rad/s $a1 = 60$ $\zeta_{Etraj} = 1$, $\omega_{Etraj} = 47.4$ rad/s

3.4.2.1 Starting performance of the boost function

Normally, the starting process of a two-stage converter-based drive can be divided into two steps. The first step is to hold a sufficient DC-bus voltage and the second step is to start

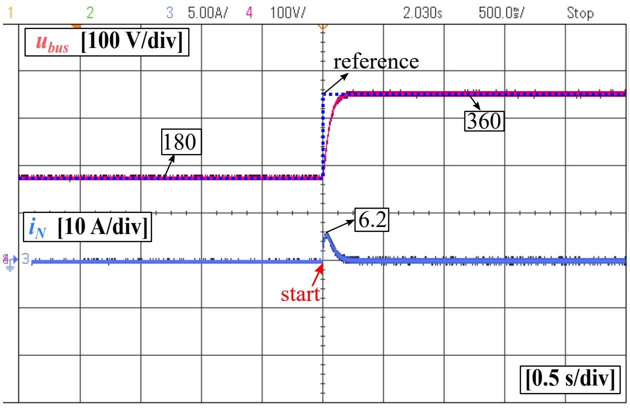

(a)

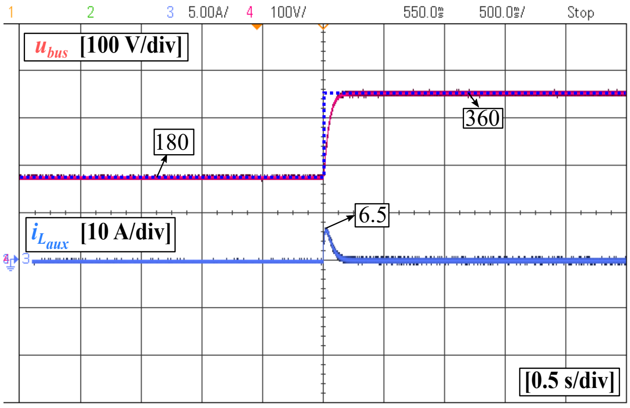

(b)

FIGURE 3.16: Starting performance of the boost function. (a) DC-bus voltage and neutral curent in the MFCS-I with a 13 mH inductor. (b) DC-bus voltage and inductor current in the two-stage converter-based drive.

the motor. To assess the starting performance, the consistent experiment is carried out on the MFCS-I and the two-stage converter-based drive, respectively. The experimental results are shown in figure 3.16.

For the MFCS-I, its DC-bus voltage is equal to the source-voltage (180 V) before starting its equivalent boost function. Once the control instruction of the equivalent boost is executed, u_{bus} is boosted to 360 V rapidly. At the beginning, the neutral current (i_N) is increased to 6.2 A to charge the DC-bus capacitor. This phenomenon demonstrates the existence of the equivalent boost function even if there is no additional chopper used in the MFCS-I.

In terms of the two-stage converter-based drive, we can observe the similar starting performance by using the same controller. In the initial stage of the starting process, the inductor current $i_{L_{aux}}$ is increased to 6.5 A. This value is larger than that of the MFCS-I because the zero-sequence inductance of the motor and L_{aux} jointly construct the filtering inductance of the equivalent boost in the MFCS-I.

3.4.2.2 Starting performance of the motor function

Since the DC-bus voltage is maintained at 360 V in both drives, the motor is ready to start. Figure 3.17 shows a starting process of the motor in which a speed step (from 0 to 1000 rpm) is given at 2.5 s. In the MFCS-I, it can be seen that the actual speed can reach the desired value within 0.5 s. Then, it is maintained at 1000 rpm stably. Although its DC-bus voltage shows a 3 V dip when the motor accelerates instantly, it can return to the stable state quickly due to the control for the equivalent boost function. Figure 3.17(c) illustrates the

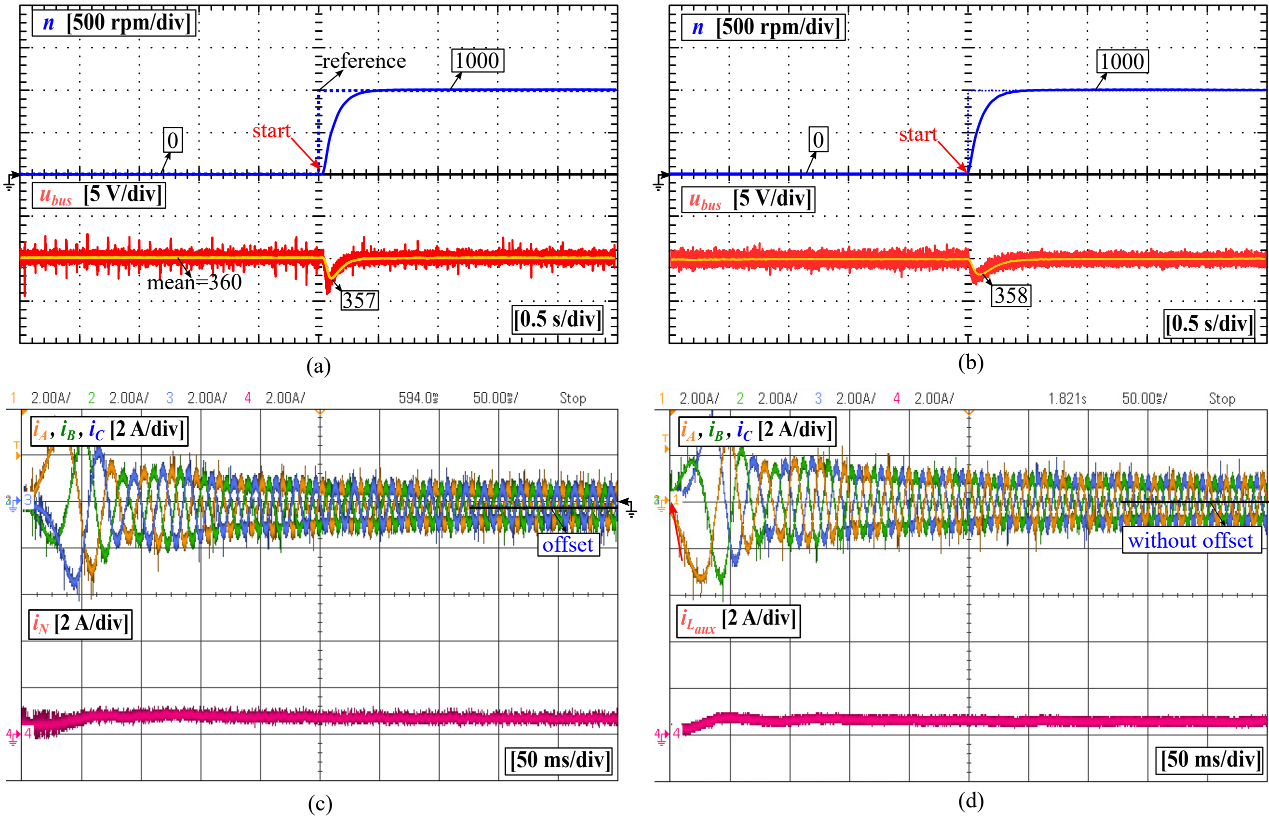

FIGURE 3.17: Starting performance of the motor. (a) Motor speed and DC-bus voltage in the MFCS-I with a 13 mH inductor. (b) Motor speed and DC-bus voltage in the two-stage converter-based drive. (c) Phase-currents and neutral current in the MFCS-I with a 13 mH inductor. (d) Phase-currents and inductor current in the two-stage converter-based drive.

zoomed-in views of phase-currents and neutral current. Interestingly, the phase-currents in the MFCS-I are no longer the standard sinusoidal waveforms. They present an offset which is caused by the zero-sequence current (or i_N). Figure 3.17(b) and (d) depict the similar starting process of the two-stage converter-based drive. By comparison, it can be concluded the starting performance of both drives is similar. It needs to point out that the phase-currents in the two-stage converter-based drive are symmetrical because its NP is not used and there is no zero-sequence current flowing into the motor.

3.4.2.3 Steady-state performance in motoring conditions

To study the influence on phase-current quality caused by the connected NP in the MFCS-I, the steady-state performance of both drives is compared where the motor is operated at the nominal condition (3000 rpm with 4 N·m load). In steady states, the phase-currents, neutral current i_N and the inductor current $i_{L_{aux}}$ are displayed in figure 3.18. The corresponding FFT analysis of phase-currents is further presented below. From figure 3.18(a), it can be seen that the phase-current offset is around -2.45 A in the MFCS-I, which is equal to -1/3 of the neutral current (the DC RMS of i_N=7.35 A). In the two-stage converter-based drive, there is no phase-current offset due to the unconnected NP, as shown in figure 3.18(b).

In terms of the phase-current FFT analysis, the proportion of zero-sequence component is 38% in the MFCS-I while it is almost null in the two-stage converter-based drive. This is reasonable because the DC/DC conversion process is achieved through the motor in the MFCS-I while the DC/DC conversion process is independent to the motor in the two-stage converter-based drive. The second-order, third-order and fourth-order harmonics in the MFCS-I are bigger than those in the two-stage converter-based drive. However, it needs to point out that the even and third-order harmonics do not affect the torque performance due to the symmetrical structure in three phases. Interestingly, the fifth-order harmonic is smaller (0.1% to 0.8%) in the MFCS-I. The phase-current THD is 6.10% in the MFCS-I while it is 5.36% in the two-stage

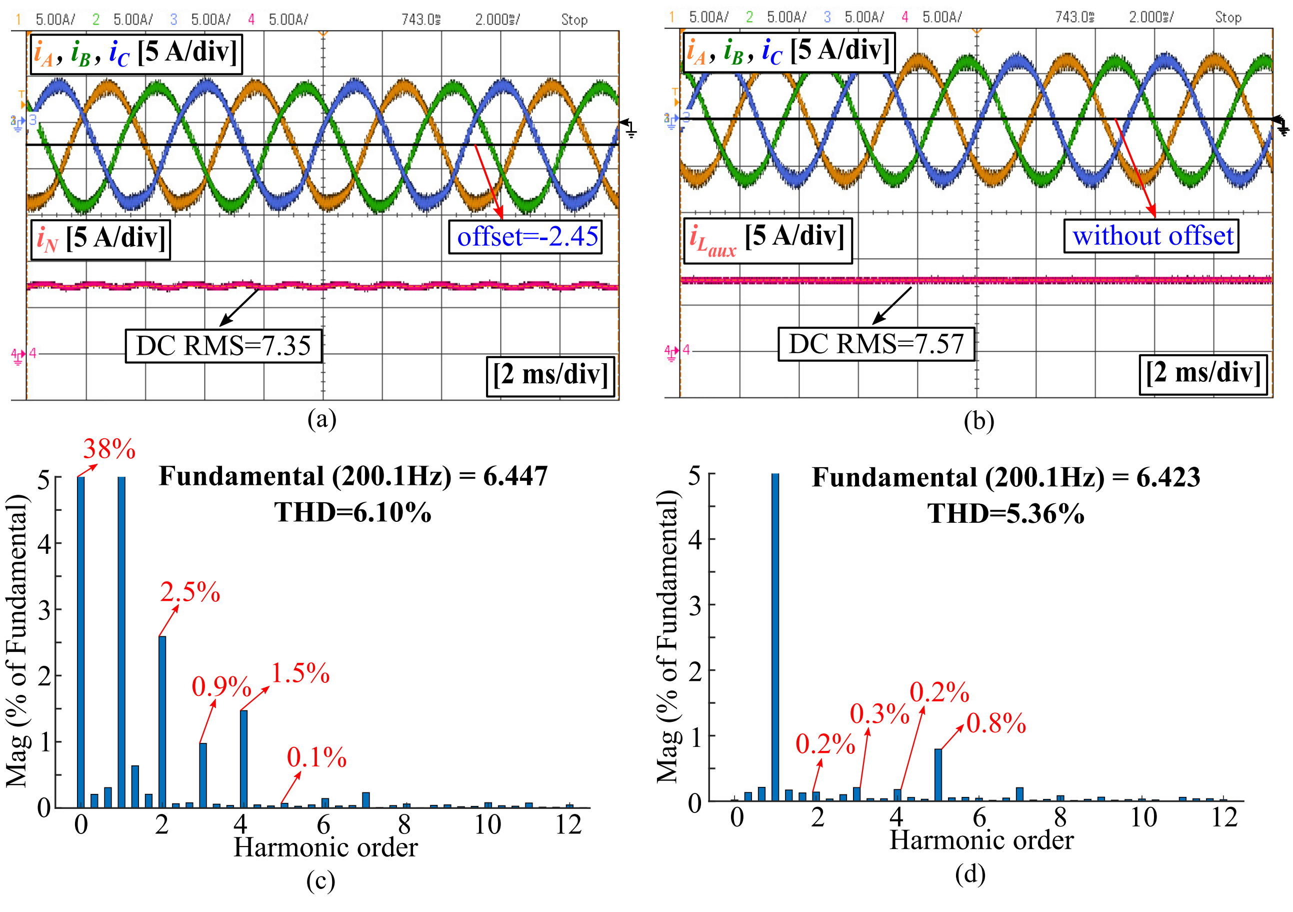

FIGURE 3.18: Steady-state performance. (a) Phase-currents and neutral current i_N in the MFCS-I with a 13 mH inductor. (b) Phase-currents and inductor current $i_{L_{aux}}$ in the two-stage converter-based drive. (c) FFT analysis of phase-currents in the MFCS-I with a 13 mH inductor. (d) FFT analysis of phase-currents in the two-stage converter-based drive.

converter-based drive.

Theoretically, the additional zero-sequence current and the increased THD will result in more losses in the motor of the MFCS-I. However, the input current ($i_N = 7.35$ A) of the MFCS-I is smaller than that ($i_{L_{aux}} = 7.57$ A) of the two-stage converter-based drive, which means that the total efficiency of the MFCS-I is higher. This phenomenon happens because there are less switching devices used in the MFCS-I, i.e. less switching losses are produced. The decreased switching losses are larger than the increased losses in the motor. In order to evaluate the total efficiency accurately, we define $Eff1 = AC\,FUNDAMENT/DC\,RMS$ as an evaluation criterion, which indicates the normalization of the fundamental AC current (related to the fundamental torque) to the input current. Thus, $Eff1 = 6.447/7.35 = 0.877$ in the MFCS-I while $Eff1 = 6.423/7.57 = 0.848$ in the two-stage converter-based drive. Compared to the two-stage converter-based drive, it can be concluded that the motoring efficiency of the MFCS-I is improved by 3.4%. By comparisons, the THD performance of phase currents is degraded by 13.8%

3.4.2.4 Dynamic performance

Experimental validations with speed and load variations are carried out to assess the dynamic performance of the MFCS-I. The experimental settings are as follows: the speed reference is 1000 rpm before 2 s. It is increased to 2000 rpm at 2 s. After 6 s, it is reset to 1000 rpm; the load torque is 1 N·m before 10 s while it is increased to 2 N·m at 10 s and reset to 1 N·m at 15 s. The experimental results are shown in figure 3.19. It can be seen that the motor in the MFCS-I shows the similar dynamic performance with that in the two-stage converter-based drive. More specifically, the actual speed can track the reference tightly during the acceleration and deceleration processes. Although it swings slightly (around 50 rpm) when the load perturbation is applied and removed, it is still able to return to 1000 rpm quickly. Therefore, it is reasonable to conclude that the connection of motor's NP in the MFCS-I does not affect the dynamic performance of the motor. In addition, the DC-bus voltage in both drives can be well maintained during the dynamic test. Although it joggles slightly (around 2 V) when the motor's power changes instantly, it can recover to 360 V quickly. This verifies the feasibility of the proposed control strategy in which the motor function and the equivalent DC/DC boost function can be controlled independently.

3.4.2.5 Regenerative braking performance

To emulate a regenerative braking scenario, the load motor is operated in the speed-controlled mode, which drags the tested PMSM to decelerate from the nominal speed to zero

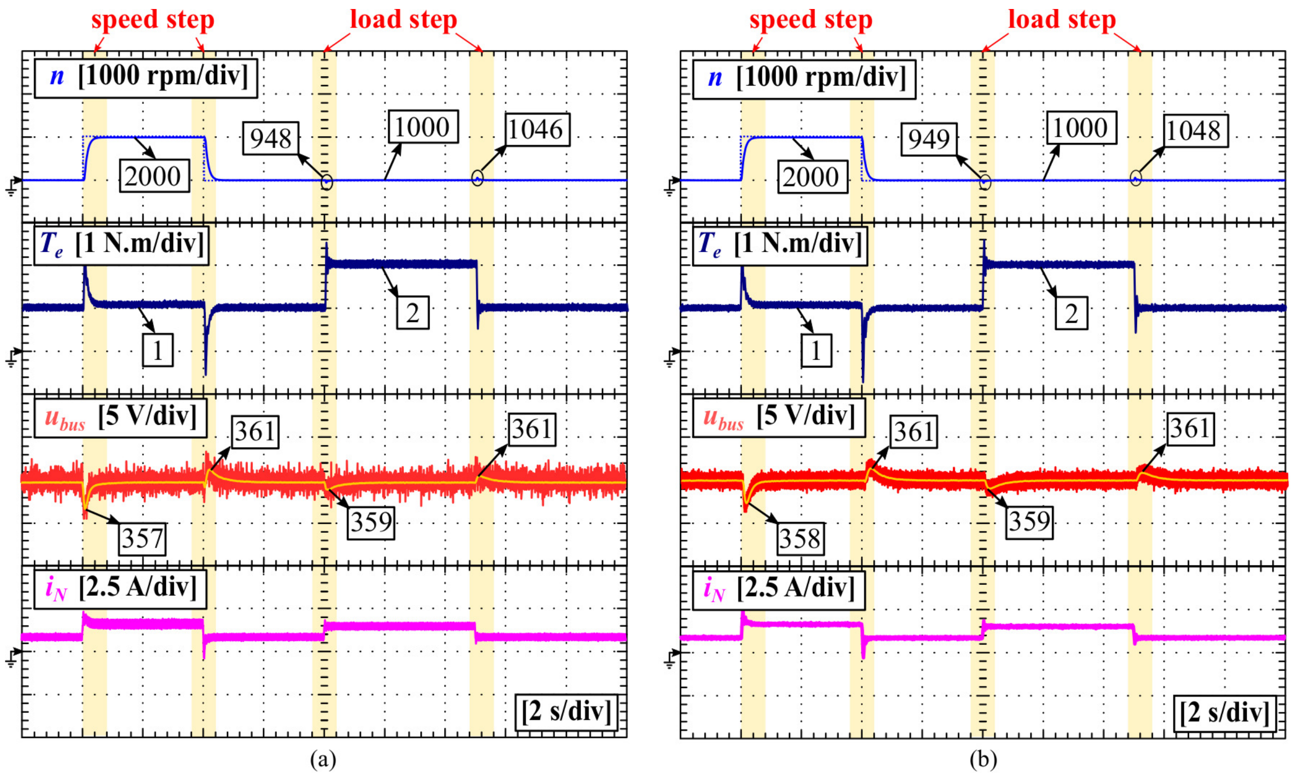

FIGURE 3.19: Dynamic performance comparison. (a) The MFCS-I with a 13 mH series inductor. (b) The two-stage converter-based drive.

speed in 3 seconds. The braking force herein is set as -4 N·m. In the same way, the experimental results of the regenerative braking process are shown in figure 3.20 where the MFCS-I is compared to the two-stage converter-based drive.

In the initial stage, both i_N and $i_{L_{aux}}$ are negative, which are equal to -5.75 A and -5.64 A respectively. This implies that both the MFCS-I and the two-stage converter-based drive can recycle the braking energy to charger the DC-source. With the decrease of the motor's speed, the i_N and $i_{L_{aux}}$ decrease. When the motor is completely stopped, i_N and $i_{L_{aux}}$ become positive (around 0.5 A) again, in order to maintain the DC-bus voltage. Therefore, it can be concluded that the MFCS-I can realize the similar regenerative braking performance even if it does not use a real directional DC/DC converter.

In steady states (3000 rpm and -4 N·m torque), the phase-currents (see figure 3.20(c)) of the MFCS-I show a positive offset, which is still equal to -1/3 of the input current (the DC RMS of i_N is 5.75 A). In terms of the phase-current FFT analysis (see figure 3.20(e)), the proportion of the zero-sequence component is 32%. The second-order, third-order and fourth-order harmonics are still larger while the fifth-order harmonic is smaller (0.3% to 0.6%). By comparing with the two-stage converter-based drive, the phase-current THD in the MFCS-I is degraded by 8.5% (6.51% to 6.00%). To evaluate the charging efficiency, defining the index $Eff2 = DC\,RMS/AC\,FUNDAMENTAL$ as an evaluation criterion, which indicates the normalization of the input current to the fundamental AC current (related to the fundamental

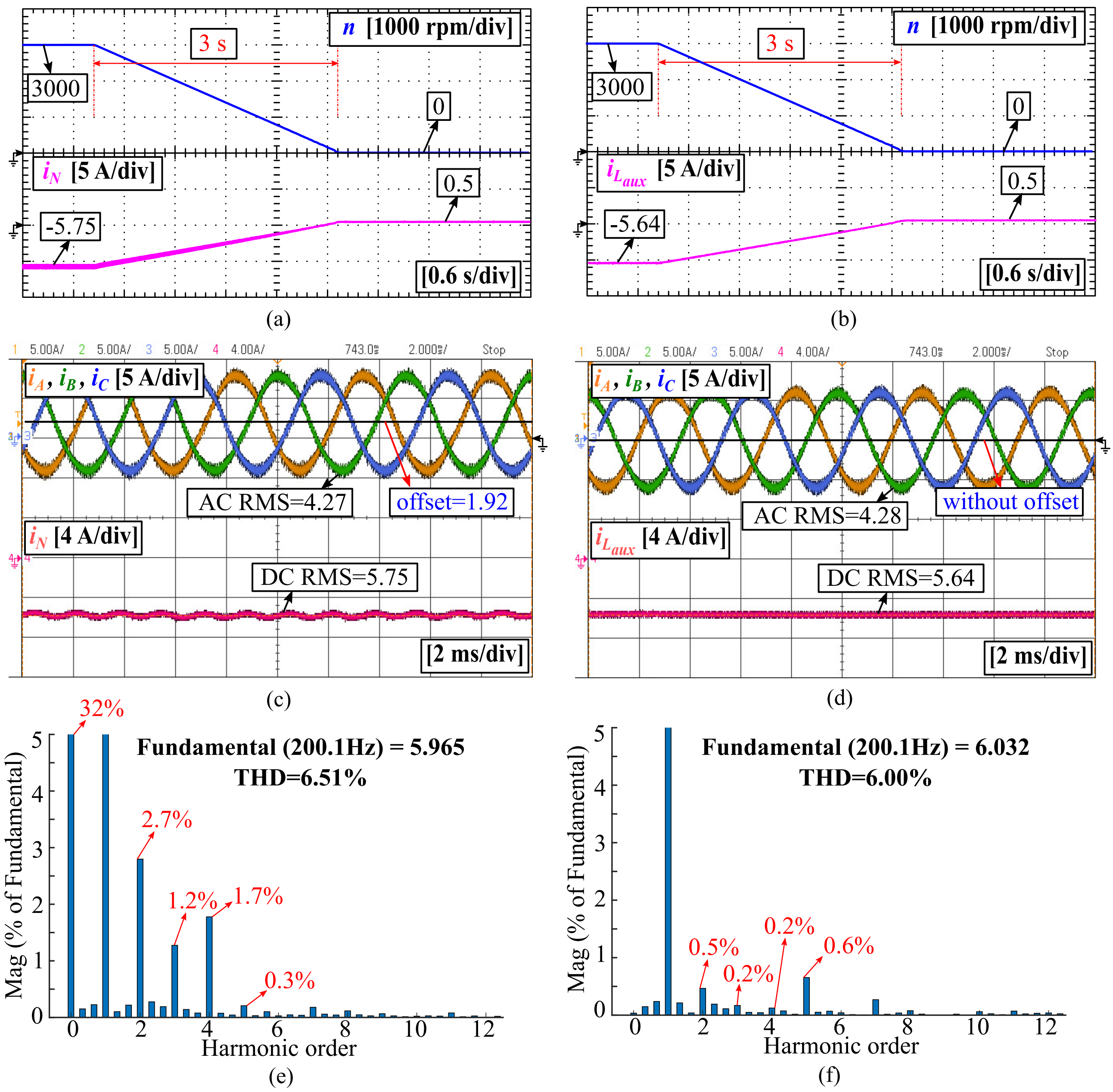

FIGURE 3.20: Regenerative braking performance. (a) Motor speed and neutral current in the MFCS-I with a 13 mH inductor. (b) Motor speed and inductor current in the two-stage converter-based drive. (c) Zoomed in phase-currents and neutral current in the MFCS-I with a 13 mH inductor. (d) Zoomed in phase-currents and inductor current in the two-stage converter-based drive. (e) FFT analysis of phase-currents in the MFCS-I with a 13 mH inductor. (f) FFT analysis of phase-currents in the two-stage converter-based drive.

torque). Thus, $Eff2 = 5.75/5.965 = 0.964$ in the MFCS-I while $Eff2 = 5.64/6.032 = 0.935$ in the two-stage converter-based drive. Therefore, it can be concluded that the charging efficiency is improved by 3.1% due to the reduction of switching devices.

Consequently, by combining with above experimental results, the characteristics of the MFCS-I compared to the two-stage converter-based drive are summarized in Table 3.3. It can be seen that the MFCS-I only requires 6 switching devices while the two-stage converter-based drive needs 8 switching devices. We can say that the cost of the MFCS-I is decreased by 25%. Regarding the current THD of the MFCS-I, it is degraded by (0.51% to 0.74%) in the motoring pattern and the regenerative braking pattern, respectively. In terms of the system efficiency of the MFCS-I, it is improved by (3.1% to 3.4%) in the motoring pattern and the regenerative braking pattern, respectively.

TABLE 3.3: Characteristics of the MFCS-I compared to the two-stage converter-based drive.

PMSM drives	Switching Devices	Current THD at Motoring Pattern	Current THD at Rengenerative Braking Pattern	$Eff1$	$Eff2$
Two-stage converter	8	5.36%	6.00%	0.848	0.935
MFCS-I	6	6.10%	6.51%	0.877	0.964
Comparison	Decreased by 25%	Degraded by 13.8%	Degraded by 8.5%	Improved by 3.4%	Improved by 3.1%

3.4.3 Performance of the MFCS-II

Compared to the MFCS-I, the MFCS-II is able to have an equivalent boost function, which has a higher effective step-up ratio thanks to the new DOF provided by the fourth leg according to the aforementioned analysis. To verify the higher effective step-up ratio in the MFCS-II, a 40 V DC-source is used. Experimental validations are still carried out on the 1.2 kW PMSM test-bench, which is configured in the form of the MFCS-II. We set $\alpha_h = 0.5$ throughout. Therefore, the equivalent duty cycle of the equivalent boost function is $\alpha_E = \alpha_F - 0.5$.

3.4.3.1 Relationship between u_{bus} and α_F

According to the theoretical analysis, the DC-bus voltage u_{bus} approximates (u_{in}/α_E) by neglecting the resistance of the motor in steady states. In open-loop modes, the relationship between u_{bus} and α_F can be easily tested. To this end, we decrease the value of α_F from 1 to 0.6 with a 0.05 interval gradually. Then, the value of u_{bus} is recorded, as shown in figure 3.21.

At first, α_F is equal to 1. In this case, the equivalent duty cycle α_E of the equivalent boost function is equal to 0.5. Therefore, the theoretical u_{bus} will be 80 V. From figure 3.21, we can see that u_{bus} is equal to 80 V in the initial stage. Actually, the MFCS-II in this special case is similar to the MFCS-I because $\alpha_F = 1$ means the DOF of the fourth leg is not utilized. Then, with the decrease of α_F, u_{bus} increases from 80 to 381 V. Theoretically, u_{bus} can reach 400 V when $\alpha_F = 0.6$. The difference between the theoretical analysis and the experimental result can be explained by the effect of dead time and the voltage drop across the switching devices and the motor's resistance.

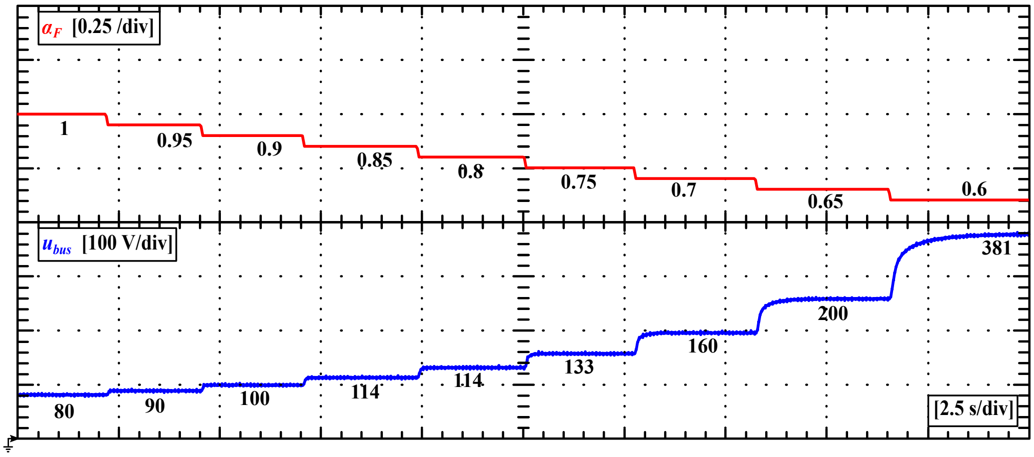

FIGURE 3.21: Relationship between u_{bus} and α_F.

3.4.3.2 Steady-state performance

The steady-state performance of the MFCS-II is presented in figure 3.22, where the equivalent boost is controlled in a closed-loop way. In figure 3.22(a), the motor is operated at 1000 rpm. In figure 3.22(b), the motor is operated at 2000 rpm.

First, it can be observed that the DC-bus voltage u_{bus} can be regulated at 360 V stably even if the DC-source voltage u_{in} is only 40 V. In this case, the step-up ratio of the equivalent boost function is 9. With the 40 V DC-source, the motor can not only be operated in the low-speed condition (1000 rpm) but also the high-speed condition (2000 rpm). Obviously, the effective step-up ratio of the MFCS-II is larger than that of the MFCS-I.

However, it needs to note that, if the DC-source voltage is too small, the neutral current (input current in the MFCS-II) will be large. This means that the zero-sequence current in the motor may be larger than the amplitude of the fundamental current. For example, we can see that i_A in figure 3.22(a) shows a big upward offset which is caused by the zero-sequence current. The offset is equal to 1/3 of i_N. In figure 3.22(b), i_A is almost completely positive. This phenomenon happens because the zero-sequence current of the motor is bigger than the

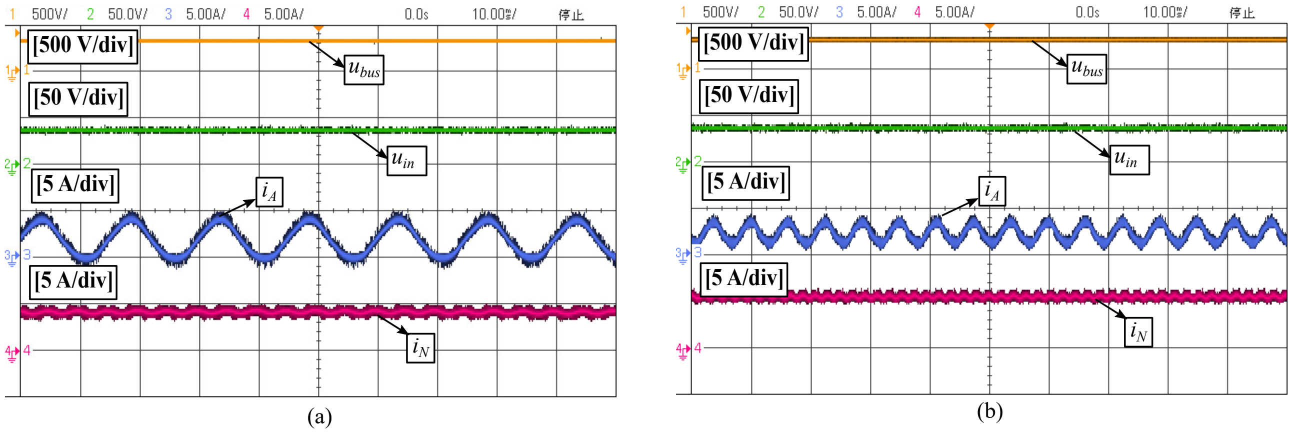

FIGURE 3.22: Steady-state performance of the MFCS-II: DC-source voltage, phase-A current and neutral current. (a) When the motor is operated at 1000 rpm. (b) When the motor is operated at 2000 rpm.

amplitude of the fundamental current.

Figure 3.23 shows the steady-state performance of the MFCS-II when the motor is operated at 200 rpm with the full load (4 N·m). Obviously, this verifies that the motor can still operate at the nominal load condition in the MFCS-II. The FFT analysis of phase-currents is further presented on the right. The THD of phase currents is around 4.87%.

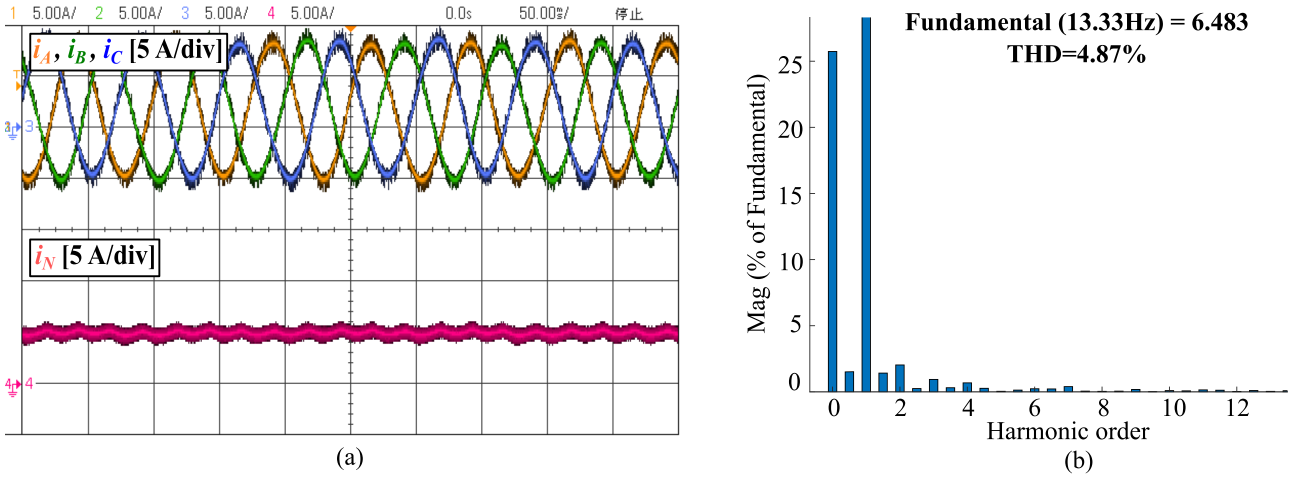

FIGURE 3.23: Steady-state performance of the MFCS-II when the motor is operated under the condition of 200 rpm with the full load. (a) Phase-currents and neutral current. (b) FFT analysis of phase currents

3.4.3.3 Dynamic performance

Experimental validations with speed and load variations are carried out to assess the dynamic performance of the MFCS-II. The dynamic settings are as follows: the speed reference is 1000 rpm before 2 s. It is increased to 1500 rpm at 2 s. After 6 s, it is reset to 1000 rpm; no load torque is applied before 10 s while it is increased to 1 N·m at 10 s and removed at 15 s. The experimental results are shown in figure 3.24. It can be seen that the motor can still show a remarkable dynamic performance. More specifically, the actual speed can track the reference tightly during the acceleration and deceleration processes. Although it swings slightly (around 60 rpm) when the load perturbation is applied and removed, it is still able to return to 1000 rpm quickly. In addition, the DC-bus voltage can be well maintained at 360 V during the dynamic test. Although it joggles slightly (around 3 V) when the power of the motor changes instantly, it can recover to 360 V quickly.

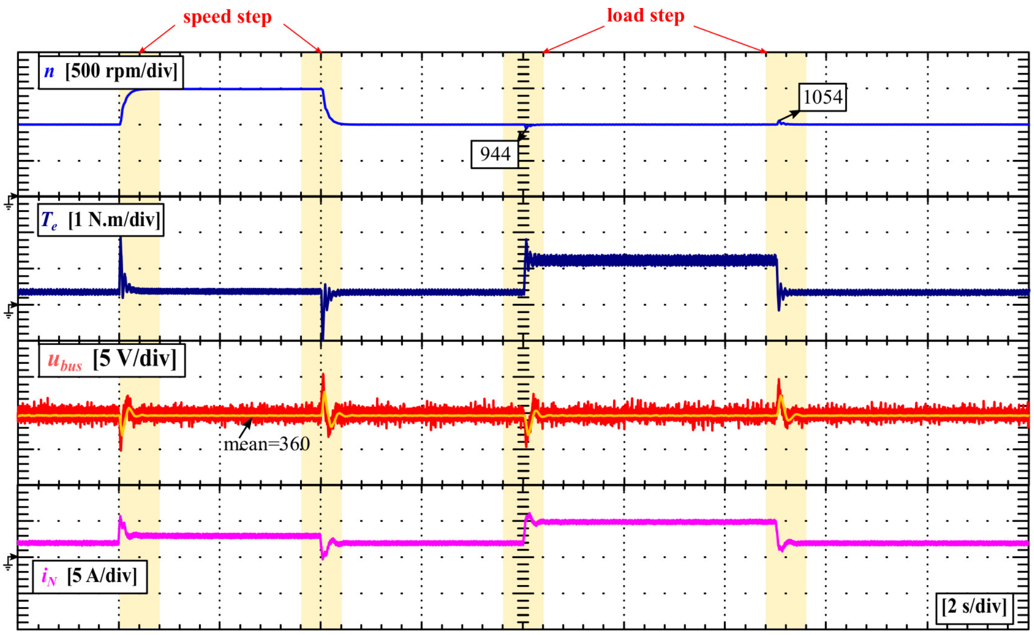

FIGURE 3.24: Dynamic performance of the MFCS-II.

Conclusion

To suppress the big current ripple of the basic MFCS, an improvement named as MFCS-I is proposed by using a series inductor. Based on the concept of a re-floating NP, the value of the series inductor can be easily selected. Theoretically, a series inductor with five times the zero-sequence inductance of the motor can create a similar NP with the conventional drive. To comprehensively evaluate the MFCS-I, a two-stage converter-based drive is compared, where the same inductor L_{aux} is used in its boost stage. Experimental results show that, without using a physical chopper, the MFCS-I is also able to boost its DC-bus voltage to double the DC-bus voltage. The starting performance of the equivalent boost is similar with the real boost in the two-stage converter-based drive. Moreover, the starting performance of the motor in the MFCS-I is also similar with that in the two-stage converter-based drive. The steady-state and dynamic performance is further compared in detail. According to the experimental results, the phase-current THD of the MFCS-I is degraded by $(8.5\% - 13.8\%)$ compared to that in the two-stage converter-based drive. But total efficiency of the MFCS-I is improved by $(3.1\% - 3.4\%)$ thanks to the reduced number of switching devices. In addition, the similar dynamic performance of the two drives also reveals that the connection of motor's NP in the MFCS-I does not affect the acceleration and deceleration ability of the motor.

To improve the effective step-up ratio, another improvement named as MFCS-II is proposed by using an auxiliary leg. The theoretical analysis indicates that both the step-up ratio of the equivalent boost and the DCSUR increase with the decrease of α_F. Different from a real single-phase DC/DC boost converter which can not achieve an ultra high step-up ratio due to the limit of its duty cycle, the MFCS-II can reach an ultra high step-up ratio when α_F approaches 0.5. According to the experimental validations, it can be concluded that the DC-source voltage can reach 360 V even if a 40 V DC-source is supplied. Meanwhile, the motor can still be operated at low-speed (200 rpm) and high-speed (2000 rpm) conditions. However, it needs to note that the phase-currents may be always positive if the motor power is too high.

In conclusion, the MFCS-I is more suitable for the application where the desired DC-bus voltage is less than double the DC-source voltage. If one needs an ultra high step-up ratio, the MFCS-II can be considered.

Chapter 4

Fault-tolerant control of MFCS-I toward open-phase faults

Contents

Introduction

Open-phase fault (OPF) is one of the most prevalent failures in VSI fed motor drives, which eventually results in the outage of motor windings. The fault may be caused by internal failures of stator windings, open-circuit and short-circuit failures of power electronic switches, and mechanical failures of terminal connectors. If it is not treated with remedial measures, the motor will suffer from big electromagnetic torque ripples hence induce serious mechanical vibrations. Long time operations with the fault will further lead to a secondary damage even irreparable breakdown.

As one of the key parts of EVs, the electrical drive is desired to be equipped with the ability of continuous operations in case of the appearance of an OPF. Especially, the uninterrupted torque output ability should be insured on uphill and downhill conditions in order to guarantee the personal safety of passengers. According to the literature review presented in Chapter 1, there are four typical fault-tolerant topologies (CFI, SFI, CFNI and SFNI). In terms of the two (CFNI and SFNI) who use the NP of the motor, they can tolerate an OPF which occurs no matter on the inverter side or on the machine side. Thanks to the circulation of the zero-sequence path, the motor can still generate a circular rotating magnetic field with only two active phases. However, the CFNI and SFNI always require some assistant hardwares (a pair of split capacitors, two auxiliary IGBT and a TRIAC) to achieve the fault-tolerance. These assistant devices will not only increase the cost of the whole system but also complicate the control circuit because additional control signals need to be added to the main control board. This will indirectly affect the reliability of the drive system.

Thanks to the inherently connected NP in the MFCS-I, the path needed by the zero-sequence current exists throughout. Therefore, the MFCS-I is supposed to possess the fault-tolerance towards an OPF without using any auxiliary device. This chapter intends to explore the fault-tolerant potential of the MFCS-I, which is organized as follows

- In Section 1, the fault-tolerant potential of the MFCS-I is discussed. To guarantee a constant torque output and a stable average DC-bus voltage in post-fault conditions, three constraints are found. Based on the three constraints, a new current vector trajectory is proposed. The power conversion process and the post-fault output capability of the MFCS-I are analyzed.

- In Section 2, the corresponding fault-tolerant control strategy is proposed. Since the d-axis and 0-axis current references are not constant in post-fault operations, two current tracking controllers are developed.

- In Section 3 and 4, the effectiveness of the proposed fault-tolerant scheme is verified on the 52.5 W and the 1.2 kW PMSMs respectively.

4.1 Fault-tolerant potential

In the CFNI and SFNI, the path required by the zero-sequence current under post-fault conditions is provided by the fourth leg. This leg can be constructed by either a pair of DC-bus split capacitors or an auxiliary leg. To switch the circuit configuration from the pre-fault to post-fault condition, a TRIAC is also required. In the MFCS-I, the path required by the zero-sequence current exists, thanks to the inherently connected NP. Therefore, it is reasonable to expect that the MFCS-I has the fault-tolerant potential without using any extra hardware. To realize this possibility, the key point is how to maintain a constant torque output as well as a stable DC-bus voltage under post-fault conditions.

4.1.1 Derivation of post-fault current trajectories

The circuit configuration of the MFCS-I under the post-fault condition (phase-A is open) is shown in figure 4.1. Since the phase-A is disconnected from the power supply, it can not be utilized to generate the rotating magnetic field. In other words, only phase-B and C are available under the post-fault condition. In the following, we are going to find three constraints, which are necessary to realize the fault-tolerant potential for the MFCS-I. For the sake of analysis, the subscript ($\_f$) denotes a variable which is in post-fault conditions. The subscript ($\_n$) denotes a variable which is in healthy conditions.

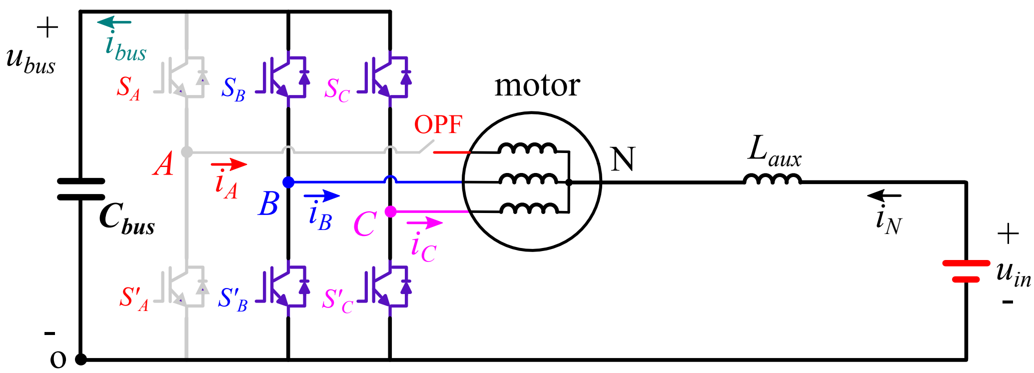

FIGURE 4.1: Circuit configuration of the MFCS-I when phase-A is open.

4.1.1.1 Constraint 1: torque conservation

Generally speaking, the primary objective of fault-tolerant operations in motor drives is to preserve the stable torque output under post-fault conditions. Thus, for a surface-mounted PMSM, the post-fault q-axis current i_{q_f} is desired to be consistent with that (i_{q_n}) in normal condition. Therefore, it yields the first constraint, as

$$i_{q\_f} = i_{q\_n} \tag{4.1}$$

4.1.1.2 Constraint 2: post-fault d-q-0 current relationship

According to Clarke transformation (shown in appendix A), we obtain

$$\begin{bmatrix} i_{\alpha\_f} \\ i_{\beta\_f} \\ i_{0\_f} \end{bmatrix} = \frac{2}{3} \begin{bmatrix} 1 & -\frac{1}{2} & -\frac{1}{2} \\ 0 & \frac{\sqrt{3}}{2} & -\frac{\sqrt{3}}{2} \\ \frac{1}{2} & \frac{1}{2} & \frac{1}{2} \end{bmatrix} \begin{bmatrix} i_{A\_f} \\ i_{B\_f} \\ i_{C\_f} \end{bmatrix} \tag{4.2}$$

where i_α is the α-axis current; i_β is the β-axis current.

Once the OPF occurs, i_{A_f} will be 0 A. By considering this condition, we obtain

$$i_{0\_f} = -i_{\alpha\_f} \tag{4.3}$$

According to the rotation transformation (shown in appendix A) from α-β to d-q coordinates, we further obtain

$$\begin{cases} i_{d\_f} = i_{\alpha\_f} cos\theta_e + i_{\beta\_f} sin\theta_e \\ i_{q\_f} = -i_{\alpha\_f} sin\theta_e + i_{\beta\_f} cos\theta_e \end{cases} \tag{4.4}$$

Substituting (4.3) into (4.4) and eliminating the term of i_{β_f}, the d-q-0 current relationship in the post-fault condition is found to be

$$i_{0\_f} = i_{q\_f} sin\theta_e - i_{d\_f} cos\theta_e \tag{4.5}$$

Therefore, (4.5) is the second constraint, which indicates that the value of i_{0_f} is related to i_{d_f}, i_{q_f} and the position θ_e. In healthy conditions, $i_{d\_n} = 0$. i_{q_n} and i_{0_n} are constant, which are determined by the load and speed of the motor, i.e. the operating power of the motor. If both i_{d_f} and i_{q_f} are maintained to be consistent with i_{d_n} and i_{q_n}[1], obviously, i_{0_f} will be a non-constant value. According to (4.5), it will be a sinusoidal function of θ_e whose period

[1] A common fault-tolerant strategy in the CFNI and SFNI.

is equal to the electrical period. Therefore, the neutral current i_{N_f} under post-fault conditions will also be sinusoidal. In this case, the sinusoidal i_{N_f} indicates that the transient input power $P_{in\_f} = u_{in} i_{N\_f} = -3u_{in} i_{0\_f}$ will also be sinusoidal. For the sinusoidal input power, its average value is null. This implies that the DC-source will be incapable to provide the required power to the motor. Therefore, by setting $i_{d\_f} = i_{d\_n}$ and $i_{q\_f} = i_{q\_n}$, the MFCS-I is impossible to work.

4.1.1.3 Constraint 3: average power conservation

From the healthy to post-fault conditions, the output power of the motor is desired to be invariant because the torque and speed of the motor are expected to be stable. Therefore, in order to maintain the balance between the average input power and output power, the average value of i_{0_f} should meet:

$$\begin{gathered}\overline{P}_{in\_f} = u_{in}\overline{i}_{N\_f} = -3u_{in}\overline{i}_{0\_f} = \frac{P_{mec\_n}}{\eta} = P_{in\_n} = -3u_{in} i_{0\_n} \\ \Downarrow \\ \overline{i}_{0\_f} = i_{0\_n}\end{gathered} \tag{4.6}$$

where the superscript $\overline{x}$ indicates the mean of a variable (x) within one electrical period; the total efficiency η and source-voltage u_{in} are supposed invariable from the healthy to post-fault conditions.

According to (4.6), we know the third constraint, which deduces that the mean of i_{0_f} should be consistent with i_{0_n}.

4.1.1.4 Fault-tolerant d-q-0 current trajectories

Then, by combining the constraints 1 (see (4.1)), 2 (see (4.5)) and 3 (see (4.6)) simultaneously, theoretical i_{d_f}, i_{q_f} and i_{0_f} which can fulfill fault-tolerant operations are proposed as follows:

$$\begin{cases} i_{d\_f} = i_{d\_n} - 2i_{0\_n}cos\theta_e \\ i_{q\_f} = i_{q\_n} \\ i_{0\_f} = i_{q\_n}sin\theta_e - i_{d\_n}cos\theta_e + 2i_{0\_n}cos^2\theta_e \\ \qquad = i_{q\_n}sin\theta_e - i_{d\_n}cos\theta_e + i_{0\_n} + i_{0\_n}cos2\theta_e \end{cases} \tag{4.7}$$

From (4.7), it can be observed that the post-fault currents are associated with their previous states (i_{d_n}, i_{q_n} and i_{0_n}). To be specific, i_{d_f} consists of a DC component (i_{d_n}) and a periodic component ($-2i_{0\_n}cos\theta_e$). i_{q_f} is completely the same as i_{q_n}. i_{0_f} contains a frequency-doubled component ($i_{0\_n}cos2\theta_e$) in addition to a DC component (i_{0_n}) and a periodic component ($i_{q\_n}sin\theta_e - i_{d\_n}cos\theta_e$). By using the inverse Park transformation (amplitude invariant), the post-fault phase-currents can be expressed as:

$$\begin{cases} i_{A\_f} = 0 \\ i_{B\_f} = -2m_0 i_{q\_n} cos\theta_e cos(\theta_e - 2\pi/3) - i_{q\_n} sin(\theta_e - 2\pi/3) \\ \qquad + i_{q\_n}(sin\theta_e + 2m_0 cos^2\theta_e) \\ i_{C\_f} = -2m_0 i_{q\_n} cos\theta_e cos(\theta_e + 2\pi/3) - i_{q\_n} sin(\theta_e + 2\pi/3) \\ \qquad + i_{q\_n}(sin\theta_e + 2m_0 cos^2\theta_e) \end{cases} \tag{4.8}$$

where i_{d_n} is considered as 0 for a surface-mounted PMSM; $m_0 = i_{0\_n}/i_{q\_n}$ is defined as the proportion between i_{0_n} and i_{q_n}.

Furthermore, i_{B_f} and i_{C_f} can be rewritten in the form of Fourier series expansions, as shown below

$$\begin{cases} i_{B\_f} = \dfrac{a_0}{2} + \displaystyle\sum_{k=1}^{2}[a_k cos(k\theta_e) + b_k sin(k\theta_e)] \\ i_{C\_f} = \dfrac{a_0}{2} + \displaystyle\sum_{k=1}^{2}[a_k^{'} cos(k\theta_e) + b_k^{'} sin(k\theta_e)] \\ a_0 = 3m_0 i_{q\_n}, \quad a_1 = \dfrac{\sqrt{3}}{2} i_{q\_n}, \quad a_1^{'} = -\dfrac{\sqrt{3}}{2} i_{q\_n}, \\ a_2 = a_2^{'} = \dfrac{3}{2} m_0 i_{q\_n}, \quad b_1 = b_1^{'} = \dfrac{3}{2} i_{q\_n}, \\ b_2 = -\dfrac{\sqrt{3}}{2} m_0 i_{q\_n}, \quad b_2^{'} = \dfrac{\sqrt{3}}{2} m_0 i_{q\_n} \end{cases} \tag{4.9}$$

Therefore, the RMS of remaining phase-currents under the post-fault condition can be

Table 4.1: d-q-0 currents under post-fault conditions considering different fault locations.

Fault location	i_{d_f}	i_{q_f}	i_{0_f}
Phase A	$-2i_{0\_n}cos\theta_e$	i_{q_n}	$i_{q\_n}sin\theta_e + i_{0\_n}\left[1 + cos(2\theta_e)\right]$
Phase B	$-2i_{0\_n}cos(\theta_e - \frac{2\pi}{3})$	i_{q_n}	$i_{q\_n}sin(\theta_e - \frac{2\pi}{3}) + i_{0\_n}\left[1 + cos[2(\theta_e - \frac{2\pi}{3})]\right]$
Phase C	$-2i_{0\_n}cos(\theta_e + \frac{2\pi}{3})$	i_{q_n}	$i_{q\_n}sin(\theta_e + \frac{2\pi}{3}) + i_{0\_n}\left[1 + cos[2(\theta_e + \frac{2\pi}{3})]\right]$

calculated by:

$$\begin{aligned} I_{RMS\_f} &= \sqrt{\left(\frac{a_0}{2}\right)^2 + \left(\frac{\sqrt{a_1^2+b_1^2}}{\sqrt{2}}\right)^2 + \left(\frac{\sqrt{a_2^2+b_2^2}}{\sqrt{2}}\right)^2} \\ &= \sqrt{\frac{15m_0^2+6}{4}} \cdot i_{q\_n} \end{aligned} \tag{4.10}$$

If an OPF occurs in phase-B or C, the post-fault currents can be derived in the same way. For clarity, all the representations of post-fault currents are summarized in table 4.1.

4.1.2 Analysis of post-fault power conversion process

Theoretical curves of d-q-0 currents and phase currents are illustrated in figure 4.2(c) and (d) where m_0 corresponds to -0.15, -0.25 and -0.45 respectively. It can be observed that i_{d_f} is a cosine function of θ_e. i_{q_f} is a constant in order to maintain the stable torque. i_{0_f} is neither a constant nor a standard sine function. With the decrease of m_0, the unconventional shape of i_{0_f} becomes conspicuous. According to (4.7), the unconventional shape is caused by the frequency-doubled term ($i_{0\_n} cos2\theta_e$). Although the shape of i_{0_f} is special, the mean of i_{0_f} is equal to i_{0_n} over one electrical period in order to guarantee the balance between the average input power and output power. Regarding the phase-currents which are shown in figure 4.2(d), i_{A_f} is exactly 0 A because of the fault. i_{B_f} and i_{C_f} do not present the sinusoidal waveforms with a 60° phase-shift. With the decrease of m_0, the unconventionality of i_{B_f} and i_{C_f} is noticeable.

According to the formulas of post-fault currents, the post-fault current vector ($\boldsymbol{i_{s\_f}}$) can be visualized in $\alpha - \beta - 0$ coordinate. For comparison, the current vector ($\boldsymbol{i_{s\_n}}$) which is in healthy conditions is also presented. Figure 4.2(a) displays these vector trajectories when the proportion of i_{0_n} and i_{q_n} is equal to -0.45 ($m_0 = -0.45$). Besides, their projections on α-β plane are further presented, which are referred to as $\boldsymbol{i_{s\_fpj}}$ and $\boldsymbol{i_{s\_npj}}$, respectively. Under the normal condition, the trajectory of $\boldsymbol{i_{s\_n}}$ is a standard circle. Its 0-axis component i_{0_n} is equal to -0.45i_{q_n}. Moreover, the trajectory of $\boldsymbol{i_{s\_npj}}$ is also circular, which is exactly the same as that of the current vector in a standard drive (without zero-sequence current components). Interestingly, under the fault-tolerant condition, both $\boldsymbol{i_{s\_f}}$ and $\boldsymbol{i_{s\_fpj}}$ are no longer circular. They present a heart-shaped trajectory. Concretely, the evolution of $\boldsymbol{i_{s\_fpj}}$ with respect to m_0 is shown in figure 4.2(b). It can be observed that the heart-shaped feature becomes more and more distinct with the decrease of m_0. In other words, if the zero-sequence is bigger, the heart-shaped feature is more apparent.

Normally, the mechanical power (output power) P_{mec_f} of the motor needs to be maintained

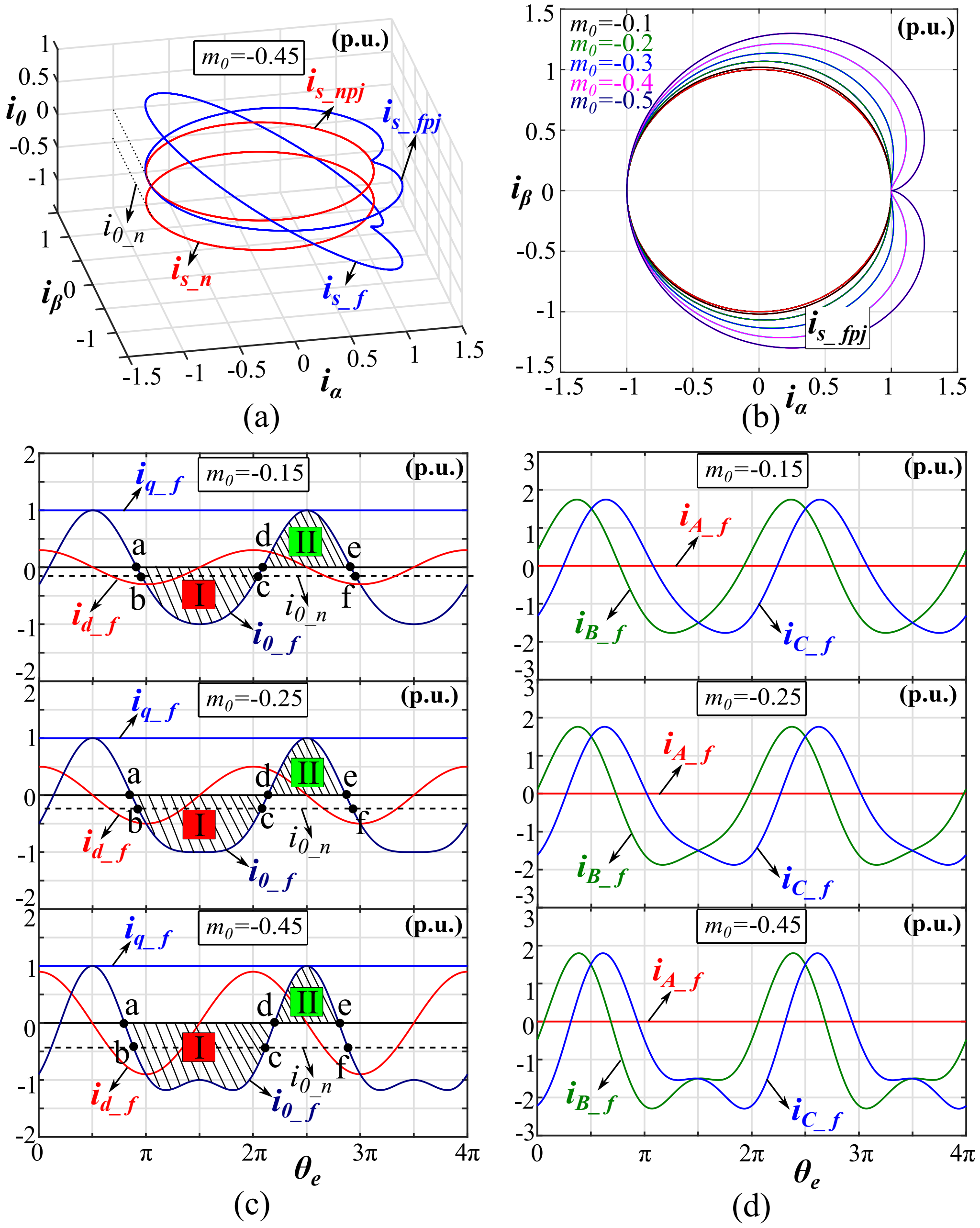

FIGURE 4.2: Theoretical currents in the post-fault condition (phase-A is open). (a) Space current vectors and their projections on α-β plane under normal and fault-tolerant conditions. (b) Trend of $\boldsymbol{i_{s\_fpj}}$ with respect to m_0. (c) d-q-0 currents under fault-tolerant conditions for different m_0. (d) Phase-currents under fault-tolerant conditions for different m_0.

when the fault occurs, i.e. the motor speed and torque should be preserved. However, it is obvious that the zero-sequence current i_{0_f} is not a constant, as shown in figure 4.2(c). The non-constant i_{0_f} implies that the input power P_{in_f} of the system is variable in one electrical period. In other words, the mismatch between the transient input power and output power is inevitable. According to energy conservation law, the mismatched energy will be absorbed or released by the passive components in the system. Therefore, in the post-fault condition, the DC-bus capacitor will function as an energy buffer to balance the mismatched energy between the transient input power of the drive system and the mechanical output power of the motor. To explicitly elaborate the power conversion process in the post-fault condition, i_{0_f} is divided into two areas ('I' and 'II' marked in figure 4.2(c)) to discuss. In area 'I', P_{in_f} is positive because of the negative i_{0_f} (i.e. the positive i_{N_f}). Thus, the DC-source provides power to the drive system. From the operating point 'a' to 'b', P_{in_f} is lower than the power required by the motor because the absolute value of i_{0_f} is smaller than that of i_{0_n}. Thus, the DC-bus capacitor has to fill in the power shortage so as to support the motor holding the constant mechanical power. As a result, u_{bus_f} will decrease in this period. At the operating point 'b', i_{0_f} is equal to i_{0_n}. In this case, the transient input power is balanced with the transient output power. From the operating point 'b' to 'c', P_{in_f} is larger than the power required by the motor because the absolute value of i_{0_f} is bigger than that of i_{0_n}. Thus, the DC-bus capacitor has to absorb the energy which is not consumed by the motor. As a result, u_{bus_f} will increase in this process. At the operating point 'c', u_{bus_f} will reach the peak. From the operating point 'c' to 'd, P_{in_f} is lower than the power required by the motor again. Thus, u_{bus_f} will decrease once more. In turn, P_{in_f} is negative in area 'II' because of the positive i_{0_f} (i.e. the negative i_{N_f}). This implies that the DC-source begins to absorb power from the drive system. In this case, the DC-bus capacitor not only powers the motor but also charges the DC-source. As a result, u_{bus_f} will continue decreasing. At the operating point 'f', u_{bus_f} will reach the valley. In steady states, the power conversion process is periodic. The oscillation of u_{bus_f} is related to the integral of i_{0_f}, i.e. the amplitude and frequency of i_{0_f}.

In figure 4.2(c), the energy ($\Delta E_{\_f}$) provided by the DC-source (u_{in}) from point 'b' to 'c' can be calculated by

$$\Delta E_{\_f} = \int_b^c P_{in\_f}(t)dt = 3u_{in} \int_b^c i_{0\_f}(t)dt \tag{4.11}$$

According to the above analysis, the energy ($\Delta E_{\_f}$) will be stored in the DC-bus capacitor. Therefore, we obtain

$$\begin{gathered}\Delta E_{\_f} = \frac{1}{2}C_{bus}u^2_{bus\_fmax} - \frac{1}{2}C_{bus}u^2_{bus\_fmin} \\ \Downarrow \\ \frac{2\Delta E_{\_f}}{C_{bus}} = u^2_{bus\_fmax} - u^2_{bus\_min} = (u_{bus\_fmax} + u_{bus\_fmin})\underbrace{(u_{bus\_fmax} - u_{bus\_fmin})}_{\Delta u_{bus}}\end{gathered} \tag{4.12}$$

where u_{bus_fmax} denotes the peak value of u_{bus}; u_{bus_fmin} denotes the valley value of u_{bus}; Δu_{bus} denotes the DC-bus voltage ripple.

If the average value ($\overline{u}_{bus\_f}$) of the DC-bus voltage is regulated at the voltage reference ($\overline{u}^*_{bus}$), we can consider that $(u_{bus\_fmax} + u_{bus\_fmin})/2 \approx u^*_{bus}$. By taking this into (4.12), the DC-bus voltage ripple can be calculate by

$$\Delta u_{bus} \approx \frac{\Delta E_{\_f}}{C_{bus} u^*_{bus}} \tag{4.13}$$

Then, by substituting (4.11) into (4.13), the DC-bus voltage ripple can be expressed as

$$\Delta u_{bus} \approx \frac{3u_{in} i_{q\_n}}{2\pi C_{bus} u^*_{bus} f_{ele}} \left(m_0(\pi - 2arcsin\frac{M}{4m_0}) + \frac{\sqrt{2}}{8m_0}\sqrt{4m_0^2 + M}(4 + M) \right) \tag{4.14}$$

where $M = \sqrt{8m_0^2 + 1} - 1$; $f_{ele} = \frac{\omega_e}{2\pi}$ is the electrical frequency of the motor.

According to (4.14), we can know that Δu_{bus} decreases with the decrease of i_{q_n} and the increase of f_{ele}. In other words, Δu_{bus} will be smaller at high-speed and in low-load conditions.

4.1.3 Analysis of post-fault output capability

The output capability of a drive system in post-fault conditions is restricted to voltage and current limits. In healthy conditions, the DC-bus voltage of the MFCS-I can be raised to twice the source voltage thanks to the equivalent boost function. The line-to-line voltage of the motor is limited by the leg-to-leg voltage of the inverter, hence $\pm u_{bus}$. Although the DC-bus voltage will oscillate with the neutral current based on the analysis of the post-fault power conversion process, its mean value can still be maintained. The oscillation amplitude is relatively small when a sufficient DC-bus capacitor is employed. Therefore, it can be supposed that the situation of remaining phases of the motor does not change before and after the fault. In this case, the voltage limit for each motor phase is the same. Actually, this scenario is similar to the CFNI where the motor's NP is connected to the midpoint of the DC-bus.

In terms of the torque output capability in post-fault conditions, it is reasonable to premise that the inverter is designed to withstand the rated phase-current RMS of healthy conditions. When one of motor phases is disconnected, the torque degradation is inevitable in case of the remaining phase-currents violate the current limit.

By using the inverse Park transformation (amplitude invariant), the phase-currents under healthy conditions can be formulated by:

$$\begin{cases} i_{A\_n} = i_{d\_n} cos(\theta_e) - i_{q\_n} sin(\theta_e) + m_0 i_{q\_n} \\ i_{B\_n} = i_{d\_n} cos(\theta_e - 2\pi/3) - i_{q\_n} sin(\theta_e - 2\pi/3) + m_0 i_{q\_n} \\ i_{C\_n} = i_{d\_n} cos(\theta_e + 2\pi/3) - i_{q\_n} sin(\theta_e + 2\pi/3) + m_0 i_{q\_n} \end{cases} \tag{4.15}$$

Furthermore, the phase-current RMS under healthy conditions is thus calculated as:

$$\begin{aligned} I_{RMS\_n} &= \sqrt{\left(\frac{\sqrt{i_{d\_n}^2 + i_{q\_n}^2}}{\sqrt{2}}\right)^2 + (m_0 i_{q\_n})^2} \\ &= \sqrt{\left(\frac{1}{2} + m_0^2\right)} \cdot i_{q\_n} \end{aligned} \tag{4.16}$$

where $i_{d\_n} = 0$ for a surface-mounted PMSM.

In order to quantify the post-fault torque output capability, the current overrating ratio (m_i) is defined. It can be calculated by combining (4.10) with (4.16), as

$$m_i = \frac{I_{RMS\_n}}{I_{RMS\_f}} = \sqrt{\frac{4m_0^2 + 2}{15m_0^2 + 4}} = \sqrt{\frac{4\left(\dfrac{\Phi_f p \omega_m}{2u_{in}\eta}\right)^2 + 2}{15\left(\dfrac{\Phi_f p \omega_m}{2u_{in}\eta}\right)^2 + 4}} \tag{4.17}$$

Theoretically, m_i denotes the proportion between the phase-current RMS of healthy conditions and that of post-fault conditions. In other words, m_i is related to how much equivalent torque the motor can obtain when the post-fault current RMS reaches the current limit. The evolution of m_i with respect to the motor speed and system efficiency is displayed in figure 4.3 where Φ_f, p and u_{in} correspond to the parameters of the 1.2 kW PMSM. It can be

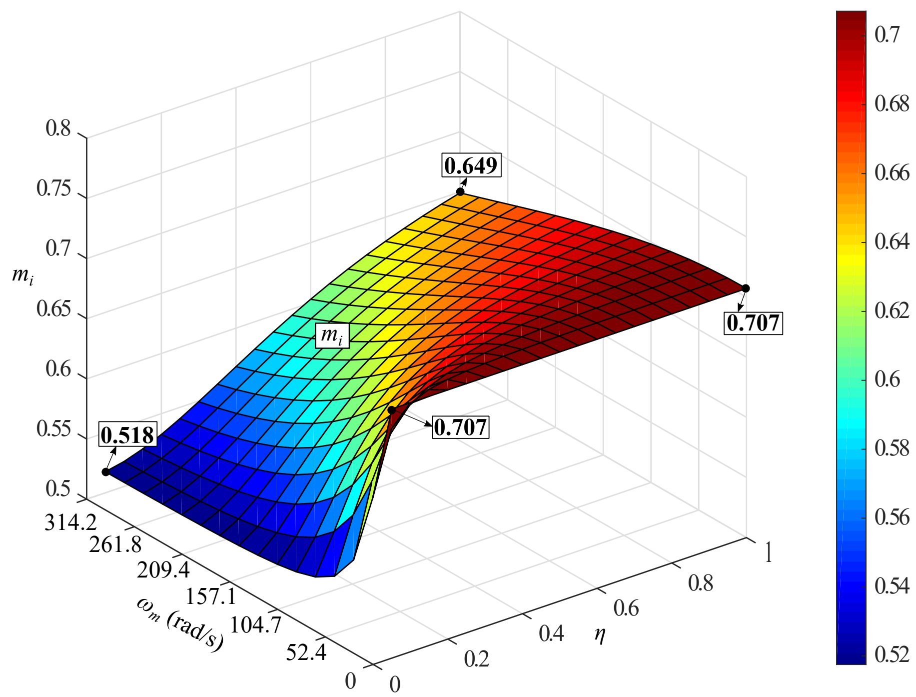

FIGURE 4.3: Current overrating ratio (m_i) with respect to motor speed and system efficiency.

observed that the range of m_i is between 0.518 and 0.707 with the change of the motor speed and the system efficiency. m_i increases with the decrease of ω_m and increase of η. Theoretically, the motor can output 0.518 to 0.707 of the nominal torque in the post-fault condition.

4.1.4 Post-fault equivalent circuit

When the OPF occurs in phase-A, the circuit structure of the MFCS-I is changed. The leg-A of the inverter is isolated from the motor. Thus, the control DOF of leg-A (i.e. the duty cycle α_A) is useless to the whole drive system under the post-fault condition. Essentially, the motor has been degenerated into a two-phase motor.

If we consider the MFCS-I as a two-phase system in post-fault conditions, the average model and equivalent circuit should be rebuilt. According to the time-averaging equivalent modeling approach and Kirchhoff's law, the mathematical model of the MFCS-I under the OPF can be built as

$$\begin{bmatrix} u_{BO} \\ u_{CO} \end{bmatrix} = \begin{bmatrix} \alpha_B \\ \alpha_C \end{bmatrix} u_{bus} = \begin{bmatrix} Ri_B + L_{BB}\frac{\mathrm{d}i_B}{\mathrm{d}t} + M_{BC}\frac{\mathrm{d}i_C}{\mathrm{d}t} + e_B \\ Ri_C + L_{CC}\frac{\mathrm{d}i_C}{\mathrm{d}t} + M_{CB}\frac{\mathrm{d}i_B}{\mathrm{d}t} + e_C \end{bmatrix} + \begin{bmatrix} -L_{aux}\frac{\mathrm{d}i_N}{\mathrm{d}t} + u_{in} \\ -L_{aux}\frac{\mathrm{d}i_N}{\mathrm{d}t} + u_{in} \end{bmatrix} \tag{4.18a}$$

$$\begin{cases} i_B + i_C + i_N = 0 \\ i_{bus} = C_{bus}\dfrac{\mathrm{d}u_{bus}}{\mathrm{d}t} = -\alpha_B i_B - \alpha_C i_C \end{cases} \tag{4.18b}$$

Then, by adding the two equations of (4.18a) and combining with (4.18b), the zero-sequence voltage equation can be formulated as

$$\begin{aligned} \alpha_{h\_f} u_{bus} &= -\frac{R}{2} i_N - \left(\frac{L_{BB} + M_{BC}}{2} + L_{aux}\right)\frac{\mathrm{d}i_N}{\mathrm{d}t} - \frac{e_A}{2} + u_{in} \\ &= -\frac{R}{2} i_N - \underbrace{\left(\frac{L_\sigma}{2} + \frac{L_\Sigma}{4} + L_{aux}\right)}_{L_{E\_f}}\frac{\mathrm{d}i_N}{\mathrm{d}t} - \frac{e_A}{2} + u_{in} \end{aligned} \tag{4.19}$$

where

- $\alpha_{h\_f} = \frac{\alpha_B + \alpha_C}{2}$ is the mean duty cycle in post-fault conditions, whose range is still (0-1).
- L_{E_f} denotes the equivalent inductance.
- $e_A = -\Phi_f \omega_e sin\theta_e$ is the back-EMF of phase-A.

By comparing (4.19) with (2.17b), we can find that the zero-sequence voltage equation has changed in the post-fault condition. It is not completely consistent with the average model of a common DC/DC boost converter. To be specific, it contains an additional term which is equal to the back-EMF ($-e_A/2$) of phase-A. Meanwhile, the equivalent zero-sequence inductance (L_{E_f}) includes not only the leakage inductance (L_σ) of the motor and the auxiliary inductance (L_{aux}), but also the average inductance L_Σ of the motor. Because the range of α_{h_f} is still between 0 and 1, we can still use an equivalent chopper to reflect the physical significance of α_{h_f}. Therefore, according to (4.19), the equivalent circuit of the MFCS-I in the post-fault condition (phase-A is open) can be further built. For comparison, the zero-sequence circuits of the MFCS-I in healthy and post-fault conditions are illustrated in figure 4.4.

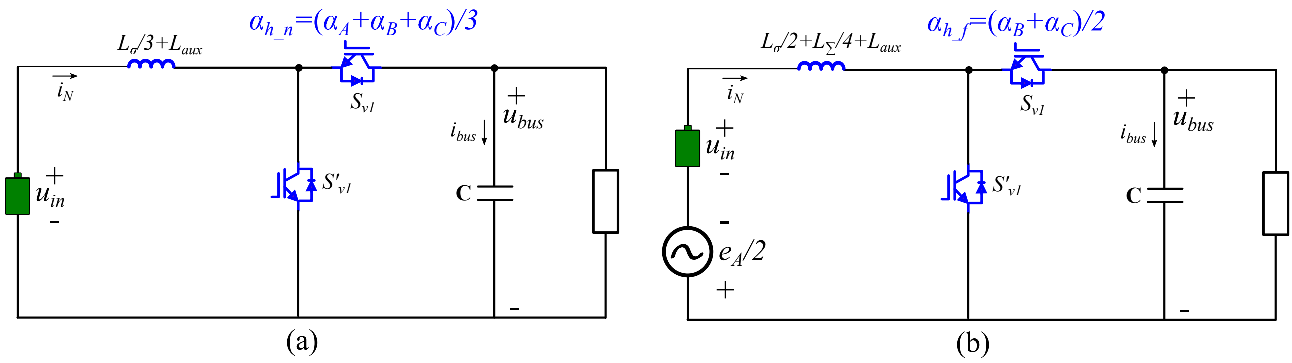

FIGURE 4.4: Zero-sequence equivalent circuits. (a) In healthy conditions. (b) In the post-fault condition (phase-A is open).

From figure 4.4(b), it can be seen that the MFCS-I in the post-fault condition can be approximated to a special boost converter where the back-EMF ($e_A/2$) of phase-A is seen as a disturbance term to the input voltage u_{in}. The amplitude of this disturbance is related to the motor speed. According to the analysis of post-fault power conversion process, we know that the DC-bus voltage is unable to be maintained at a constant value since i_{0_f} or i_{N_f} is not constant. In other words, if we choose to preserve a constant torque output of the motor preferentially, we can not maintain a stable voltage on the DC-bus. Obviously, the stable torque output should be guaranteed in priority in the post-fault operations.

4.2 Fault-tolerant control strategy

4.2.1 Uniform control framework

For the CFNI and SFNI, the control framework is usually changed in post-fault conditions due to the reconfiguration of motor's NP. In the CFNI, the NP of the motor is connected to the midpoint of the DC-bus when an OPF occurs. In the SFNI, it is connected with the fourth leg after an OPF. Since the NP of the motor is connected, the relationship between the output voltage of the inverter and the applied voltage on motor phases has changed. Therefore, both the CFNI and SFNI require to add some modifications in the modulation, transformation matrices or the whole control architecture, which are complicated. For example, in [72], the authors proposed a feed forward compensation strategy for the SFNI to compensate the error between the d-q voltage provided by the inverter and the d-q voltage applied to the motor. This compensation strategy can still guarantee a constant d-q voltage so that the current controller can avoid the tracking of sinusoidal components. Therefore, the PI controller can still be used. In [41], the authors do not compensate the voltage error caused by the unbalanced condition. In turn, they proposed a novel transformation matrix so that the position-dependent sinusoidal current commands are transformed to DC variables. Thus, the PI current controller can still be used. In [47], the authors proposed an analytical model for PMSMs, which are in post-fault conditions. By using the model, a fault-tolerant FOC for the CFNI and SFNI is achieved.

For MFCS-I, the situation of the NP has not changed from pre-fault to post-fault conditions. Therefore, the concept of a virtual healthy system can be adopted. In this way, the fault-tolerant control can be fulfilled by simply replacing the current references $i^*_{d\_n}$, $i^*_{q\_n}$ and $i^*_{0\_n}$ with the fault-tolerant current references $i^*_{d\_f}$, $i^*_{q\_f}$ and $i^*_{0\_f}$. In the virtual healthy system, the control objective for phase-A is to actively force i_{A_f} to be 0 A even if this goal is naturally achieved.

Since the post-fault current references are associated with those in healthy conditions, it is necessary to obtain the value of $i^*_{0\_n}$. In healthy conditions, the DC-bus voltage is stable. Therefore, the power conservation equation can be derived as:

$$P_{in} = u_{in} i_N = -3 u_{in} i_0 = \frac{P_{mec}}{\eta} = \frac{\omega_m T_e}{\eta} \tag{4.20}$$

According to (4.20), the zero-sequence current reference $i^*_{0\_n}$ can be calculated by

$$i^*_{0\_n} = \frac{-\Phi_f p \omega_m}{2 u_{in} \eta} i^*_{q\_n} \tag{4.21}$$

Since the drive system in the post-fault condition can be seen as a virtual healthy system with the control objective of forcing $i_{A\_f} = 0$, a uniform control framework is introduced, as shown in figure 4.5. The d-axis current reference $i^*_{d\_n}$ is set as 0 A for a surface-mounted PMSM without flux weakening control. The q-axis current reference $i^*_{q\_n}$ is guided by the speed controller. The zero-sequence current reference $i^*_{0\_n}$ can be calculated by (4.21) directly. However, in (4.21), the real-time efficiency η is hard to be known accurately in practice. If we adopt an approximated value of η, we will obtain an inaccurate $i^*_{0\_n}$. The inaccuracy in $i^*_{0\_n}$ may result in the under-voltage or over-voltage hazard on the DC-bus over a large time scale. Therefore, to maintain a stable DC-bus voltage, a PI controller is used to regulate the mean of the DC-bus voltage. The control parameters of the PI controller can be designed in the way of a common DC/DC boost converter. Based on the analysis of post-fault power conversion process, the oscillation period of the DC-bus voltage is equal to the electrical period. Over one electrical period, the mean of the DC-bus voltage is invariable. Therefore, a low-pass filter (LPF) is required to obtain the actual mean of the DC-bus voltage (u_{bus_filter}). The cutoff frequency of the LPF should be lower than the fundamental frequency of the motor. Finally, $i^*_{0\_n}$ is determined by the combination of the direct calculation (4.21) and the DC-bus voltage controller.

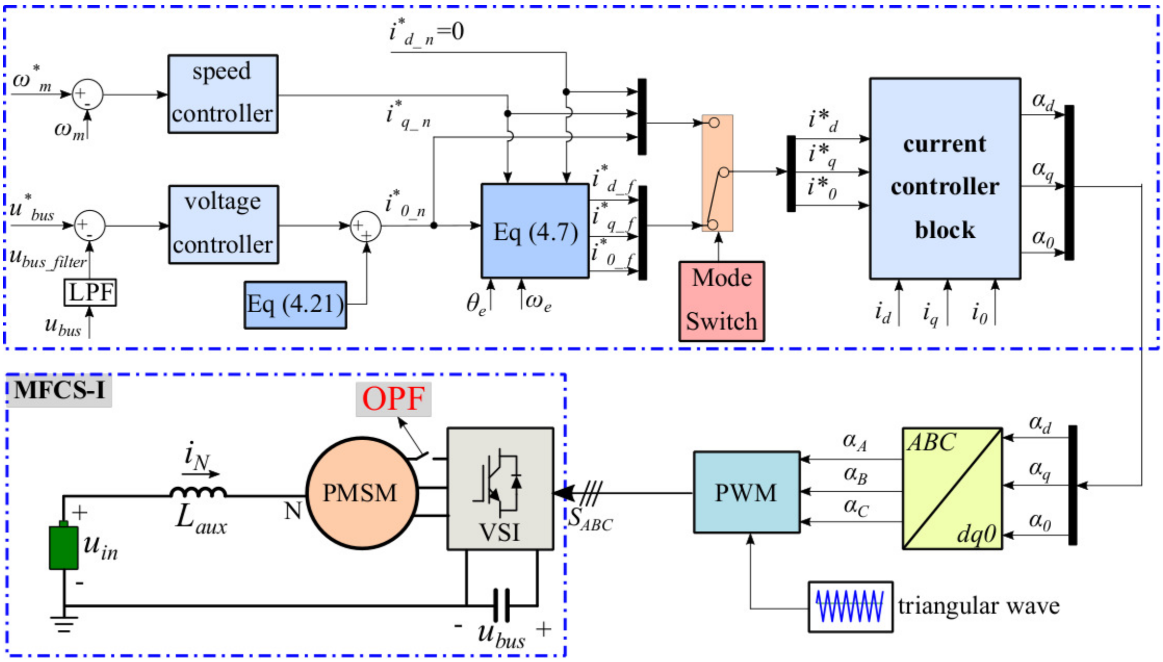

FIGURE 4.5: Uniform control framework.

In the healthy mode, $i^*_{d\_n}$, $i^*_{q\_n}$ and $i^*_{0\_n}$ are directly fed into the current controller. In the post-fault mode, $i^*_{d\_f}$, $i^*_{q\_f}$ and $i^*_{0\_f}$ calculated by (4.7) are used as the references for the current controllers. According to figure 4.2, we know that $i^*_{d\_f}$ and $i^*_{0\_f}$ are non-constant. In order to track this kind of current references, a current controller with high bandwidth, fast response and optimum tracking ability is necessary. To this end, we will develop two controllers in the following.

4.2.2 Deadbeat predictive current tracking controller

Model predictive control (MPC) is a promising controller for motor drives due to its merits of simplicity, fast response and multi-variable control flexibility[98]. The basic principle of MPC is to predict the behavior of the controlled system using its model in the future. Usually, the controller uses this information to choose the optimal actuator state based on a predefined optimization criterion[99]. MPC can be classified into two categories: continuous control set (CCS) MPC[100] and finite control set (FCS) MPC[101][102]. FCS-MPC only considers a finite number of switching states thus directly gives the optimal switching state. A salient drawback of the FCS-MPC is that it needs a high sampling frequency to guarantee the accurate tracking performance thus requires a high computational burden on the microprocessor. CCS-MPC requires a modulator in the control system. When the choice of the voltage vector is made in order to return the error to 0 at the end of the sample period, the CCS-MPC is often called as deadbeat controller.

In order to verify the proposed fault-tolerant scheme of the MFCS-I quickly and efficiently, the deadbeat predictive controller is adopted to track the time-varying post-fault current references since there is no control parameters needed to be tuned. Because the sampling frequency is much higher than the fundamental frequency, the DC-bus voltage and motor speed measurable by voltage and speed sensors are supposed to be invariable within one sampling period. By applying Euler forward approximation to the voltage model presented (3.3b), the d-q-0 currents at the $(k+1)^{th}$ sampling period can be expressed by

$$\begin{aligned}\begin{bmatrix} i_d(k+1) \\ i_q(k+1) \\ i_0(k+1) \end{bmatrix} = & \underbrace{\begin{bmatrix} 1-\dfrac{RT_s}{L_d} & \dfrac{\omega_e(k)L_qT_s}{L_d} & 0 \\ -\dfrac{\omega_e(k)L_dT_s}{L_q} & 1-\dfrac{RT_s}{L_q} & 0 \\ 0 & 0 & 1-\dfrac{RT_s}{3L_E} \end{bmatrix}}_{\boldsymbol{A}} \begin{bmatrix} i_d(k) \\ i_q(k) \\ i_0(k) \end{bmatrix} \\ & + \underbrace{\begin{bmatrix} \dfrac{T_s u_{bus}(k)}{L_d} & 0 & 0 \\ 0 & \dfrac{T_s u_{bus}(k)}{L_q} & 0 \\ 0 & 0 & \dfrac{T_s u_{bus}(k)}{3L_E} \end{bmatrix}}_{\boldsymbol{B}} \begin{bmatrix} \alpha_d(k) \\ \alpha_q(k) \\ \alpha_0(k) \end{bmatrix} + \underbrace{\begin{bmatrix} 0 \\ -\dfrac{\omega_e(k)\Phi_m T_s}{L_q} \\ -\dfrac{u_{in}T_s}{3L_E} \end{bmatrix}}_{\boldsymbol{C}} \end{aligned} \tag{4.22}$$

where $\boldsymbol{A}$, $\boldsymbol{B}$ and $\boldsymbol{C}$ are the matrices of the discrete equation; T_s is the sampling period.

In order to eliminate current error at the $(k+1)^{th}$ sampling interval, the d-q-0 currents at the $(k+1)^{th}$ sampling period should follow

$$\begin{cases} i_d(k+1) = i_d^* \\ i_q(k+1) = i_q^* \\ i_0(k+1) = i_0^* \end{cases} \tag{4.23}$$

By replacing (4.23) into (4.22), the required d-q-0 duty cycles at the k^{th} sampling period can be calculated by

$$\begin{bmatrix} \alpha_d(k) \\ \alpha_q(k) \\ \alpha_0(k) \end{bmatrix} = \boldsymbol{B}^{-1} \left(\begin{bmatrix} i_d^* \\ i_q^* \\ i_0^* \end{bmatrix} - \boldsymbol{A} \begin{bmatrix} i_d(k) \\ i_q(k) \\ i_0(k) \end{bmatrix} - \boldsymbol{C} \right) \tag{4.24}$$

Since the deadbeat current controller is completely constructed by the mathematical model of the PMSM, no tuning is required. However, it is sensitive to parameter variations. The steady errors caused by the parameter variations can usually be mitigated through online parameter identification[103].

4.2.3 Differential flatness-based current tracking controller

The property of differential flatness allows an alternate representation of a system where the state and input variables can be directly expressed by the flat output and a finite number of its derivatives[104]. With the differential flatness, state feedback can be chosen in such a way that the closed-loop dynamic behavior is linear. Therefore, the differential flatness-based control is appropriate for trajectory tracking control and has been used in motor drives[105][106].

A differential flatness-based current controller is also proposed for post-fault current tracking. The DC-bus voltage and motor speed are still supposed to be invariable within one sampling period. The output $\mathbf{y} = [y_1, y_2, y_3]^T$, control variable $\mathbf{u} = [u_1, u_2, u_3]^T$ and state variable $\mathbf{x} = [x_1, x_2, x_3]^T$ are respectively chosen as:

$$\mathbf{y} = \begin{bmatrix} i_d \\ i_q \\ i_0 \end{bmatrix}, \qquad \mathbf{u} = \begin{bmatrix} \alpha_d \\ \alpha_q \\ \alpha_0 \end{bmatrix}, \qquad \mathbf{x} = \begin{bmatrix} i_d \\ i_q \\ i_0 \end{bmatrix} \tag{4.25}$$

Thus, according to the model presented in (3.3b), $\mathbf{u}$ can be expressed by:

$$\begin{cases} \alpha_d = \dfrac{1}{u_{bus}}(Ry_1 + L_d\dot{y}_1 - \omega_e L_q y_2) = f_1(y_1, \dot{y}_1, y_2) \\ \alpha_q = \dfrac{1}{u_{bus}}(Ry_2 + L_q\dot{y}_2 + \omega_e(L_d y_1 + \Phi_m)) = f_2(y_2, \dot{y}_2, y_1) \\ \alpha_0 = \dfrac{1}{u_{bus}}(Ry_3 + 3L_E\dot{y}_3 + u_{in}) = f_3(y_3, \dot{y}_3) \end{cases} \tag{4.26}$$

It needs to note that, in the post-fault condition, we do not utilize the equivalent DC/DC boost function to regulate the real-time DC-bus voltage. We only control the 0-axis current.

In this case, it is obvious that both $\mathbf{u}$ and $\mathbf{x}$ can be represented by the output $\mathbf{y}$ and its first-order derivative. Therefore, the system can be considered as a flat system. Then, to track the desired current references so that the tracking errors ($e_1 = y_1 - y_{1ref}, e_2 = y_2 - y_{2ref}, e_3 = y_3 - y_{3ref}$) asymptotically vanish, feedback control laws are given as follows:

$$\begin{cases} (\dot{y}_1 - \dot{y}_{1ref}) + K_{d1}(y_1 - y_{1ref}) + K_{d2}\int (y_1 - y_{1ref})dt = 0 \\ (\dot{y}_2 - \dot{y}_{2ref}) + K_{q1}(y_2 - y_{2ref}) + K_{q2}\int (y_2 - y_{2ref})dt = 0 \\ (\dot{y}_3 - \dot{y}_{3ref}) + K_{01}(y_3 - y_{3ref}) + K_{02}\int (y_3 - y_{3ref})dt = 0 \end{cases} \tag{4.27}$$

where $K_{d1} = 2\zeta_1\omega_1$, $K_{d2} = \omega_1^2$, $K_{q1} = 2\zeta_2\omega_2$, $K_{q2} = \omega_2^2$, $K_{01} = 2\zeta_3\omega_3$ and $K_{02} = \omega_3^2$ can be designed according to the following characteristic polynomials:

$$\begin{cases} \ddot{e}_1 + 2\zeta_1\omega_1\dot{e}_1 + \omega_1^2 e_1 = 0 \\ \ddot{e}_2 + 2\zeta_2\omega_2\dot{e}_2 + \omega_2^2 e_2 = 0 \\ \ddot{e}_3 + 2\zeta_3\omega_3\dot{e}_3 + \omega_3^2 e_3 = 0 \end{cases} \tag{4.28}$$

where ζ_1, ω_1, ζ_2, ω_2, ζ_3, ω_3 are the desired dominant damping ratios and natural frequencies.

Therefore, we obtain:

$$\begin{cases} \dot{y}_1 = \dot{y}_{1ref} + K_{d1}(y_1 - y_{1ref}) + K_{d2}\int (y_1 - y_{1ref})dt \\ \dot{y}_2 = \dot{y}_{2ref} + K_{q1}(y_2 - y_{2ref}) + K_{q2}\int (y_2 - y_{2ref})dt \\ \dot{y}_3 = \dot{y}_{3ref} + K_{01}(y_1 - y_{3ref}) + K_{02}\int (y_3 - y_{3ref})dt \end{cases} \tag{4.29}$$

Substituting (4.29) into (4.26), it is clear that the closed-loop system is asymptotically stable when $K_{d1}, K_{d2} > 0$, $K_{q1}, K_{q2} > 0$ and $K_{01}, K_{02} > 0$. Once the flat output is stabilized, the whole system will be exponentially stable because the state variable is completely expressed in the form of the flat output.

4.3 Implementation on the 52.5 W PMSM

Simulations and experiments are firstly implemented on the 52.5 W PMSM to verify the effectiveness of the proposed fault-tolerant scheme. The parameters of the 52.5 W PMSM have been presented in table 2.1. In the following test, the DC-source voltage is 15 V and the DC-bus voltage is regulated at 30 V. The deadbeat predictive current controller is used to track the current references in both healthy and fault-tolerant conditions.

4.3.1 Simulation results

Figure 4.6 depicts a fault-tolerant transition process of the 52.5 W PMSM based MFCS-I. In the healthy condition, the motor is operated at 1000 rpm with a 25 mN·m load. The

DC-bus voltage u_{bus} is boosted at 30 V stably thanks to the equivalent boost function. The phase-currents (i_A, i_B and i_C) are sinusoidal. The torque ripple is around 15 mN·m. At 0.6 s, an OPF occurs in phase-A, which results in $i_A = 0$ A instantly. From 0.6 s to 0.7 s, the fault-tolerant control strategy is not triggered. Therefore, it can be seen that i_B and i_C are distorted during this period. At the same time, the torque ripples increase to 80 mN·m. In addition to the big torque ripples, the DC-bus voltage (u_{bus}) can no longer be maintained stable. It begins to oscillate with a 4 V ripple.

At 0.7 s, the fault-tolerant control strategy is engaged. Thus, it can be observed that the torque performance can be well preserved. In steady states, the torque ripples recover to the same value (16 mN·m) with that in the healthy operation. Meanwhile, we can see that the shapes of i_B and i_C are similar with the theoretical analysis presented in figure 4.2(d), corresponding to the second case where $m_0 = -0.25$.

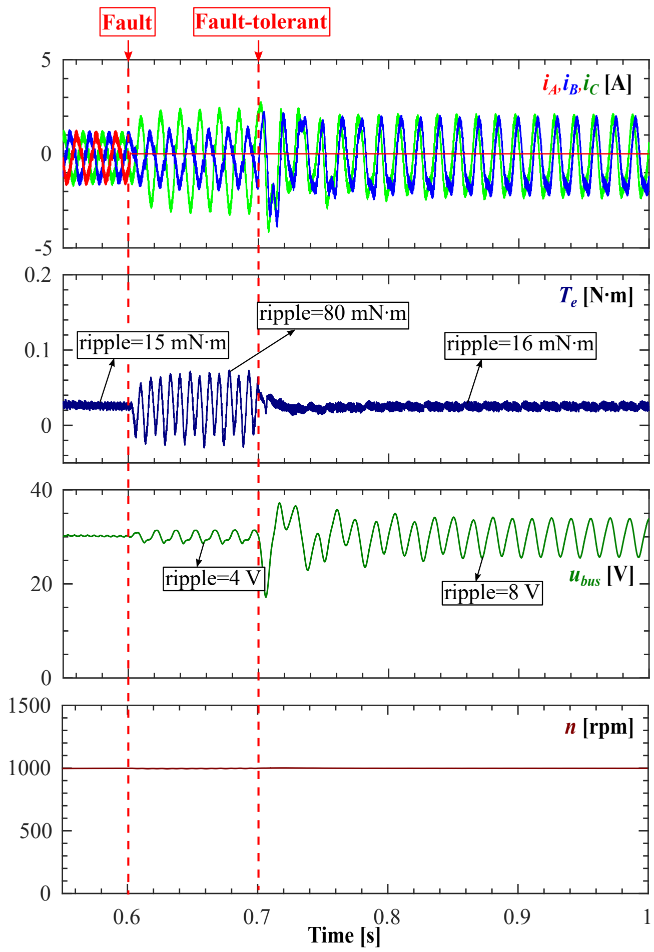

FIGURE 4.6: Simulation results of a fault-tolerant transition of the 52.5 W PMSM based MFCS-I when the motor is operated under 1000 rpm with a 25 mN·m load.

Concerning the DC-bus voltage, the ripple of u_{bus} is around 8 V in the fault-tolerant condition, which is even larger than that in the faulty case where the fault-tolerant control is not triggered. In fact, this phenomenon can be expected and is reasonable. As we emphasized in the analysis of post-fault power conversion process, the zero-sequence current i_{0_f} will be non-constant in fault-tolerant conditions. This implies that the transient input power provided by the DC-source is non-constant in fault-tolerant conditions. However, the mean of i_{0_f} is equal to i_{0_n}. I.e. the average input power is still constant. In order to balance the mismatch between the transient input power and the output power of the motor, the DC-bus capacitor will become an energy buffer. Therefore, u_{bus} oscillates regularly with the zero-sequence current i_{0_f} within one electrical period. The oscillation amplitude is determined by the power of the motor. However, the mean of u_{bus} can be still maintained at 30 V.

In order to check the tracking performance of the deadbeat predictive current controller, the current references and actual currents under the fault-tolerant condition are detailed in figure 4.7. Obviously, the shapes of the actual i_B and i_C are identical with their references. This indicates that the deadbeat predictive current controller shows a remarkable performance in tracking a changeful trajectory.

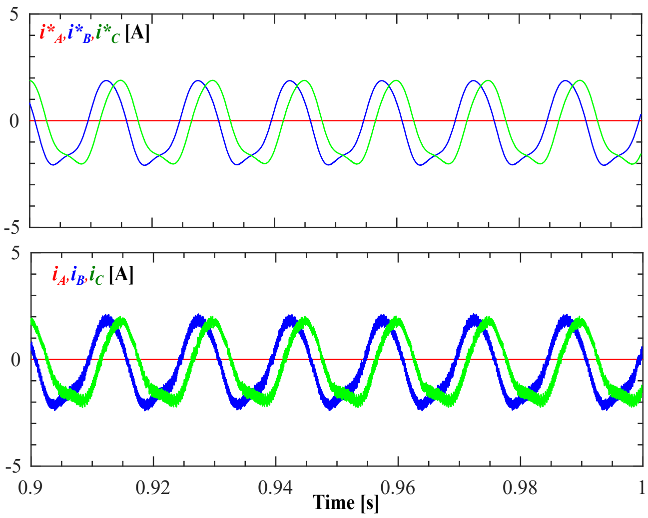

FIGURE 4.7: Comparison of the phase-current references and actual phase-currents under the fault-tolerant mode in the 52.5 W PMSM based MFCS-I.

Based on above simulation results, the feasibility of the MFCS-I to tolerate an OPF is validated. In conclusion, it is able to maintain a stable torque and a stable average DC-bus voltage by the proposed current trajectory.

4.3.2 Experimental results

Since the feasibility of fault-tolerant operations is verified by simulations, experimental implementations are further carried out on the real 52.5 W PMSM based MFCS-I test-bench. To create an OPF, we use a circuit interrupter which is connected in series with phase-A.

4.3.2.1 Fault-tolerant transition performance without load

The experimental results of a fault-tolerant transition process is shown in figure 4.8 where the motor is operated at 2000 rpm without load. Only the frictional torque is applied on the shaft. First, under the healthy operation, the motor speed (n) is regulated at 2000 rpm stably. The torque ripple is about 10 mN·m. The DC-bus voltage (u_{bus}) is boosted at 30 V. Meanwhile, the d-axis current (i_{d_n}) is 0 A and the q-axis current (i_{q_n}) is 0.58 A. The zero-sequence current and neutral current (i_{0_n} and i_{N_n}) are respectively -0.15 A and 0.45 A. Roughly speaking, all the electrical and mechanical states are stable in the healthy condition. In this case, the zero-sequence current proportion (m_0) can be calculated as -0.26.

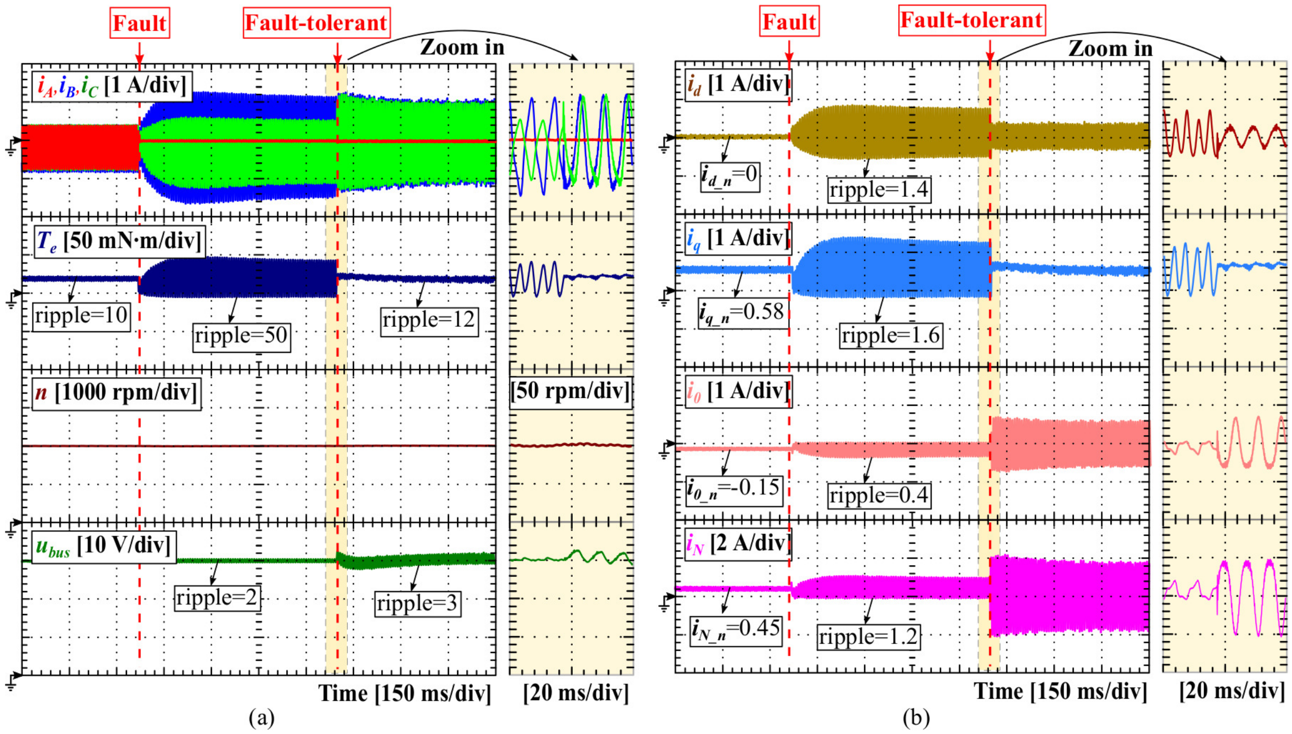

FIGURE 4.8: Experimental results of a fault-tolerant transition when the motor is operated under 2000 rpm without load in the 52.5 W PMSM based MFCS-I. (a) Phase-currents, torque, speed and DC-bus voltage. (b) d-axis current, q-axis current, zero-sequence current and neutral current.

When the OPF occurs, i_A decreases to 0 A instantly. At the beginning, the fault-tolerant control strategy is not triggered. Therefore, we can see that the torque ripple increases to 50 mN·m. The ripples of i_q also show a big fluctuation in amplitude of 1.6 A. The ripples of u_{bus} increase to 2 V as well. The ripples of i_d, i_0 and i_N are 1.4, 0.4 and 1.2 A respectively. Obviously, if no treatment means is conducted to the system, the motor will continue producing strenuous vibrations and even be damaged.

Then, we start the fault-tolerant control. Once the fault-tolerant mode is triggered, the ripple of T_e is decreased to 12 mN·m quickly, which is almost consistent with that in the healthy condition. The ripple of i_q is also similar with that in the healthy condition. Therefore, we can say that the performance of T_e and i_q is preserved rapidly. For greater details, enlarged views are displayed to the right of each graph. First, regarding i_d, its shape is distorted before the action of the fault-tolerant control. Since the fault-tolerant control functions, the shape of i_d tends to be cosinoidal, which is in line with the theoretical waveform presented in figure 4.2(c). Meanwhile, i_0 is also similar to the theoretical curve. The period of i_d and i_0 is consistent with that of i_B and i_C, which is equal to the fundamental period (T_f = 7.5 ms). As analyzed before, in order to maintain the constant torque, the DC-bus capacitor has to absorb and release some transient energy within one electrical period. Therefore, we can see that u_{bus} is synchronized with the change of i_N. The ripple of u_{bus} increases to 3 V, which is in accord with the theoretical result (around 3.1 V) according to (4.14). However, it needs to be emphasized that the mean of u_{bus} is still 30 V.

In order to verify the tracking performance of the deadbeat predictive current controller, figure 4.9 illustrates the detailed comparison between the theoretical and actual remaining

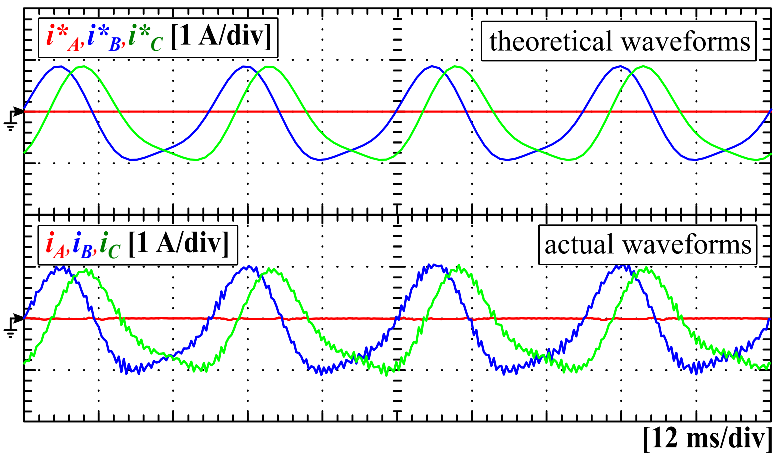

FIGURE 4.9: Experimental comparison of phase-current references and actual phase-currents under the fault-tolerant condition when the motor is operated at 2000 rpm without load.

phase-currents. Obviously, the actual i_B and i_C show good agreement with their theoretical results.

4.3.2.2 Fault-tolerant transition performance with load

In order to further verify the fault-tolerant transition performance of the MFCS-I, the motor is operated with a load. Figure 4.10 depicts the experimental results where the motor speed is 2000 rpm and the load is 60 mN·m. First, under the healthy operation, n is controlled at 2000 rpm steadily. T_e is about 60 mN·m, which is almost half the nominal torque. The torque ripple is around 9 mN·m. u_{bus} is still boosted at 30 V stably. i_{d_n} is 0 A and i_{q_n} is about 1.79 A. i_{0_n} is -0.46 A and i_{N_n} is 1.37 A.

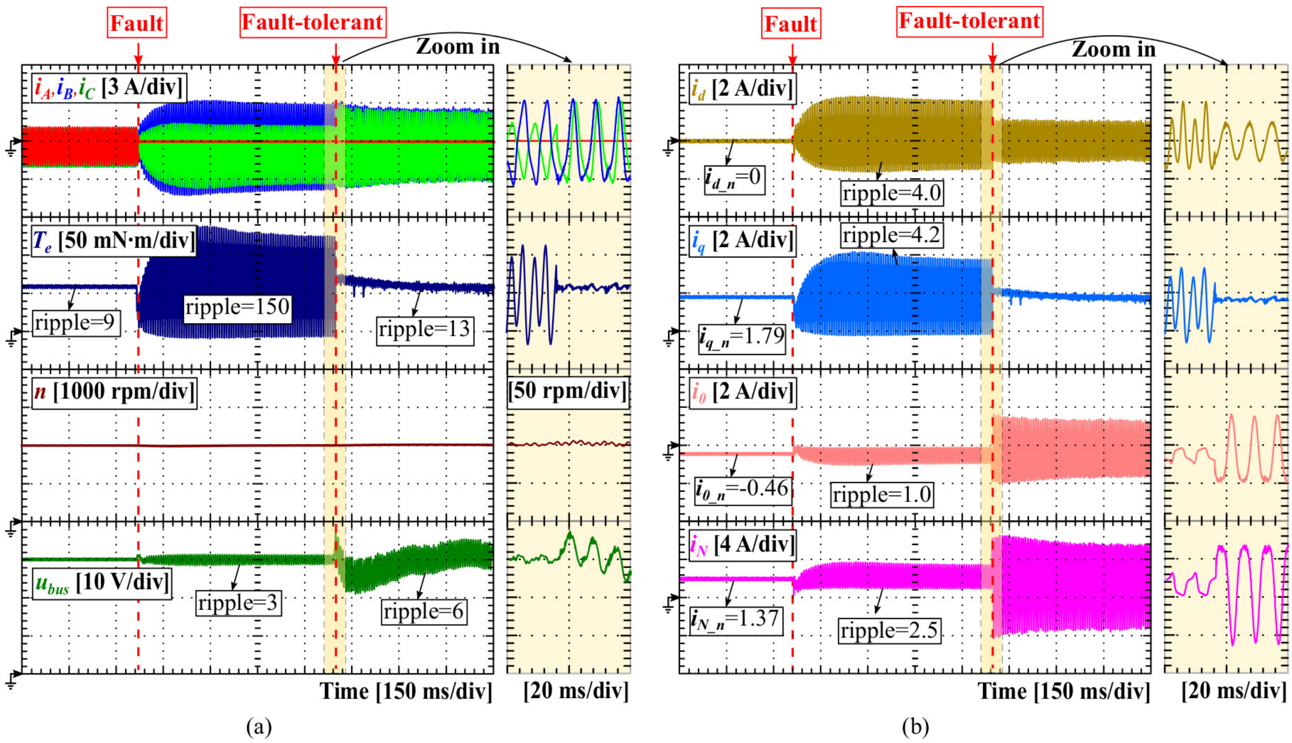

FIGURE 4.10: Experimental results of a fault-tolerant transition when the motor is operated under 2000 rpm with a 60 mN·m load in the 52.5 W PMSM based MFCS-I. (a) Phase-currents, torque, speed and DC-bus voltage. (b) d-axis current, q-axis current, zero-sequence current and neutral current.

When the OPF occurs, i_A decreases 0 A rapidly. In the same way, the fault-tolerant control is not engaged at the beginning. Therefore, we can see that the ripple of T_e is increased to 150 mN·m dramatically. The ripple of i_q becomes 4.2 A. The ripples of i_d, i_0 and i_N are respectively 4, 1.0 and 2.5 A. The motor shows severe vibrations and its temperature starts to rise.

Then, we switch on the fault-tolerant control strategy. Thanks to the remedial measure, T_e returns to 60 mN·m quickly with the ripple of 13 mN·m. In the enlarged views, i_d is still a cosine waveform, which is in accord with the theoretical analysis. Moreover, the period of i_d and i_0 is still consistent with the fundamental period. With the increase of motor's power, the peak value of i_N increases to 5.6 A. This means that the transient energy which should be absorbed or released by the DC-bus capacitor becomes bigger. As a result, it can be seen that the ripple of u_{bus} is increased to 6 V. However, the mean of u_{bus} is still 30 V due to the DC-bus voltage controller. The detailed comparison between the theoretical and actual phase-currents is illustrated in figure 4.11. Obviously, the actual i_B and i_C can still track the theoretical references well.

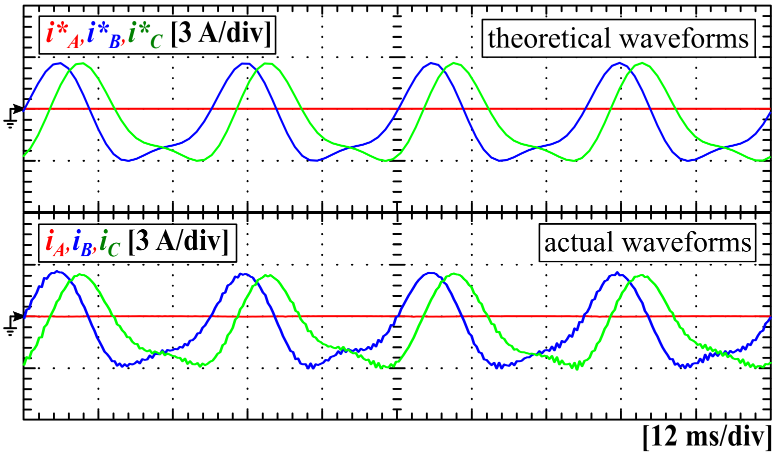

FIGURE 4.11: Experimental comparison between phase-current references and actual phase-currents under the fault-tolerant mode when the motor is operated at 2000 rpm with a 60 mN·m load.

4.3.2.3 Dynamic condition

When the motor is operated in post-fault conditions, it still has dynamic requirements, such as acceleration, deceleration and load variations. Thus, in order to further validate the practicability of the MFCS-I to be against an OPF, dynamic experiments under post-fault conditions are further conducted, as shown in figure 4.12. The setup of the dynamic experiment is as follows: the speed reference n^* is set as 1000 rpm before 2 s. It is set to 1500 rpm between 2 and 5 s while it is reset to 1000 rpm after 5 s. A 50 mN·m load is imposed at 10 s and removed at 15 s.

From figure 4.12, we can see that i_A is always 0 A because of the fault. Even so, the motor speed can still track the reference signal well. The torque performance can be preserved during the acceleration, deceleration, loading and deloading processes. When the motor accelerates

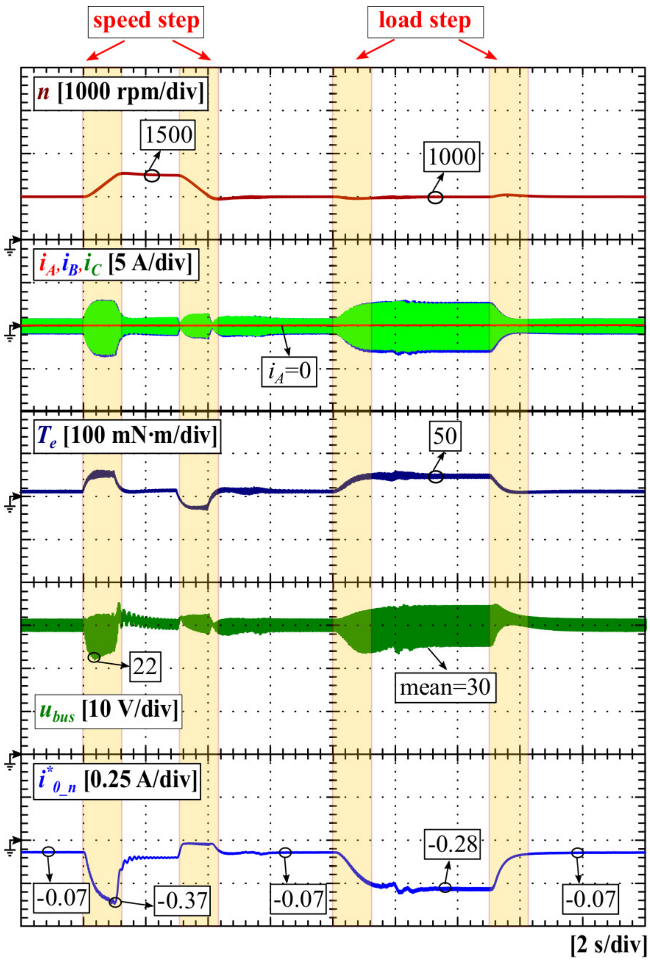

FIGURE 4.12: Experimental results of the 52.5 W PMSM based MFCS-I under fault-tolerant conditions with dynamic tests.

instantly, u_{bus} declines to 22 V firstly. Thanks to the control to the mean of u_{bus}, the zero-sequence current reference $i^*_{0\_n}$ decreases from -0.07 to -0.37 A. I.e. $i^*_{N\_n}$ increases from 0.21 to 1.11 A rapidly so that the DC-source can output more average power to the drive system. Therefore, it can be seen that the mean of u_{bus} can return to 30 V. Similarly, $i^*_{0\_n}$ can also be adjusted cleverly during the load change processes. It changes from -0.07 to -0.28 A then returns to -0.07 A again. This demonstrates that it is feasible to use a PI controller to regulate the mean of u_{bus} which enables an appropriate value for determining the value of $i^*_{0\_n}$.

4.4 Implementation on the 1.2 kW PMSM

In this section, the effectiveness of fault-tolerant operations of the MFCS-I will be verified on a 1.2 kW PMSM. The test-bench has already been presented in figure 3.12, whose parameters are already displayed in table 3.1. The DC-source voltage is 180 V and the desired DC-bus voltage is 360 V. A circuit breaker which is connected in series with phase-A is used to simulate an OPF. In this experiment, the differential flatness-based current tracking controller is adopted, whose parameters are set as: $\zeta_1 = \zeta_2 = \zeta_3 = 1$, $\omega_1 = 2500$ rad/s, $\omega_2 = \omega_3 = 5000$ rad/s. Considering that the long-time operation with the OPF without fault-tolerant control is adverse to the lifetime of the motor, a predictive current-based OPF detection method is used to detect the OPF. In this way, the fault-tolerant control strategy can be put into action as soon as possible after the occurrence of the fault.

4.4.1 Open-phase fault Detection

The conventional OPF detection method in the typical three-phase fault-tolerant drives relies on the magnitude of fault-induced current harmonics, which is only related to d,q-axes currents. Normally, the magnitude is proportional to the load[107]. In the MFCS-I, there are not only d,q-axes currents but also the zero-sequence current in healthy conditions. Therefore, the zero-sequence current can be an additional signal for the OPF detection.

According to (3.3a), the voltage equation of the MFCS-I can be discretized. The sampling interval is T_s. Thus, in healthy conditions, i_d, i_q and i_0 in the $(k+1)^{th}$ interval can be predicted by using their measurements in the $(k)^{th}$ interval, as:

$$
\begin{aligned}
\begin{bmatrix} \hat{i}_d(k+1) \\ \hat{i}_q(k+1) \\ \hat{i}_0(k+1) \end{bmatrix} &= \begin{bmatrix} 1-\dfrac{RT_s}{L_d} & \dfrac{\omega_e(k)L_qT_s}{L_d} & 0 \\ -\dfrac{\omega_e(k)L_dT_s}{L_q} & 1-\dfrac{RT_s}{L_q} & 0 \\ 0 & 0 & 1-\dfrac{RT_s}{3L_E} \end{bmatrix} \begin{bmatrix} i_d(k) \\ i_q(k) \\ i_0(k) \end{bmatrix} \\
&+ \begin{bmatrix} \dfrac{T_s u_{bus}(k)}{L_d} & 0 & 0 \\ 0 & \dfrac{T_s u_{bus}(k)}{L_q} & 0 \\ 0 & 0 & \dfrac{T_s u_{bus}(k)}{3L_E} \end{bmatrix} \begin{bmatrix} \alpha_d(k) \\ \alpha_q(k) \\ \alpha_0(k) \end{bmatrix} + \begin{bmatrix} 0 \\ -\dfrac{\omega_e(k)\Phi_f T_s}{L_q} \\ -\dfrac{u_{in}T_s}{3L_E} \end{bmatrix}
\end{aligned}
\tag{4.30}
$$

where $\hat{i}_d(k+1)$, $\hat{i}_q(k+1)$ and $\hat{i}_0(k+1)$ are the predicted values; $i_d(k)$, $i_q(k)$ and $i_0(k)$ are the measured values.

If the motor is operated in healthy conditions, the measured currents in the (k+1)th interval will show good agreements with the predicted currents. Even if we consider the time delay and the inaccuracy of the system model, the deviation between the measured and predicted currents is relatively small. However, once the OPF occurs, the predicted currents will be far away from the measured currents due to the unbalanced condition, which is caused by the fault. In this case, the deviation between the measured and predicted currents will be bigger. We can use this feature to detect the OPF. To take the d-q-0 currents into account simultaneously, an error index ε is defined as follows:

$$\varepsilon = |\hat{i}_d(k+1) - i_d(k+1)| + |\hat{i}_q(k+1) - i_q(k+1)| + |\hat{i}_0(k+1) - i_0(k+1)| \tag{4.31}$$

If ε exceeds a threshold ε_{th}, the occurrence rate of OPFs is high. [108] introduced an analytic method to estimate the appropriate value of ε_{th} by quantifying the effects caused by inverter's dead time, voltage drop of semiconductor devices, parasitic parameters and sensor noise. However, in practice, it still needs to consider a redundant margin for the theoretically calculated value. In our work, an experimental trial is adopted to set ε_{th}, which is simpler and more effective in case of false alarms. To consider different operating condition and avoid false alarms, we have done a progressive trial where the motor speed and load are increased gradually. The experimental results are shown in figure 4.13. It can be observed that the motor speed is increased from 52.3 rad/s to the nominal value (314.2 rad/s). The load is increased from around 0 to the nominal value (4 N·m). From figure 4.13, we can see that, although the value of ε changes a little when the speed and load change, it is always smaller than 1. Therefore, we choose $\varepsilon_{th} = 1$ as a safe indicator to detect the OPF in the following fault-tolerant experiments.

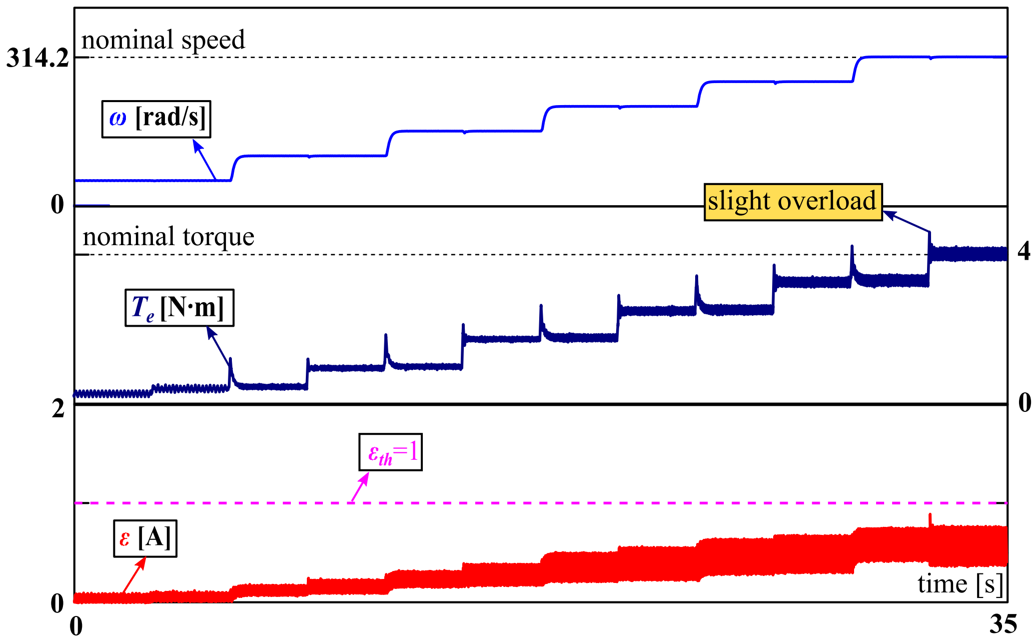

FIGURE 4.13: An experimental trial for the choose of ε_{th}.

4.4.2 Fault-tolerant transition performance

4.4.2.1 High-speed without load

Figure 4.14 depicts a fault-tolerant transition process from pre-fault to post-fault operations when the motor is operated at the high-speed (262 rad/s) without load condition. The value of ε, fault flag, DC-bus voltage (u_{bus}) and its average vaule (u_{bus_filter}) are respectively presented. From figure 4.14, it can be observed that the value of ε is around 0.7 in the healthy condition. Thus, the fault flag is not triggered. Meanwhile, u_{bus} is boosted at 360 V stably thanks to the equivalent boost function. u_{bus_filter} is also 360 V in the healthy condition. In terms of the torque T_e, it is around 0.4 N·m with the ripple of 0.18 N·m. Although there is no load torque applied on the motor, the friction torque is the main load to the motor.

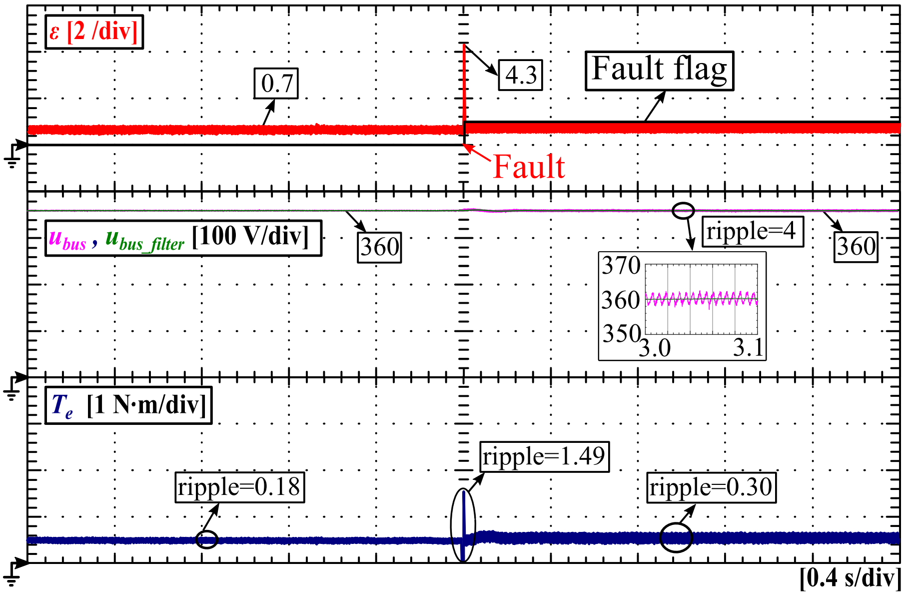

FIGURE 4.14: Experimental results of a fault-tolerant transition process when the motor is operated under a high-speed (262 rad/s) in no load condition: ε, fault flag, DC-bus voltage u_{bus}, average value of the DC-bus voltage u_{bus_filter} and torque T_e.

Then, the OPF of phase-A is made by the circuit breaker. At that moment, it can be seen that the value of ε increases to 4.3. This is accompanied by a big torque ripple (1.49 N·m). Since ε exceeds 1, the fault flag is triggered, which means that the fault-tolerant control strategy works. As a result, the motor torque is preserved instantly. In steady states, the torque ripple recovers to around 0.3 N·m. In post-fault operations, we can see that the transient DC-bus voltage is no longer constant anymore. Its ripples are around 4 V. However, the average DC-bus voltage u_{bus_filter} can be still remained at 360 V.

In order to evaluate the fault-tolerant performance in detail, zoomed in views are further presented in figure 4.15. In addition to u_{bus}, the phase-currents (i_A, i_B and i_C), d-q-0 currents (i_d, i_q and i_0) and their references (i_d^*, i_q^* and i_0^*) and corresponding tracking errors (e_d, e_q and

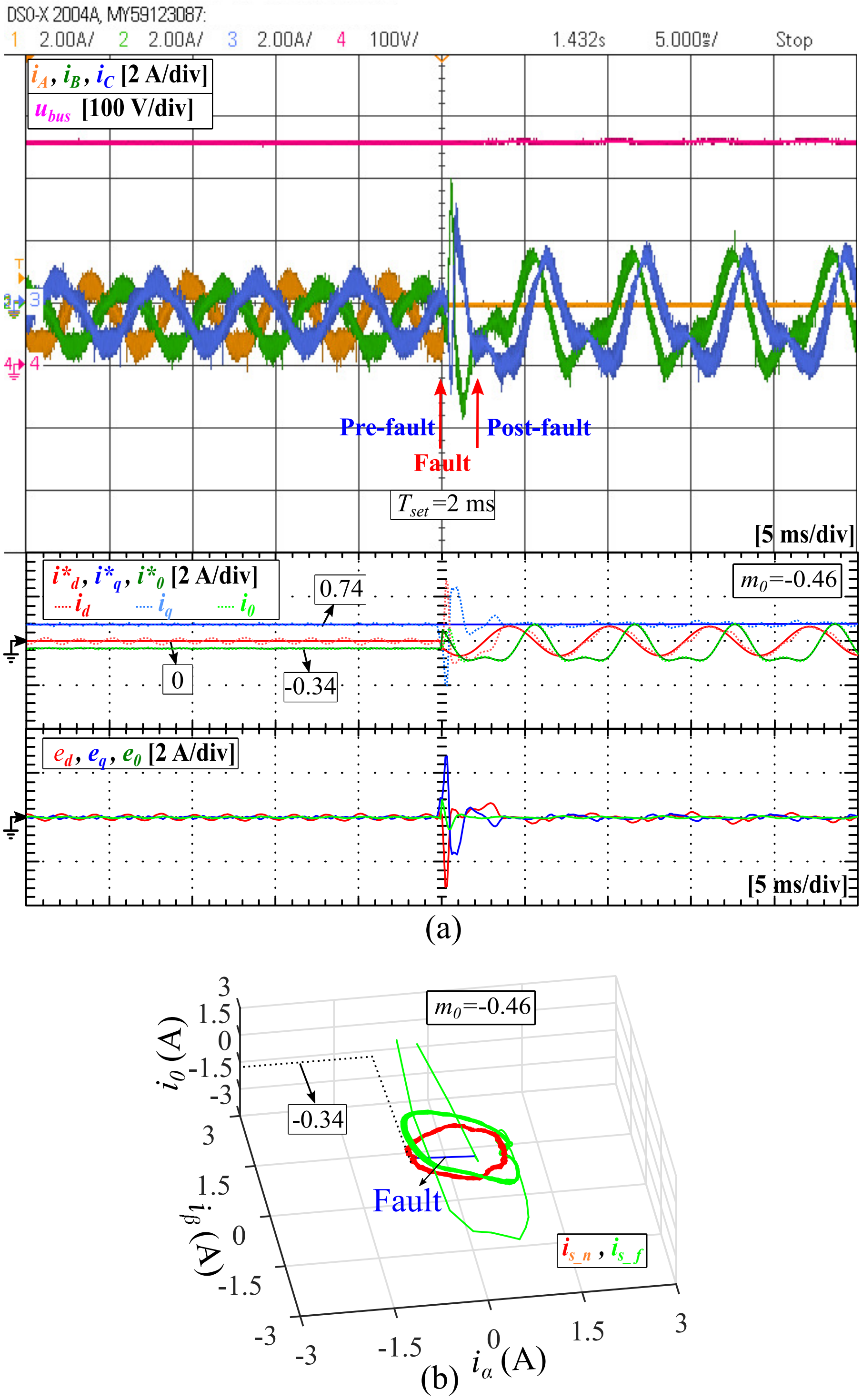

FIGURE 4.15: Experimental results of a fault-tolerant transition process when the motor is operated under high-speed (262 rad/s) in no load condition. (a) Zoomed-in DC-bus voltage and phase-currents. (b) Current vectors during the transition.

e_0) are drawn. In the healthy condition, i_A, i_B and i_C present normal shapes with a downward offset due to the zero-sequence current. i_d^*, i_q^* and i_0^* are 0, 0.74 and -0.34 A respectively. In this case, the value of zero-sequence proportion m_0 is calculated as -0.46. Thus, this situation can be approximated to the third case in figure 4.2(c) and (d) where m_0 is equal to -0.45. The actual i_d, i_q and i_0 can track the references well. The tracking errors e_d, e_q and e_0 are less than 0.4 A. Then, the OPF is made artificially by the circuit breaker. At that moment, i_A becomes 0 A instantly. However, the fault flag is not triggered immediately. Therefore, the motor is operating in the faulty condition without the fault-tolerant control. In that period, it can be seen that all the currents are distorted and the tracking errors e_d, e_q and e_0 become big. In around 2 ms, the fault flag is triggered and the fault-tolerant control is put into operations. In the post-fault operation, all the currents recover to stable states. The shapes of i_B and i_C show good agreements with the theoretical shapes presented in figure 4.2(d), corresponding to the case of $m_0 = -0.45$. Meanwhile, the shapes of i_d^*, i_q^* and i_0^* are also consistent with the theoretical analysis. The tracking errors return to around 0.4 A again, which is almost similar to that in the healthy condition. Therefore, we can conclude that the OPF detection time T_{set} is about 2 ms. Moreover, we can also conclude that the proposed flatness-based current controller is feasible to track the non-constant current references in the post-fault condition.

According to the current information and the position information, the trajectory of the current vectors in 3-D space are further calculated and drawn, as shown in figure 4.14(b). In the healthy condition, the current trajectory $\boldsymbol{i_{s\_n}}$ is a circle whose zero-sequence component is -0.34 A, which is equal to i_0. In the faulty condition, the current trajectory is mismatched. In the post-fault condition with the fault-tolerant control, the current trajectory $\boldsymbol{i_{s\_f}}$ is like a heart. This verifies the correctness of the theoretical analysis.

4.4.2.2 Low-speed with load

To further test the fault-tolerant performance when the motor is operated with load, we have recorded the new experimental results, as shown in figure 4.16. In this case, the motor speed is 104.7 rad/s and the load is around 2 N·m. From figure 4.16, it can be seen that ε is equal to 0.6 in the healthy condition. u_{bus} is boosted at 360 V and u_{bus_filter} is also 360 V due to the equivalent boost function. The ripple of the torque T_e is around 0.16 N·m. Then, the OPF occurs, it results in the increase of ε. We can see that ε reaches 6. As a result, the torque ripple is increased to 3.8 N·m. Since ε exceeds 1, the fault flag is triggered, which means that the fault-tolerant control strategy is put into operations. Therefore, the motor torque is preserved instantly. In steady states, the torque ripple recovers to around 0.31 N·m. In post-fault operations, the transient DC-bus voltage can not be maintained constant anymore. Its ripple is increased to 25 V, which is bigger than that in the no load condition. This phenomenon is reasonable because the amplitude of the zero-sequence current is bigger in the load condition. In other words, the DC-bus capacitor needs to absorb and release more energy within one electrical period in the post-fault condition. However, the average DC-bus voltage u_{bus_filter} can still be remained at 360 V due to the control for the mean of u_{bus}.

Then, to analyze the fault-tolerant performance in detail, zoomed in views are further presented in figure 4.17. In the healthy condition, i_A, i_B and i_C present normal shapes with a downward offset due to the zero-sequence current. i_d, i_q and i_0 are 0, 3.39 and -0.49 A respectively. In this case, the value of zero-sequence proportion m_0 is calculated as -0.14. This situation can be approximated to the first case in figure 4.2(c) and (d) where m_0 is equal to -0.15. The actual i_d, i_q and i_0 can track the references well. The tracking errors e_d, e_q and e_0 are less than 0.6 A. Then, the OPF is made artificially by the circuit breaker. At that moment, i_A becomes 0 A instantly. However, the fault flag is not triggered immediately. Therefore, the motor is operating in the faulty condition without the fault-tolerant control. In that period, it can be seen that all the currents are distorted and the tracking errors e_d, e_q and e_0 become big. In around 3 ms, the fault-flag is triggered and the fault-tolerant control is put into operations. In the post-fault operation, all the currents recover to stable states. The shapes of i_B and i_C show good agreements with the theoretical shapes presented in figure 4.2(d), corresponding to the case of $m_0 = -0.15$. Meanwhile, the shapes of i_d^*, i_q^* and i_0^* are also consistent with the

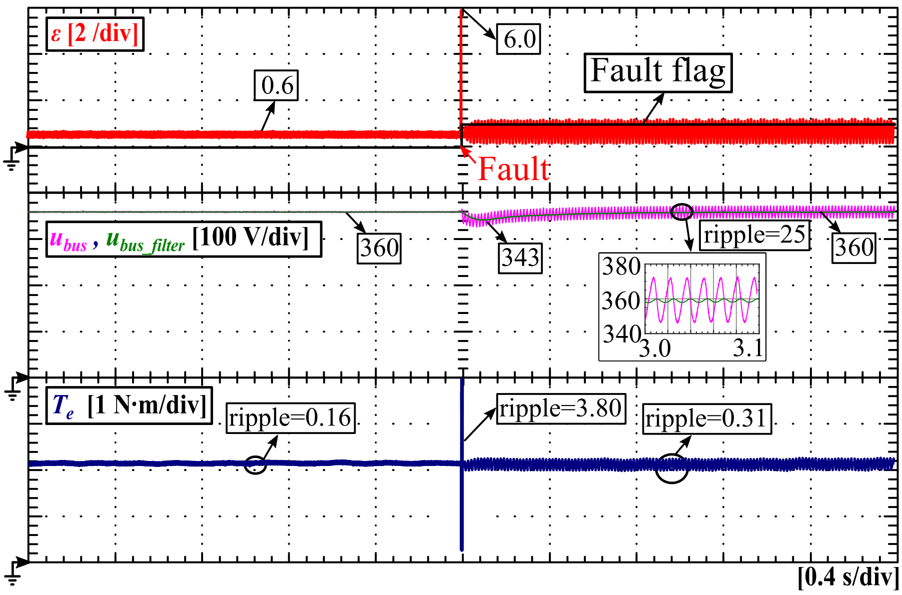

Figure 4.16: Experimental results of a fault-tolerant transition process when the motor is operated under low-speed (104.7 rad/s) with load (2 N·m) condition: ε, fault flag, DC-bus voltage and torque.

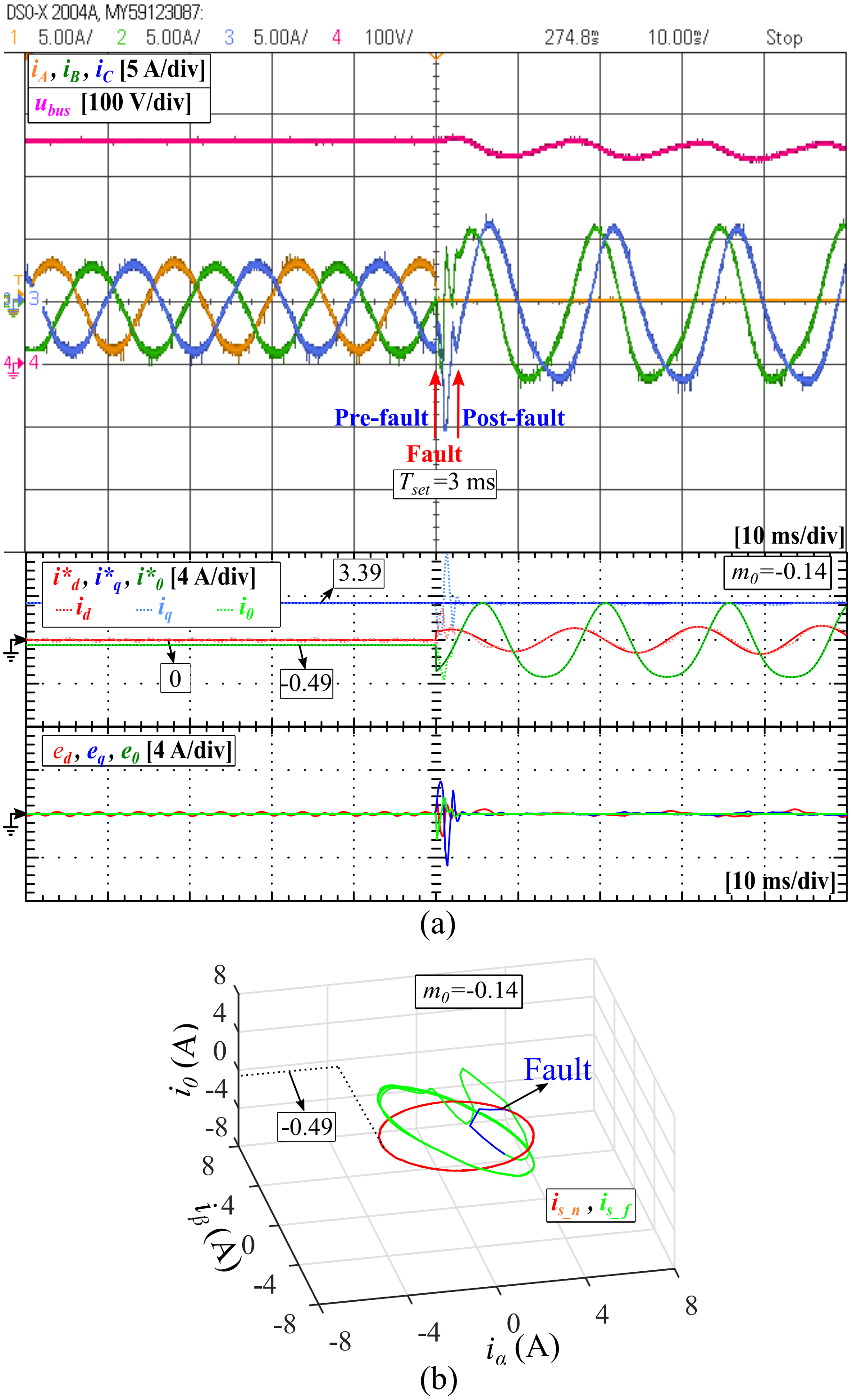

FIGURE 4.17: Experimental results of a fault-tolerant transition process when the motor is operated under low-speed (104.7 rad/s) with load (2 N·m) condition. (a) Zoomed-in DC-bus voltage and phase-currents. (b) Current vectors during the transition.

theoretical analysis. The tracking errors return to around 0.6 A again, which is almost similar with that in the healthy condition. Therefore, we can conclude that the fault detection time T_{set} is about 3 ms. Moreover, we can also conclude that the proposed flatness-based current controller is feasible to track the non-constant current references in the post-fault condition.

According to the current information and the position information, the trajectory of the current vector in 3-D space are further calculated and drawn, as shown in figure 4.17(b). In the healthy condition, the current trajectory $\boldsymbol{i_{s\_n}}$ is a circle whose zero-sequence component is -0.49, which is the same as i_0. In the faulty condition, the current trajectory is mismatched. In the post-fault condition with the fault-tolerant control, the current trajectory $\boldsymbol{i_{s\_f}}$ is like an ellipse. This verifies the correctness of the theoretical analysis.

4.4.3 Evaluation of available speed and torque ranges

To evaluate the reachable speed range in post-fault operations, the motor is operated respectively at a very low speed (20.9 rad/s) and the full speed (314.2 rad/s). The steady-state phase-currents and neutral current are shown in figure 4.18. By comparison, the unique shapes of remaining phase-currents and neutral current are more distinct under the full-speed condition. This phenomenon is in accord with the theoretical analysis because the absolute value of m_0 at the full speed is larger than that in the low speed condition. The actual current shapes also show good agreements with the theoretical curves. It needs to note that the waveform of i_N is reverse compared to the shape of i_{0_f} because i_N is equal to -3i_0. In conclusion, we can say that the motor is still able to work within a wide speed range under the post-fault operation. Especially, it can still reach the nominal speed.

Then, to evaluate the post-fault torque output capability, contrast experiments are carried out on the 1.2 kW PMSM respectively. The motor is operated in the healthy condition and fault-tolerant condition respectively. In the healthy operation, the motor is operated at 157.1 rad/s with 4.0 N·m torque (rated torque). The experimental results are shown in figure 4.19. First, from figure 4.19(a), it can be seen that the RMS value of phase-currents in the healthy condition is 4.565 A, whose offset is around -1.28 A due to the zero-sequence current. The offset is equal to -1/3 of i_N whose value is 3.84 A. From figure 4.19(b), the phase-current THD is 4.97% and the zero-sequence proportion is 24.73%. From figure 4.19(c), it can be observed that the torque is stable at 4.0 N·m with the ripple of 0.4 N·m. Therefore, we know that the phase-current RMS is 4.565 A when the motor is operated with the nominal torque in healthy conditions. We can take this value as the rated current limit.

Afterwards, the motor is operated in the post-fault condition with the same speed but

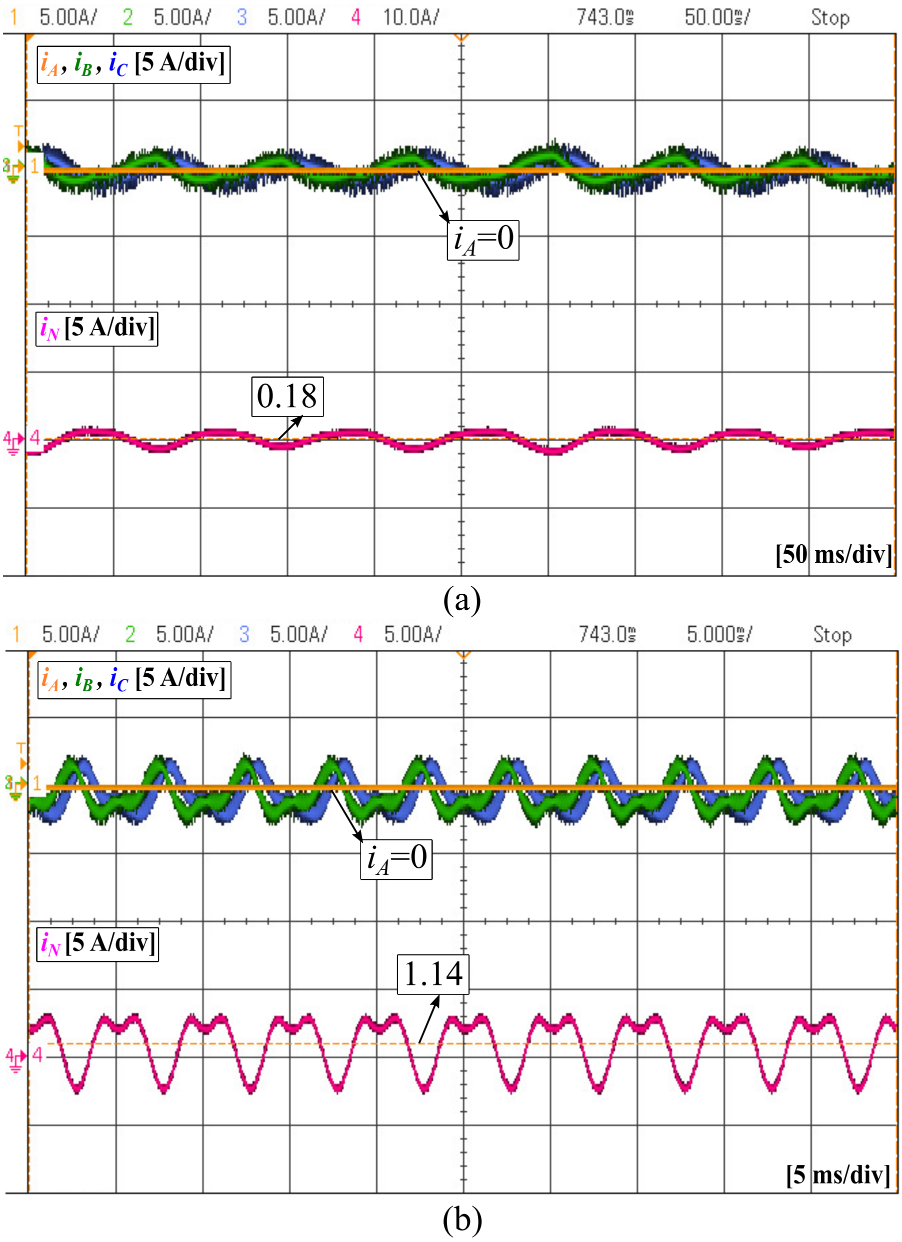

FIGURE 4.18: Steady-state phase-currents and neutral currents under post-fault operations. (a) At a very low speed (20.9 rad/s). (b) At the full speed (314.2 rad/s).

without load. Then, by increasing the load, the RMS value of remaining phase-currents reaches around 4.561 A. The experimental results are shown in figure 4.20. Since the post-fault phase-current RMS is equal to the healthy phase-current RMS, we consider that the post-fault phase-currents have reached the same current limit to that in the healthy condition. In this case, the torque is recorded, whose value is around 2.2 N·m, as shown in figure 4.20(c). Therefore, we can conclude that the post-fault torque output capability is 55% of the nominal torque, which is in accord with the theoretical result (0.518-0.707) shown in figure 4.3.

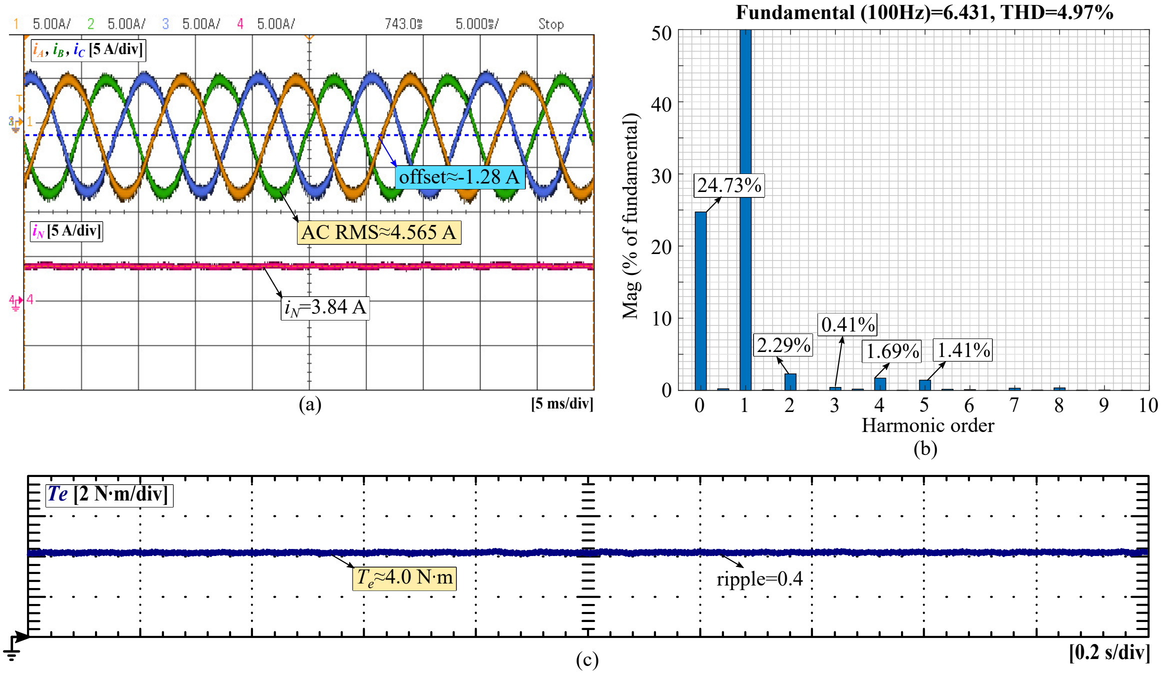

FIGURE 4.19: Steady-state performance of the MFCS-I when it is operated in the healthy condition (157.1 rad/s and 4 N·m load). (a) Phase-currents and neutral current. (b) THD of phase-currents. (c) Motor torque.

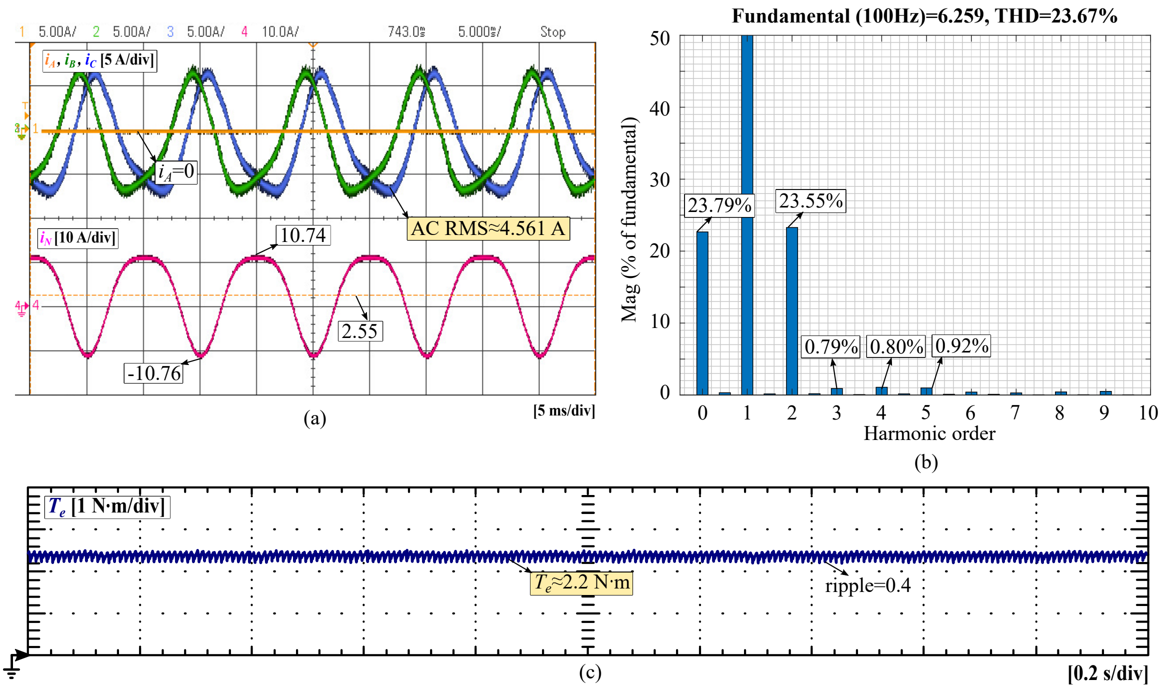

FIGURE 4.20: Steady-state performance of the MFCS-I when it is operated in the fault-tolerant condition (157.1 rad/s and 2.2 N·m load). (a) Phase-currents and neutral current. (b) THD of phase-currents. (c) Motor torque.

From figure 4.20(a), we can still see the unique shapes of remaining phase-currents and the neutral current. The positive and negative amplitudes of the neutral current is respective 10.74 and - 10.76 A. The mean of the neutral current is around 2.55 A. From figure 4.20(b), it can be seen that the remaining phase-currents includes 23.79% of zero-sequence components and 23.55% second-order components. Therefore, the THD of remaining phase-currents is around 23.67%, which is much bigger than that in the healthy condition. Actually, this phenomenon is reasonable because the zero-sequence components and second-order components make the possibility of keeping the q-axis current at a constant value in the post-fault condition.

4.4.4 Dynamic Performance

In post-fault operations, the motor may still have the requirements of acceleration, deceleration, loading and deloading. To assess the dynamic performance in post-fault operations, contrastive experiments are further carried out on the 1.2 kW PMSM where it is operated in healthy conditions and fault-tolerant conditions respectively. The dynamic setup is set as follows: ω_m is 104.7 rad/s before 2 s. It is increased to 209.4 rad/s at 2 s and is reset to 104.7 rad/s at 6 s. A 2 N·m load is applied and removed at 10 s and 15 s respectively.

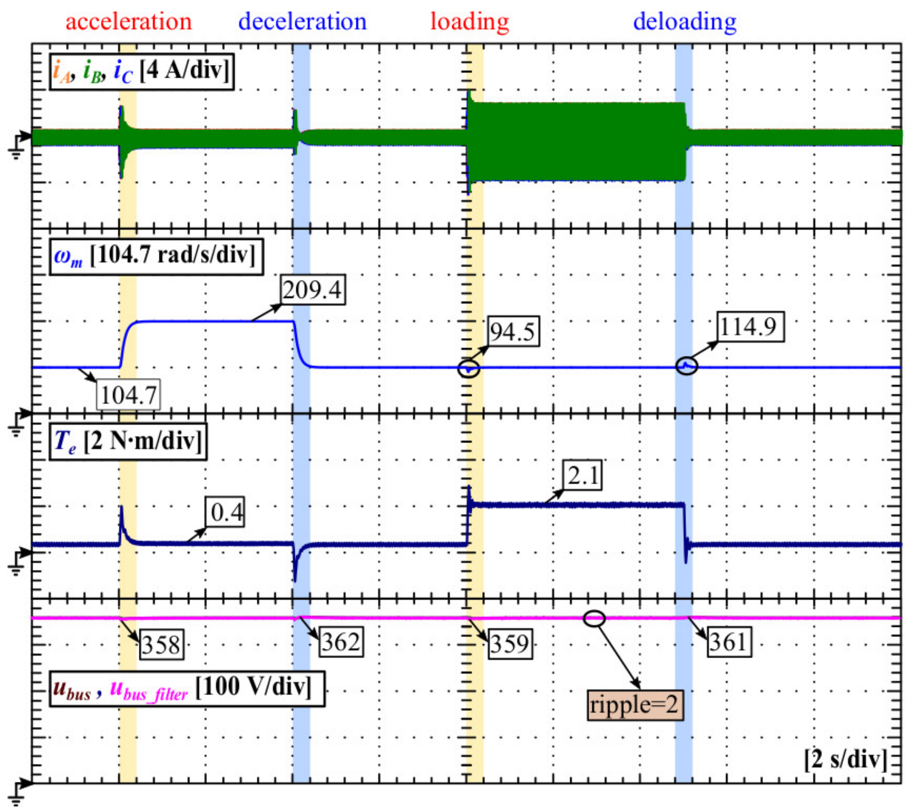

FIGURE 4.21: Experimental results of a dynamic test when the motor is operated under healthy operations.

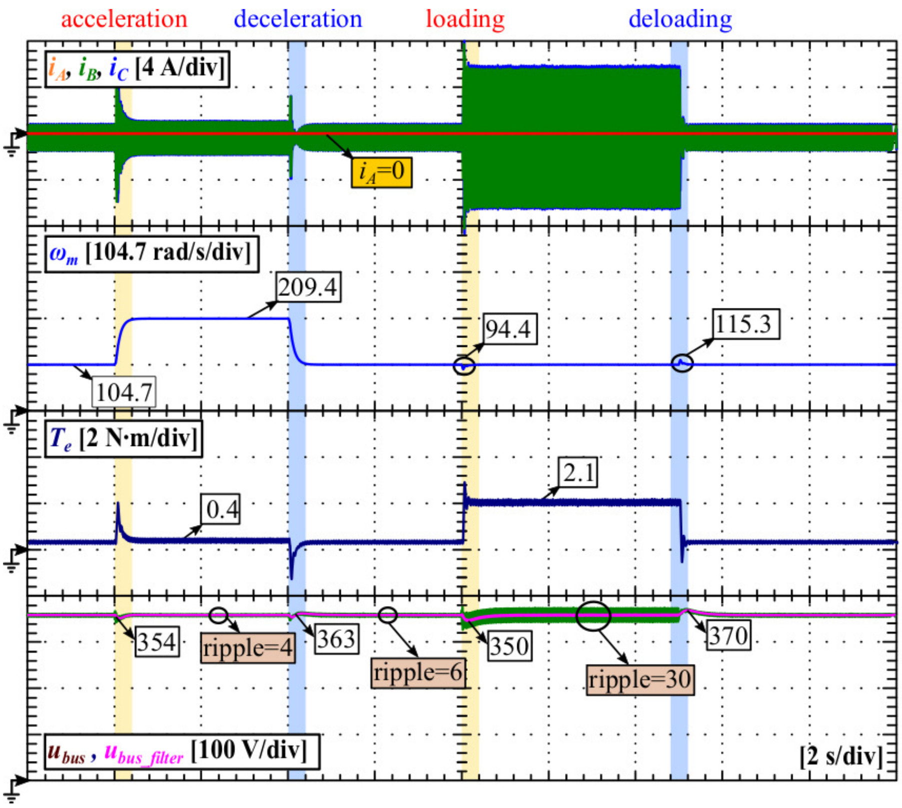

FIGURE 4.22: Experimental results of a dynamic test when the motor is operated under post-fault operations.

For the healthy operation, the experimental results are shown in figure 4.21. It can be seen that the motor shows a remarkable and fast dynamic performance. To be specific, the actual speed can track the reference well during the acceleration and deceleration processes. When a 2 N·m load is imposed and removed, the motor speed shows around 10 rad/s fluctuations for a while, and then it turns to the stable state quickly. In terms of the DC-bus voltage, it can be maintained at 360 V stably with only a 2 V ripple during the whole test.

For the post-fault operation, the experimental results are shown in figure 4.22. First, it can be seen that the amplitude of remaining phase-currents is bigger than that in the healthy operation. This phenomenon is in accord with the theoretical analysis because the motor requires bigger currents to generate the same magnetic field in the post-fault condition when phase-A is not available. Regarding the acceleration and deceleration performance, the motor herein almost shows a consistent dynamic with that in the healthy operation. However, it needs to note that the fluctuation on the DC-bus voltage is bigger. According to the theoretical analysis, we have revealed that the transient input power is not constant in post-fault operations, in order to maintain a constant q-axis current. Therefore, the DC-bus capacitor becomes an energy buffer in the post-fault condition to balance the mismatch between the transient input power and the output power. From figure 4.22, we can observe that the fluctuation of the DC-bus voltage is 6 V at the condition of 104.7 rad/s with 0.4 N·m, 4 V at the condition of 209.4 rad/s with 0.4 N·m, 30 V at the condition of 104.7 rad/s with 2.1 N·m. I.e. the fluctuation becomes bigger when the load is higher and speed is lower. Obviously, this phenomenon is in accord with the theoretical analysis. Actually, this issue is similar to the midpoint voltage fluctuation in the CFNI which is also caused by a non-constant neutral current. Normally, the issue can be solved by using a sufficient DC-bus capacitor. Since the DC-bus voltage can be measured in each sampling period which can be taken into account in the modulation, the DC-bus fluctuation does not affect the control performance to the motor. Although the real-time DC-bus voltage is oscillating, its mean value is still stable at 360 V due to the control for the mean of the DC-bus voltage. Consequently, we can say that the MFCS-I can not only tolerate the OPF without using extra costs but also meet variable speed and variable load operations with only two available phases. The post-fault dynamic performance of the motor can still be maintained.

Conclusion

Conventional fault-tolerant topologies of three-phase two-level VSI fed AC drives require auxiliary hardwares to achieve the fault-tolerant operation towards an OPF. These auxiliary hardwares definitely increase the cost and complexity of the drive system. The two fault-tolerant solutions (CFNI and SFNI) that utilize the NP are popular in industries because they can not only tolerate an OPF which occurs in the inverter side but also in the motor side. Considering the innately connected motor's NP in the MFCS-I, this chapter explored its fault-tolerant potential for the first time without using additional hardwares. To preserve the stable torque output in fault-tolerant operations, a novel current vector trajectory was derived. In post-fault operations, the current vector trajectory is no longer a standard circle. It presents a heart-shaped form. Moreover, the d-axis and 0-axis currents are not constant anymore. The remaining phase-currents are also not exactly sinusoidal due to the generation of a second-order component. A simple uniform control framework was proposed for the MFCS-I where the fault-tolerant control can be fulfilled by simply replacing the d-q-0 current references. The real-time DC-bus voltage is not regulated anymore. In turn, its mean value is the control objective in this framework. To track the non-constant current trajectories in fault-tolerant conditions, the predictive deadbeat controller and differential flatness-based controller are developed for the current-loop.

Experimental validations are carried out on the 52.5 W and the 1.2 kW PMSMs to verify the effectiveness of the proposed fault-tolerant scheme, respectively. According to the experimental results, the OPF can be well tolerated once the fault-control program is executed.

TABLE 4.2: Characteristics of the MFCS-I compared to the four typical fault-tolerant topologies.

Topology	Free Boost Function	Split DC Bus	Accessible Motor Neutral	Auxiliary Silicon Components	Post-Fault Power Rating Factor (PPRF)	Silicon Overrating Cost Factor (SOCF)	Tolerate Fault Occurring in	
							Motor Side	Inverter Side
CFI	NO	YES	NO	3 (TRIAC)	0.50	1.50	X	√
SFI	NO	NO	NO	2 (IGBT) 3 (TRIAC)	1	1.83	X	√
CFNI	NO	YES	YES	1 (TRIAC)	0.50	1.29	√	√
SFNI	NO	NO	YES	2 (IGBT) 1 (TRIAC)	0.58	1.87	√	√
MFCS-I	**YES**	**NO**	YES	**null**	(0.52-0.71) (theoretical range) 0.55 (experimental case)	**1**	√	√

In post-fault operations, the motor can still be operated in a wide speed range. The post-fault torque output capability is around 55% of the nominal torque in the 1.2 kW PMSM based MFCS-I. Both the predictive deadbeat controller and the differential flatness-based controller show a remarkable current tracking performance even if the current references are not constant. Moreover, the motor in post-fault operations can still have a consistent dynamic performance compared to that in healthy operations.

Consequently, the MFCS-I has two advantages: One is the integrated DC/DC boost function without using a real chopper. The other is the cost-effective fault-tolerance towards an OPF without using additional hardwares. Finally, compared to the four typical fault-tolerant topologies, the main characteristics of the MFCS-I are summarized in table 4.2.

General conclusion

Conclusion

The main objective of this dissertation was to develop a low-cost and high-reliability alternative for the typical two-stage converter-based three-phase PMSM drive system in HEV and EV applications. Inspired by the original idea of the basic MFCS which utilizes the NP of a three-phase motor to realize a free DC/DC boost function upon a three-phase two-level VSI, a comprehensive study with respect to the modeling, control, improvement and fault-tolerant capability of MFCSs has been conducted. This dissertation starts with an overview of the applications using the NP to obtain additional benefits.

- **In chapter 2,** the PMSM model considering zero-sequence components is given. For a PMSM with ideally sinusoidal back-EMFs, its 0-axis model is regarded as a first-order system. Then, the average model expressed with inverter's duty cycles of a PMSM-based basic MFCS is built in A-B-C firstly and further converted into d-q-0 coordinate. It reveals that the d-q model of the basic MFCS is still same as that of a conventional drive while the 0-axis model can be equivalent to a DC/DC boost function due to the connection of the NP. Moreover, three equivalent circuits are developed to facilitate the understanding of the equivalent boost function, which indicates that the average duty cycle of the inverter can be a control DOF for the equivalent boost. To enable the average duty cycle of the inverter (i.e. the control DOF of the equivalent boost), a specialized modulation technique named ZSVIPWM is proposed. As a result, the motor function and the equivalent boost function can be controlled independently. According to the theoretical analysis, the maximum effective step-up ratio of the equivalent boost is 2 and the DCSUR of the basic MFCS is 1. Simulation and experiment are carried out on a 52.5 W test-bench to verify the phenomenon of the equivalent boost and the proposed ZSVIPWM. By comparison, it can be concluded that the basic MFCS supplied by a 15 V DC-source (without a real boost stage) can have the similar steady-state and dynamic performances with a standard drive supplied by a 30 V DC-source. However, as a compromise, the current ripple of the basic MFCS is bigger.

Key contribution: We explicitly explain the mechanism of the basic MFCS. A specialized modulation technique named ZSVIPWM is proposed so that the control DOFs of the equivalent boost function and the motor function can be synthesized together for digital implementations.

- **In chapter 3,** two improved solutions are proposed to ameliorate the basic MFCS, which lead to two new variants named MFCS-I and MFCS-II respectively. For the former, a series inductor connected with the NP is employed to reduce the current ripple. A sizing method of the series inductor is given based on a concept of a re-floating NP. Normally, a series inductor with the value of 5 times the zero-sequence inductance of the motor is sufficient. For the latter, an auxiliary inverter leg is used to improve the effective step-up ratio of the equivalent boost. Theoretical analysis shows that both the step-up ratio and DCSUR of the MFCS-II can be increased when the duty cycle of the auxiliary leg is decreased from 1 to 0.5. To control different MFCSs, a universal closed-loop control strategy is proposed, in which the classic FOC can still be used to control the motor function and a differential flatness-based controller is used to regulate the DC-bus voltage. Experimental results carried on a 1.2 kW experimental platform are given to verify the effectiveness of the MFCS-I and MFCS-II. Specifically, the MFCS-I is compared with a conventional two-stage converter-based drive in detail. The results illustrate that the efficiency of the MFCS-I is improved by a factor of 3.1%-3.4% than that of the two-stage converter-based drive due to the reduction of switching losses. In the MFCS-II, the motor can be operated in a wide range (from 200 rpm to 2000 rpm) even if a 40 V DC-source (the rated DC-bus voltage should be 360 V) is supplied. This indicates that the effective step-up ratio of the equivalent boost of the MFCS-II can reach 9 even higher. However, the issue of a throughout positive phase-current should be noticed.

  Key contribution: Two improved solutions are proposed to ameliorate the basic MFCS. A universal closed-loop control strategy is proposed for different MFCSs for the first time.

- **In chapter 4,** the possibility of fault-tolerant operations of the MFCS-I towards an OPF without using any auxiliary hardware is discussed for the first time by considering the innately connected NP. To achieve this possibility, three crucial constraints are found and a novel current vector trajectory is proposed for fault-tolerant operations. In post-fault conditions, the q-axis current is still being held constant to preserve a stable torque. Interestingly, both d-axis and 0-axis currents are not constant anymore. To be specific, the post-fault d-axis current is a cosine function. The post-fault 0-axis current contains and a constant component and a second-order component in addition to the the sinusoidal component. The remaining phase-currents in post-fault conditions are also not exactly sinusoidal. The post-fault power conversion process is analyzed in detail, which indicates that the DC-bus capacitor becomes an energy buffer to balance the mismatch between the transient input power and output power. A deadbeat predictive current controller and a differential flatness-based current controller are developed to track the non-constant current references. Simulation and experiment are carried on a 52.5 W and a 1.2 kW tech-benches to verify the effectiveness, which illustrate that the motor torque can be well preserved by using the proposed fault-tolerant scheme when an OPF occurs. The motor can still be operated within a wide speed range and can still output half the nominal torque under the limit of rated currents.

Key contribution: The fault-tolerant possibility without using any redundant configuration for three-phase PMSMs is investigated and achieved for the first time based on the concept of MFCSs.

Perspectives

Following the works presented in Chapters 1-4, some perspectives can be envisaged:

- **Change the power electronics system:** With the development of high switching-frequency power electronic devices (such as SiC and GaN), the inverter can be operated at a higher switching frequency. Therefore, the current ripple of phase-currents in motor drives can be reduced. In this case, the basic MFCS may be directly used in real cases or the MFCS-I with a smaller series inductor will be sufficient. From another point of view, the MFCS concept can also be extended to multi-level (3-level, 5-level or higher level) inverter systems since the current ripple of multi-level inverter systems is smaller. In addition, it will also be interesting to apply the MFCS concept to some grid-connected drives (AC/AC motor drives), where the NP of the motor can be connected to a single-phase AC source.

- **More analysis and considerations in motor design:** In MFCSs, the motor is actually operated in unconventional conditions where a DC component is superposed to the fundamental components. Thus, more analysis such as magnetic saturation and thermal dissipation of the motor in MFCSs can be further studied. Moreover, some guidance can be given to design a special machine with a larger L_0.

- **Considering third-harmonic back-EMF:** If a PMSM contains third-harmonic back-EMFs, the zero-sequence back-EMF (e_0) in (2.6) is not 0. Therefore, it will generate the third-harmonic torque since the zero-sequence current is not null. To eliminate the third-harmonic torque, new modulation method and control strategy should be developed.
- **Variable DC-bus voltage control:** Since the MFCSs integrate an equivalent DC/DC boost function, its DC-bus voltage can be consistently controlled to be the minimum value, which can exactly meet the operating demand of the motor (Normally, under low-speed conditions, a low DC-bus voltage is sufficient). In this case, the overall operating efficiency of the drive system may be improved with a variable DC-bus voltage when the motor is constantly operated under acceleration or deceleration conditions. To this end, a variable DC-bus voltage control strategy may be significant for MFCSs. Moreover, for the MFCS-II, the average duty cycle (α_h) of the inverter can also be used as a DOF instead of the constant value (0.5) used in this manuscript. In this case, an allocation strategy between α_h and α_F may be interesting with respect to the required DC-bus voltage.
- **Considering interior PMSM (IPMSM) or synchronous reluctance motor (SynRM) in the fault-tolerant control of the MFCS-I:** For an IPMSM or an SynRM, the reluctance torque is not zero due to $L_d \neq L_q$. In this case, the proposed post-fault current references are infeasible to maintain a stable torque (i_{d_f} is a cosine function, which will induce a torque fluctuation when $L_d \neq L_q$). To expand the fault-tolerant capability to the interior PMSM and the SynRM-based MFCS-I, new fault-tolerant current vector trajectory should be proposed.

List of publications

International journals

1) **X. Zhang***, J. -Y. Gauthier and X. Lin-Shi, "Innovative Fault-Tolerant Three-Phase SPMSM Drive Without Split Capacitors, Auxiliary Legs, or TRIACs," ***IEEE Transactions on Power Electronics***, vol. 36, no. 7, pp. 8128-8140, July 2021.
2) **X. Zhang***, J. -Y. Gauthier, X. Lin-Shi, R. Delpoux and J. -F. Trégouët,"Modeling, Control, and Experimental Evaluation of Multifunctional Converter System," ***IEEE Transactions on Industrial Electronics***, vol. 68, no. 9, pp. 7747-7756, Sept. 2021.
3) **X. Zhang***, J. -Y. Gauthier and X. Lin-Shi, "Cost-Efficient Fault-Tolerant Scheme for Three-Phase SPMSMs Fed by Multi-Functional Converter System Under Open-Phase Faults," ***IEEE Transactions on Industrial Electronics***, vol. 69, no. 6, pp. 5502-5513, June 2022.

International conferences

1) **X. Zhang**, J. -Y. Gauthier and X. Lin-Shi, "Neutral Point Supply Scheme for PMSM Drive to Boost DC Voltage," *IECON 2019 - 45th Annual Conference of the IEEE Industrial Electronics Society*, Lisbon, Portugal, 2019, pp. 3215-3220.
2) **X. Zhang**, J. -Y. Gauthier and X. Lin-Shi, "Equivalent Model and Control of a Neutral Point Supply SynRM Drive," *2020 22nd European Conference on Power Electronics and Applications (EPE'20 ECCE Europe)*, Lyon, France, 2020, pp. 1-8.
3) **X. Zhang**, J. -Y. Gauthier and X. Lin-Shi, "A Composite Converter with Reduced Power Electronics for Electric Powertrain Applications," *2021 IEEE Energy Conversion Congress and Exposition (ECCE)*, Vancouver, BC, Canada, 2021, pp. 1468-1475.

Appendix A

Transformation matrices

The matrices of the Park transformation (power invariant) are shown below:

$$\boldsymbol{T}_C = \sqrt{\frac{2}{3}} \begin{bmatrix} cos(\theta_e) & cos(\theta_e - \frac{2\pi}{3}) & cos(\theta_e + \frac{2\pi}{3}) \\ -sin(\theta_e) & -sin(\theta_e - \frac{2\pi}{3}) & -sin(\theta_e + \frac{2\pi}{3}) \\ \sqrt{\frac{1}{2}} & \sqrt{\frac{1}{2}} & \sqrt{\frac{1}{2}} \end{bmatrix} \tag{A.1a}$$

$$\boldsymbol{T}_C^{-1} = \sqrt{\frac{2}{3}} \begin{bmatrix} cos(\theta_e) & -sin(\theta_e) & \sqrt{\frac{1}{2}} \\ cos(\theta_e - \frac{2\pi}{3}) & -sin(\theta_e - \frac{2\pi}{3}) & \sqrt{\frac{1}{2}} \\ cos(\theta_e + \frac{2\pi}{3}) & -sin(\theta_e + \frac{2\pi}{3}) & \sqrt{\frac{1}{2}} \end{bmatrix} \tag{A.1b}$$

The matrices of the Park transformation (amplitude invariant) are shown below:

$$\boldsymbol{T}_P = \frac{2}{3} \begin{bmatrix} cos(\theta_e) & cos(\theta_e - \frac{2\pi}{3}) & cos(\theta_e + \frac{2\pi}{3}) \\ -sin(\theta_e) & -sin(\theta_e - \frac{2\pi}{3}) & -sin(\theta_e + \frac{2\pi}{3}) \\ \frac{1}{2} & \frac{1}{2} & \frac{1}{2} \end{bmatrix} \tag{A.2a}$$

$$\boldsymbol{T}_P^{-1} = \frac{2}{3} \begin{bmatrix} cos(\theta_e) & -sin(\theta_e) & 1 \\ cos(\theta_e - \frac{2\pi}{3}) & -sin(\theta_e - \frac{2\pi}{3}) & 1 \\ cos(\theta_e + \frac{2\pi}{3}) & -sin(\theta_e + \frac{2\pi}{3}) & 1 \end{bmatrix} \tag{A.2b}$$

The matrices of Clarke transformation are shown below:

$$\boldsymbol{T}_{clarke} = \frac{2}{3}\begin{bmatrix} 1 & -\frac{1}{2} & -\frac{1}{2} \\ 0 & \frac{\sqrt{3}}{2} & -\frac{\sqrt{3}}{2} \\ \frac{1}{2} & \frac{1}{2} & \frac{1}{2} \end{bmatrix} \tag{A.3a}$$

$$\boldsymbol{T}_{clarke}^{-1} = \begin{bmatrix} 1 & 0 & 1 \\ -\frac{1}{2} & \frac{\sqrt{3}}{2} & 1 \\ -\frac{1}{2} & -\frac{\sqrt{3}}{2} & 1 \end{bmatrix} \tag{A.3b}$$

The matrices of rotation transformation are shown below:

$$\boldsymbol{T}_{R} = \begin{bmatrix} cos(\theta_e) & sin(\theta_e) & 0 \\ -sin(\theta_e) & cos(\theta_e) & 0 \\ 0 & 0 & 1 \end{bmatrix} \tag{A.4a}$$

$$\boldsymbol{T}_{R}^{-1} = \begin{bmatrix} cos(\theta_e) & -sin(\theta_e) & 0 \\ sin(\theta_e) & cos(\theta_e) & 0 \\ 0 & 0 & 1 \end{bmatrix} \tag{A.4b}$$

Appendix B

Derivation of duty cycles by using the classic SVPWM

The six basic voltage-vectors and two zero-vectors (see figure B.1(a)) are defined as V_1, V_2, V_3, V_4, V_5, V_6, V_0 and V_7, respectively. Their action time is respectively T_1, T_2, T_3, T_4, T_5, T_6, T_0 and T_7. The switching period is T_s, the amplitude of basic voltage-vectors is $\frac{2}{3}u_{bus}$, the amplitude of zero-vector is 0. When the referenced vector $\boldsymbol{V_{ref}}$ is located in sector 1 ($0 < \theta_e < \frac{\pi}{3}$), there is

$$\boldsymbol{V_{ref}}T_s = \boldsymbol{V_1}T_1 + \boldsymbol{V_2}T_2 \tag{B.1}$$

According to the law of sines, we obtain

$$\begin{cases} |\boldsymbol{V_{ref}}|cos\theta_e = \dfrac{T_1}{T_s}|\boldsymbol{V_1}| + \dfrac{T_2}{T_s}|\boldsymbol{V_2}|cos\dfrac{\pi}{3} \\ |\boldsymbol{V_{ref}}|sin\theta_e = \dfrac{T_2}{T_s}|\boldsymbol{V_2}|sin\dfrac{\pi}{3} \end{cases} \tag{B.2}$$

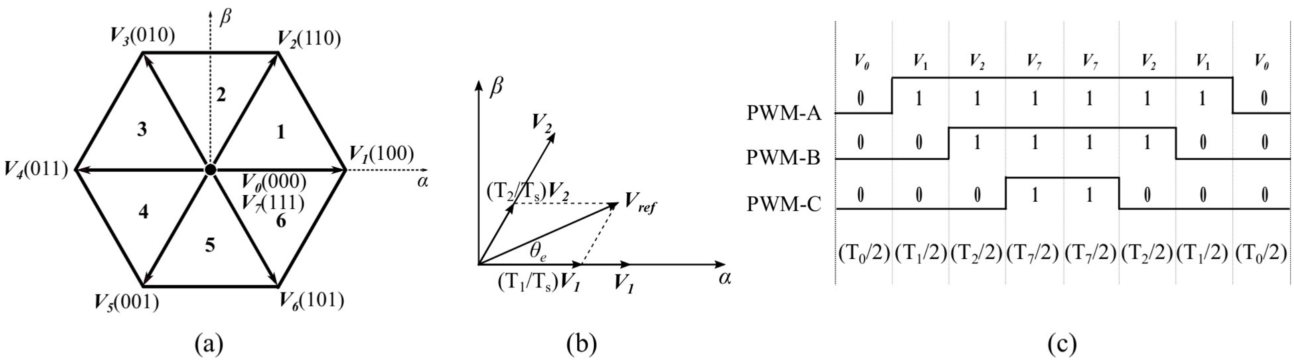

FIGURE B.1: Explanations for the calculations of inverter's mean duty-cycle by using the classic SVPWM. (a) Voltage vectors. (b) When $\boldsymbol{V_{ref}}$ is located in sector 1. (c) The shape of the 7-segment SVPWM in sector 1.

The modulation ratio m is $m = \sqrt{3}|\boldsymbol{V_{ref}}|/u_{bus}$ (fundamental voltage amplitude to carrier amplitude). Because $|\boldsymbol{V_1}| = |\boldsymbol{V_2}| = \frac{2}{3}U_{bus}$, T_1 and T_2 can be calculated by

$$\begin{cases} T_1 = mT_s sin(\frac{\pi}{3} - \theta_e) \\ T_2 = mT_s sin\theta_e \end{cases} \tag{B.3}$$

If the 7-Segment SVPWM (see figure B.1(c)) is adopted, T_0 and T_7 can be calculated by

$$T_0 = T_7 = (T_s - T_1 - T_2)/2 \tag{B.4}$$

Therefore, the duty-cycles α_A, α_B and α_C can be calculated by

$$\begin{cases} \alpha_A = (T_1 + T_2 + T_7)/T_s = \frac{1}{2}[1 + mcos(\theta_e - \frac{\pi}{6})] \\ \alpha_B = (T_2 + T_7)/T_s = msin(\theta_e) + \frac{1}{2}[1 - mcos(\theta_e - \frac{\pi}{6})] \\ \alpha_C = (T_7)/T_s = \frac{1}{2}[1 - mcos(\theta_e - \frac{\pi}{6})] \end{cases} \tag{B.5}$$

When $\boldsymbol{V_{ref}}$ is located in the other sectors, the duty-cycles can be calculated in the same way. The results are summarized in tableB.1. According to tableB.1, it is easy to calculate the inverter's mean duty-cycle by $\alpha_h = (\alpha_A + \alpha_B + \alpha_C)/3$ and draw its curve.

TABLE B.1: Duty-cycle calculations by using the classic SVPWM.

Sector	α_A	α_B	α_C
1	$\frac{1}{2}[1 + mcos(\theta_e - \frac{\pi}{6})]$	$msin(\theta_e) + \frac{1}{2}[1 - mcos(\theta_e - \frac{\pi}{6})]$	$\frac{1}{2}[1 - mcos(\theta_e - \frac{\pi}{6})]$
2	$msin(\theta_e + \frac{\pi}{3}) + \frac{1}{2}[1 - msin(\theta_e)]$	$\frac{1}{2}[1 + msin(\theta_e)]$	$\frac{1}{2}[1 - msin(\theta_e)]$
3	$\frac{1}{2}[1 - msin(\theta_e - \frac{\pi}{3})]$	$\frac{1}{2}[1 + msin(\theta_e - \frac{\pi}{3})]$	$-msin(\theta_e + \frac{\pi}{3}) + \frac{1}{2}[1 - msin(\theta_e - \frac{\pi}{3})]$
4	$\frac{1}{2}[1 + mcos(\theta_e - \frac{\pi}{6})]$	$msin(\theta_e - \frac{\pi}{3}) + \frac{1}{2}[1 + mcos(\theta_e - \frac{\pi}{6})]$	$\frac{1}{2}[1 - mcos(\theta_e - \frac{\pi}{6})]$
5	$msin(\frac{\pi}{3} - \theta_e) + \frac{1}{2}[1 + msin(\theta_e)]$	$\frac{1}{2}[1 + msin(\theta_e)]$	$\frac{1}{2}[1 - msin(\theta_e)]$
6	$\frac{1}{2}[1 + mcos(\theta_e + \frac{\pi}{6})]$	$\frac{1}{2}[1 - mcos(\theta_e + \frac{\pi}{6})]$	$-msin(\theta_e) + \frac{1}{2}[1 - mcos(\theta_e + \frac{\pi}{6})]$

Appendix C

Small-signal model of the equivalent DC/DC boost function

According to the equivalent circuit, we know that the zero-sequence circuit of the basic functions as an equivalent boost converter and the d-q circuit functions as an equivalent DC motor drive. If the equivalent DC motor drive is treated as an equivalent load (R_{eq}) to the equivalent boost converter, the equivalent circuit can be simplified, as shown in figure C.1. D represents the duty-cycle of $S_{v1}^{'}$ and $\alpha_h = 1 - D$ by neglecting the dead time. In addition, according to the proposed ZSVIPWM, the average duty cycle of the inverter α_h can be an independent control DOF for the equivalent boost. Therefore, we can use a classic cascaded PI controller to regulate the DC-bus voltage and the neutral current. In terms of the control of the motor, the classic FOC can be used. Finally, a simple control strategy for the basic MFCS is shown in figure C.2. First, the classic FOC enables the d-q voltage references u_d^* and u_q^*. Then, the fundamental voltage references u_{AN1}^*, u_{BN1}^* and u_{CN1}^* are calculated by using the inverse Park transformation (amplitude invariant). The cascaded PI controller enables the value of D thus α_h can be calculated. According to (2.23), the actual duty cycles (α_A, α_B and α_C) are obtained. Finally, PWM signals are generated to the control the inverter.

Due to the non-linear characteristic of a boost converter, we need to use the small-signal model to design the control parameters for the cascaded PI controller. To linearize the boost model, we should choose an equilibrium point. Herein, we choose the point while the motor is operating at the nominal condition. By neglecting the losses, the equivalent load R_{eq} can be calculated approximatively as

$$R_{eq} \approx \frac{u_{bus}^{*2}}{P_n} \tag{C.1}$$

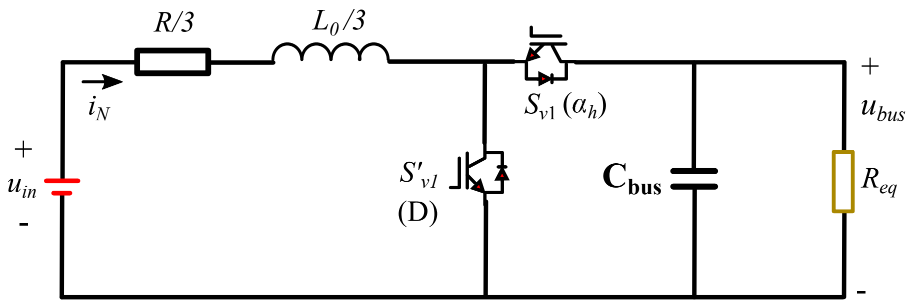

FIGURE C.1: Simplified equivalent circuit of the MFCS.

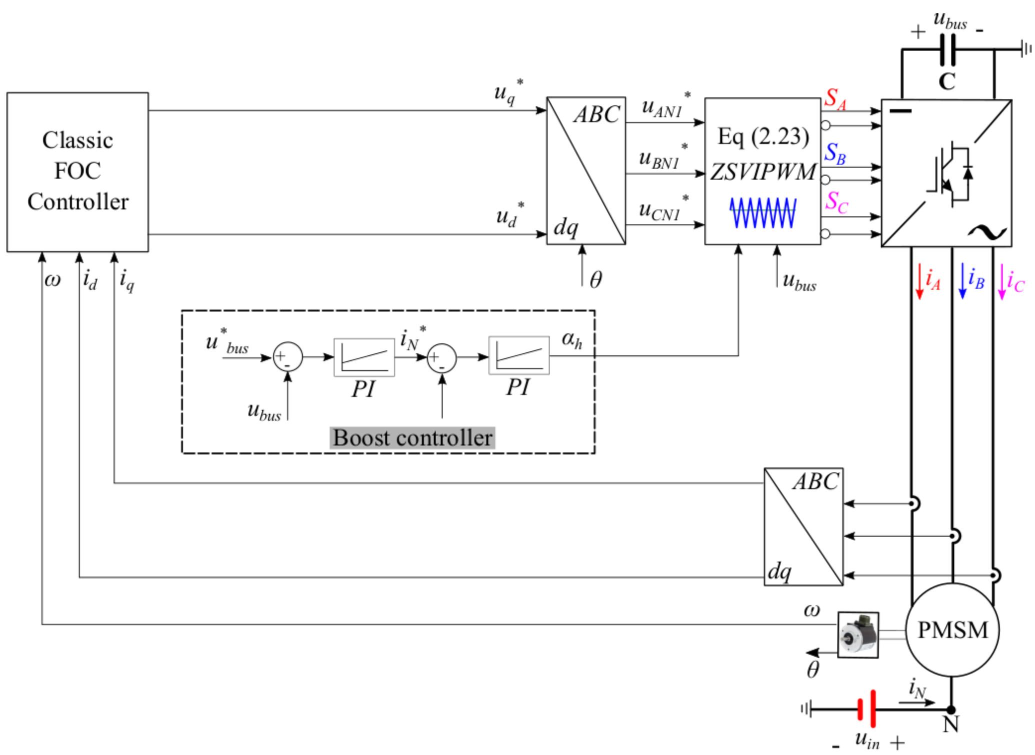

FIGURE C.2: A simple control strategy for the basic MFCS.

The equilibrium states (D_s and i_{Ns}) of the equivalent boost are

$$\begin{cases} D_s = 1 - \dfrac{u_{in}}{u_{bus}^*} \\ i_{Ns} = \dfrac{u_{bus}^{*2}}{u_{in} R_{eq}} \end{cases} \tag{C.2}$$

Therefore, the small-signal model can be built as

$$\begin{bmatrix} \dot{\tilde{i}}_N \\ \dot{\tilde{u}}_{bus} \end{bmatrix} = \begin{bmatrix} 0 & \dfrac{D_s - 1}{L_0/3} \\ \dfrac{1 - D_s}{C_{bus}} & \dfrac{-1}{R_{eq} C_{bus}} \end{bmatrix} \begin{bmatrix} \tilde{i}_N \\ \tilde{u}_{bus} \end{bmatrix} + \begin{bmatrix} \dfrac{u_{bus}^*}{L_0/3} \\ \dfrac{-i_{Ns}}{C_{bus}} \end{bmatrix} \tilde{D} \tag{C.3}$$

According to the small-signal model, the system transfer functions can be derived as

$$H1(s) = \frac{\tilde{i}_N(s)}{\tilde{D}(s)} = \frac{\dfrac{u^*_{bus}}{L_0/3}s + \dfrac{u^*_{bus}}{R_{eq}(L_0/3)C_{bus}} + \dfrac{(1-D_s)}{(L_0/3)C_{bus}}i_{Ns}}{s^2 + \dfrac{1}{R_{eq}C_{bus}}s + \dfrac{(1-D_s)^2}{(L_0/3)C_{bus}}} \tag{C.4}$$

$$H2(s) = \frac{\tilde{u}_{bus}(s)}{\tilde{D}(s)} = \frac{\dfrac{-i_{Ns}}{C_{bus}}s + \dfrac{(1-D_s)}{(L_0/3)C_{bus}}u^*_{bus}}{s^2 + \dfrac{1}{R_{eq}C_{bus}}s + \dfrac{(1-D_s)^2}{(L_0/3)C_{bus}}} \tag{C.5}$$

$$H3(s) = \frac{\tilde{u}_{bus}(s)}{\tilde{i}_N(s)} = \frac{H2(s)}{H1(s)} \tag{C.6}$$

According to $H1(s)$ and $H3(s)$, the PI parameters for the current-loop and voltage-loop of the equivalent boost can be tuned.

Bibliography

[1] I. Aghabali, J. Bauman, P. J. Kollmeyer, Y. Wang, B. Bilgin, and A. Emadi, "800-V electric vehicle powertrains: Review and analysis of benefits, challenges, and future trends," *IEEE Transactions on Transportation Electrification*, pp. 927–948, 2021.

[2] B. Guo and Y. Chen, "Robust adaptive fault-tolerant control of four-wheel independently actuated electric vehicles," *IEEE Transactions on Industrial Informatics*, pp. 2882–2894, 2020.

[3] E. M. Adzic, M. S. Adzic, V. A. Katic, D. P. Marcetic, and N. L. Celanovic, "Development of high-reliability EV and hev im propulsion drive with ultra-low latency hil environment," *IEEE Transactions on Industrial Informatics*, pp. 630–639, 2013.

[4] B. Bilgin, P. Magne, P. Malysz, Y. Yang, V. Pantelic, M. Preindl, A. Korobkine, W. Jiang, M. Lawford, and A. Emadi, "Making the case for electrified transportation," *IEEE Transactions on Transportation Electrification*, pp. 4–17, 2015.

[5] L. Kumar, K. K. Gupta, and S. Jain, "Power electronic interface for vehicular electrification," in *Proc. IEEE Int. Symp. Industrial Electronics*, 2013, pp. 1–6.

[6] O. C. Onar, J. Kobayashi, and A. Khaligh, "A fully directional universal power electronic interface for EV, hev, and phev applications," *IEEE Transactions on Power Electronics*, pp. 5489–5498, 2013.

[7] C.-H. Kim, M.-Y. Kim, H.-S. Park, and G.-W. Moon, "A modularized two-stage charge equalizer with cell selection switches for series-connected lithium-ion battery string in an hev," *IEEE Transactions on Power Electronics*, pp. 3764–3774, 2012.

[8] D. Zhou, J. Wang, N. Hou, Y. Li, and J. Zou, "Dual-port inverters with internal DC–dc conversion for adjustable DC-link voltage operation of electric vehicles," *IEEE Transactions on Power Electronics*, pp. 6917–6928, 2021.

[9] T. A. Burress, C. L. Coomer, *et al.*, "Evaluation of the 2007 Toyota Camry Hybrid Synergy Drive System," Tech. Rep., 2008.

[10] T. Burress, C. Coomer, *et al.*, "Evaluation of the 2008 Lexus LS 600H Hybrid Synergy Drive System," Tech. Rep., 2009.

[11] T. A. Burress, S. L. Campbell, *et al.*, "Evaluation of the 2010 Toyota Prius Hybrid Synergy Drive System," Oak Ridge National Laboratory, Tech. Rep., 2011.

[12] H. Chen, H. Kim, R. Erickson, and D. Maksimović, "Electrified automotive powertrain architecture using composite DC–dc converters," *IEEE Transactions on Power Electronics*, pp. 98–116, 2017.

[13] Y.-S. Lin, K.-W. Hu, T.-H. Yeh, and C.-M. Liaw, "An electric-vehicle ipmsm drive with interleaved front-end DC/dc converter," *IEEE Transactions on Vehicular Technology*, pp. 4493–4504, 2016.

[14] N. M. L. Tan, T. Abe, and H. Akagi, "Design and performance of a bidirectional isolated DC–dc converter for a battery energy storage system," *IEEE Transactions on Power Electronics*, pp. 1237–1248, 2012.

[15] T. Schoenen, M. S. Kunter, M. D. Hennen, and R. W. De Doncker, "Advantages of a variable DC-link voltage by using a DC-dc converter in hybrid-electric vehicles," in *Proc. IEEE Vehicle Power and Propulsion Conf*, 2010, pp. 1–5.

[16] S. Kinoshita, K. Fujita, and J. Ito, "Electric system for electric vehicle," U.S. Patent, 2000.

[17] S. Sumikazu, S. Shoichi, E. Sato, K. Masayuki, M. Kazunari, O. Hiroki, and I. Yukio, "Power output device," U.S. Patent, 2003.

[18] H. Nakai, K. Moriya, H. Ohtani, H. Fuma, and Y. Inaguma, "Overview of multi-functional converter systems," *R&D Review of Toyota CRDL*, pp. 27–32, 2004.

[19] K. Moriya, H. Nakai, Y. Inaguma, H. Ohtani, and S. Sasaki, "A novel multi-functional converter system equipped with input voltage regulation and current ripple suppression," in *Proc. Fourtieth IAS Annual Meeting. Conf. Record of the 2005 Industry Applications Conf*, 2005, pp. 1636–1642.

[20] A. Shetty, B. G. Fernandes, J. O. Ojo, and J. A. Ferreira, "Three phase PWM rectifier with integrated battery for automotive applications," in *Proc. IEEE Industry Applications Society Annual Meeting (IAS)*, 2018, pp. 1–6.

[21] D. Tschanz, H. Lovatt, A. Vezzini, and V. Perrenoud, "A multi-functional converter for a reduced cost, solar powered, water pump," in *Proc. IEEE Int. Symp. Industrial Electronics*, 2010, pp. 568–572.

[22] T. Hackner and J. Pforr, "Optimization of the winding arrangement to increase the leakage inductance of a synchronous machine with multi-functional converter drive," in *Proc. IEEE Energy Conversion Congress and Exposition*, 2011, pp. 1541–1548.

[23] T. Hackner, J. Pforr, H. Polinder, and J. A. Ferreira, "Optimization of the winding arrangement to increase the zero-sequence inductance of a synchronous machine with

multifunctional converter drive," *IEEE Transactions on Industry Applications*, pp. 2277–2286, 2012.

[24] J.-i. Itoh and D. Ikarashi, "Investigation of a two-stage boost converter using the neutral point of a motor," in *Proc. Int. Power Electronics Conf. - ECCE ASIA -*, 2010, pp. 1189–1194.

[25] ——, "Investigation of a two-stage boost converter using the neutral point of a motor," *IEEE Transactions on Industry Applications*, pp. 1392–1399, 2013.

[26] H. Plesko, J. Biela, J. Luomi, and J. W. Kolar, "Novel concepts for integrating the electric drive and auxiliary dc-dc converter for hybrid vehicles," in *Proc. APEC 07 - Twenty-Second Annual IEEE Applied Power Electronics Conf. and Exposition*, 2007, pp. 1025–1031.

[27] H. Plesko, J. Biela, J. Luomi, and J. W. Kolar, "Novel concepts for integrating the electric drive and auxiliary DC–dc converter for hybrid vehicles," *IEEE Transactions on Power Electronics*, pp. 3025–3034, 2008.

[28] H. Plesko, J. Biela, and J. W. Kolar, "Novel modulation concepts for a drive-integrated auxiliary dc-dc converter for hybrid vehicles," in *Proc. Twenty-Fourth Annual IEEE Applied Power Electronics Conf. and Exposition*, 2009, pp. 164–170.

[29] S.-K. Sul and S.-J. Lee, "An integral battery charger for four-wheel drive electric vehicle," *IEEE Transactions on Industry Applications*, pp. 1096–1099, 1995.

[30] L. Solero, "Nonconventional on-board charger for electric vehicle propulsion batteries," *IEEE Transactions on Vehicular Technology*, pp. 144–149, 2001.

[31] G. Pellegrino, E. Armando, and P. Guglielmi, "An integral battery charger with power factor correction for electric scooter," *IEEE Transactions on Power Electronics*, pp. 751–759, 2010.

[32] S. Haghbin, S. Lundmark, M. Alakula, and O. Carlson, "Grid-connected integrated battery chargers in vehicle applications: Review and new solution," *IEEE Transactions on Industrial Electronics*, pp. 459–473, 2013.

[33] Y. Xiao, C. Liu, and F. Yu, "An integrated on-board EV charger with safe charging operation for three-phase ipm motor," *IEEE Transactions on Industrial Electronics*, pp. 7551–7560, 2019.

[34] G Forstner, A Kugi, and W Kemmetmüller, "Fault-tolerant torque control of a three-phase permanent magnet synchronous motor with inter-turn winding short circuit," *Control Engineering Practice*, p. 104 846, 2021.

[35] S. Cheng and T. G. Habetler, "Using only the DC current information to detect stator turn faults in automotive claw-pole generators," *IEEE Transactions on Industrial Electronics*, pp. 3462–3471, 2013.

[36] Z. Gao, C. Cecati, and S. X. Ding, "A survey of fault diagnosis and fault-tolerant techniques—part ii: Fault diagnosis with knowledge-based and hybrid/active approaches," *IEEE Transactions on Industrial Electronics*, pp. 3768–3774, 2015.

[37] G. F. H. Beng, X. Zhang, and D. M. Vilathgamuwa, "Sensor fault-resilient control of interior permanent-magnet synchronous motor drives," *IEEE/ASME Transactions on Mechatronics*, pp. 855–864, 2015.

[38] B. Lu and S. K. Sharma, "A literature review of IGBT fault diagnostic and protection methods for power inverters," *IEEE Transactions on Industry Applications*, pp. 1770–1777, 2009.

[39] M. Riera-Guasp, J. A. Antonino-Daviu, and G.-A. Capolino, "Advances in electrical machine, power electronic, and drive condition monitoring and fault detection: State of the art," *IEEE Transactions on Industrial Electronics*, pp. 1746–1759, 2015.

[40] H. Henao, G.-A. Capolino, M. Fernandez-Cabanas, F. Filippetti, C. Bruzzese, E. Strangas, R. Pusca, J. Estima, M. Riera-Guasp, and S. Hedayati-Kia, "Trends in fault diagnosis for electrical machines: A review of diagnostic techniques," *IEEE Industrial Electronics Magazine*, pp. 31–42, 2014.

[41] X. Zhou, J. Sun, H. Li, and X. Song, "High performance three-phase pmsm open-phase fault-tolerant method based on reference frame transformation," *IEEE Transactions on Industrial Electronics*, pp. 7571–7580, 2019.

[42] Y. Sui, P. Zheng, Z. Yin, M. Wang, and C. Wang, "Open-circuit fault-tolerant control of five-phase pm machine based on reconfiguring maximum round magnetomotive force," *IEEE Transactions on Industrial Electronics*, pp. 48–59, 2019.

[43] F.-J. Lin, Y.-C. Hung, and M.-T. Tsai, "Fault-tolerant control for six-phase pmsm drive system via intelligent complementary sliding-mode control using tskfnn-amf," *IEEE Transactions on Industrial Electronics*, pp. 5747–5762, 2013.

[44] A. S. Abdel-Khalik, M. S. Hamad, A. M. Massoud, and S. Ahmed, "Postfault operation of a nine-phase six-terminal induction machine under single open-line fault," *IEEE Transactions on Industrial Electronics*, pp. 1084–1096, 2018.

[45] D. Campos-Delgado, D. Espinoza-Trejo, and E. Palacios, "Fault-tolerant control in variable speed drives: A survey," *IET Electric Power Applications*, pp. 121–134, 2008.

[46] G. Scarcella, G. Scelba, M. Pulvirenti, and R. D. Lorenz, "Fault-tolerant capability of deadbeat-direct torque and flux control for three-phase pmsm drives," *IEEE Transactions on Industry Applications*, pp. 5496–5508, 2017.

[47] A. Gaeta, G. Scelba, and A. Consoli, "Modeling and control of three-phase pmsms under open-phase fault," *IEEE Transactions on Industry Applications*, pp. 74–83, 2013.

[48] N. Bianchi, S. Bolognani, M. Zigliotto, and M. Zordan, “Innovative remedial strategies for inverter faults in ipm synchronous motor drives,” *IEEE Transactions on Energy Conversion*, pp. 306–314, 2003.

[49] O. Wallmark, L. Harnefors, and O. Carlson, “Control algorithms for a fault-tolerant pmsm drive,” *IEEE Transactions on Industrial Electronics*, pp. 1973–1980, 2007.

[50] R. L. de Araujo Ribeiro, C. B. Jacobina, E. R. C. da Silva, and A. M. N. Lima, “Fault-tolerant voltage-fed PWM inverter AC motor drive systems,” *IEEE Transactions on Industrial Electronics*, pp. 439–446, 2004.

[51] M. Beltrao de Rossiter Correa, C. Brandao Jacobina, E. R. Cabral da Silva, and A. M. Nogueira Lima, “An induction motor drive system with improved fault tolerance,” *IEEE Transactions on Industry Applications*, pp. 873–879, 2001.

[52] R. R. Errabelli and P. Mutschler, “Fault-tolerant voltage source inverter for permanent magnet drives,” *IEEE Transactions on Power Electronics*, pp. 500–508, 2012.

[53] J.-H. Kim and S.-K. Sul, “A carrier-based PWM method for three-phase four-leg voltage source converters,” *IEEE Transactions on Power Electronics*, pp. 66–75, 2004.

[54] X. Zhou, J. Sun, H. Li, M. Lu, and F. Zeng, “Pmsm open-phase fault-tolerant control strategy based on four-leg inverter,” *IEEE Transactions on Power Electronics*, pp. 2799–2808, 2020.

[55] M. Tousizadeh, H. S. Che, J. Selvaraj, N. A. Rahim, and B.-T. Ooi, “Fault-tolerant field-oriented control of three-phase induction motor based on unified feedforward method,” *IEEE Transactions on Power Electronics*, pp. 7172–7183, 2019.

[56] W. Zhang, D. Xu, P. N. Enjeti, H. Li, J. T. Hawke, and H. S. Krishnamoorthy, “Survey on fault-tolerant techniques for power electronic converters,” *IEEE Transactions on Power Electronics*, pp. 6319–6331, 2014.

[57] L. Wu, Y. Guo, X. Huang, Y. Fang, and J. Liu, “Harmonic torque suppression methods for single-phase open-circuit fault-tolerant operation of pmsm considering third harmonic bemf,” *IEEE Transactions on Power Electronics*, pp. 1116–1129, 2021.

[58] M. Naidu, S. Gopalakrishnan, and T. W. Nehl, “Fault-tolerant permanent magnet motor drive topologies for automotive x-by-wire systems,” *IEEE Transactions on Industry Applications*, pp. 841–848, 2010.

[59] F. Meinguet, E. Semail, and J. Gyselinck, “Enhanced control of a pmsm supplied by a four-leg voltage source inverter using the homopolar torque,” in *Proc. 18th Int. Conf. Electrical Machines*, 2008, pp. 1–6.

[60] M. Farhadi, M. T. Fard, M. Abapour, and M. T. Hagh, “DC–ac converter-fed induction motor drive with fault-tolerant capability under open- and short-circuit switch failures,” *IEEE Transactions on Power Electronics*, pp. 1609–1621, 2018.

[61] H. Tang, W. Li, J. Li, H. Gao, Z. Wu, and X. Shen, "Calculation and analysis of the electromagnetic field and temperature field of the pmsm based on fault-tolerant control of four-leg inverters," *IEEE Transactions on Energy Conversion*, pp. 2141–2151, 2020.

[62] Y. Zhao and T. A. Lipo, "An approach to modeling and field-oriented control of a three phase induction machine with structural imbalance," in *Proc. Applied Power Electronics Conf.. APEC '96*, 1996, 380–386 vol.1.

[63] C. M. Hackl, U. Pecha, and K. Schechner, "Modeling and control of permanent-magnet synchronous generators under open-switch converter faults," *IEEE Transactions on Power Electronics*, pp. 2966–2979, 2019.

[64] K. Hu, Z. Liu, Y. Yang, F. Iannuzzo, and F. Blaabjerg, "Ensuring a reliable operation of two-level IGBT-based power converters: A review of monitoring and fault-tolerant approaches," *IEEE Access*, pp. 89 988–90 022, 2020.

[65] B. A. Welchko, T. A. Lipo, T. M. Jahns, and S. E. Schulz, "Fault tolerant three-phase AC motor drive topologies: A comparison of features, cost, and limitations," *IEEE Transactions on Power Electronics*, pp. 1108–1116, 2004.

[66] B. Mirafzal, "Survey of fault-tolerance techniques for three-phase voltage source inverters," *IEEE Transactions on Industrial Electronics*, pp. 5192–5202, 2014.

[67] M. S. Zaky and M. K. Metwaly, "A performance investigation of a four-switch three-phase inverter-fed im drives at low speeds using fuzzy logic and pi controllers," *IEEE Transactions on Power Electronics*, pp. 3741–3753, 2017.

[68] Y. Hu, L. Zhang, W. Huang, and F. Bu, "A fault-tolerant induction generator system based on instantaneous torque control (itc)," *IEEE Transactions on Energy Conversion*, pp. 412–421, 2010.

[69] C. Zhu, Z. Zeng, and R. Zhao, "Comprehensive analysis and reduction of torque ripples in three-phase four-switch inverter-fed pmsm drives using space vector pulse-width modulation," *IEEE Transactions on Power Electronics*, pp. 5411–5424, 2017.

[70] K. Hu, Z. Liu, I. A. Tasiu, and T. Chen, "Fault diagnosis and tolerance with low torque ripple for open-switch fault of im drives," *IEEE Transactions on Transportation Electrification*, pp. 133–146, 2021.

[71] T.-H. Liu, J.-R. Fu, and T. A. Lipo, "A strategy for improving reliability of field-oriented controlled induction motor drives," *IEEE Transactions on Industry Applications*, pp. 910–918, 1993.

[72] S. Bolognani, M. Zordan, and M. Zigliotto, "Experimental fault-tolerant control of a pmsm drive," *IEEE Transactions on Industrial Electronics*, pp. 1134–1141, 2000.

[73] A. Kiselev, G. R. Catuogno, A. Kuznietsov, and R. Leidhold, “Finite-control-set MPC for open-phase fault-tolerant control of pm synchronous motor drives,” *IEEE Transactions on Industrial Electronics*, pp. 4444–4452, 2020.

[74] Y. Guo, L. Wu, X. Huang, Y. Fang, and J. Liu, “Adaptive torque ripple suppression methods of three-phase pmsm during single-phase open-circuit fault-tolerant operation,” *IEEE Transactions on Industry Applications*, pp. 4955–4965, 2020.

[75] A. M. S. Mendes and A. J. Marques Cardoso, “Fault-tolerant operating strategies applied to three-phase induction-motor drives,” *IEEE Transactions on Industrial Electronics*, pp. 1807–1817, 2006.

[76] F. Meinguet and J. Gyselinck, “Control strategies and reconfiguration of four-leg inverter pmsm drives in case of single-phase open-circuit faults,” in *Proc. IEEE Int. Electric Machines and Drives Conf*, 2009, pp. 299–304.

[77] M. Tousizadeh, H. S. Che, J. Selvaraj, N. A. Rahim, and B.-T. Ooi, “Performance comparison of fault-tolerant three-phase induction motor drives considering current and voltage limits,” *IEEE Transactions on Industrial Electronics*, pp. 2639–2648, 2019.

[78] M.-C. Wong, J. Tang, N.-Y. Dai, and Y.-D. Han, “Fundamental study of 3 dimensional pulse width modulation,” in *Proc. Int. Conf. Power System Technology*, 2002, 560–564 vol.1.

[79] M. Abassi, A. Khlaief, O. Saadaoui, A. Chaari, and M. Boussak, “Performance analysis of foc and dtc for pmsm drives using svpwm technique,” in *Proc. 16th Int. Conf. Sciences and Techniques of Automatic Control and Computer Engineering (STA)*, 2015, pp. 228–233.

[80] L. Xiao, J. Li, Y. Xiong, J. Chen, and H. Gao, “Strategy and implementation of harmonic-reduced synchronized svpwm for high-power traction machine drives,” *IEEE Transactions on Power Electronics*, pp. 12 457–12 471, 2020.

[81] S. R. Bowes and Y.-S. Lai, “The relationship between space-vector modulation and regular-sampled PWM,” *IEEE Transactions on Industrial Electronics*, pp. 670–679, 1997.

[82] C. Zeng, D. Liu, and Q. Liao, “Simulation research of space vector PWM based on harmonic injection,” in *Proc. 4th IEEE Conf. Industrial Electronics and Applications*, 2009, pp. 2312–2315.

[83] W. Liang, J. Wang, P. C.-K. Luk, W. Fang, and W. Fei, “Analytical modeling of current harmonic components in pmsm drive with voltage-source inverter by svpwm technique,” *IEEE Transactions on Energy Conversion*, pp. 673–680, 2014.

[84] T. Jun, “Analysis of inductor-current of boost dc-dc converters and its design for intrinsic safety,” in *2010 International Conference on Electrical and Control Engineering*, IEEE, 2010, pp. 430–432.

[85] Q. Wang and T. Gao, "Boost inductor optimizing design based on finite element simulation," in *Proc. Electronic and Automation (ICCNEA) 2017 Int. Conf. Computer Network*, 2017, pp. 336–340.

[86] R.-J. Wai and L.-C. Shih, "Design of voltage tracking control for DC–dc boost converter via total sliding-mode technique," *IEEE Transactions on Industrial Electronics*, pp. 2502–2511, 2011.

[87] S. Oucheriah and L. Guo, "PWM-based adaptive sliding-mode control for boost DC–dc converters," *IEEE Transactions on Industrial Electronics*, pp. 3291–3294, 2013.

[88] Y. I. Son and I. H. Kim, "Complementary PID controller to passivity-based nonlinear control of boost converters with inductor resistance," *IEEE Transactions on Control Systems Technology*, pp. 826–834, 2012.

[89] S. Pang, B. Nahid-Mobarakeh, S. Pierfederici, M. Phattanasak, Y. Huangfu, G. Luo, and F. Gao, "Interconnection and damping assignment passivity-based control applied to on-board DC–dc power converter system supplying constant power load," *IEEE Transactions on Industry Applications*, pp. 6476–6485, 2019.

[90] P. Thounthong, "Control of a three-level boost converter based on a differential flatness approach for fuel cell vehicle applications," *IEEE Transactions on Vehicular Technology*, pp. 1467–1472, 2012.

[91] J. R. García-Sánchez, E. Hernández-Márquez, J. Ramírez-Morales, M. Marciano-Melchor, M. Marcelino-Aranda, H. Taud, and R. Silva-Ortigoza, "A robust differential flatness-based tracking control for the "mimo DC/dc boost converter–inverter–dc motor" system: Experimental results," *IEEE Access*, pp. 84 497–84 505, 2019.

[92] M. Fliess, J. Lévine, P. Martin, and P. Rouchon, "Flatness and defect of non-linear systems: Introductory theory and examples," *International journal of control*, pp. 1327–1361, 1995.

[93] G. G. Rigatos, *Nonlinear control and filtering using differential flatness approaches: applications to electromechanical systems*. Springer, 2015.

[94] P. Thounthong, S. Sikkabut, N. Poonnoy, P. Mungporn, B. Yodwong, P. Kumam, N. Bizon, B. Nahid-Mobarakeh, and S. Pierfederici, "Nonlinear differential flatness-based speed/torque control with state-observers of permanent magnet synchronous motor drives," *IEEE Transactions on Industry Applications*, pp. 2874–2884, 2018.

[95] A. Shahin, H. Moussa, I. Forrisi, J.-P. Martin, B. Nahid-Mobarakeh, and S. Pierfederici, "Reliability improvement approach based on flatness control of parallel-connected inverters," *IEEE Transactions on Power Electronics*, pp. 681–692, 2017.

[96] P. Thounthong, S. Pierfederici, and B. Davat, "Analysis of differential flatness-based control for a fuel cell hybrid power source," *IEEE Transactions on Energy Conversion*, pp. 909–920, 2010.

[97] L. Gil-Antonio, B. Saldivar, O. Portillo-Rodríguez, G. Vázquez-Guzmán, and S. M. De Oca-Armeaga, "Trajectory tracking control for a boost converter based on the differential flatness property," *IEEE Access*, pp. 63 437–63 446, 2019.

[98] M. P. Kazmierkowski and L. Malesani, "Current control techniques for three-phase voltage-source PWM converters: A survey," *IEEE Transactions on Industrial Electronics*, pp. 691–703, 1998.

[99] M. S. R. Saeed, W. Song, B. Yu, and X. Wu, "Low-complexity deadbeat model predictive current control with duty ratio for five-phase pmsm drives," *IEEE Transactions on Power Electronics*, pp. 12 085–12 099, 2020.

[100] P. Cortes, M. P. Kazmierkowski, R. M. Kennel, D. E. Quevedo, and J. Rodriguez, "Predictive control in power electronics and drives," *IEEE Transactions on Industrial Electronics*, pp. 4312–4324, 2008.

[101] M. A. Perez, J. Rodriguez, E. J. Fuentes, and F. Kammerer, "Predictive control of AC–ac modular multilevel converters," *IEEE Transactions on Industrial Electronics*, pp. 2832–2839, 2012.

[102] F. Donoso, A. Mora, R. Cárdenas, A. Angulo, D. Sáez, and M. Rivera, "Finite-set model-predictive control strategies for a 3l-npc inverter operating with fixed switching frequency," *IEEE Transactions on Industrial Electronics*, pp. 3954–3965, 2018.

[103] X. Zhang, L. Zhang, and Y. Zhang, "Model predictive current control for pmsm drives with parameter robustness improvement," *IEEE Transactions on Power Electronics*, pp. 1645–1657, 2019.

[104] M. Fliess, J. Levine, P. Martin, and P. Rouchon, "A lie-backlund approach to equivalence and flatness of nonlinear systems," *IEEE Transactions on Automatic Control*, pp. 922–937, 1999.

[105] D. Faustner, W. Kemmetmüller, and A. Kugi, "Flatness-based torque control of saturated surface-mounted permanent magnet synchronous machines," *IEEE Transactions on Control Systems Technology*, pp. 1201–1213, 2016.

[106] V. M. Hernández-Guzmán, R. Silva-Ortigoza, and J. Orrante-Sakanassi, "Velocity control of a pmsm fed by an inverter-DC/dc buck power electronic converter," *IEEE Access*, pp. 69 448–69 460, 2020.

[107] S.-C. Yang, Y.-L. Hsu, P.-H. Chou, G.-R. Chen, and D.-R. Jian, "Online open-phase fault detection for permanent magnet machines with low fault harmonic magnitudes," *IEEE Transactions on Industrial Electronics*, pp. 4039–4050, 2018.

[108] A. Kontarček, P. Bajec, M. Nemec, V. Ambrožič, and D. Nedeljković, "Cost-effective three-phase pmsm drive tolerant to open-phase fault," *IEEE Transactions on Industrial Electronics*, pp. 6708–6718, 2015.

FOLIO ADMINISTRATIF

THESE DE L'UNIVERSITE DE LYON OPEREE AU SEIN DE L'INSA LYON

NOM : ZHANG DATE de SOUTENANCE : 24/03/2022

Prénoms : Xiaokang

TITRE : Multi-functional converter for three-phase motor drives: modeling, analysis and fault-tolerant Control (Convertisseur multifonctionnel pour l'alimentation des moteurs triphasés : modélisation, analyse et commande tolérante aux fautes)

NATURE : Doctorat Numéro d'ordre : 2022LYSEI021

Ecole doctorale : ÉLECTRONIQUE, ÉLECTROTECHNIQUE et AUTOMATIQUE (EEA)

Spécialité : Génie Electrique

RESUME : Cette thèse porte sur un système d'entraînement de machine synchrone à aimants permanents triphasée alimentée par un onduleur qui intègre un étage de conversion continu/continu, en utilisant le point neutre de la machine. Cette architecture, appelée système de convertisseur multifonctionnel (MFCS), peut être avantageusement utilisée dans des applications de traction automobile dans le cas où une élévation de tension est nécessaire. Premièrement, une analyse approfondie est présentée afin de comprendre et de modéliser le MFCS. Une méthode de modulation spécifique est, de plus, proposée utilisant la particularité que le courant homopolaire n'est pas nul. Deuxièmement, deux nouvelles variantes nommées MFCS-I et MFCS-II ont été conçues afin d'améliorer le MFCS de base. Pour la première, une inductance en série est ajoutée pour diminuer l'ondulation du courant. Pour la seconde, l'ajout d'un bras d'onduleur auxiliaire améliore le rapport d'élévati on effectif de la tension. Pour contrôler ces variantes de MFCSs, une stratégie de commande universelle est développée dans laquelle une commande vectorielle peut être prise en compte pour la fonction moteur et un contrôleur basé sur la platitude différentielle est utilisé pour réguler la tension du bus continu. Troisièmement, compte tenu de la connexion intrinsèque du point neutre dans le MFCS-I, son potentiel de tolérance aux fautes contre un défaut de phase ouverte est exploré pour la première fois. Une étude théorique permet de formuler les conditions pour atteindre cette propriété et une nouvelle trajectoire vectorielle de courant est proposée, générant un couple constant et une tension moyenne stable du bus continu après un défaut. Pour finir, les idées et les stratégies de contrôle présentées ci-dessus sont systématiquement validées expérimentalement sur des plateformes de prototypage rapide de lois de commande.

MOTS-CLÉS : Système de convertisseur multifonctionnel, machine synchrone à aimants permanents triphasée, point neutre, commande tolérante aux fautes.

Laboratoire (s) de recherche : Laboratoire Ampère – UMR CNRS 5005 – INSA Lyon

Directeur de thèse: LIN-SHI Xuefang

Président de jury : DIALLO Demba

Composition du jury :

Rapporteurs :	NAHID-MOBARAKEH Babak, BETHOUX Olivier
Examinateur :	DIALLO Demba
Directrice de thèse :	LIN-SHI Xuefang
Co-encadrants de thèse :	GAUTHIER Jean-Yves